Detonation and hypersonics simulation with AMROC – Part I

Ralf Deiterding

Aerodynamics and Flight Mechanics Research Group
University of Southampton
Highfield Campus
Southampton SO17 1BJ, UK
Email: r.deiterding@soton.ac.uk

Xiamen
23rd July, 2019

Outline

Adaptive Cartesian finite volume methods
- Block-structured AMR with complex boundaries
- Parallelization approach

Combustion modeling
- Governing equations
- Finite volume schemes

Detonation simulation
- Shock induced combustion from projectile flight
- Thermal ignition
- Propagation of regular detonations in 2d
- Cellular structures in 3d and their ignition
- Detonation-boundary layer interaction

Summary
- Conclusions

Collaboration with

Detonations

- Bok Jik Lee (Gwangju Institute of Science and Technology, South Korea)
- Xiaodong Cai, Jiang Liang, Zhiyong Lin (National University of Defense Technology, Changsha)
- Jack Ziegler (now Northrop Grumman), Dale Pullin, Joe Shepherd (Graduate Aeronautical Laboratory, California Institute of Technology)
- Yong Sun, Matthias Ihme (Stanford University)

Hypersonics simulation

- Chay Atkins, Adriano Cerminara, Neil Sandham (University of Southampton)

Block-structured adaptive mesh refinement (SAMR)

For simplicity $\partial_t \mathbf{q}(x,y,t) + \partial_x \mathbf{f}(\mathbf{q}(x,y,t)) + \partial_y \mathbf{g}(\mathbf{q}(x,y,t)) = 0$

- Refined blocks overlay coarser ones

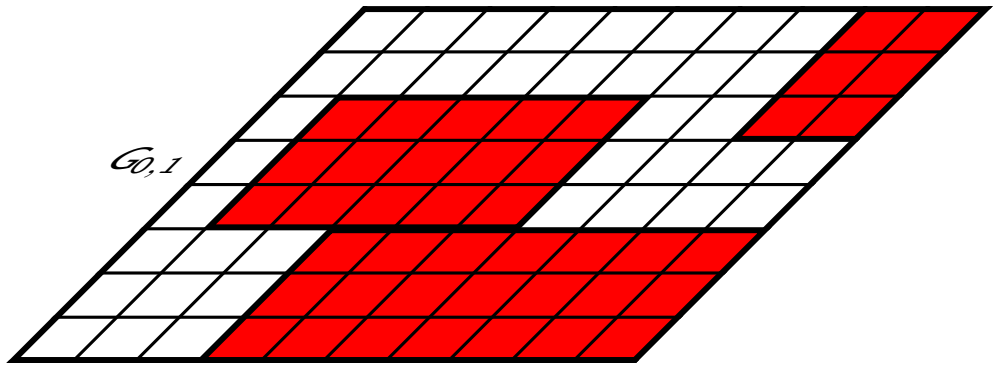

Block-structured adaptive mesh refinement (SAMR)

For simplicity $\partial_t \mathbf{q}(x,y,t) + \partial_x \mathbf{f}(\mathbf{q}(x,y,t)) + \partial_y \mathbf{g}(\mathbf{q}(x,y,t)) = 0$

- Refined blocks overlay coarser ones

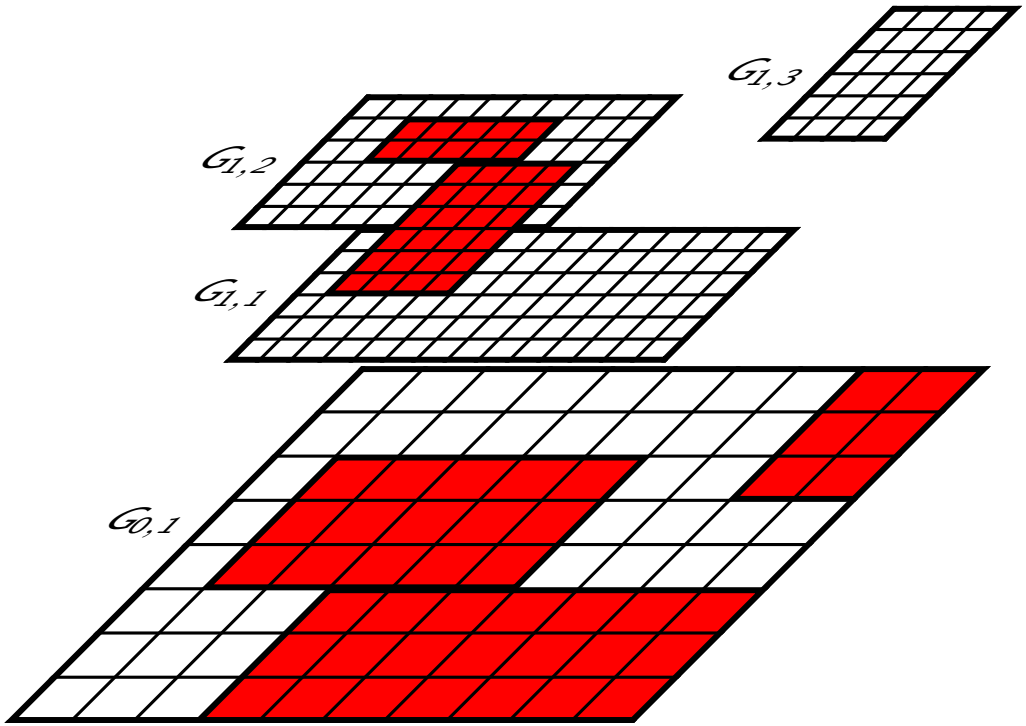

Block-structured adaptive mesh refinement (SAMR)

For simplicity $\partial_t \mathbf{q}(x,y,t) + \partial_x \mathbf{f}(\mathbf{q}(x,y,t)) + \partial_y \mathbf{g}(\mathbf{q}(x,y,t)) = 0$

- Refined blocks overlay coarser ones

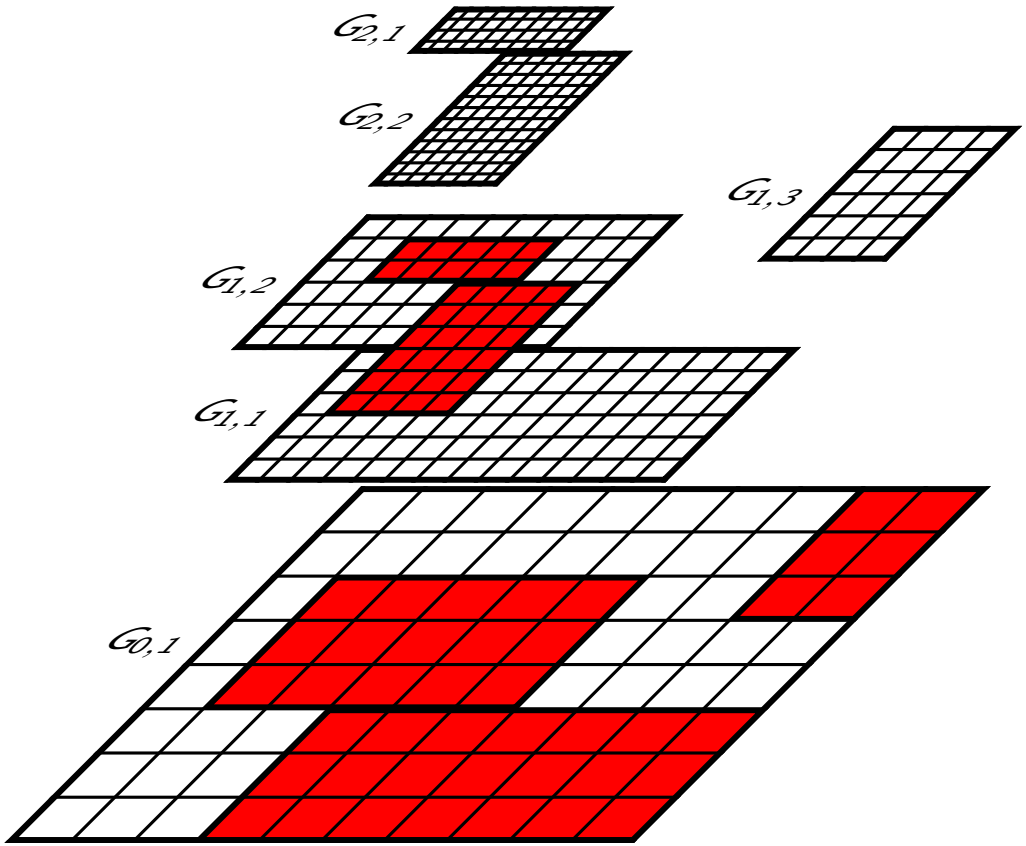

Block-structured adaptive mesh refinement (SAMR)

For simplicity $\partial_t \mathbf{q}(x,y,t) + \partial_x \mathbf{f}(\mathbf{q}(x,y,t)) + \partial_y \mathbf{g}(\mathbf{q}(x,y,t)) = 0$

- Refined blocks overlay coarser ones
- Refinement in space *and time* by factor r_l [Berger and Colella, 1988]
- Block (aka patch) based data structures
- \+ Numerical scheme

$$\mathbf{Q}_{jk}^{n+1} = \mathbf{Q}_{jk}^{n} - \frac{\Delta t}{\Delta x}\left[\mathbf{F}_{j+\frac{1}{2},k} - \mathbf{F}_{j-\frac{1}{2},k}\right] - \frac{\Delta t}{\Delta y}\left[\mathbf{G}_{j,k+\frac{1}{2}} - \mathbf{G}_{j,k-\frac{1}{2}}\right]$$

only for single patch necessary

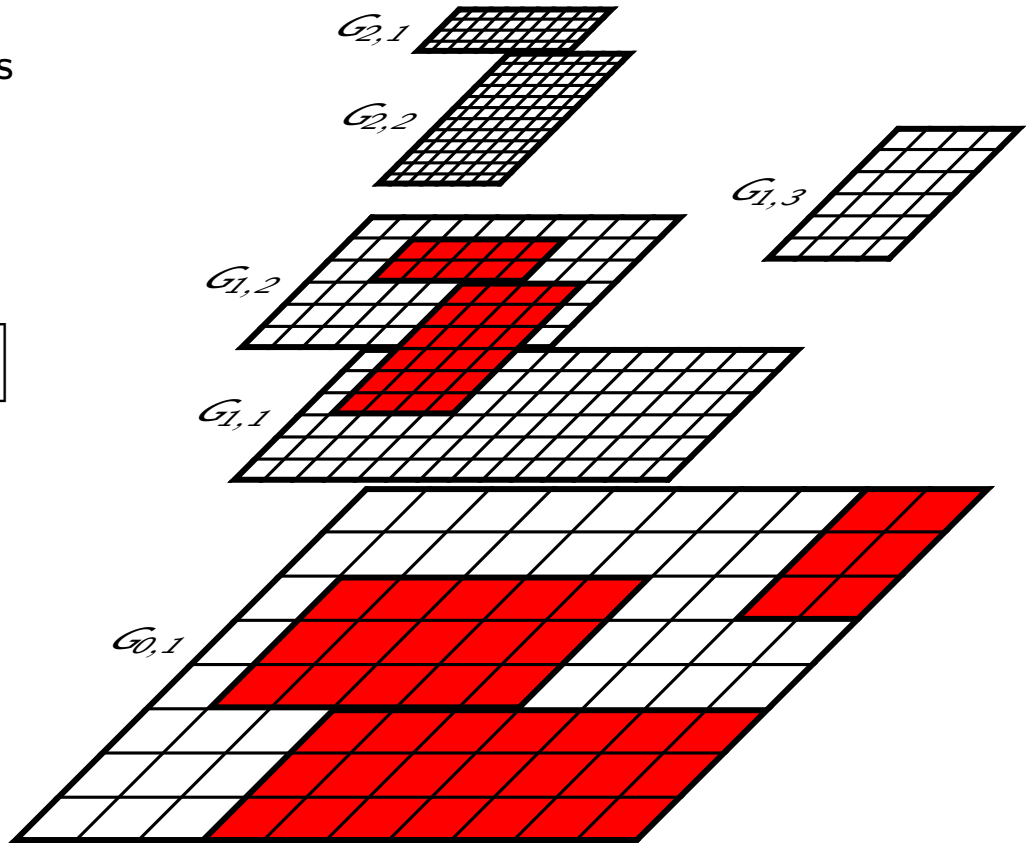

Block-structured adaptive mesh refinement (SAMR)

For simplicity $\partial_t \mathbf{q}(x,y,t) + \partial_x \mathbf{f}(\mathbf{q}(x,y,t)) + \partial_y \mathbf{g}(\mathbf{q}(x,y,t)) = 0$

- Refined blocks overlay coarser ones
- Refinement in space *and time* by factor r_l [Berger and Colella, 1988]
- Block (aka patch) based data structures
- \+ Numerical scheme

$$\mathbf{Q}_{jk}^{n+1} = \mathbf{Q}_{jk}^{n} - \frac{\Delta t}{\Delta x}\left[\mathbf{F}_{j+\frac{1}{2},k} - \mathbf{F}_{j-\frac{1}{2},k}\right] - \frac{\Delta t}{\Delta y}\left[\mathbf{G}_{j,k+\frac{1}{2}} - \mathbf{G}_{j,k-\frac{1}{2}}\right]$$

  only for single patch necessary
- \+ Efficient cache-reuse / vectorization possible
- \- Cluster-algorithm necessary
- Papers: [Deiterding, 2011a, Deiterding et al., 2009b, Deiterding et al., 2007]

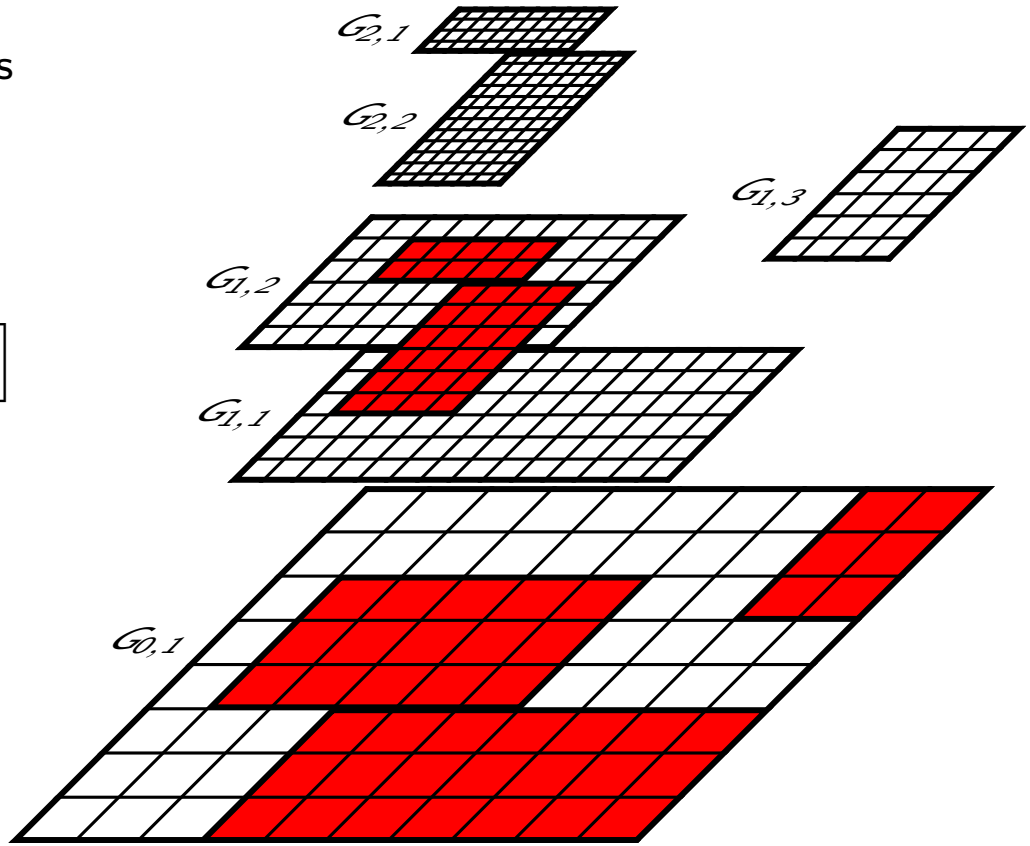

Level transfer / setting of ghost cells

Conservative averaging (restriction):

$$\hat{\mathbf{Q}}^{l}_{jk} := \frac{1}{(r_{l+1})^2} \sum_{\kappa=0}^{r_{l+1}-1} \sum_{\iota=0}^{r_{l+1}-1} \mathbf{Q}^{l+1}_{v+\kappa,w+\iota}$$

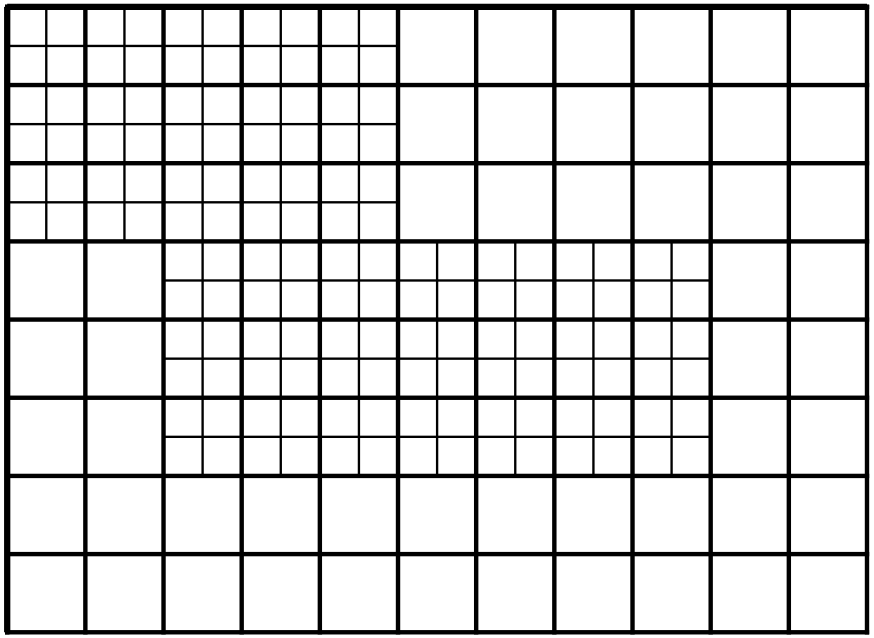

Level transfer / setting of ghost cells

Conservative averaging (restriction):

$$\hat{\mathbf{Q}}^{l}_{jk} := \frac{1}{(r_{l+1})^2} \sum_{\kappa=0}^{r_{l+1}-1} \sum_{\iota=0}^{r_{l+1}-1} \mathbf{Q}^{l+1}_{v+\kappa,w+\iota}$$

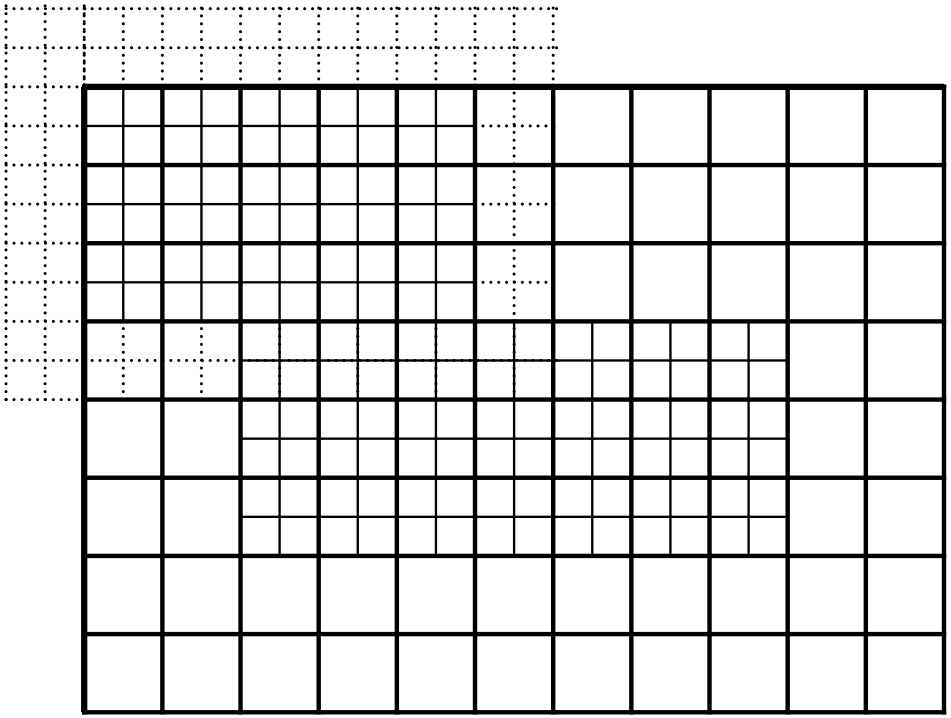

Level transfer / setting of ghost cells

Conservative averaging (restriction):

$$\hat{\mathbf{Q}}^{l}_{jk} := \frac{1}{(r_{l+1})^2} \sum_{\kappa=0}^{r_{l+1}-1} \sum_{\iota=0}^{r_{l+1}-1} \mathbf{Q}^{l+1}_{v+\kappa,w+\iota}$$

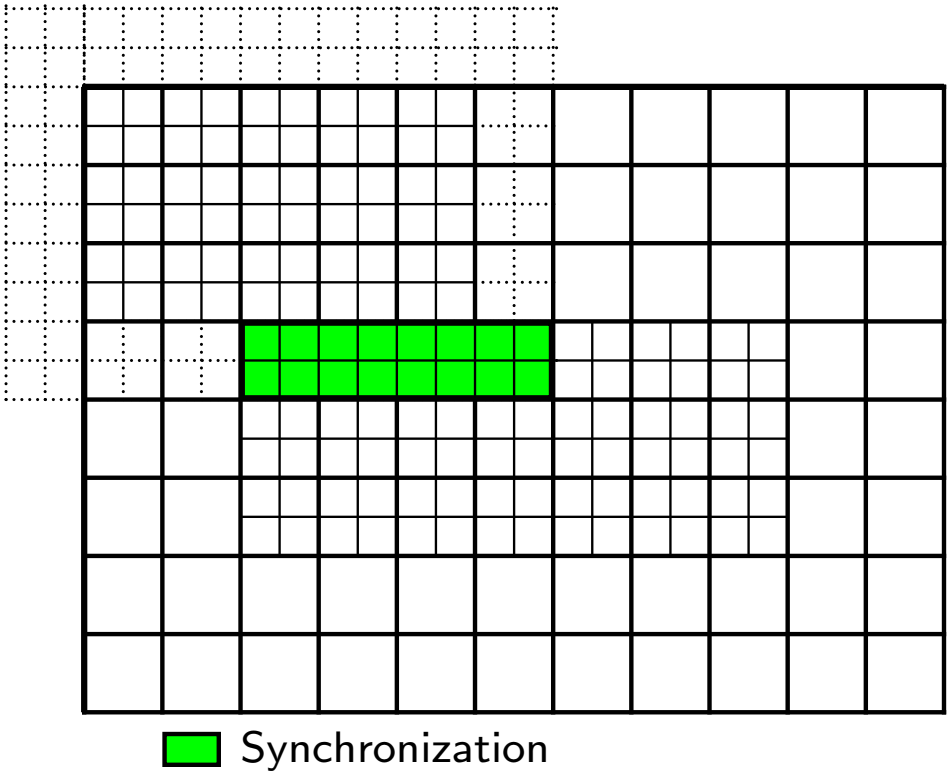

Level transfer / setting of ghost cells

Conservative averaging (restriction):

$$\hat{\mathbf{Q}}^{l}_{jk} := \frac{1}{(r_{l+1})^2} \sum_{\kappa=0}^{r_{l+1}-1} \sum_{\iota=0}^{r_{l+1}-1} \mathbf{Q}^{l+1}_{v+\kappa,w+\iota}$$

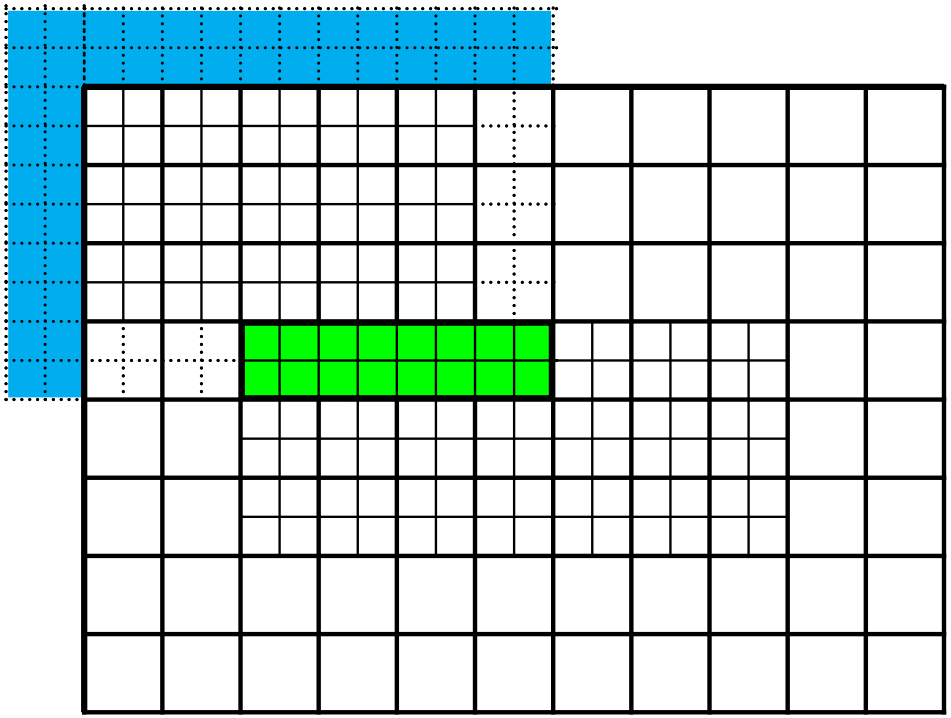

Level transfer / setting of ghost cells

Conservative averaging (restriction):

$$\hat{\mathbf{Q}}^{l}_{jk} := \frac{1}{(r_{l+1})^2} \sum_{\kappa=0}^{r_{l+1}-1} \sum_{\iota=0}^{r_{l+1}-1} \mathbf{Q}^{l+1}_{v+\kappa,w+\iota}$$

Bilinear interpolation (prolongation):

$$\begin{aligned}\check{\mathbf{Q}}^{l+1}_{vw} := {} & (1-f_1)(1-f_2)\,\mathbf{Q}^{l}_{j-1,k-1} \\ & + f_1(1-f_2)\,\mathbf{Q}^{l}_{j,k-1} + \\ & (1-f_1)f_2\,\mathbf{Q}^{l}_{j-1,k} + f_1 f_2\,\mathbf{Q}^{l}_{jk}\end{aligned}$$

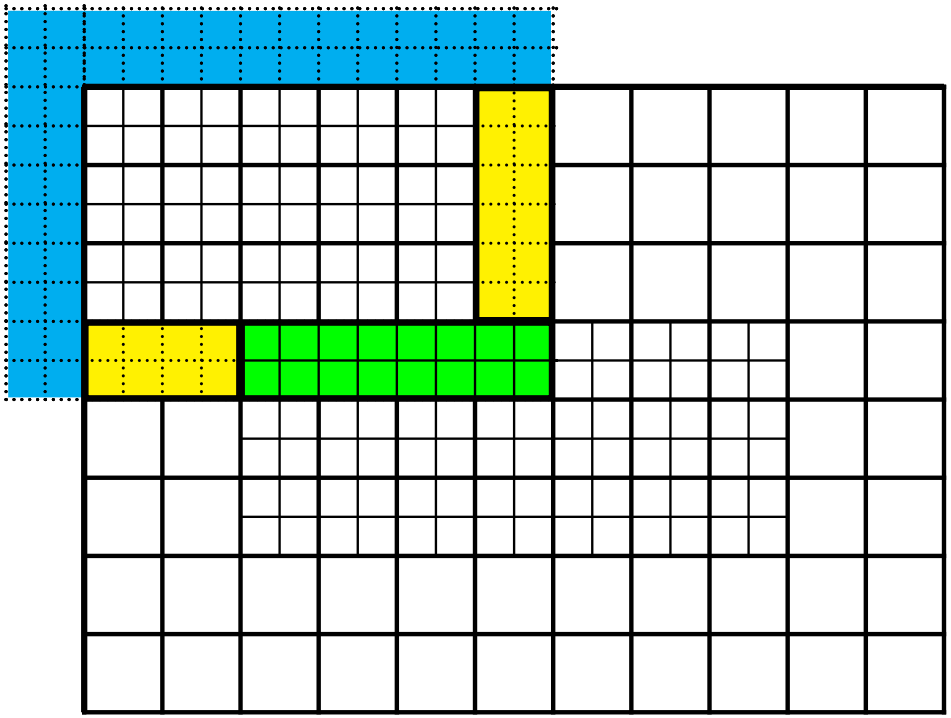

For boundary conditions: linear time interpolation

$$\tilde{\mathbf{Q}}^{l+1}(t+\kappa\Delta t_{l+1}) := \left(1-\frac{\kappa}{r_{l+1}}\right)\check{\mathbf{Q}}^{l+1}(t) + \frac{\kappa}{r_{l+1}}\check{\mathbf{Q}}^{l+1}(t+\Delta t_l) \quad \text{for } \kappa = 0,\ldots r_{l+1}$$

Recursive integration order

- Space-time interpolation of coarse data to set $I_l^s, l > 0$

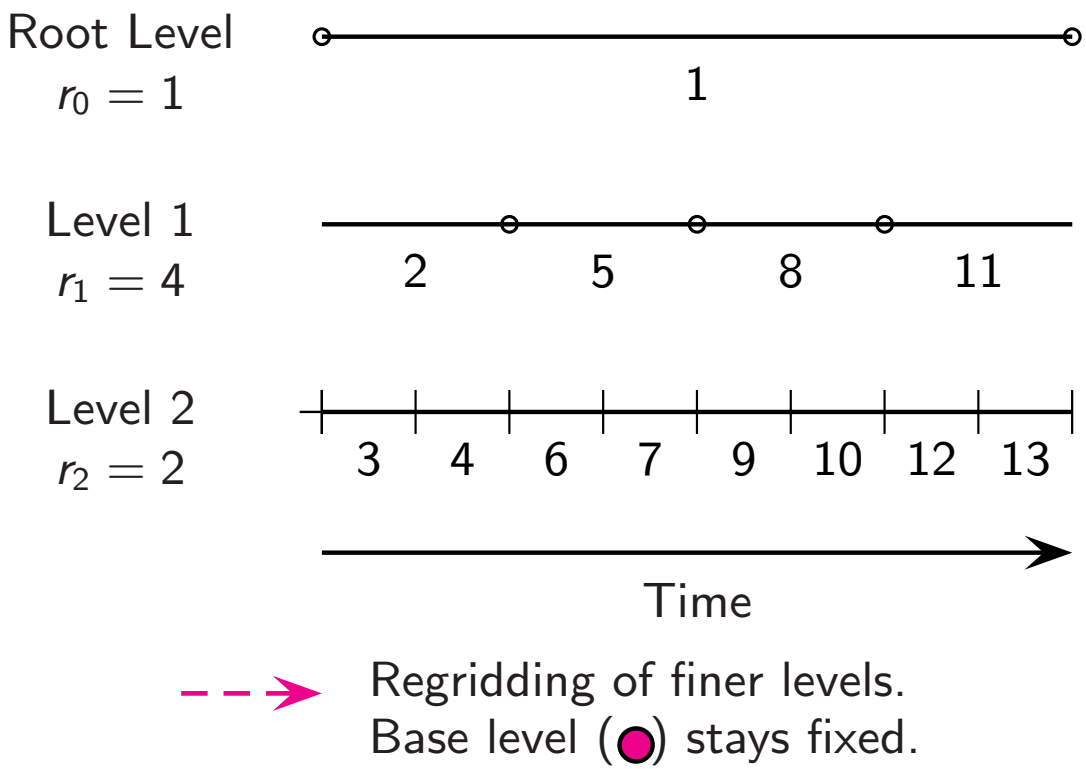

Recursive integration order

- Space-time interpolation of coarse data to set $I_l^s, l > 0$
- Regridding:
  - Creation of new grids, copy existing cells on level $l > 0$
  - Spatial interpolation to initialize new cells on level $l > 0$

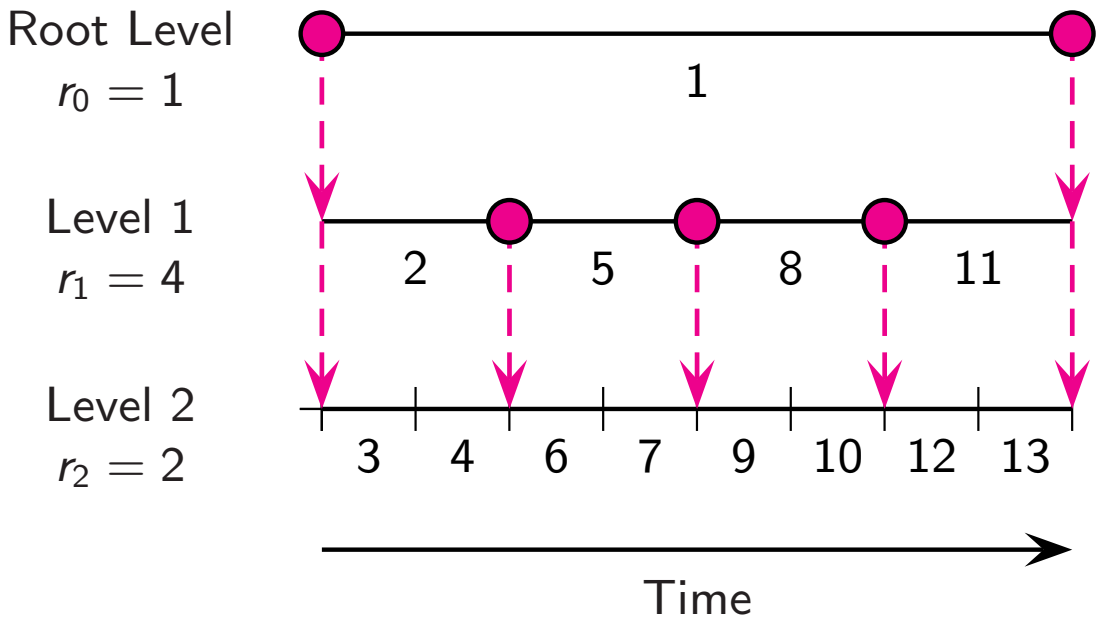

Conservative flux correction

Example: Cell j, k

$$\check{\mathbf{Q}}^l_{jk}(t+\Delta t_l) = \mathbf{Q}^l_{jk}(t) - \frac{\Delta t_l}{\Delta x_{1,l}} \left(\mathbf{F}^l_{j+\frac{1}{2},k} - \frac{1}{r^2_{l+1}} \sum_{\kappa=0}^{r_{l+1}-1} \sum_{\iota=0}^{r_{l+1}-1} \mathbf{F}^{l+1}_{v+\frac{1}{2},w+\iota}(t+\kappa\Delta t_{l+1}) \right)$$
$$- \frac{\Delta t_l}{\Delta x_{2,l}} \left(\mathbf{G}^l_{j,k+\frac{1}{2}} - \mathbf{G}^l_{j,k-\frac{1}{2}} \right)$$

Correction pass:

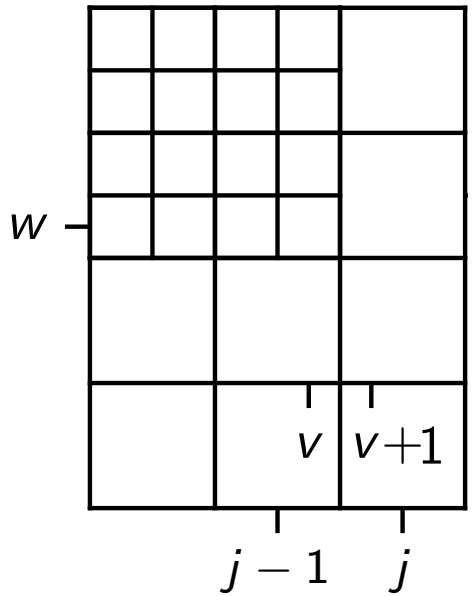

Conservative flux correction

Example: Cell j, k

$$\check{\mathbf{Q}}^l_{jk}(t+\Delta t_l) = \mathbf{Q}^l_{jk}(t) - \frac{\Delta t_l}{\Delta x_{1,l}} \left(\mathbf{F}^l_{j+\frac{1}{2},k} - \frac{1}{r^2_{l+1}} \sum_{\kappa=0}^{r_{l+1}-1} \sum_{\iota=0}^{r_{l+1}-1} \mathbf{F}^{l+1}_{v+\frac{1}{2},w+\iota}(t+\kappa\Delta t_{l+1}) \right)$$
$$- \frac{\Delta t_l}{\Delta x_{2,l}} \left(\mathbf{G}^l_{j,k+\frac{1}{2}} - \mathbf{G}^l_{j,k-\frac{1}{2}} \right)$$

Correction pass:

1. $\delta\mathbf{F}^{l+1}_{j-\frac{1}{2},k} := -\mathbf{F}^l_{j-\frac{1}{2},k}$

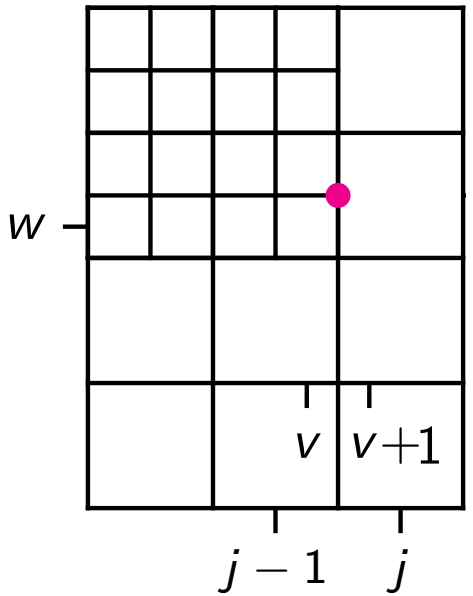

Conservative flux correction

Example: Cell j, k

$$\check{\mathbf{Q}}^l_{jk}(t+\Delta t_l) = \mathbf{Q}^l_{jk}(t) - \frac{\Delta t_l}{\Delta x_{1,l}} \left(\mathbf{F}^l_{j+\frac{1}{2},k} - \frac{1}{r^2_{l+1}} \sum_{\kappa=0}^{r_{l+1}-1} \sum_{\iota=0}^{r_{l+1}-1} \mathbf{F}^{l+1}_{v+\frac{1}{2},w+\iota}(t+\kappa\Delta t_{l+1}) \right)$$
$$- \frac{\Delta t_l}{\Delta x_{2,l}} \left(\mathbf{G}^l_{j,k+\frac{1}{2}} - \mathbf{G}^l_{j,k-\frac{1}{2}} \right)$$

Correction pass:

1. $\delta\mathbf{F}^{l+1}_{j-\frac{1}{2},k} := -\mathbf{F}^l_{j-\frac{1}{2},k}$
2. $\delta\mathbf{F}^{l+1}_{j-\frac{1}{2},k} := \delta\mathbf{F}^{l+1}_{j-\frac{1}{2},k} + \frac{1}{r^2_{l+1}} \sum_{\iota=0}^{r_{l+1}-1} \mathbf{F}^{l+1}_{v+\frac{1}{2},w+\iota}(t+\kappa\Delta t_{l+1})$

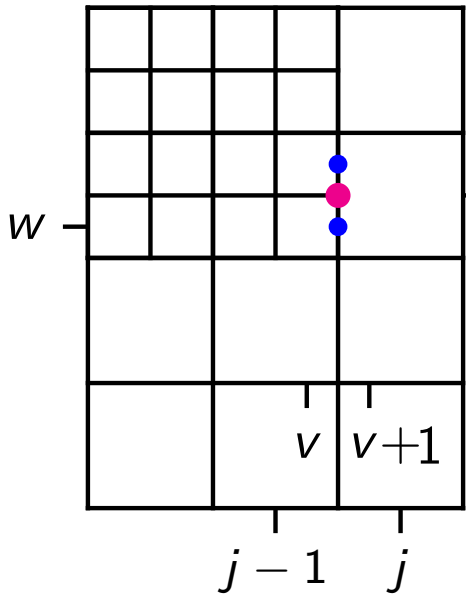

Conservative flux correction

Example: Cell j, k

$$\check{\mathbf{Q}}^l_{jk}(t+\Delta t_l) = \mathbf{Q}^l_{jk}(t) - \frac{\Delta t_l}{\Delta x_{1,l}} \left(\mathbf{F}^l_{j+\frac{1}{2},k} - \frac{1}{r^2_{l+1}} \sum_{\kappa=0}^{r_{l+1}-1} \sum_{\iota=0}^{r_{l+1}-1} \mathbf{F}^{l+1}_{v+\frac{1}{2},w+\iota}(t+\kappa\Delta t_{l+1}) \right)$$
$$- \frac{\Delta t_l}{\Delta x_{2,l}} \left(\mathbf{G}^l_{j,k+\frac{1}{2}} - \mathbf{G}^l_{j,k-\frac{1}{2}} \right)$$

Correction pass:

1. $\delta\mathbf{F}^{l+1}_{j-\frac{1}{2},k} := -\mathbf{F}^l_{j-\frac{1}{2},k}$
2. $\delta\mathbf{F}^{l+1}_{j-\frac{1}{2},k} := \delta\mathbf{F}^{l+1}_{j-\frac{1}{2},k} + \frac{1}{r^2_{l+1}} \sum_{\iota=0}^{r_{l+1}-1} \mathbf{F}^{l+1}_{v+\frac{1}{2},w+\iota}(t+\kappa\Delta t_{l+1})$
3. $\check{\mathbf{Q}}^l_{jk}(t+\Delta t_l) := \mathbf{Q}^l_{jk}(t+\Delta t_l) + \frac{\Delta t_l}{\Delta x_{1,l}} \delta\mathbf{F}^{l+1}_{j-\frac{1}{2},k}$

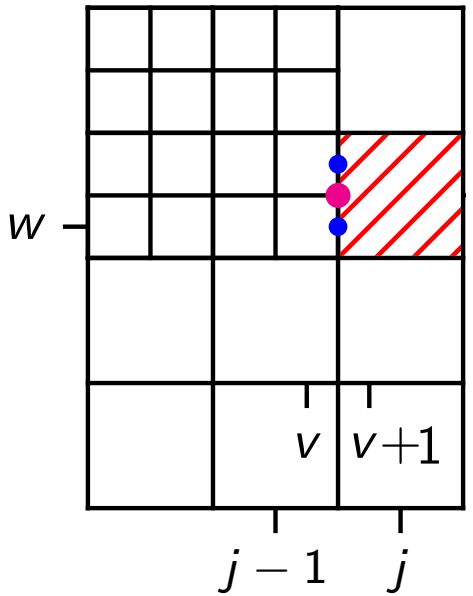

Level-set method for boundary embedding

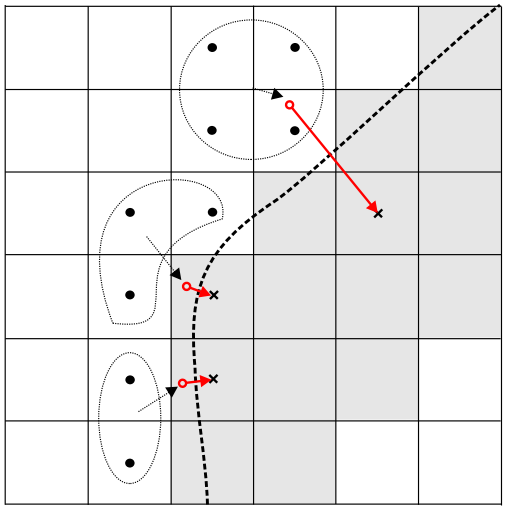

- Implicit boundary representation via distance function φ, normal $\mathbf{n} = \nabla\varphi/|\nabla\varphi|$
- Complex boundary moving with local velocity $\mathbf{w}$, treat interface as moving rigid wall [Deiterding et al., 2007]
- Construction of values in embedded boundary cells by interpolation / extrapolation [Deiterding, 2009, Deiterding, 2011a]
- Creation of level set from triangulated surface data with closest-point-transform (CPT) algorithm [Mauch, 2003, Deiterding et al., 2006]

Level-set method for boundary embedding

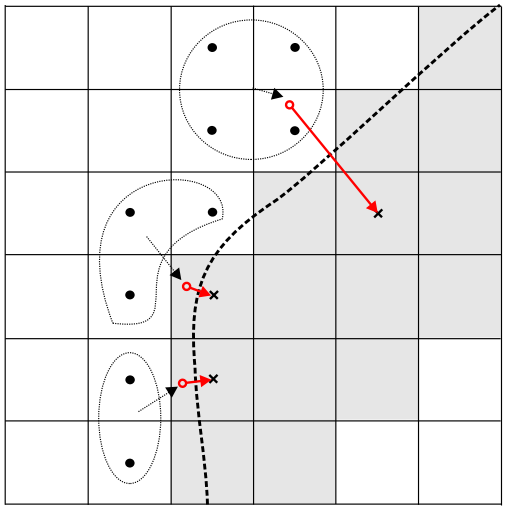

- Implicit boundary representation via distance function φ, normal $\mathbf{n} = \nabla\varphi/|\nabla\varphi|$
- Complex boundary moving with local velocity $\mathbf{w}$, treat interface as moving rigid wall [Deiterding et al., 2007]
- Construction of values in embedded boundary cells by interpolation / extrapolation [Deiterding, 2009, Deiterding, 2011a]
- Creation of level set from triangulated surface data with closest-point-transform (CPT) algorithm [Mauch, 2003, Deiterding et al., 2006]

Interpolate / constant value extrapolate values at

$$\tilde{\mathbf{x}} = \mathbf{x} + 2\varphi\mathbf{n}$$

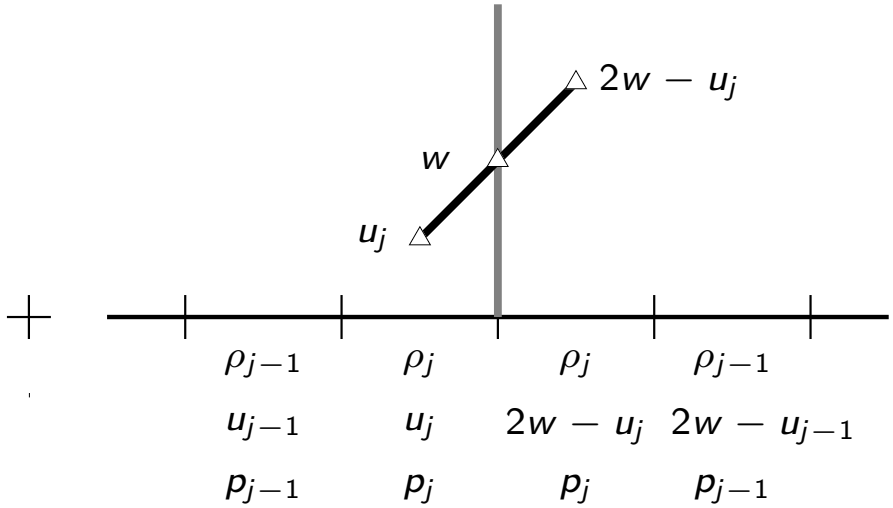

Level-set method for boundary embedding

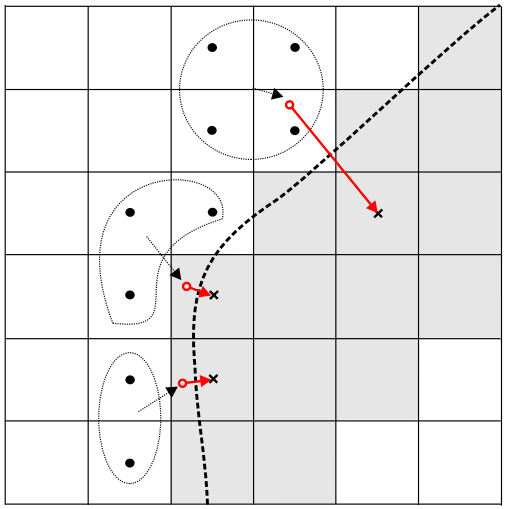

- Implicit boundary representation via distance function φ, normal $\mathbf{n} = \nabla\varphi/|\nabla\varphi|$
- Complex boundary moving with local velocity $\mathbf{w}$, treat interface as moving rigid wall [Deiterding et al., 2007]
- Construction of values in embedded boundary cells by interpolation / extrapolation [Deiterding, 2009, Deiterding, 2011a]
- Creation of level set from triangulated surface data with closest-point-transform (CPT) algorithm [Mauch, 2003, Deiterding et al., 2006]

Interpolate / constant value extrapolate values at

$$\tilde{\mathbf{x}} = \mathbf{x} + 2\varphi\mathbf{n}$$

Velocity in ghost cells (slip):

$$\begin{aligned}\mathbf{u}' &= (2\mathbf{w}\cdot\mathbf{n} - \mathbf{u}\cdot\mathbf{n})\mathbf{n} + (\mathbf{u}\cdot\mathbf{t})\mathbf{t} \\ &= 2\left((\mathbf{w}-\mathbf{u})\cdot\mathbf{n}\right)\mathbf{n} + \mathbf{u}\end{aligned}$$

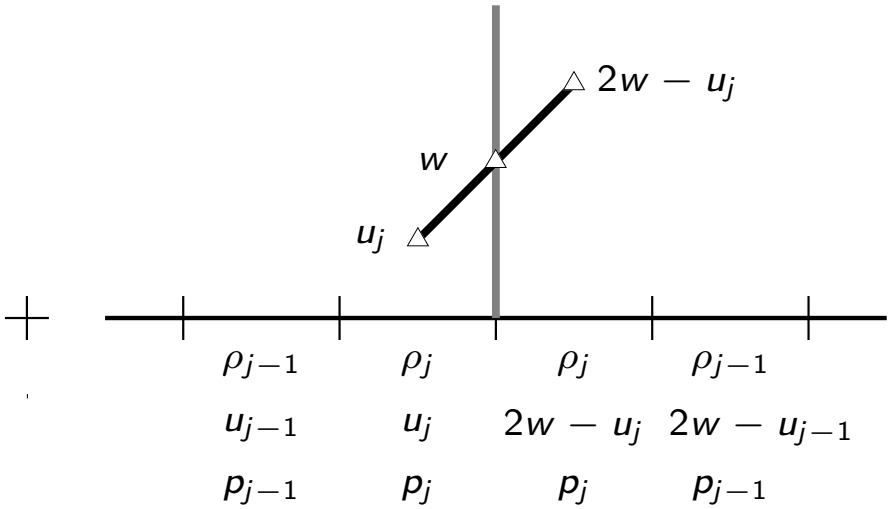

Parallelization

Rigorous domain decomposition

- Data of all levels resides on same node
- Grid hierarchy defines unique "floor-plan"
- Workload estimation

$$\mathcal{W}(\Omega) = \sum_{l=0}^{l_{\max}} \left[\mathcal{N}_l (G_l \cap \Omega) \prod_{\kappa=0}^{l} r_\kappa \right]$$

Parallelization

Rigorous domain decomposition

- Data of all levels resides on same node
- Grid hierarchy defines unique "floor-plan"
- Workload estimation

$$\mathcal{W}(\Omega) = \sum_{l=0}^{l_{\max}} \left[\mathcal{N}_l(G_l \cap \Omega) \prod_{\kappa=0}^{l} r_\kappa \right]$$

- Parallel operations
  - Synchronization of ghost cells
  - Redistribution of data blocks within regridding operation
  - Flux correction of coarse grid cells
- Dynamic partitioning with space-filling curve

Parallelization

Rigorous domain decomposition

- Data of all levels resides on same node
- Grid hierarchy defines unique "floor-plan"
- Workload estimation

$$\mathcal{W}(\Omega) = \sum_{l=0}^{l_{\max}} \left[\mathcal{N}_l(G_l \cap \Omega) \prod_{\kappa=0}^{l} r_\kappa \right]$$

- Parallel operations
  - Synchronization of ghost cells
  - Redistribution of data blocks within regridding operation
  - Flux correction of coarse grid cells
- Dynamic partitioning with space-filling curve

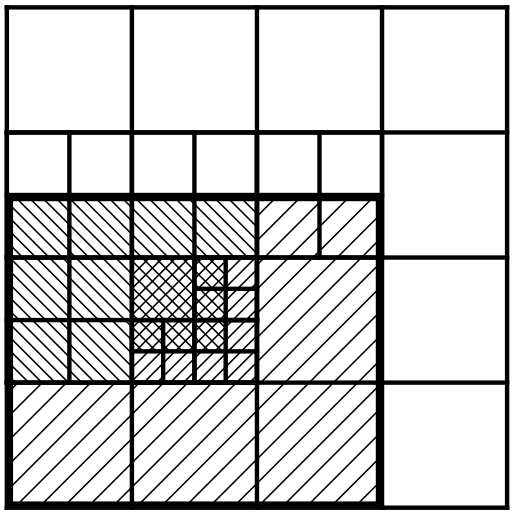

Parallelization

Rigorous domain decomposition

- Data of all levels resides on same node
- Grid hierarchy defines unique "floor-plan"
- Workload estimation

$$\mathcal{W}(\Omega) = \sum_{l=0}^{l_{\max}} \left[\mathcal{N}_l(G_l \cap \Omega) \prod_{\kappa=0}^{l} r_\kappa \right]$$

- Parallel operations
  - Synchronization of ghost cells
  - Redistribution of data blocks within regridding operation
  - Flux correction of coarse grid cells
- Dynamic partitioning with space-filling curve

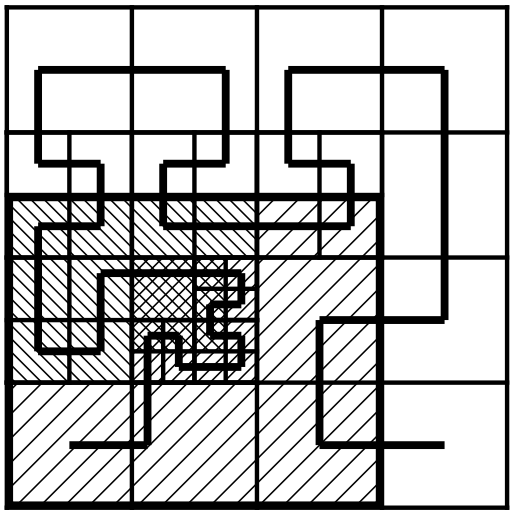

Parallelization

Rigorous domain decomposition

- Data of all levels resides on same node
- Grid hierarchy defines unique "floor-plan"
- Workload estimation

$$\mathcal{W}(\Omega) = \sum_{l=0}^{l_{\max}} \left[\mathcal{N}_l(G_l \cap \Omega) \prod_{\kappa=0}^{l} r_\kappa \right]$$

- Parallel operations
  - Synchronization of ghost cells
  - Redistribution of data blocks within regridding operation
  - Flux correction of coarse grid cells
- Dynamic partitioning with space-filling curve

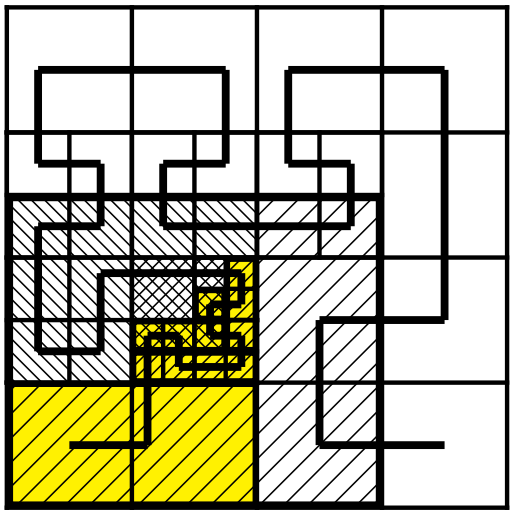

Parallelization

Rigorous domain decomposition

- Data of all levels resides on same node
- Grid hierarchy defines unique "floor-plan"
- Workload estimation

$$\mathcal{W}(\Omega) = \sum_{l=0}^{l_{\max}} \left[\mathcal{N}_l(G_l \cap \Omega) \prod_{\kappa=0}^{l} r_\kappa \right]$$

- Parallel operations
  - Synchronization of ghost cells
  - Redistribution of data blocks within regridding operation
  - Flux correction of coarse grid cells
- Dynamic partitioning with space-filling curve

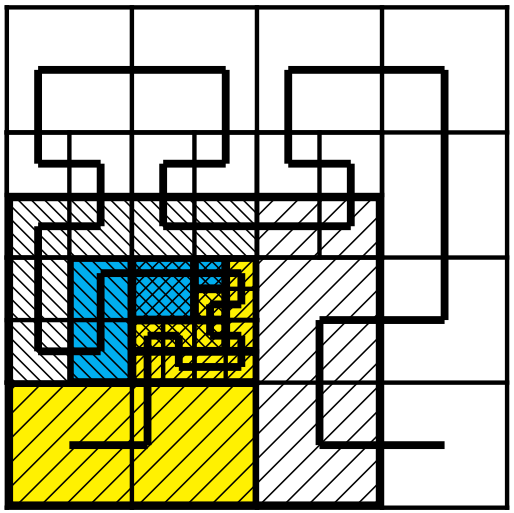

Parallelization

Rigorous domain decomposition

- Data of all levels resides on same node
- Grid hierarchy defines unique "floor-plan"
- Workload estimation

$$\mathcal{W}(\Omega) = \sum_{l=0}^{l_{\max}} \left[\mathcal{N}_l(G_l \cap \Omega) \prod_{\kappa=0}^{l} r_\kappa \right]$$

- Parallel operations
  - Synchronization of ghost cells
  - Redistribution of data blocks within regridding operation
  - Flux correction of coarse grid cells
- Dynamic partitioning with space-filling curve

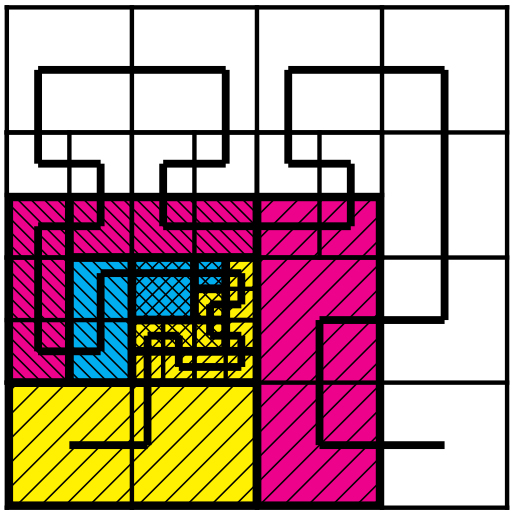

Parallelization

Rigorous domain decomposition

- Data of all levels resides on same node
- Grid hierarchy defines unique "floor-plan"
- Workload estimation

$$\mathcal{W}(\Omega) = \sum_{l=0}^{l_{\max}} \left[\mathcal{N}_l(G_l \cap \Omega) \prod_{\kappa=0}^{l} r_\kappa \right]$$

- Parallel operations
  - Synchronization of ghost cells
  - Redistribution of data blocks within regridding operation
  - Flux correction of coarse grid cells
- Dynamic partitioning with space-filling curve

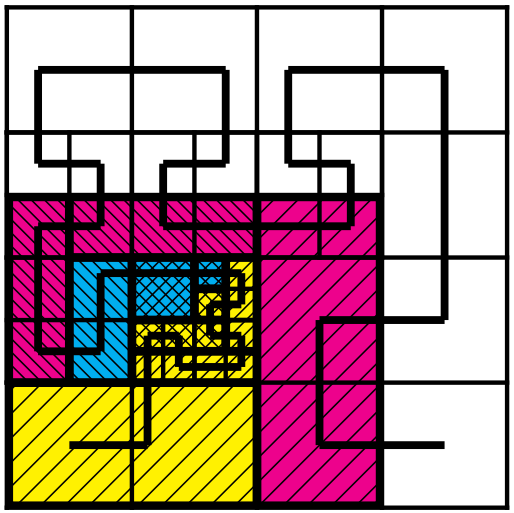

[Deiterding, 2005, Deiterding, 2011a]

AMROC framework and most important patch solvers

- Implements described algorithms and facilitates easy exchange of the block-based numerical scheme
- Shock-induced combustion with detailed chemistry: [Deiterding, 2003, Deiterding and Bader, 2005, Deiterding, 2011b, Cai et al., 2016, Cai et al., 2018]
- Hybrid WENO methods for LES and DNS: [Pantano et al., 2007, Lombardini and Deiterding, 2010, Ziegler et al., 2011, Cerminara et al., 2018]
- Lattice Boltzmann method for LES: [Fragner and Deiterding, 2016, Feldhusen et al., 2016, Deiterding and Wood, 2016]
- FSI deformation from water hammer: [Cirak et al., 2007, Deiterding et al., 2009a, Perotti et al., 2013, Wan et al., 2017]
- Level-set method for Eulerian solid mechanics: [Barton et al., 2013]
- Ideal magneto-hydrodynamics: [Gomes et al., 2015, Souza Lopes et al., 2018]
- $\sim 500,000$ LOC in C++, C, Fortran-77, Fortran-90
- V2.0 plus FSI coupling routines as open source at http://www.vtf.website
- Used here V3.0 with significantly enhanced parallelization (V2.1 not released)

AMROC strong scalability tests

3D wave propagation method with Roe scheme: spherical blast wave

- Tests run IBM BG/P (mode VN)

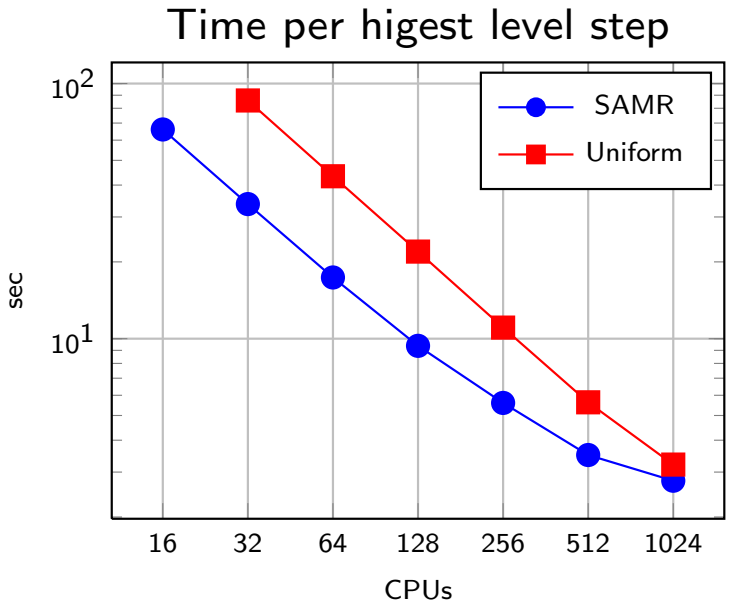

$64 \times 32 \times 32$ base grid, 2 additional levels with factors 2, 4; uniform $512 \times 256 \times 256 = 33.6 \cdot 10^6$ cells

Level	Grids	Cells
0	1709	65,536
1	1735	271,048
2	2210	7,190,208

AMROC strong scalability tests

3D wave propagation method with Roe scheme: spherical blast wave

- Tests run IBM BG/P (mode VN)

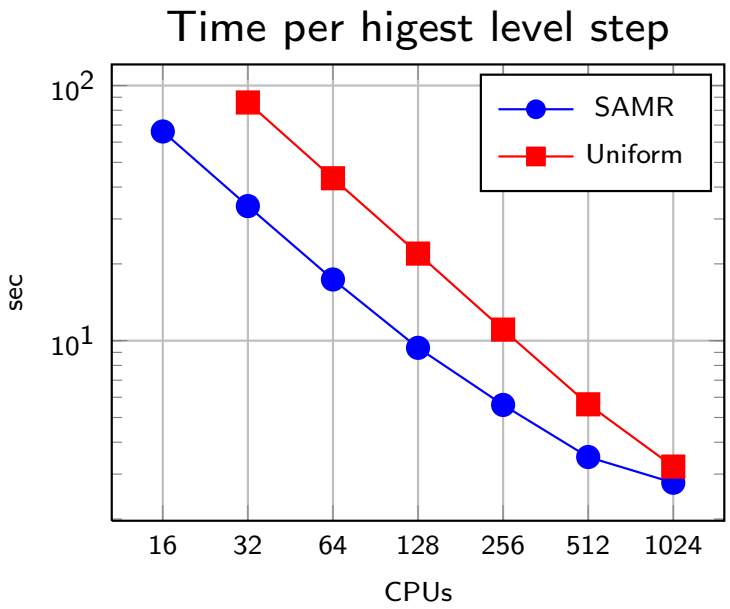

$64 \times 32 \times 32$ base grid, 2 additional levels with factors 2, 4; uniform $512 \times 256 \times 256 = 33.6 \cdot 10^6$ cells

Level	Grids	Cells
0	1709	65,536
1	1735	271,048
2	2210	7,190,208

3D SRT-lattice Boltzmann scheme: flow over rough surface of $19 \times 13 \times 2$ spheres

- Tests run Cray XC30m (Archer)

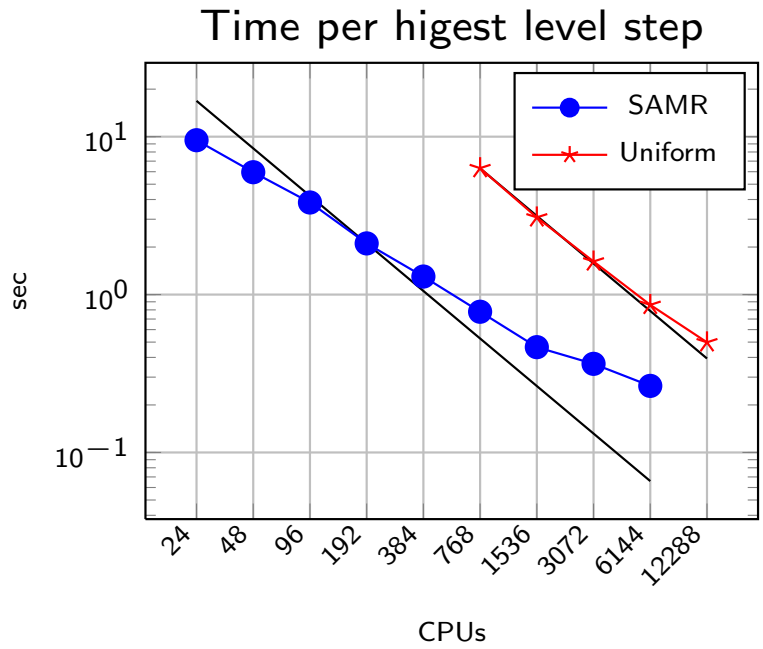

$360 \times 240 \times 108$ base grid, 2 additional levels with factors 2, 4; uniform $1440 \times 1920 \times 432 = 1.19 \cdot 10^9$ cells

Level	Grids	Cells
0	788	9,331,200
1	21367	24,844,504
2	1728	10,838,016

Axisymmetric Navier-Stokes equations with chemical reaction

$$\frac{\partial \mathbf{q}}{\partial t} + \frac{\partial (\mathbf{f} - \mathbf{f}_v)}{\partial x} + \frac{\partial (\mathbf{g} - \mathbf{g}_v)}{\partial y} = \frac{\alpha}{y}(\mathbf{c} - \mathbf{g} + \mathbf{g}_v) + \mathbf{s}$$

$$\mathbf{q} = \begin{bmatrix} \rho_i \\ \rho u \\ \rho v \\ \rho E \end{bmatrix}, \ \mathbf{f} = \begin{bmatrix} \rho_i u \\ \rho u^2 + p \\ \rho u v \\ u(\rho E + p) \end{bmatrix}, \ \mathbf{g} = \begin{bmatrix} \rho_i v \\ \rho u v \\ \rho v^2 + p \\ v(\rho E + p) \end{bmatrix}, \ \mathbf{c} = \begin{bmatrix} 0 \\ 0 \\ p - \tau_{\theta\theta} \\ 0 \end{bmatrix}, \ \mathbf{s} = \begin{bmatrix} \dot{\omega}_i \\ 0 \\ 0 \\ 0 \end{bmatrix}$$

Axisymmetric Navier-Stokes equations with chemical reaction

$$\frac{\partial \mathbf{q}}{\partial t} + \frac{\partial (\mathbf{f} - \mathbf{f}_v)}{\partial x} + \frac{\partial (\mathbf{g} - \mathbf{g}_v)}{\partial y} = \frac{\alpha}{y}(\mathbf{c} - \mathbf{g} + \mathbf{g}_v) + \mathbf{s}$$

$$\mathbf{q} = \begin{bmatrix} \rho_i \\ \rho u \\ \rho v \\ \rho E \end{bmatrix}, \ \mathbf{f} = \begin{bmatrix} \rho_i u \\ \rho u^2 + p \\ \rho uv \\ u(\rho E + p) \end{bmatrix}, \ \mathbf{g} = \begin{bmatrix} \rho_i v \\ \rho uv \\ \rho v^2 + p \\ v(\rho E + p) \end{bmatrix}, \ \mathbf{c} = \begin{bmatrix} 0 \\ 0 \\ p - \tau_{\theta\theta} \\ 0 \end{bmatrix}, \ \mathbf{s} = \begin{bmatrix} \dot{\omega}_i \\ 0 \\ 0 \\ 0 \end{bmatrix}$$

$$\mathbf{f}_v = \begin{bmatrix} \rho D_i \dfrac{\partial Y_i}{\partial x} \\ \tau_{xx} \\ \tau_{xy} \\ k\dfrac{\partial T}{\partial x} + \rho \sum h_j D_j \dfrac{\partial Y_j}{\partial x} + u\tau_{xx} + v\tau_{xy} \end{bmatrix}$$

$$\mathbf{g}_v = \begin{bmatrix} \rho D_i \dfrac{\partial Y_i}{\partial y} \\ \tau_{xy} \\ \tau_{yy} \\ k\dfrac{\partial T}{\partial y} + \rho \sum h_j D_j \dfrac{\partial Y_j}{\partial y} + u\tau_{xy} + v\tau_{yy} \end{bmatrix}$$

$$\tau_{xx} = -\frac{2}{3}\mu(\nabla \cdot \mathbf{v}) + 2\mu\frac{\partial u}{\partial x}$$

$$\tau_{yy} = -\frac{2}{3}\mu(\nabla \cdot \mathbf{v}) + 2\mu\frac{\partial v}{\partial y}$$

$$\tau_{\theta\theta} = -\frac{2}{3}\mu(\nabla \cdot \mathbf{v}) + 2\mu\frac{v}{y}$$

$$\tau_{xy} = \mu\left(\frac{\partial u}{\partial y} + \frac{\partial v}{\partial x}\right)$$

$$\nabla \cdot \mathbf{v} = \left(\frac{\partial u}{\partial x} + \frac{\partial v}{\partial y} + \alpha\frac{v}{y}\right)$$

Equation of state

Ideal gas law and Dalton's law for gas-mixtures

$$p(\rho_1, \ldots, \rho_K, T) = \sum_{i=1}^{K} p_i = \sum_{i=1}^{K} \rho_i \frac{\mathcal{R}}{W_i} T = \rho \frac{\mathcal{R}}{W} T \quad \text{with} \quad \sum_{i=1}^{K} \rho_i = \rho \,, Y_i = \frac{\rho_i}{\rho}$$

Equation of state

Ideal gas law and Dalton's law for gas-mixtures

$$p(\rho_1, \ldots, \rho_K, T) = \sum_{i=1}^{K} p_i = \sum_{i=1}^{K} \rho_i \frac{\mathcal{R}}{W_i} T = \rho \frac{\mathcal{R}}{W} T \quad \text{with} \quad \sum_{i=1}^{K} \rho_i = \rho \,, Y_i = \frac{\rho_i}{\rho}$$

Caloric equation

$$h(Y_1, \ldots, Y_K, T) = \sum_{i=1}^{K} Y_i h_i(T) \quad \text{with} \quad h_i(T) = h_i^0 + \int_0^T c_{pi}(s) ds$$

Equation of state

Ideal gas law and Dalton's law for gas-mixtures

$$p(\rho_1, \ldots, \rho_K, T) = \sum_{i=1}^{K} p_i = \sum_{i=1}^{K} \rho_i \frac{\mathcal{R}}{W_i} T = \rho \frac{\mathcal{R}}{W} T \quad \text{with} \quad \sum_{i=1}^{K} \rho_i = \rho \,, Y_i = \frac{\rho_i}{\rho}$$

Caloric equation

$$h(Y_1, \ldots, Y_K, T) = \sum_{i=1}^{K} Y_i h_i(T) \quad \text{with} \quad h_i(T) = h_i^0 + \int_0^T c_{pi}(s) ds$$

Computation of $T = T(\rho_1, \ldots, \rho_K, e)$ from implicit equation

$$\sum_{i=1}^{K} \rho_i \, h_i(T) - \mathcal{R} T \sum_{i=1}^{K} \frac{\rho_i}{W_i} - \rho e = 0$$

for *thermally perfect* gases with $\gamma_i(T) = c_{pi}(T)/c_{vi}(T)$ using an iterative Newton or bisection method

Chemistry and transport properties

Arrhenius-kinetics:

$$\dot{\omega}_i = \sum_{j=1}^{M} (\nu_{ji}^r - \nu_{ji}^f) \left[k_j^f \prod_{n=1}^{K} \left(\frac{\rho_n}{W_n} \right)^{\nu_{jn}^f} - k_j^r \prod_{n=1}^{K} \left(\frac{\rho_n}{W_n} \right)^{\nu_{jn}^r} \right] \quad i = 1, \ldots, K$$

Chemistry and transport properties

Arrhenius-kinetics:

$$\dot{\omega}_i = \sum_{j=1}^{M} (\nu_{ji}^r - \nu_{ji}^f) \left[k_j^f \prod_{n=1}^{K} \left(\frac{\rho_n}{W_n} \right)^{\nu_{jn}^f} - k_j^r \prod_{n=1}^{K} \left(\frac{\rho_n}{W_n} \right)^{\nu_{jn}^r} \right] \quad i = 1, \ldots, K$$

- Parsing of mechanisms and evaluation of $\dot{\omega}_i$ with Chemkin-II
- $c_{pi}(T)$ and $h_i(T)$ tabulated, linear interpolation between values

Chemistry and transport properties

Arrhenius-kinetics:

$$\dot{\omega}_i = \sum_{j=1}^{M} (\nu_{ji}^r - \nu_{ji}^f) \left[k_j^f \prod_{n=1}^{K} \left(\frac{\rho_n}{W_n} \right)^{\nu_{jn}^f} - k_j^r \prod_{n=1}^{K} \left(\frac{\rho_n}{W_n} \right)^{\nu_{jn}^r} \right] \quad i = 1, \ldots, K$$

- Parsing of mechanisms and evaluation of $\dot{\omega}_i$ with Chemkin-II
- $c_{pi}(T)$ and $h_i(T)$ tabulated, linear interpolation between values

Mixture viscosity $\mu = \mu(T, Y_i)$ with Wilke formula

$$\mu = \sum_{i=1}^{K} \frac{Y_i \mu_i}{W_i \sum_{m=1}^{K} Y_m \Phi_{im} / W_m} \text{ with } \Phi_{im} = \frac{1}{\sqrt{8}} \left(1 + \frac{W_i}{W_m} \right)^{-\frac{1}{2}} \left(1 + \left(\frac{\mu_i}{\mu_m} \right)^{\frac{1}{2}} \left(\frac{W_m}{W_j} \right)^{\frac{1}{4}} \right)^2$$

Chemistry and transport properties

Arrhenius-kinetics:

$$\dot{\omega}_i = \sum_{j=1}^{M} (\nu_{ji}^r - \nu_{ji}^f) \left[k_j^f \prod_{n=1}^{K} \left(\frac{\rho_n}{W_n} \right)^{\nu_{jn}^f} - k_j^r \prod_{n=1}^{K} \left(\frac{\rho_n}{W_n} \right)^{\nu_{jn}^r} \right] \quad i = 1, \ldots, K$$

- Parsing of mechanisms and evaluation of $\dot{\omega}_i$ with Chemkin-II
- $c_{pi}(T)$ and $h_i(T)$ tabulated, linear interpolation between values

Mixture viscosity $\mu = \mu(T, Y_i)$ with Wilke formula

$$\mu = \sum_{i=1}^{K} \frac{Y_i \mu_i}{W_i \sum_{m=1}^{K} Y_m \Phi_{im} / W_m} \text{ with } \Phi_{im} = \frac{1}{\sqrt{8}} \left(1 + \frac{W_i}{W_m} \right)^{-\frac{1}{2}} \left(1 + \left(\frac{\mu_i}{\mu_m} \right)^{\frac{1}{2}} \left(\frac{W_m}{W_j} \right)^{\frac{1}{4}} \right)^2$$

Mixture thermal conductivity $k = k(T, Y_i)$ following Mathur

$$k = \frac{1}{2} \left(W \sum_{i=1}^{K} \frac{Y_i k_i}{W_i} + \frac{1}{W \sum_{i=1}^{K} Y_i / (W_i k_i)} \right)$$

Chemistry and transport properties

Arrhenius-kinetics:

$$\dot{\omega}_i = \sum_{j=1}^{M} (\nu_{ji}^r - \nu_{ji}^f) \left[k_j^f \prod_{n=1}^{K} \left(\frac{\rho_n}{W_n} \right)^{\nu_{jn}^f} - k_j^r \prod_{n=1}^{K} \left(\frac{\rho_n}{W_n} \right)^{\nu_{jn}^r} \right] \quad i = 1, \ldots, K$$

- Parsing of mechanisms and evaluation of $\dot{\omega}_i$ with Chemkin-II
- $c_{pi}(T)$ and $h_i(T)$ tabulated, linear interpolation between values

Mixture viscosity $\mu = \mu(T, Y_i)$ with Wilke formula

$$\mu = \sum_{i=1}^{K} \frac{Y_i \mu_i}{W_i \sum_{m=1}^{K} Y_m \Phi_{im} / W_m} \text{ with } \Phi_{im} = \frac{1}{\sqrt{8}} \left(1 + \frac{W_i}{W_m} \right)^{-\frac{1}{2}} \left(1 + \left(\frac{\mu_i}{\mu_m} \right)^{\frac{1}{2}} \left(\frac{W_m}{W_j} \right)^{\frac{1}{4}} \right)^2$$

Mixture thermal conductivity $k = k(T, Y_i)$ following Mathur

$$k = \frac{1}{2} \left(W \sum_{i=1}^{K} \frac{Y_i k_i}{W_i} + \frac{1}{W \sum_{i=1}^{K} Y_i / (W_i k_i)} \right)$$

Mixture diffusion coefficients $D_i = D_i(T, p, Y_i)$ from binary diffusion $D_{mi}(T, p)$ as

$$D_i = \frac{1 - Y_i}{W \sum_{m \neq i} Y_m / (W_m D_{mi})}$$

- Evaluation with Chemkin-II Transport library

Splitting methods

$$\partial_t \mathbf{q} + \partial_x(\mathbf{f} - \mathbf{f}_v) + \partial_y(\mathbf{g} - \mathbf{g}_v) = \frac{\alpha}{y}(\mathbf{c} - \mathbf{g} + \mathbf{g}_v) + \mathbf{s}$$

Splitting methods

$$\partial_t \mathbf{q} + \partial_x(\mathbf{f} - \mathbf{f}_v) + \partial_y(\mathbf{g} - \mathbf{g}_v) = \frac{\alpha}{y}(\mathbf{c} - \mathbf{g} + \mathbf{g}_v) + \mathbf{s}$$

Dimensional splitting for PDE

$$\mathcal{X}^{(\Delta t)}: \quad \partial_t \mathbf{q} + \partial_x(\mathbf{f}(\mathbf{q}) - \mathbf{f}_v(\mathbf{q})) = 0\,, \qquad \text{IC: } \mathbf{Q}(t_m) \overset{\Delta t}{\Longrightarrow} \tilde{\mathbf{Q}}^{1/2}$$

$$\mathcal{Y}^{(\Delta t)}: \quad \partial_t \mathbf{q} + \partial_y(\mathbf{g}(\mathbf{q}) - \mathbf{g}_v(\mathbf{q})) = 0\,, \qquad \text{IC: } \tilde{\mathbf{Q}}^{1/2} \overset{\Delta t}{\Longrightarrow} \tilde{\mathbf{Q}}$$

Splitting methods

$$\partial_t \mathbf{q} + \partial_x(\mathbf{f} - \mathbf{f}_v) + \partial_y(\mathbf{g} - \mathbf{g}_v) = \frac{\alpha}{y}(\mathbf{c} - \mathbf{g} + \mathbf{g}_v) + \mathbf{s}$$

Dimensional splitting for PDE

$$\mathcal{X}^{(\Delta t)}: \quad \partial_t \mathbf{q} + \partial_x(\mathbf{f}(\mathbf{q}) - \mathbf{f}_v(\mathbf{q})) = 0\,, \qquad \text{IC: } \mathbf{Q}(t_m) \overset{\Delta t}{\Longrightarrow} \tilde{\mathbf{Q}}^{1/2}$$

$$\mathcal{Y}^{(\Delta t)}: \quad \partial_t \mathbf{q} + \partial_y(\mathbf{g}(\mathbf{q}) - \mathbf{g}_v(\mathbf{q})) = 0\,, \qquad \text{IC: } \tilde{\mathbf{Q}}^{1/2} \overset{\Delta t}{\Longrightarrow} \tilde{\mathbf{Q}}$$

Treat right-hand side as source term

$$\mathcal{C}^{(\Delta t)}: \quad \partial_t \mathbf{q} = \tfrac{\alpha}{y}(\mathbf{c}(\mathbf{q}) - \mathbf{g}(\mathbf{q}) + \mathbf{g}_v(\mathbf{q}))\,, \qquad \text{IC: } \tilde{\mathbf{Q}} \overset{\Delta t}{\Longrightarrow} \bar{\mathbf{Q}}$$

Splitting methods

$$\partial_t \mathbf{q} + \partial_x(\mathbf{f} - \mathbf{f}_v) + \partial_y(\mathbf{g} - \mathbf{g}_v) = \frac{\alpha}{y}(\mathbf{c} - \mathbf{g} + \mathbf{g}_v) + \mathbf{s}$$

Dimensional splitting for PDE

$$\mathcal{X}^{(\Delta t)}: \quad \partial_t \mathbf{q} + \partial_x(\mathbf{f}(\mathbf{q}) - \mathbf{f}_v(\mathbf{q})) = 0\,, \qquad \text{IC: } \mathbf{Q}(t_m) \overset{\Delta t}{\Longrightarrow} \tilde{\mathbf{Q}}^{1/2}$$

$$\mathcal{Y}^{(\Delta t)}: \quad \partial_t \mathbf{q} + \partial_y(\mathbf{g}(\mathbf{q}) - \mathbf{g}_v(\mathbf{q})) = 0\,, \qquad \text{IC: } \tilde{\mathbf{Q}}^{1/2} \overset{\Delta t}{\Longrightarrow} \tilde{\mathbf{Q}}$$

Treat right-hand side as source term

$$\mathcal{C}^{(\Delta t)}: \quad \partial_t \mathbf{q} = \tfrac{\alpha}{y}(\mathbf{c}(\mathbf{q}) - \mathbf{g}(\mathbf{q}) + \mathbf{g}_v(\mathbf{q}))\,, \qquad \text{IC: } \tilde{\mathbf{Q}} \overset{\Delta t}{\Longrightarrow} \bar{\mathbf{Q}}$$

Chemical source term

$$\mathcal{S}^{(\Delta t)}: \quad \partial_t \mathbf{q} = \mathbf{s}(\mathbf{q})\,, \qquad \text{IC: } \bar{\mathbf{Q}} \overset{\Delta t}{\Longrightarrow} \mathbf{Q}(t_m + \Delta t)$$

Splitting methods

$$\partial_t \mathbf{q} + \partial_x(\mathbf{f} - \mathbf{f}_v) + \partial_y(\mathbf{g} - \mathbf{g}_v) = \frac{\alpha}{y}(\mathbf{c} - \mathbf{g} + \mathbf{g}_v) + \mathbf{s}$$

Dimensional splitting for PDE

$$\mathcal{X}^{(\Delta t)}: \quad \partial_t \mathbf{q} + \partial_x(\mathbf{f}(\mathbf{q}) - \mathbf{f}_v(\mathbf{q})) = 0\,, \qquad \text{IC: } \mathbf{Q}(t_m) \overset{\Delta t}{\Longrightarrow} \tilde{\mathbf{Q}}^{1/2}$$

$$\mathcal{Y}^{(\Delta t)}: \quad \partial_t \mathbf{q} + \partial_y(\mathbf{g}(\mathbf{q}) - \mathbf{g}_v(\mathbf{q})) = 0\,, \qquad \text{IC: } \tilde{\mathbf{Q}}^{1/2} \overset{\Delta t}{\Longrightarrow} \tilde{\mathbf{Q}}$$

Treat right-hand side as source term

$$\mathcal{C}^{(\Delta t)}: \quad \partial_t \mathbf{q} = \tfrac{\alpha}{y}(\mathbf{c}(\mathbf{q}) - \mathbf{g}(\mathbf{q}) + \mathbf{g}_v(\mathbf{q}))\,, \qquad \text{IC: } \tilde{\mathbf{Q}} \overset{\Delta t}{\Longrightarrow} \bar{\mathbf{Q}}$$

Chemical source term

$$\mathcal{S}^{(\Delta t)}: \quad \partial_t \mathbf{q} = \mathbf{s}(\mathbf{q})\,, \qquad \text{IC: } \bar{\mathbf{Q}} \overset{\Delta t}{\Longrightarrow} \mathbf{Q}(t_m + \Delta t)$$

Formally 1st-order algorithm

$$\mathbf{Q}(t_m + \Delta t) = \mathcal{S}^{(\Delta t)}\mathcal{C}^{(\Delta t)}\mathcal{Y}^{(\Delta t)}\mathcal{X}^{(\Delta t)}(\mathbf{Q}(t_m))$$

but all sub-operators 2nd-order accurate or higher.

Finite volume discretization

Time discretization $t_n = n\Delta t$, discrete volumes $l_{jk} = [x_j - \frac{1}{2}\Delta x, x_j + \frac{1}{2}\Delta x[\times[y_k - \frac{1}{2}\Delta y, y_k + \frac{1}{2}\Delta y[\times =: [x_{j-1/2}, x_{j+1/2}[\times[y_{k-1/2}, y_{k+1/2}[$

Approximation $\mathbf{Q}_{jk}(t) \approx \frac{1}{|l_{jk}|} \int_{l_{jk}} \mathbf{q}(\mathbf{x}, t)\, dx$ and numerical fluxes

$$\mathbf{F}\left(\mathbf{Q}_{jk}(t), \mathbf{Q}_{j+1,k}(t)\right) \approx \mathbf{f}(\mathbf{q}(x_{j+1/2}, y_k, t)),$$

$$\mathbf{F}_v\left(\mathbf{Q}_{jk}(t), \mathbf{Q}_{j+1,k}(t)\right) \approx \mathbf{f}_v(\mathbf{q}(x_{j+1/2}, y_k, t), \nabla\mathbf{q}(x_{j+1/2}, y_k, t))$$

yield (for simplicity)

$$\mathbf{Q}_{jk}^{n+1} = \mathbf{Q}_{kj}^{n} - \frac{\Delta t}{\Delta x}\left[\mathbf{F}\left(\mathbf{Q}_{jk}^{n}, \mathbf{Q}_{j+1,k}^{n}\right) - \mathbf{F}\left(\mathbf{Q}_{j-1,k}^{n}, \mathbf{Q}_{jk}^{n}\right)\right] + \frac{\Delta t}{\Delta x}\left[\mathbf{F}_v\left(\mathbf{Q}_{jk}^{n}, \mathbf{Q}_{j+1,k}^{n}\right) - \mathbf{F}_v\left(\mathbf{Q}_{j-1,k}^{n}, \mathbf{Q}_{jk}^{n}\right)\right]$$

Finite volume discretization

Time discretization $t_n = n\Delta t$, discrete volumes $I_{jk} = [x_j - \frac{1}{2}\Delta x, x_j + \frac{1}{2}\Delta x[\times[y_k - \frac{1}{2}\Delta y, y_k + \frac{1}{2}\Delta y[\times =: [x_{j-1/2}, x_{j+1/2}[\times[y_{k-1/2}, y_{k+1/2}[$

Approximation $\mathbf{Q}_{jk}(t) \approx \frac{1}{|I_{jk}|} \int_{I_{jk}} \mathbf{q}(\mathbf{x}, t)\, dx$ and numerical fluxes

$$\mathbf{F}\left(\mathbf{Q}_{jk}(t), \mathbf{Q}_{j+1,k}(t)\right) \approx \mathbf{f}(\mathbf{q}(x_{j+1/2}, y_k, t)),$$

$$\mathbf{F}_v\left(\mathbf{Q}_{jk}(t), \mathbf{Q}_{j+1,k}(t)\right) \approx \mathbf{f}_v(\mathbf{q}(x_{j+1/2}, y_k, t), \nabla\mathbf{q}(x_{j+1/2}, y_k, t))$$

yield (for simplicity)

$$\mathbf{Q}_{jk}^{n+1} = \mathbf{Q}_{kj}^{n} - \frac{\Delta t}{\Delta x}\left[\mathbf{F}\left(\mathbf{Q}_{jk}^{n}, \mathbf{Q}_{j+1,k}^{n}\right) - \mathbf{F}\left(\mathbf{Q}_{j-1,k}^{n}, \mathbf{Q}_{jk}^{n}\right)\right] + \frac{\Delta t}{\Delta x}\left[\mathbf{F}_v\left(\mathbf{Q}_{jk}^{n}, \mathbf{Q}_{j+1,k}^{n}\right) - \mathbf{F}_v\left(\mathbf{Q}_{j-1,k}^{n}, \mathbf{Q}_{jk}^{n}\right)\right]$$

- Riemann solver to approximate $\mathbf{F}\left(\mathbf{Q}_{jk}^{n}, \mathbf{Q}_{j+1,k}^{n}\right)$

Finite volume discretization

Time discretization $t_n = n\Delta t$, discrete volumes $l_{jk} = [x_j - \frac{1}{2}\Delta x, x_j + \frac{1}{2}\Delta x[\times[y_k - \frac{1}{2}\Delta y, y_k + \frac{1}{2}\Delta y[\times =: [x_{j-1/2}, x_{j+1/2}[\times[y_{k-1/2}, y_{k+1/2}[$

Approximation $\mathbf{Q}_{jk}(t) \approx \frac{1}{|l_{jk}|} \int_{l_{jk}} \mathbf{q}(\mathbf{x}, t)\, dx$ and numerical fluxes

$$\mathbf{F}\left(\mathbf{Q}_{jk}(t), \mathbf{Q}_{j+1,k}(t)\right) \approx \mathbf{f}(\mathbf{q}(x_{j+1/2}, y_k, t)),$$

$$\mathbf{F}_v\left(\mathbf{Q}_{jk}(t), \mathbf{Q}_{j+1,k}(t)\right) \approx \mathbf{f}_v(\mathbf{q}(x_{j+1/2}, y_k, t), \nabla\mathbf{q}(x_{j+1/2}, y_k, t))$$

yield (for simplicity)

$$\mathbf{Q}_{jk}^{n+1} = \mathbf{Q}_{kj}^n - \frac{\Delta t}{\Delta x}\left[\mathbf{F}\left(\mathbf{Q}_{jk}^n, \mathbf{Q}_{j+1,k}^n\right) - \mathbf{F}\left(\mathbf{Q}_{j-1,k}^n, \mathbf{Q}_{jk}^n\right)\right] + \frac{\Delta t}{\Delta x}\left[\mathbf{F}_v\left(\mathbf{Q}_{jk}^n, \mathbf{Q}_{j+1,k}^n\right) - \mathbf{F}_v\left(\mathbf{Q}_{j-1,k}^n, \mathbf{Q}_{jk}^n\right)\right]$$

- Riemann solver to approximate $\mathbf{F}\left(\mathbf{Q}_{jk}^n, \mathbf{Q}_{j+1,k}^n\right)$
- 1st-order finite differences for $\mathbf{F}_v\left(\mathbf{Q}_{jk}^n, \mathbf{Q}_{j+1,k}^n\right)$ yield 2nd-order accurate central differences in $(*)$

Finite volume discretization

Time discretization $t_n = n\Delta t$, discrete volumes $l_{jk} = [x_j - \frac{1}{2}\Delta x, x_j + \frac{1}{2}\Delta x[\times[y_k - \frac{1}{2}\Delta y, y_k + \frac{1}{2}\Delta y[\times =: [x_{j-1/2}, x_{j+1/2}[\times[y_{k-1/2}, y_{k+1/2}[$

Approximation $\mathbf{Q}_{jk}(t) \approx \frac{1}{|l_{jk}|} \int_{l_{jk}} \mathbf{q}(\mathbf{x}, t)\, dx$ and numerical fluxes

$$\mathbf{F}\left(\mathbf{Q}_{jk}(t), \mathbf{Q}_{j+1,k}(t)\right) \approx \mathbf{f}(\mathbf{q}(x_{j+1/2}, y_k, t)),$$

$$\mathbf{F}_v\left(\mathbf{Q}_{jk}(t), \mathbf{Q}_{j+1,k}(t)\right) \approx \mathbf{f}_v(\mathbf{q}(x_{j+1/2}, y_k, t), \nabla\mathbf{q}(x_{j+1/2}, y_k, t))$$

yield (for simplicity)

$$\mathbf{Q}_{jk}^{n+1} = \mathbf{Q}_{kj}^n - \frac{\Delta t}{\Delta x}\left[\mathbf{F}\left(\mathbf{Q}_{jk}^n, \mathbf{Q}_{j+1,k}^n\right) - \mathbf{F}\left(\mathbf{Q}_{j-1,k}^n, \mathbf{Q}_{jk}^n\right)\right] + \frac{\Delta t}{\Delta x}\left[\mathbf{F}_v\left(\mathbf{Q}_{jk}^n, \mathbf{Q}_{j+1,k}^n\right) - \mathbf{F}_v\left(\mathbf{Q}_{j-1,k}^n, \mathbf{Q}_{jk}^n\right)\right]$$

- Riemann solver to approximate $\mathbf{F}\left(\mathbf{Q}_{jk}^n, \mathbf{Q}_{j+1,k}^n\right)$
- 1st-order finite differences for $\mathbf{F}_v\left(\mathbf{Q}_{jk}^n, \mathbf{Q}_{j+1,k}^n\right)$ yield 2nd-order accurate central differences in $(*)$

Stability condition used:

$$\max_{i,j,k}\left\{\frac{\Delta t}{\Delta x}(|u_{jk}| + c_{jk}) + \frac{8}{3}\frac{\mu_{jk}\Delta t}{\rho_{jk}\Delta x^2}, \frac{\Delta t}{\Delta x}(|u_{jk}| + c_{jk}) + \frac{2k_j\Delta t}{c_{v,jk}\rho_j\Delta x^2}, \frac{\Delta t}{\Delta x}(|u_{jk}| + c_{jk}) + D_{i,jk}\frac{\Delta t}{\Delta x^2}\right\} \leq 1$$

Finite volume discretization – cont.

Symmetry source term $\mathcal{C}^{(\Delta t)}$: Use

$$\mathbf{Q}_{jk}^{n+1} = \mathbf{Q}_{jk}^{n} + \Delta t \left(\frac{\alpha}{y} (\mathbf{c}(\mathbf{Q}_{jk}^{n}) - \mathbf{g}(\mathbf{Q}_{jk}^{n}) + \frac{1}{2} \left(\mathbf{G}_v \left(\mathbf{Q}_{jk}^{n}, \mathbf{Q}_{j,k+1}^{n} \right) + \mathbf{G}_v \left(\mathbf{Q}_{j,k-1}^{n}, \mathbf{Q}_{jk}^{n} \right) \right) \right)$$

within explicit 2nd-order accurate Runge-Kutta method

- Gives 2nd-order central difference approximation of $\mathbf{G}_v$

Finite volume discretization – cont.

Symmetry source term $\mathcal{C}^{(\Delta t)}$: Use

$$\mathbf{Q}_{jk}^{n+1} = \mathbf{Q}_{jk}^{n} + \Delta t \left(\frac{\alpha}{y} (\mathbf{c}(\mathbf{Q}_{jk}^{n}) - \mathbf{g}(\mathbf{Q}_{jk}^{n}) + \frac{1}{2} \left(\mathbf{G}_v \left(\mathbf{Q}_{jk}^{n}, \mathbf{Q}_{j,k+1}^{n} \right) + \mathbf{G}_v \left(\mathbf{Q}_{j,k-1}^{n}, \mathbf{Q}_{jk}^{n} \right) \right) \right)$$

within explicit 2nd-order accurate Runge-Kutta method

- Gives 2nd-order central difference approximation of $\mathbf{G}_v$
- Transport properties μ, k, D_i are stored in vector of state $\mathbf{Q}$ and kept constant throughout entire time step

Finite volume discretization – cont.

Symmetry source term $\mathcal{C}^{(\Delta t)}$: Use

$$\mathbf{Q}_{jk}^{n+1} = \mathbf{Q}_{jk}^{n} + \Delta t \left(\frac{\alpha}{y} (\mathbf{c}(\mathbf{Q}_{jk}^{n}) - \mathbf{g}(\mathbf{Q}_{jk}^{n}) + \frac{1}{2} \left(\mathbf{G}_v \left(\mathbf{Q}_{jk}^{n}, \mathbf{Q}_{j,k+1}^{n} \right) + \mathbf{G}_v \left(\mathbf{Q}_{j,k-1}^{n}, \mathbf{Q}_{jk}^{n} \right) \right) \right)$$

within explicit 2nd-order accurate Runge-Kutta method

- Gives 2nd-order central difference approximation of $\mathbf{G}_v$
- Transport properties μ, k, D_i are stored in vector of state $\mathbf{Q}$ and kept constant throughout entire time step

Chemical source term $\mathcal{S}^{(\cdot)}$:

- 4th-order accurate semi-implicit ODE-solver subcycles within each cell
- ρ, e, u, v remain unchanged!

$$\partial_t \rho_i = W_i \dot{\omega}_i(\rho_1, \ldots, \rho_K, T) \qquad i = 1, \ldots, K$$

Riemann solver for combustion

(S1) Calculate standard Roe-averages $\hat{\rho} = \frac{\sqrt{\rho_L}\rho_R + \sqrt{\rho_R}\rho_L}{\sqrt{\rho_L}+\sqrt{\rho_R}} = \sqrt{\rho_L \rho_R}$ and $\hat{w} = \frac{\sqrt{\rho_L} w_L + \sqrt{\rho_R} w_R}{\sqrt{\rho_L}+\sqrt{\rho_R}}$ for $\hat{u}$, $\hat{v}$, $\hat{H}$, $\hat{Y}_i$, $\hat{T}$.

(S2) Compute $\hat{\gamma} := \hat{c}_p / \hat{c}_v$ with $\hat{c}_{\{p/v\}i} = \dfrac{1}{T_R - T_L} \displaystyle\int_{T_L}^{T_R} c_{\{p,v\}i}(\tau)\, d\tau$.

(S3) Calculate $\hat{\phi}_i := (\hat{\gamma} - 1)\left(\frac{\hat{\mathbf{u}}^2}{2} - \hat{h}_i\right) + \hat{\gamma}\, R_i\, \hat{T}$ with standard Roe-averages $\hat{e}_i$ or $\hat{h}_i$.

(S4) Calculate $\hat{c} := \left(\sum_{i=1}^{K} \hat{Y}_i\, \hat{\phi}_i - (\hat{\gamma}-1)\hat{\mathbf{u}}^2 + (\hat{\gamma}-1)\hat{H}\right)^{1/2}$.

(S5) Use $\Delta \mathbf{q} = \mathbf{q}_R - \mathbf{q}_L$ and Δp to compute the wave strengths a_m.

(S6) Calculate $\mathcal{W}_1 = a_1 \hat{\mathbf{r}}_1$, $\mathcal{W}_2 = \displaystyle\sum_{\iota=2}^{K+d} a_\iota \hat{\mathbf{r}}_\iota$, $\mathcal{W}_3 = a_{K+d+1} \hat{\mathbf{r}}_{K+d+1}$.

(S7) Evaluate $s_1 = \hat{u} - \hat{c}$, $s_2 = \hat{u}$, $s_3 = \hat{u} + \hat{c}$.

Riemann solver for combustion

(S1) Calculate standard Roe-averages $\hat{\rho} = \frac{\sqrt{\rho_L}\rho_R + \sqrt{\rho_R}\rho_L}{\sqrt{\rho_L}+\sqrt{\rho_R}} = \sqrt{\rho_L \rho_R}$ and $\hat{w} = \frac{\sqrt{\rho_L} w_L + \sqrt{\rho_R} w_R}{\sqrt{\rho_L}+\sqrt{\rho_R}}$ for $\hat{u}$, $\hat{v}$, $\hat{H}$, $\hat{Y}_i$, $\hat{T}$.

(S2) Compute $\hat{\gamma} := \hat{c}_p / \hat{c}_v$ with $\hat{c}_{\{p/v\}i} = \dfrac{1}{T_R - T_L} \displaystyle\int_{T_L}^{T_R} c_{\{p,v\}i}(\tau)\, d\tau$.

(S3) Calculate $\hat{\phi}_i := (\hat{\gamma} - 1)\left(\frac{\hat{\mathbf{u}}^2}{2} - \hat{h}_i\right) + \hat{\gamma}\, R_i\, \hat{T}$ with standard Roe-averages $\hat{e}_i$ or $\hat{h}_i$.

(S4) Calculate $\hat{c} := \left(\sum_{i=1}^{K} \hat{Y}_i\, \hat{\phi}_i - (\hat{\gamma}-1)\hat{\mathbf{u}}^2 + (\hat{\gamma}-1)\hat{H}\right)^{1/2}$.

(S5) Use $\Delta \mathbf{q} = \mathbf{q}_R - \mathbf{q}_L$ and Δp to compute the wave strengths a_m.

(S6) Calculate $\mathcal{W}_1 = a_1 \hat{\mathbf{r}}_1$, $\mathcal{W}_2 = \displaystyle\sum_{\iota=2}^{K+d} a_\iota \hat{\mathbf{r}}_\iota$, $\mathcal{W}_3 = a_{K+d+1} \hat{\mathbf{r}}_{K+d+1}$.

(S7) Evaluate $s_1 = \hat{u} - \hat{c}$, $s_2 = \hat{u}$, $s_3 = \hat{u} + \hat{c}$.

(S8) Evaluate $\rho^\star_{L/R}$, $u^\star_{L/R}$, $e^\star_{L/R}$, $c^\star_{L/R}$ from $\mathbf{q}^\star_L = \mathbf{q}_L + \mathcal{W}_1$ and $\mathbf{q}^\star_R = \mathbf{q}_R - \mathcal{W}_3$.

(S9) If $\rho^\star_{L/R} \le 0$ or $e^\star_{L/R} \le 0$ use $\mathbf{F}_{HLL}(\mathbf{q}_L, \mathbf{q}_R)$ and go to (S12).

Riemann solver for combustion

(S1) Calculate standard Roe-averages $\hat{\rho} = \frac{\sqrt{\rho_L}\rho_R + \sqrt{\rho_R}\rho_L}{\sqrt{\rho_L}+\sqrt{\rho_R}} = \sqrt{\rho_L \rho_R}$ and $\hat{w} = \frac{\sqrt{\rho_L} w_L + \sqrt{\rho_R} w_R}{\sqrt{\rho_L}+\sqrt{\rho_R}}$ for $\hat{u}$, $\hat{v}$, $\hat{H}$, $\hat{Y}_i$, $\hat{T}$.

(S2) Compute $\hat{\gamma} := \hat{c}_p / \hat{c}_v$ with $\hat{c}_{\{p/v\}i} = \dfrac{1}{T_R - T_L} \displaystyle\int_{T_L}^{T_R} c_{\{p,v\}i}(\tau)\, d\tau$.

(S3) Calculate $\hat{\phi}_i := (\hat{\gamma} - 1)\left(\frac{\hat{\mathbf{u}}^2}{2} - \hat{h}_i\right) + \hat{\gamma}\, R_i\, \hat{T}$ with standard Roe-averages $\hat{e}_i$ or $\hat{h}_i$.

(S4) Calculate $\hat{c} := \left(\sum_{i=1}^{K} \hat{Y}_i\, \hat{\phi}_i - (\hat{\gamma}-1)\hat{\mathbf{u}}^2 + (\hat{\gamma}-1)\hat{H}\right)^{1/2}$.

(S5) Use $\Delta \mathbf{q} = \mathbf{q}_R - \mathbf{q}_L$ and Δp to compute the wave strengths a_m.

(S6) Calculate $\mathcal{W}_1 = a_1 \hat{\mathbf{r}}_1$, $\mathcal{W}_2 = \displaystyle\sum_{\iota=2}^{K+d} a_\iota \hat{\mathbf{r}}_\iota$, $\mathcal{W}_3 = a_{K+d+1} \hat{\mathbf{r}}_{K+d+1}$.

(S7) Evaluate $s_1 = \hat{u} - \hat{c}$, $s_2 = \hat{u}$, $s_3 = \hat{u} + \hat{c}$.

(S8) Evaluate $\rho^\star_{L/R}$, $u^\star_{L/R}$, $e^\star_{L/R}$, $c^\star_{L/R}$ from $\mathbf{q}^\star_L = \mathbf{q}_L + \mathcal{W}_1$ and $\mathbf{q}^\star_R = \mathbf{q}_R - \mathcal{W}_3$.

(S9) If $\rho^\star_{L/R} \le 0$ or $e^\star_{L/R} \le 0$ use $\mathbf{F}_{HLL}(\mathbf{q}_L, \mathbf{q}_R)$ and go to (S12).

(S10) Entropy correction: Evaluate $|\tilde{s}_\iota|$.

$\mathbf{F}_{Roe}(\mathbf{q}_L, \mathbf{q}_R) = \frac{1}{2}\left(\mathbf{f}(\mathbf{q}_L) + \mathbf{f}(\mathbf{q}_R) - \sum_{\iota=1}^{3} |\tilde{s}_\iota| \mathcal{W}_\iota\right)$

Riemann solver for combustion

(S1) Calculate standard Roe-averages $\hat{\rho} = \frac{\sqrt{\rho_L}\rho_R + \sqrt{\rho_R}\rho_L}{\sqrt{\rho_L}+\sqrt{\rho_R}} = \sqrt{\rho_L \rho_R}$ and $\hat{w} = \frac{\sqrt{\rho_L} w_L + \sqrt{\rho_R} w_R}{\sqrt{\rho_L}+\sqrt{\rho_R}}$ for $\hat{u}$, $\hat{v}$, $\hat{H}$, $\hat{Y}_i$, $\hat{T}$.

(S2) Compute $\hat{\gamma} := \hat{c}_p / \hat{c}_v$ with $\hat{c}_{\{p/v\}i} = \dfrac{1}{T_R - T_L} \displaystyle\int_{T_L}^{T_R} c_{\{p,v\}i}(\tau)\, d\tau$.

(S3) Calculate $\hat{\phi}_i := (\hat{\gamma} - 1)\left(\frac{\hat{\mathbf{u}}^2}{2} - \hat{h}_i\right) + \hat{\gamma}\, R_i\, \hat{T}$ with standard Roe-averages $\hat{e}_i$ or $\hat{h}_i$.

(S4) Calculate $\hat{c} := \left(\sum_{i=1}^{K} \hat{Y}_i\, \hat{\phi}_i - (\hat{\gamma}-1)\hat{\mathbf{u}}^2 + (\hat{\gamma}-1)\hat{H}\right)^{1/2}$.

(S5) Use $\Delta \mathbf{q} = \mathbf{q}_R - \mathbf{q}_L$ and Δp to compute the wave strengths a_m.

(S6) Calculate $\mathcal{W}_1 = a_1 \hat{\mathbf{r}}_1$, $\mathcal{W}_2 = \displaystyle\sum_{\iota=2}^{K+d} a_\iota \hat{\mathbf{r}}_\iota$, $\mathcal{W}_3 = a_{K+d+1} \hat{\mathbf{r}}_{K+d+1}$.

(S7) Evaluate $s_1 = \hat{u} - \hat{c}$, $s_2 = \hat{u}$, $s_3 = \hat{u} + \hat{c}$.

(S8) Evaluate $\rho^\star_{L/R}$, $u^\star_{L/R}$, $e^\star_{L/R}$, $c^\star_{L/R}$ from $\mathbf{q}^\star_L = \mathbf{q}_L + \mathcal{W}_1$ and $\mathbf{q}^\star_R = \mathbf{q}_R - \mathcal{W}_3$.

(S9) If $\rho^\star_{L/R} \le 0$ or $e^\star_{L/R} \le 0$ use $\mathbf{F}_{HLL}(\mathbf{q}_L, \mathbf{q}_R)$ and go to (S12).

(S10) Entropy correction: Evaluate $|\tilde{s}_\iota|$.
$\mathbf{F}_{Roe}(\mathbf{q}_L, \mathbf{q}_R) = \frac{1}{2}\left(\mathbf{f}(\mathbf{q}_L) + \mathbf{f}(\mathbf{q}_R) - \sum_{\iota=1}^{3} |\tilde{s}_\iota| \mathcal{W}_\iota\right)$

(S11) Positivity correction: Replace $\mathbf{F}_i$ by
$$\mathbf{F}^\star_i = \mathbf{F}_\rho \cdot \begin{cases} Y_i^l\,, & \mathbf{F}_\rho \ge 0\,, \\ Y_i^r\,, & \mathbf{F}_\rho < 0\,. \end{cases}$$

(S12) Evaluate maximal signal speed by $S = \max(|s_1|, |s_3|)$.

Shock-induced combustion around a sphere

- Spherical projectile of radius $1.5\,\mathrm{mm}$ travels with constant velocity $v_l = 2170.6\,\mathrm{m/s}$ through $\mathrm{H_2} : \mathrm{O_2} : \mathrm{Ar}$ mixture (molar ratios 2:1:7) at $6.67\,\mathrm{kPa}$ and $T = 298\,\mathrm{K}$
- Mechanism by [Westbrook, 1982]: 34 forward reactions, 9 species
- Axisymmetric Euler simulation on AMR base mesh of 70×40 cells

Shock-induced combustion around a sphere

- Spherical projectile of radius $1.5\,\mathrm{mm}$ travels with constant velocity $v_l = 2170.6\,\mathrm{m/s}$ through $\mathrm{H_2} : \mathrm{O_2} : \mathrm{Ar}$ mixture (molar ratios 2:1:7) at $6.67\,\mathrm{kPa}$ and $T = 298\,\mathrm{K}$
- Mechanism by [Westbrook, 1982]: 34 forward reactions, 9 species
- Axisymmetric Euler simulation on AMR base mesh of 70×40 cells
- Comparison of 3-level computation with refinement factors 2,2 ($\sim 5\,\mathrm{Pts}/l_{ig}$) and a 4-level computation with refinement factors 2,2,4 ($\sim 19\,\mathrm{Pts}/l_{ig}$) at $t = 350\,\mu\mathrm{s}$

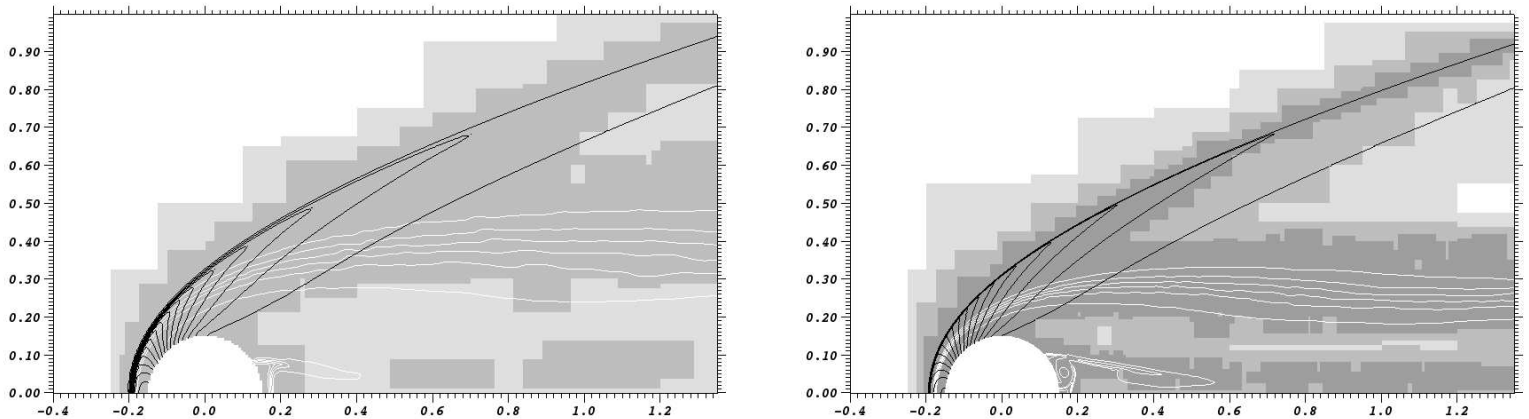

Iso-contours of p (black) and Y_{H_2} (white) on refinement domains for 3-level (left) and 4-level computation (right)

Shock-induced combustion around a sphere

- Spherical projectile of radius $1.5\,\mathrm{mm}$ travels with constant velocity $v_l = 2170.6\,\mathrm{m/s}$ through $\mathrm{H_2} : \mathrm{O_2} : \mathrm{Ar}$ mixture (molar ratios 2:1:7) at $6.67\,\mathrm{kPa}$ and $T = 298\,\mathrm{K}$
- Mechanism by [Westbrook, 1982]: 34 forward reactions, 9 species
- Axisymmetric Euler simulation on AMR base mesh of 70×40 cells
- Comparison of 3-level computation with refinement factors 2,2 ($\sim 5\,\mathrm{Pts}/l_{ig}$) and a 4-level computation with refinement factors 2,2,4 ($\sim 19\,\mathrm{Pts}/l_{ig}$) at $t = 350\,\mu\mathrm{s}$
- Higher resolved computation captures combustion zone visibly better and at slightly different position (see below)

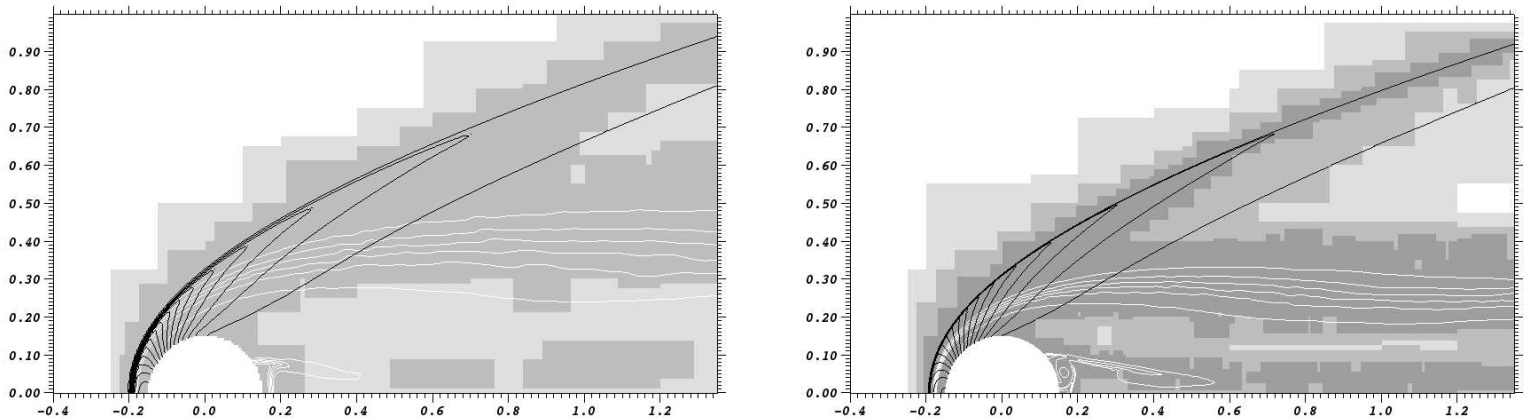

Iso-contours of p (black) and Y_{H_2} (white) on refinement domains for 3-level (left) and 4-level computation (right)

Shock-induced combustion around a sphere

- Spherical projectile of radius $1.5\,\mathrm{mm}$ travels with constant velocity $v_l = 2170.6\,\mathrm{m/s}$ through $\mathrm{H_2} : \mathrm{O_2} : \mathrm{Ar}$ mixture (molar ratios 2:1:7) at $6.67\,\mathrm{kPa}$ and $T = 298\,\mathrm{K}$
- Mechanism by [Westbrook, 1982]: 34 forward reactions, 9 species
- Axisymmetric Euler simulation on AMR base mesh of 70×40 cells
- Comparison of 3-level computation with refinement factors 2,2 ($\sim 5\,\mathrm{Pts}/l_{ig}$) and a 4-level computation with refinement factors 2,2,4 ($\sim 19\,\mathrm{Pts}/l_{ig}$) at $t = 350\,\mu\mathrm{s}$
- Higher resolved computation captures combustion zone visibly better and at slightly different position (see below)

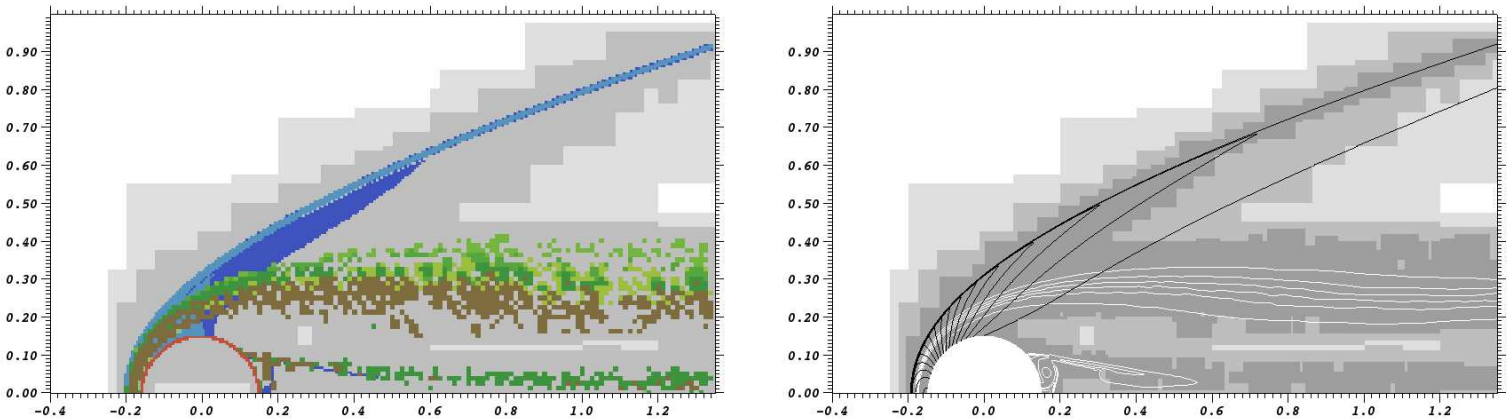

Iso-contours of p (black) and Y_{H_2} (white) on refinement domains for 3-level (left) and 4-level computation (right)

Lehr's ballistic range experiments

- Spherical-nosed projectile of radius $1.5\,\mathrm{mm}$ travels with constant velocity through stoichiometric $H_2 : O_2 : N_2$ mixture (molar ratios 2:1:3.76) at $42.663\,\mathrm{kPa}$ and $T = 293\,\mathrm{K}$ [Lehr, 1972]
- Mechanism by [Jachimowski, 1988]: 19 equilibrium reactions, 9 species. Chapman Jouguet velocity $\sim 1957\,\mathrm{m/s}$.

Lehr's ballistic range experiments

- Spherical-nosed projectile of radius $1.5\,\mathrm{mm}$ travels with constant velocity through stoichiometric $H_2 : O_2 : N_2$ mixture (molar ratios 2:1:3.76) at $42.663\,\mathrm{kPa}$ and $T = 293\,\mathrm{K}$ [Lehr, 1972]
- Mechanism by [Jachimowski, 1988]: 19 equilibrium reactions, 9 species. Chapman Jouguet velocity $\sim 1957\,\mathrm{m/s}$.
- Axisymmetric Navier-Stokes and Eulers simulations on AMR base mesh of 400×200 cells, physical domain size $6\,\mathrm{cm} \times 3\,\mathrm{cm}$
- 4-level computations with refinement factors 2,2,4 to final time $t = 170\,\mu\mathrm{s}$. Refinement downstream removed.

Lehr's ballistic range experiments

- Spherical-nosed projectile of radius $1.5\,\mathrm{mm}$ travels with constant velocity through stoichiometric $H_2 : O_2 : N_2$ mixture (molar ratios 2:1:3.76) at $42.663\,\mathrm{kPa}$ and $T = 293\,\mathrm{K}$ [Lehr, 1972]
- Mechanism by [Jachimowski, 1988]: 19 equilibrium reactions, 9 species. Chapman Jouguet velocity $\sim 1957\,\mathrm{m/s}$.
- Axisymmetric Navier-Stokes and Eulers simulations on AMR base mesh of 400×200 cells, physical domain size $6\,\mathrm{cm} \times 3\,\mathrm{cm}$
- 4-level computations with refinement factors 2,2,4 to final time $t = 170\,\mu\mathrm{s}$. Refinement downstream removed.
- Main configurations
  - Velocity $v_l = 1931\,\mathrm{m/s}$ ($M = 4.79$), $\sim 40\,\mathrm{Pts}/l_{ig}$
  - Velocity $v_l = 1806\,\mathrm{m/s}$ ($M = 4.48$), $\sim 60\,\mathrm{Pts}/l_{ig}$
- Various previous studies with not entirely consistent results. E.g. [Yungster and Radhakrishnan, 1996], [Axdahl et al., 2011]

Lehr's ballistic range experiments

- Spherical-nosed projectile of radius $1.5\,\mathrm{mm}$ travels with constant velocity through stoichiometric $H_2 : O_2 : N_2$ mixture (molar ratios 2:1:3.76) at $42.663\,\mathrm{kPa}$ and $T = 293\,\mathrm{K}$ [Lehr, 1972]
- Mechanism by [Jachimowski, 1988]: 19 equilibrium reactions, 9 species. Chapman Jouguet velocity $\sim 1957\,\mathrm{m/s}$.
- Axisymmetric Navier-Stokes and Eulers simulations on AMR base mesh of 400×200 cells, physical domain size $6\,\mathrm{cm} \times 3\,\mathrm{cm}$
- 4-level computations with refinement factors 2,2,4 to final time $t = 170\,\mu\mathrm{s}$. Refinement downstream removed.
- Main configurations
  - Velocity $v_l = 1931\,\mathrm{m/s}$ ($M = 4.79$), $\sim 40\,\mathrm{Pts}/l_{ig}$
  - Velocity $v_l = 1806\,\mathrm{m/s}$ ($M = 4.48$), $\sim 60\,\mathrm{Pts}/l_{ig}$
- Various previous studies with not entirely consistent results. E.g. [Yungster and Radhakrishnan, 1996], [Axdahl et al., 2011]
- Stagnation point location and pressure tracked in every time step
- All computations were on 32 cores requiring $\sim 1500\,\mathrm{h}$ CPU each

Viscous case – $M = 4.79$

- 5619 iterations with CFL=0.9 to $t = 170\,\mu\mathrm{s}$
- Oscillation frequency in last $20\,\mu\mathrm{s}$: $\sim 722\,\mathrm{kHz}$ (viscous), $\sim 737\,\mathrm{kHz}$ (inviscid)
- Experimental value: $\sim 720\,\mathrm{kHz}$

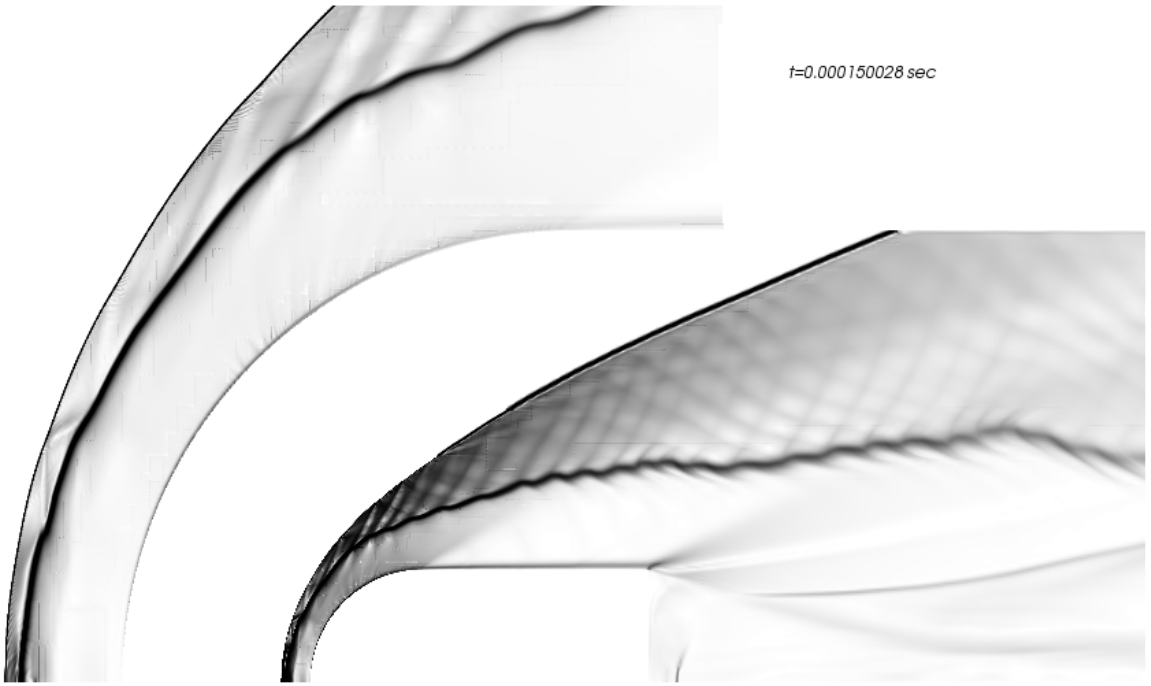

Schlieren plot of density

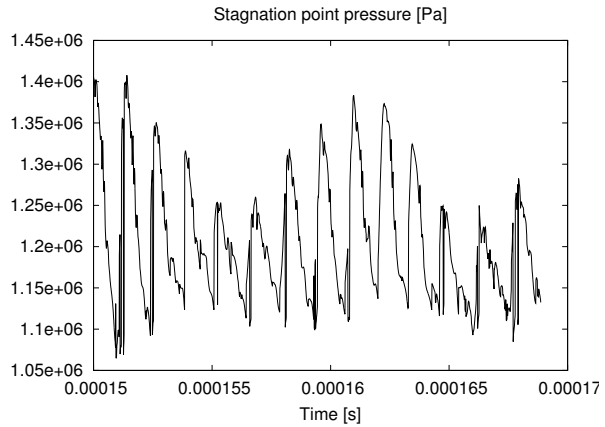

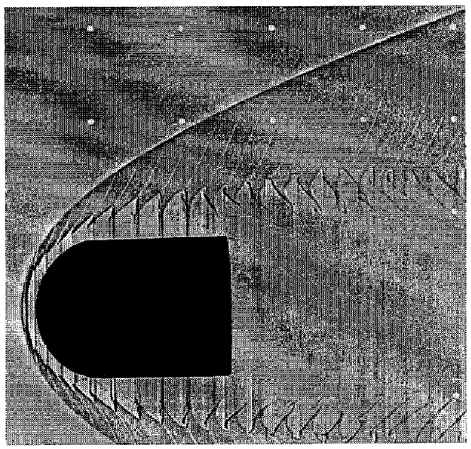

Viscous case – $M = 4.79$ – mesh adaptation

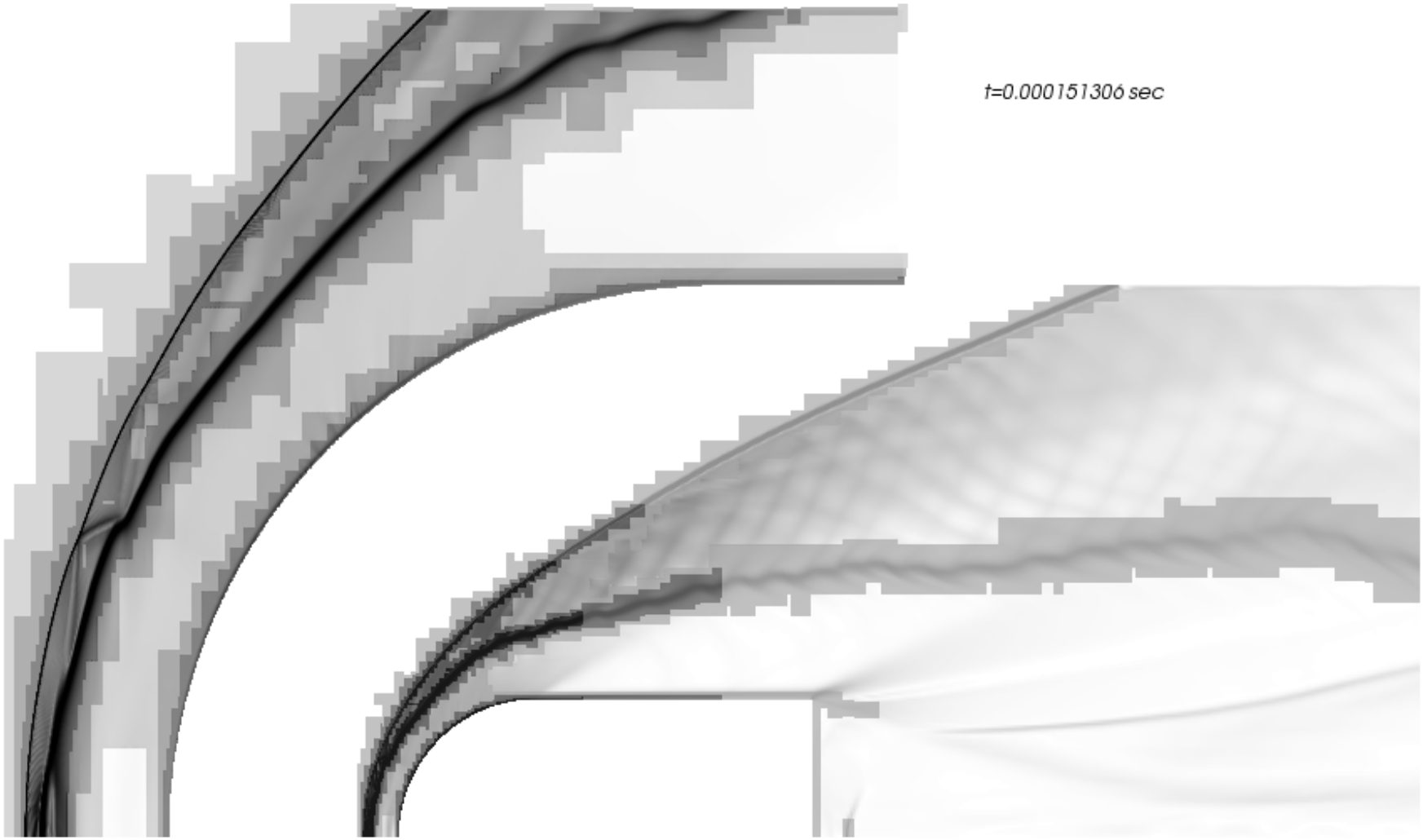

Comparison of temperature field

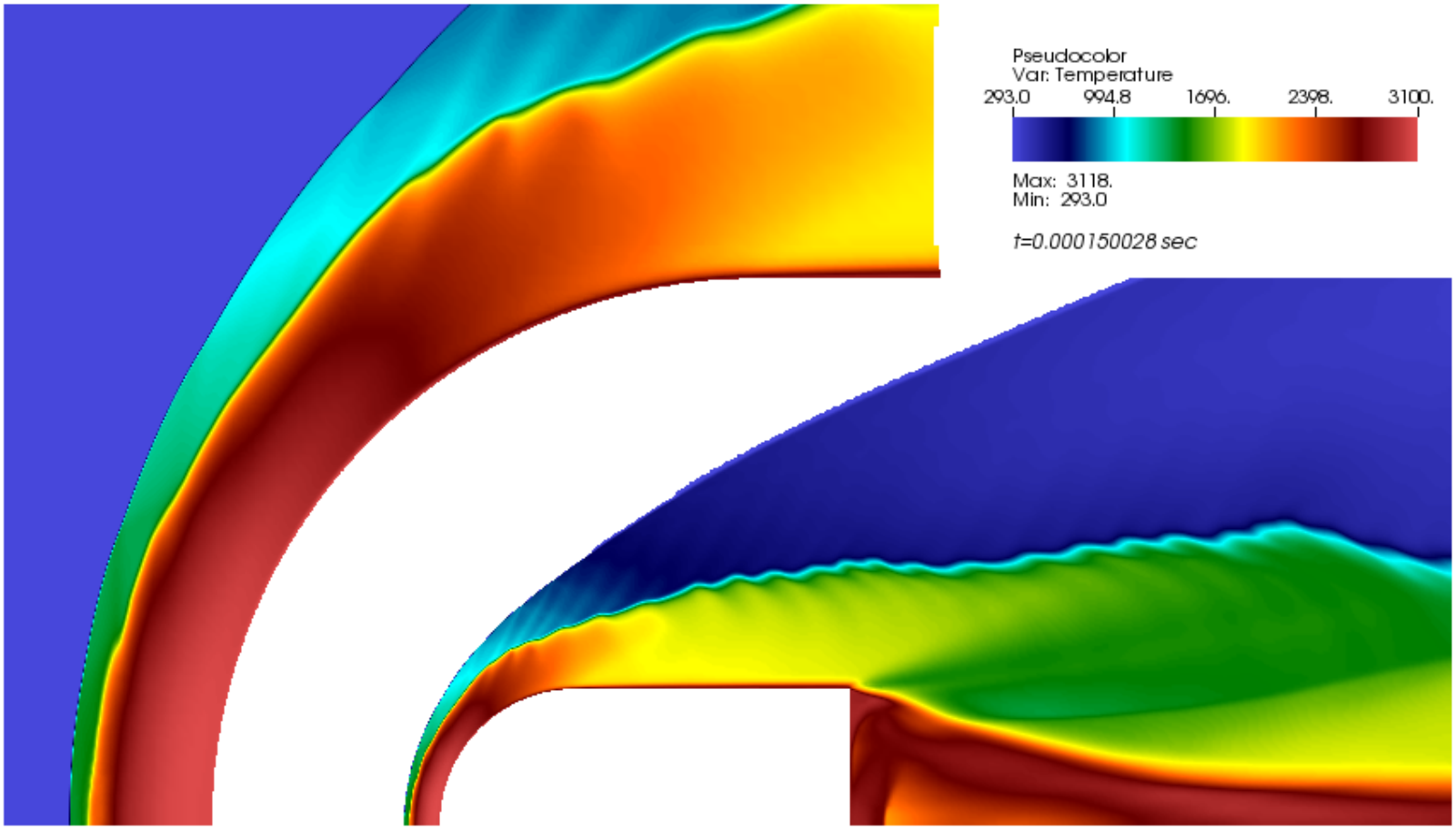

Viscous

Comparison of temperature field

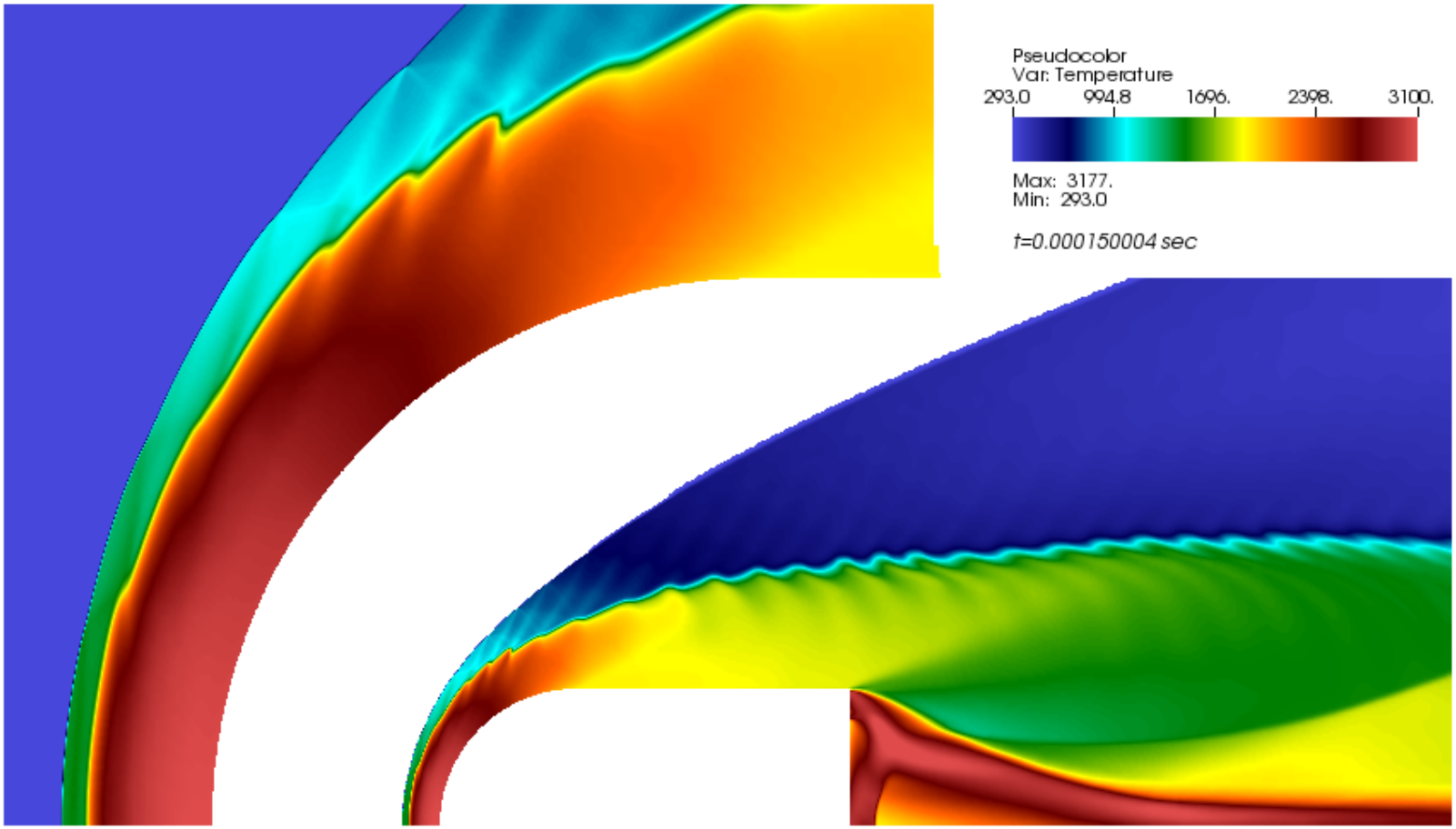

Inviscid

Viscous case – $M = 4.48$

- 5432 iterations with CFL=0.9 to $t = 170\,\mu\mathrm{s}$
- Oscillation frequency in last $20\,\mu\mathrm{s}$: $\sim 417\,\mathrm{kHz}$
- Experimental value: $\sim 425\,\mathrm{kHz}$

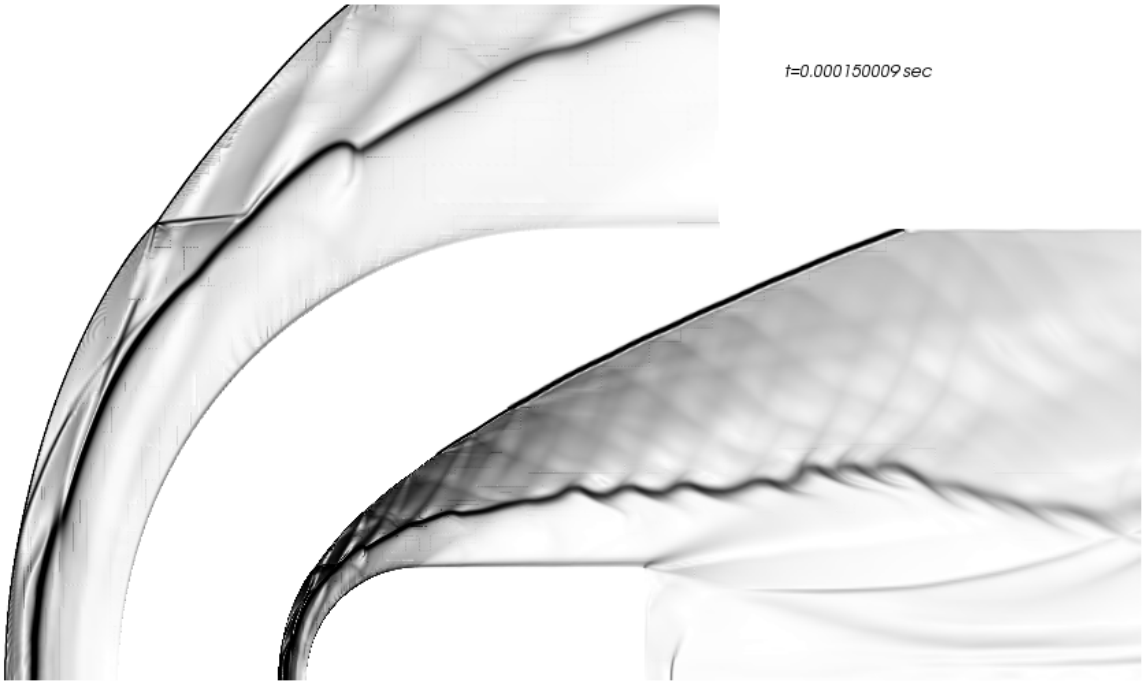

Schlieren plot of density

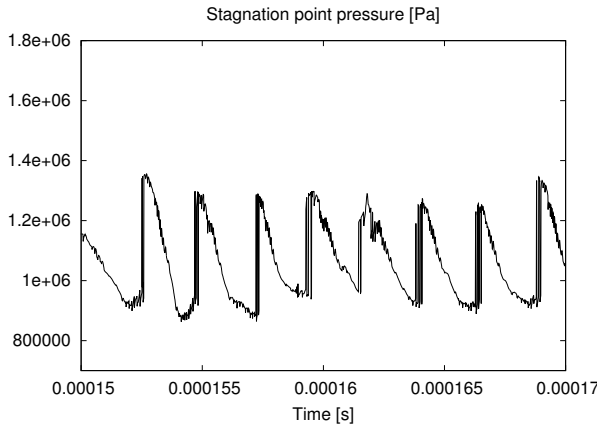

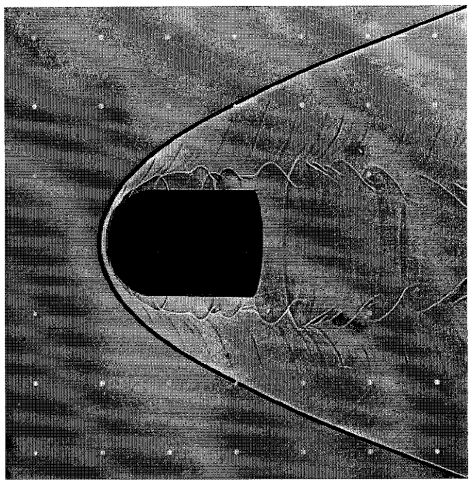

Oscillation mechanism

Schlieren of density

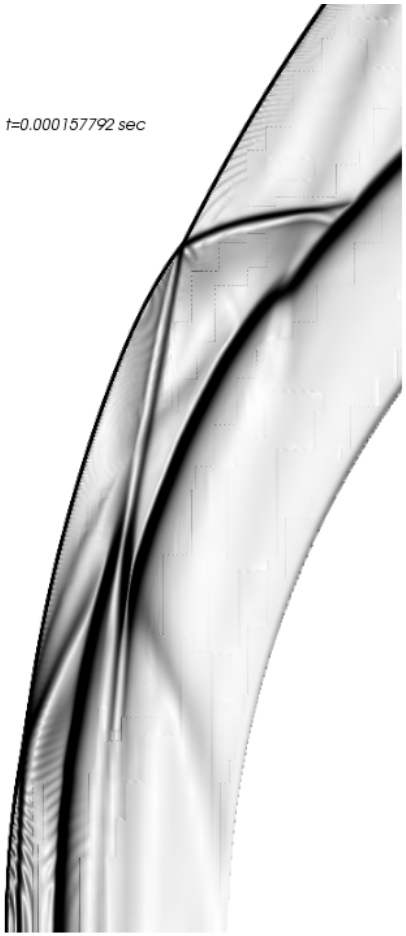

Temperature

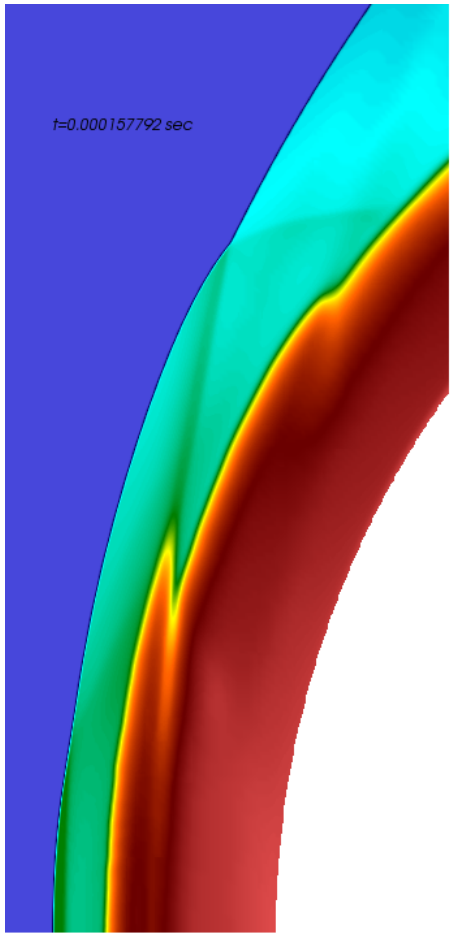

Mass fraction OH

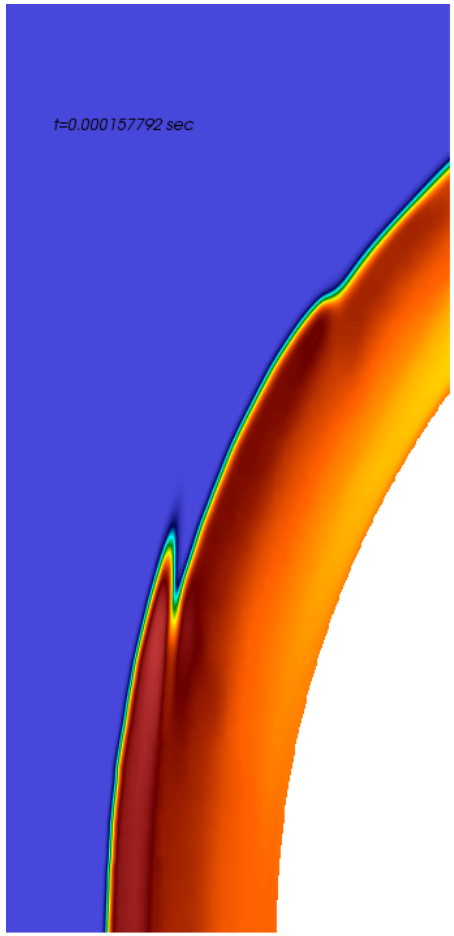

Pressure

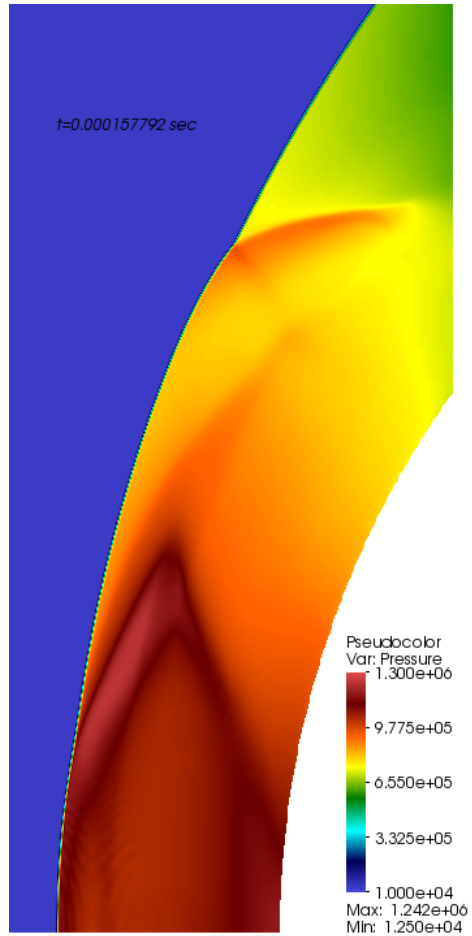

Oscillation mechanism

Schlieren of density

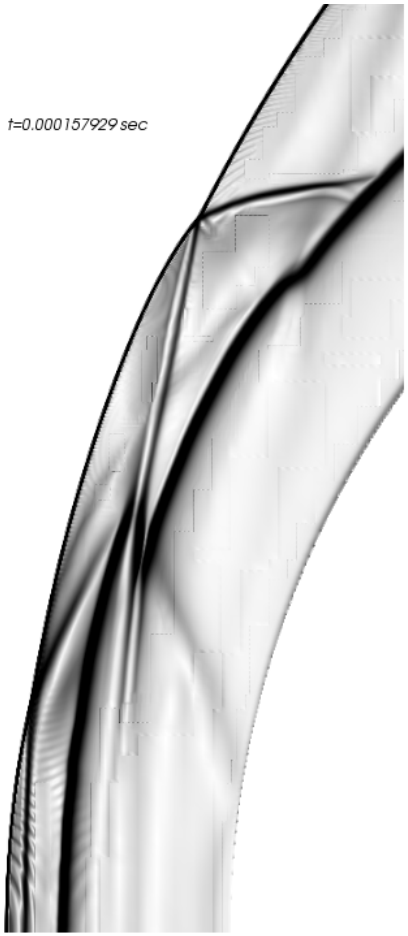

Temperature

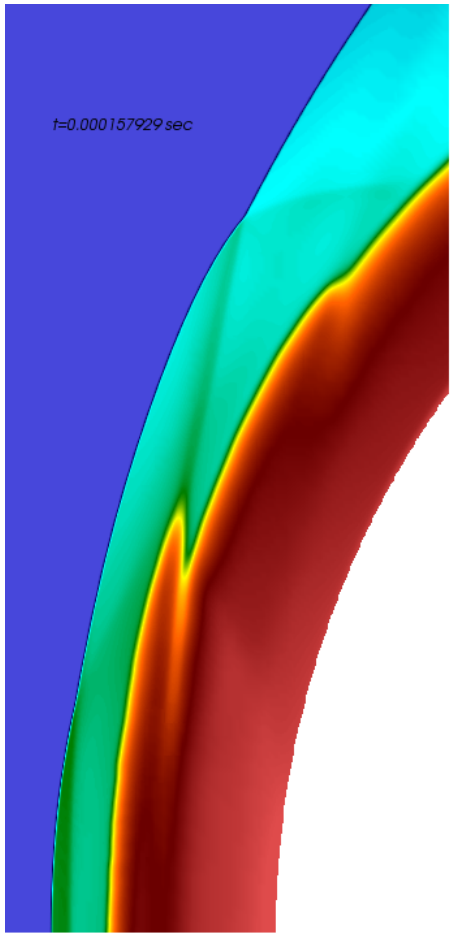

Mass fraction OH

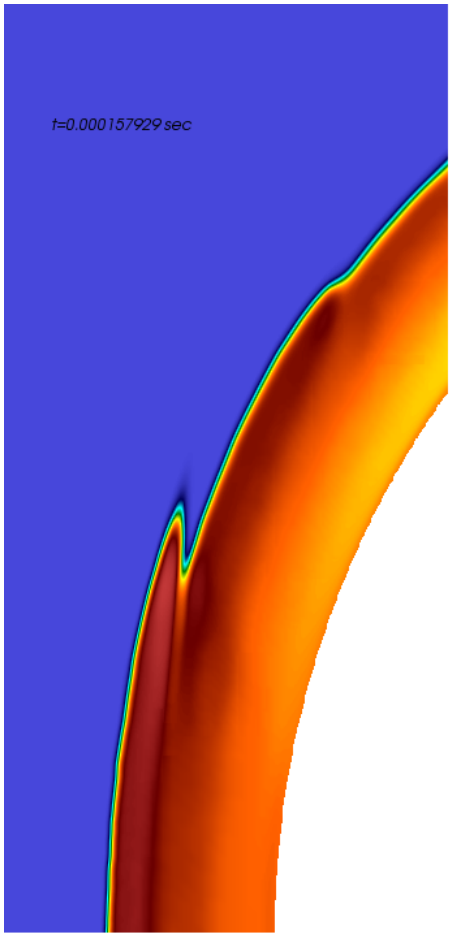

Pressure

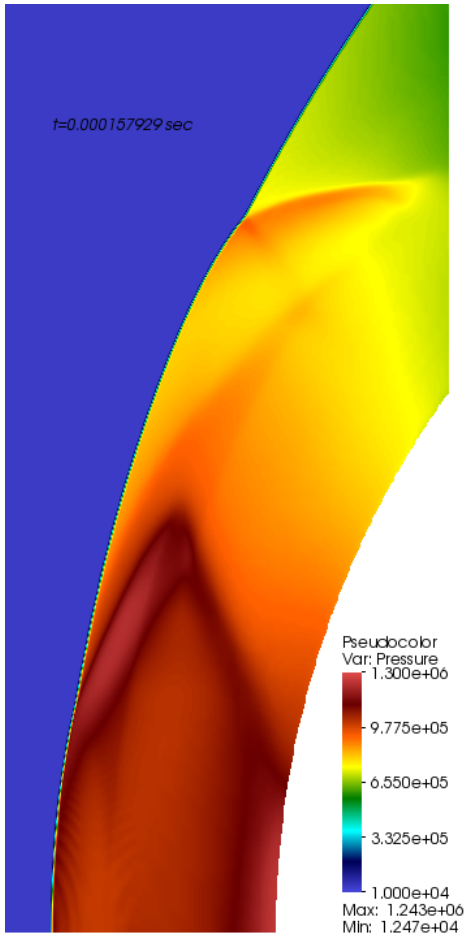

Oscillation mechanism

Schlieren of density

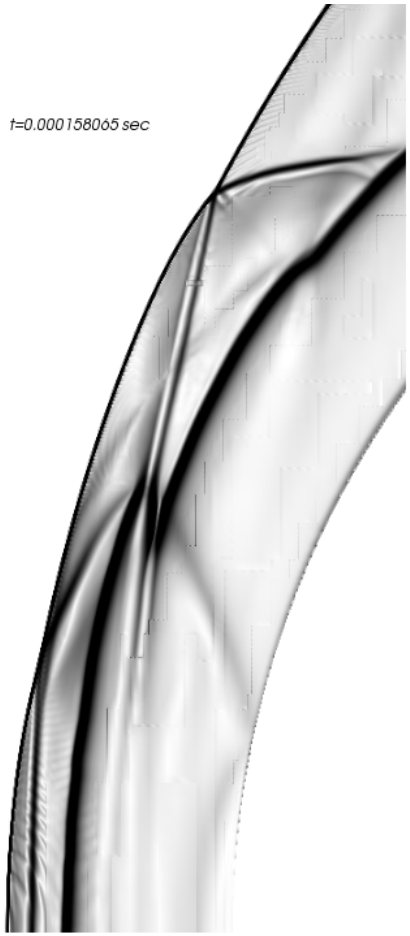

Temperature

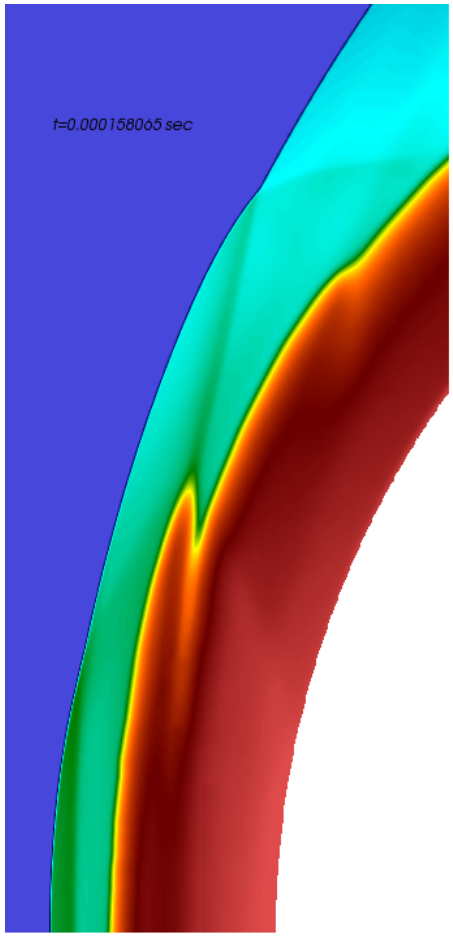

Mass fraction OH

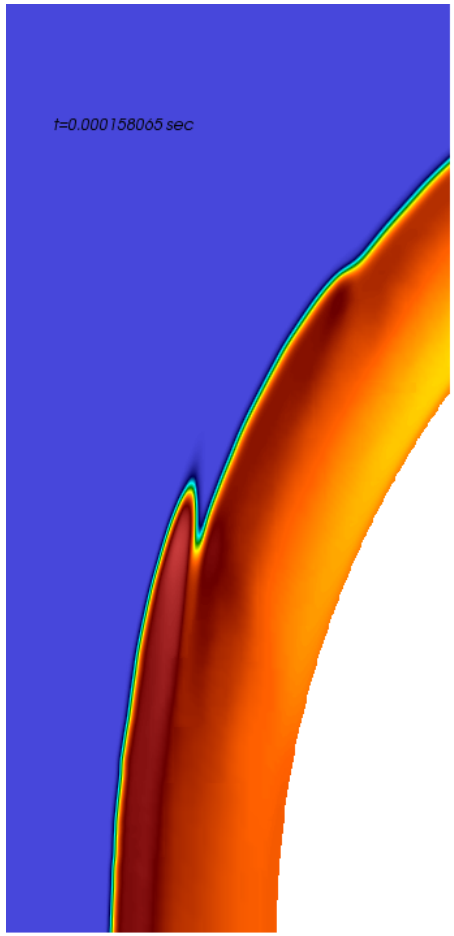

Pressure

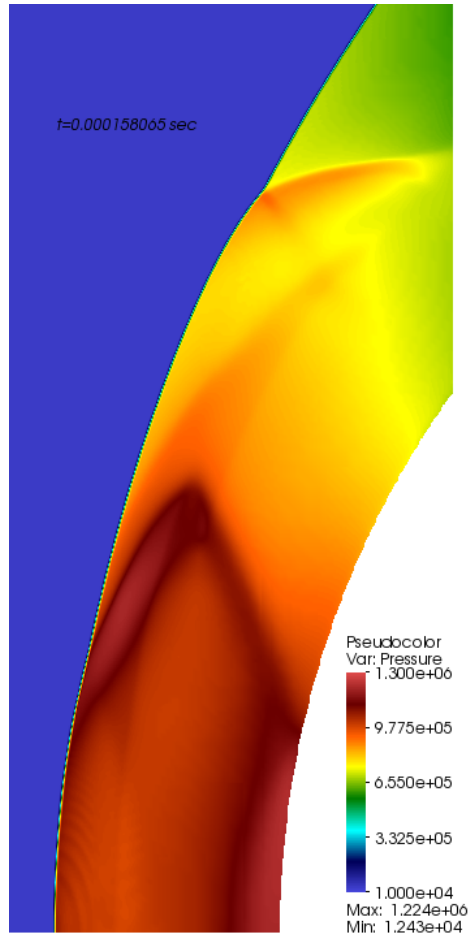

Oscillation mechanism

Schlieren of density

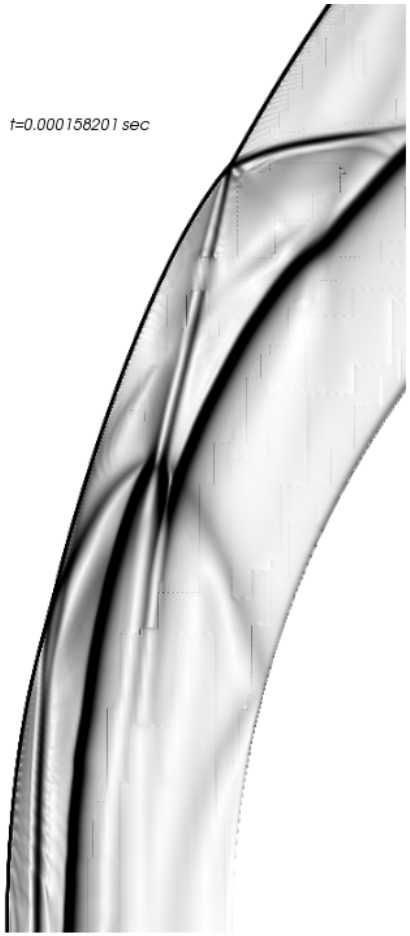

Temperature

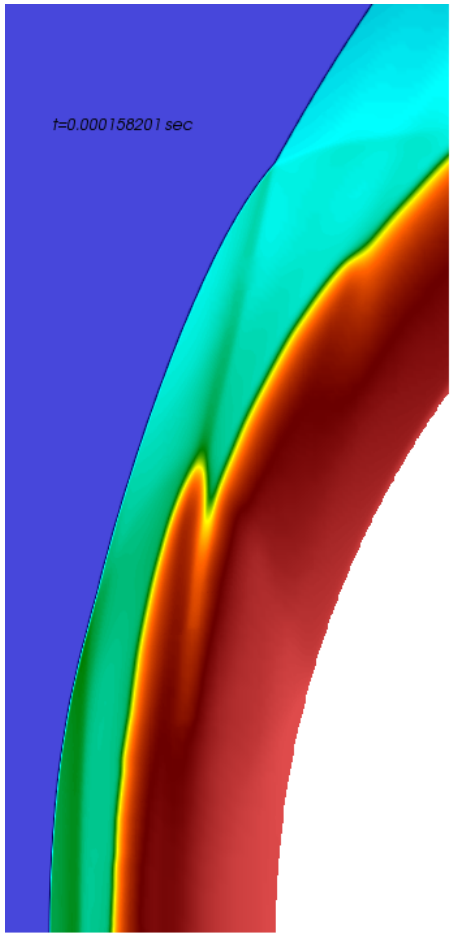

Mass fraction OH

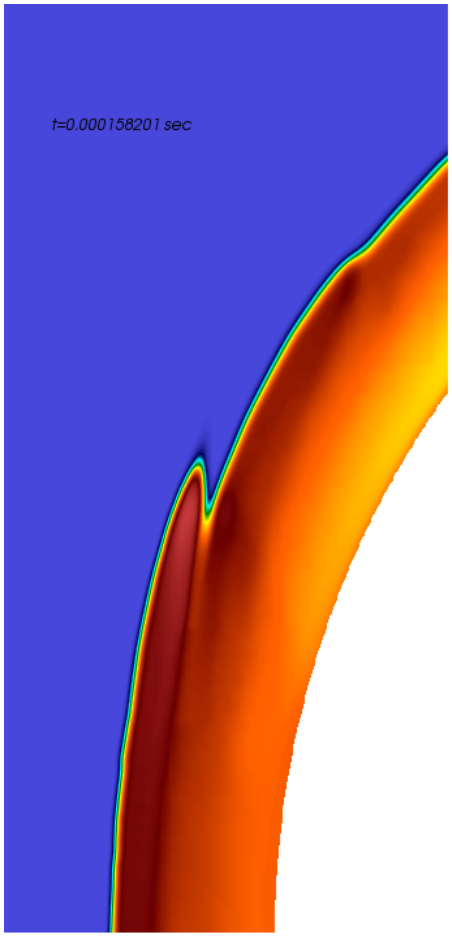

Pressure

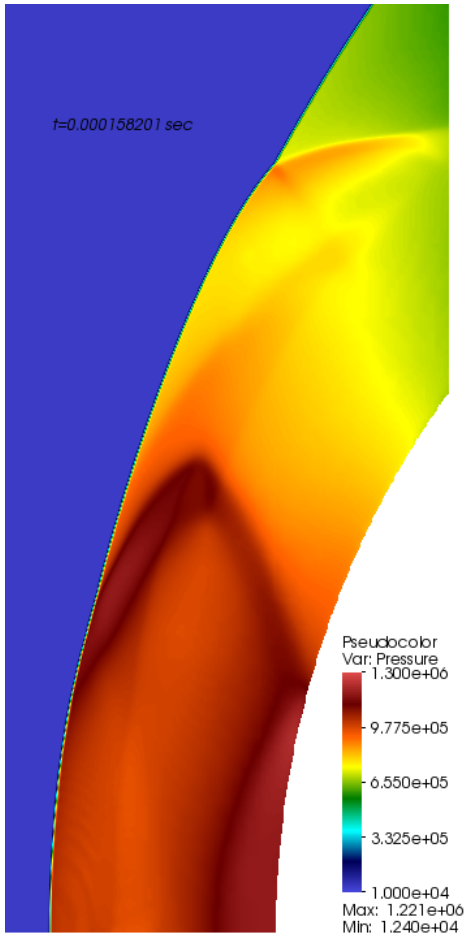

Oscillation mechanism

Schlieren of density

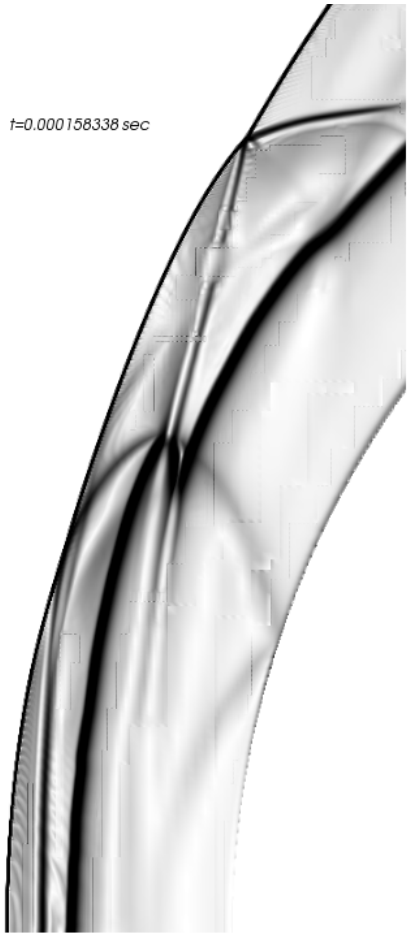

Temperature

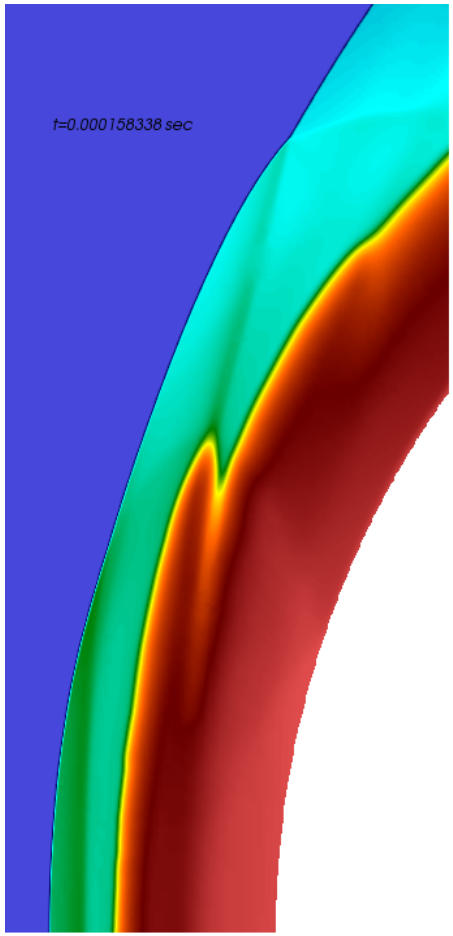

Mass fraction OH

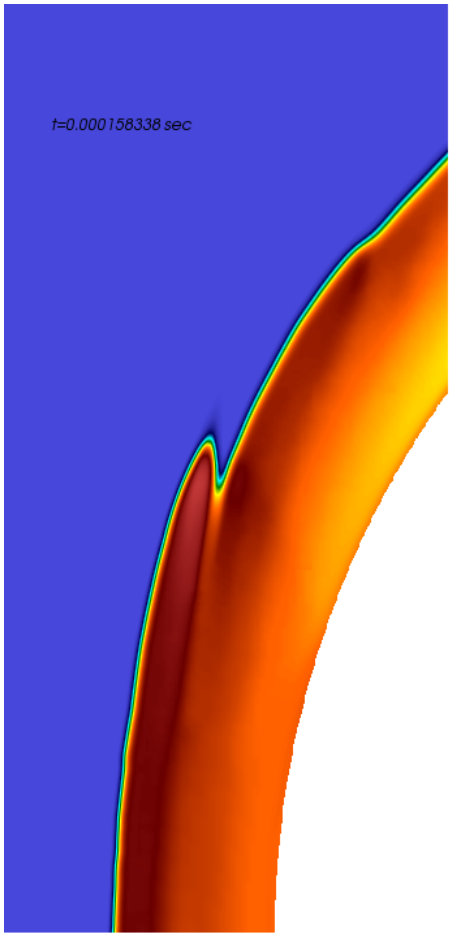

Pressure

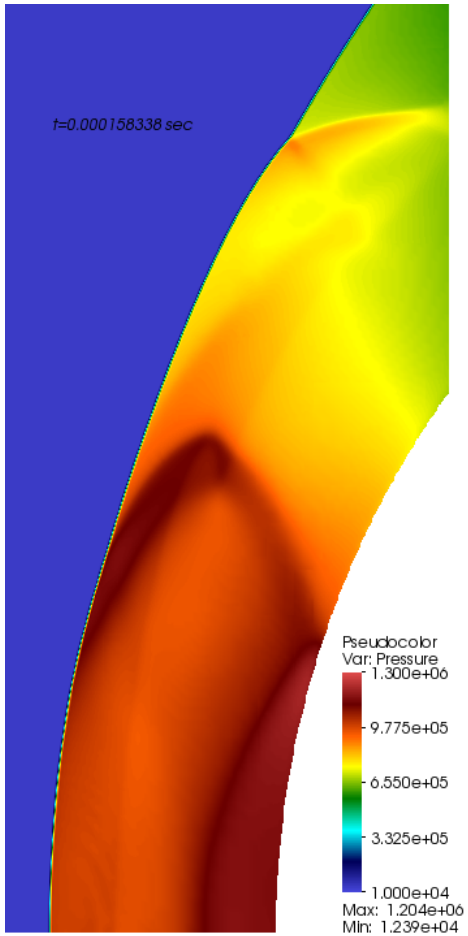

Oscillation mechanism

Schlieren of density

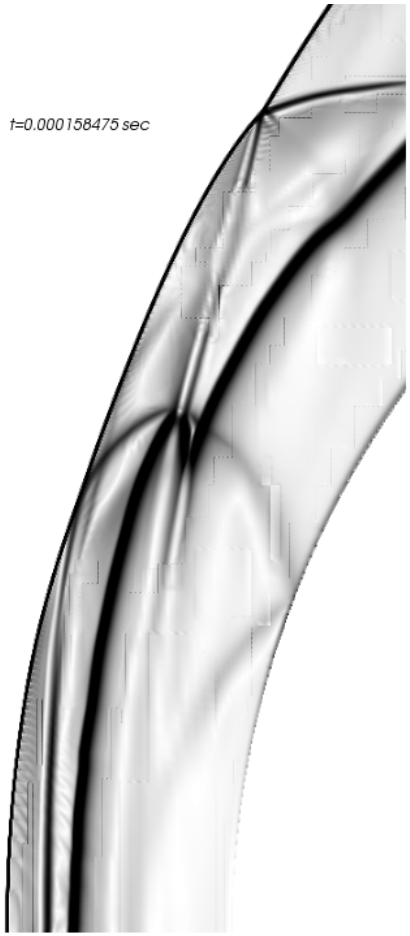

Temperature

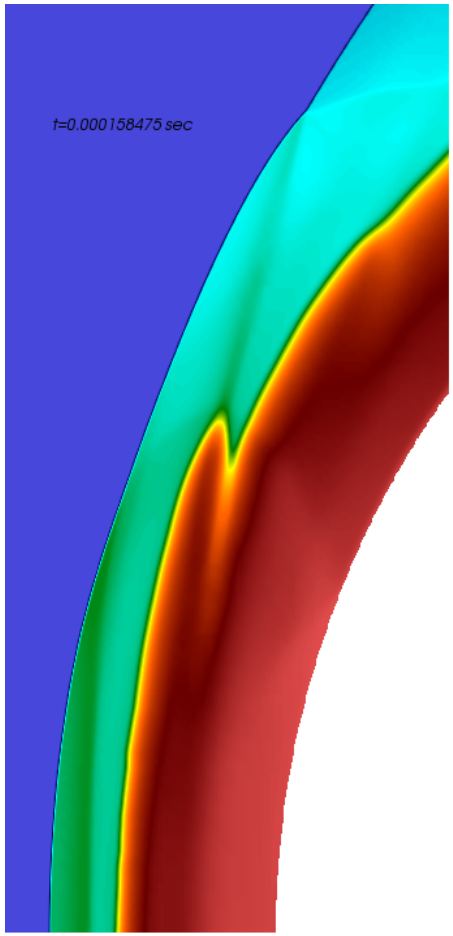

Mass fraction OH

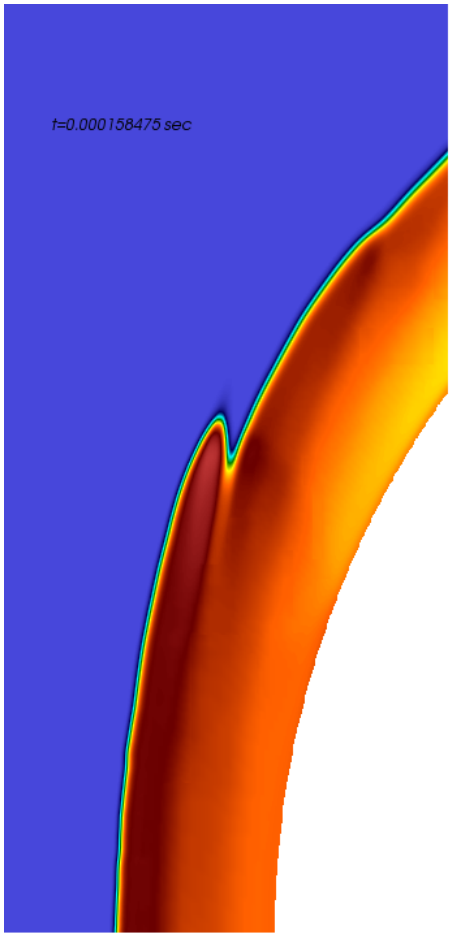

Pressure

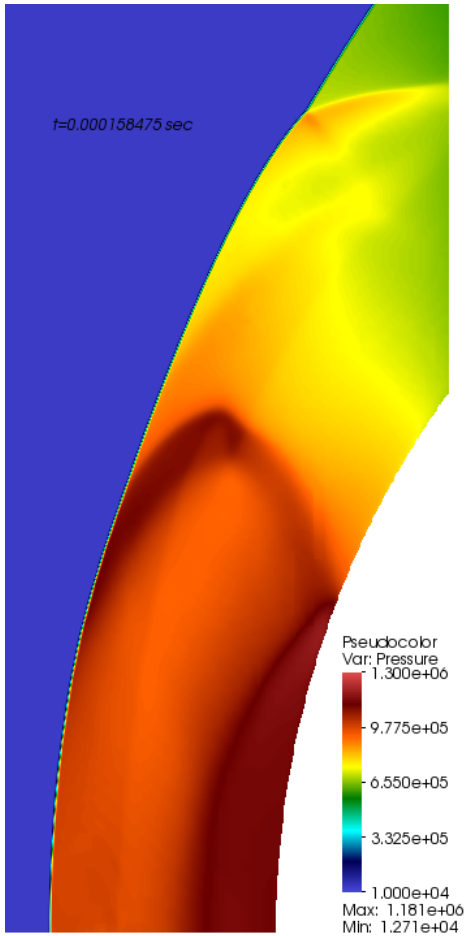

Oscillation mechanism

Schlieren of density

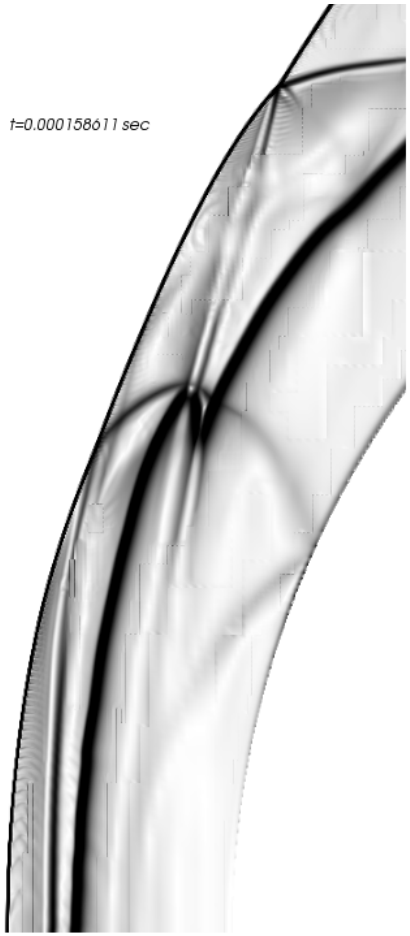

Temperature

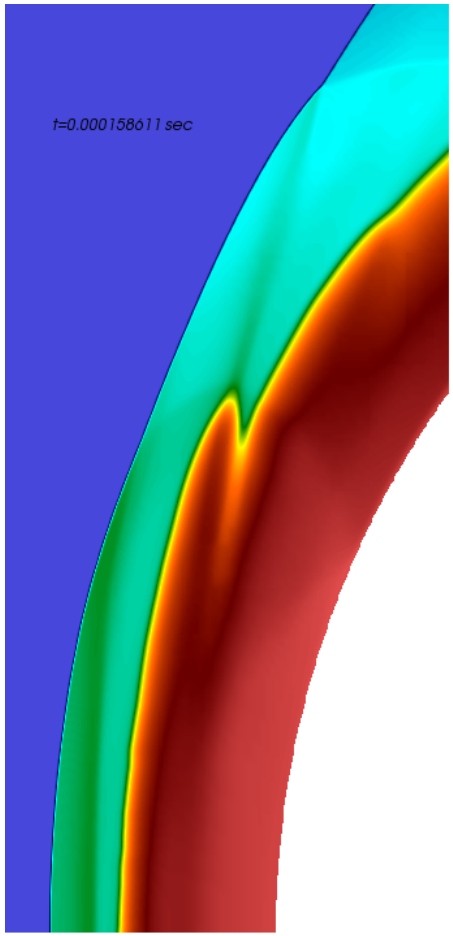

Mass fraction OH

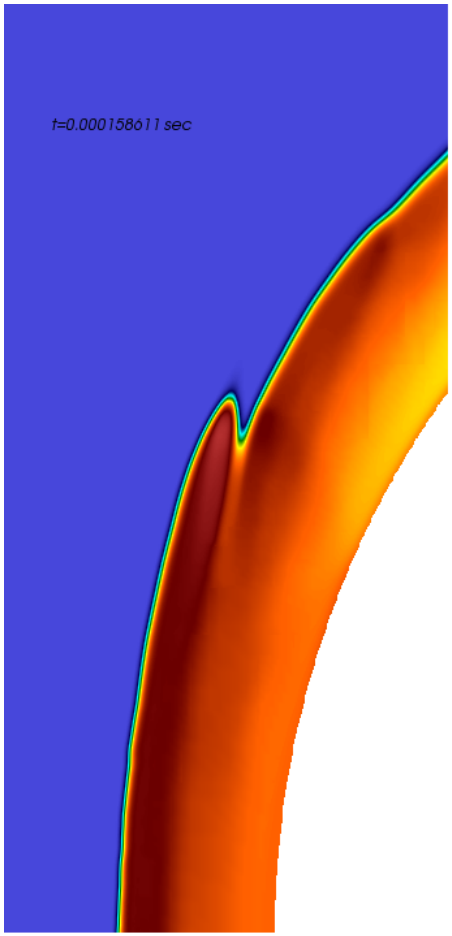

Pressure

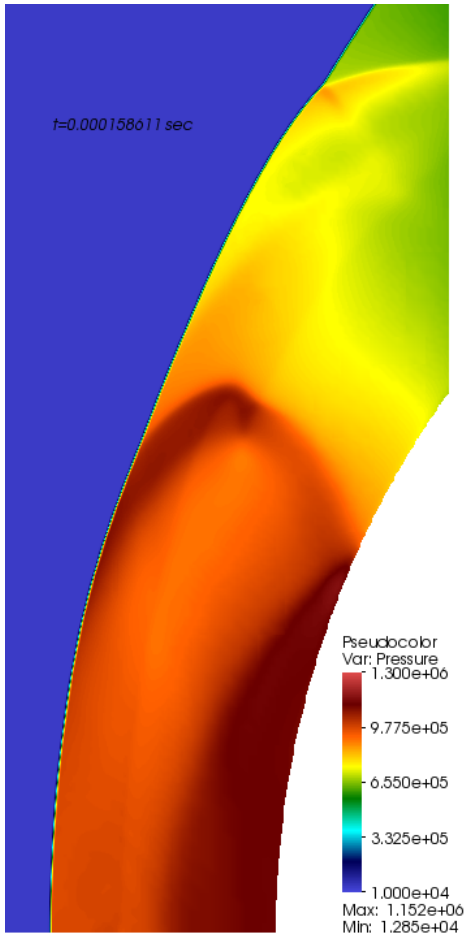

Oscillation mechanism

Schlieren of density

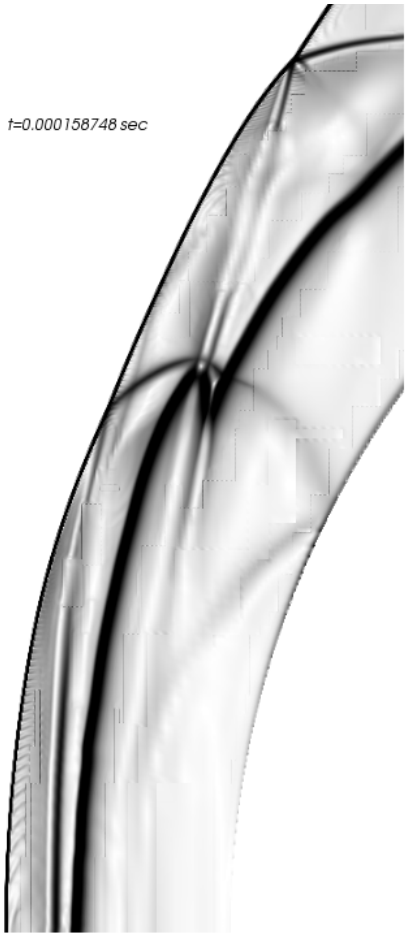

Temperature

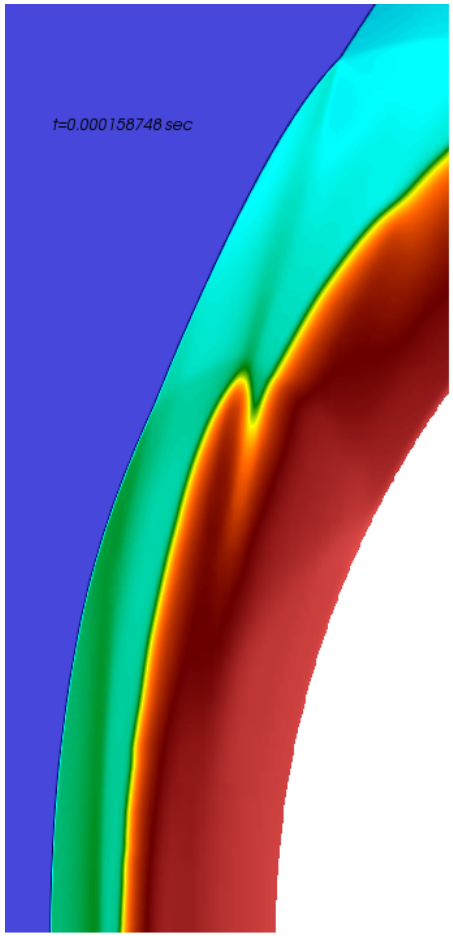

Mass fraction OH

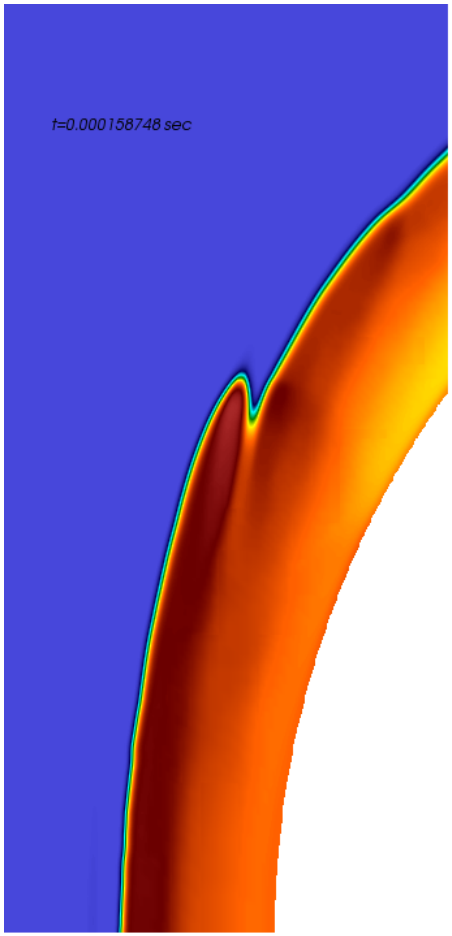

Pressure

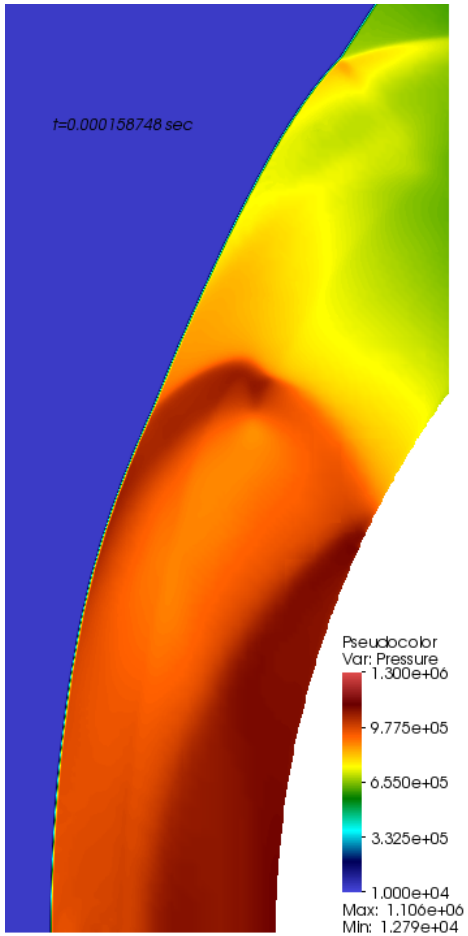

Oscillation mechanism

Schlieren of density

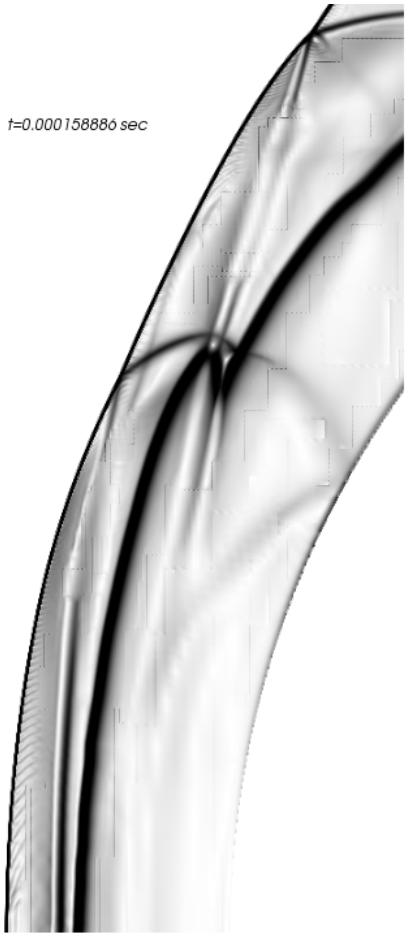

Temperature

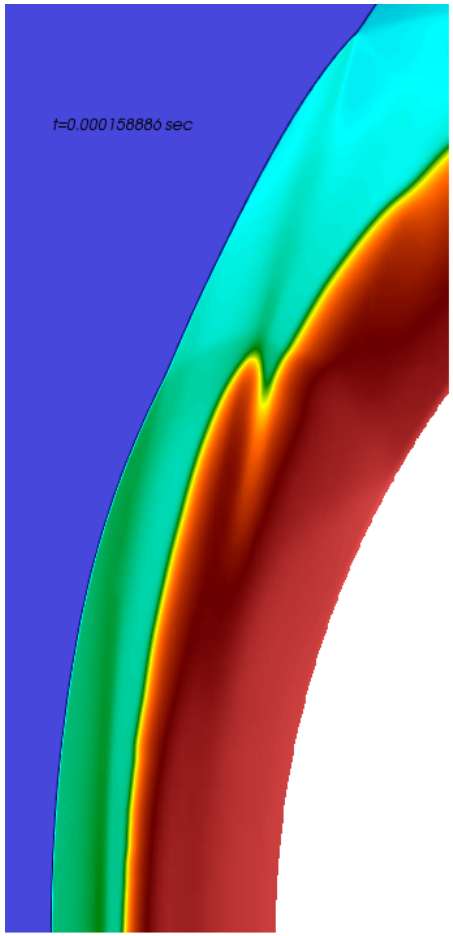

Mass fraction OH

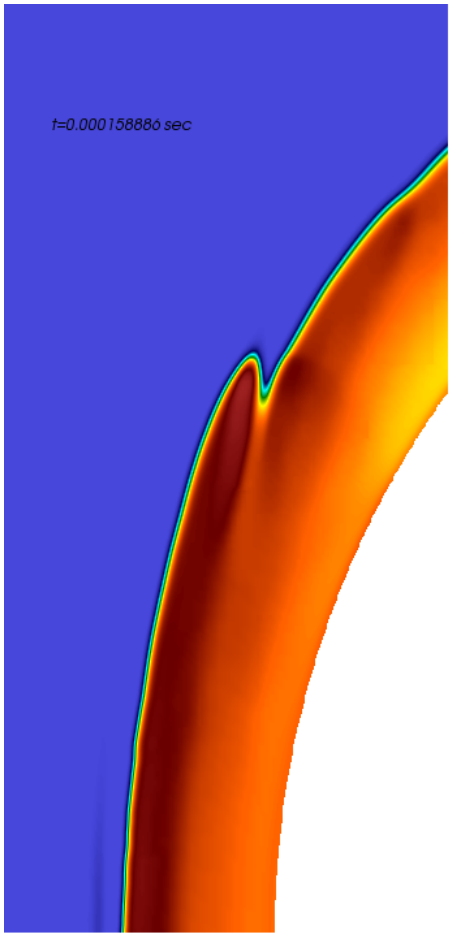

Pressure

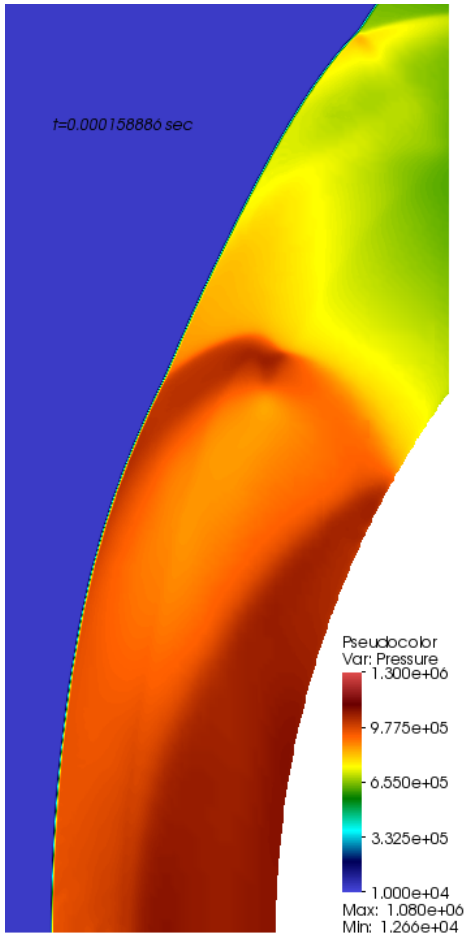

Oscillation mechanism

Schlieren of density

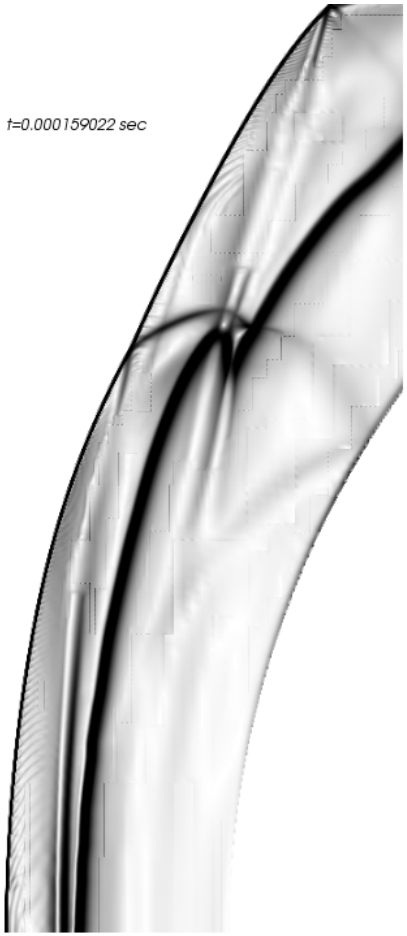

Temperature

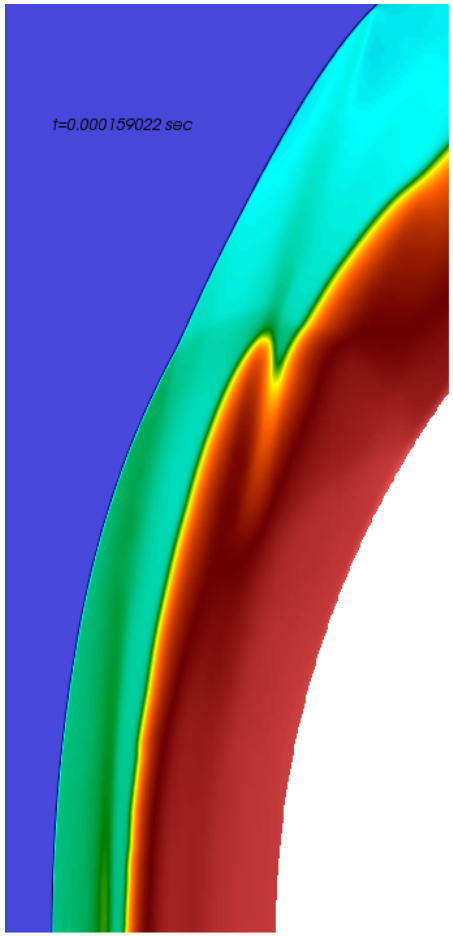

Mass fraction OH

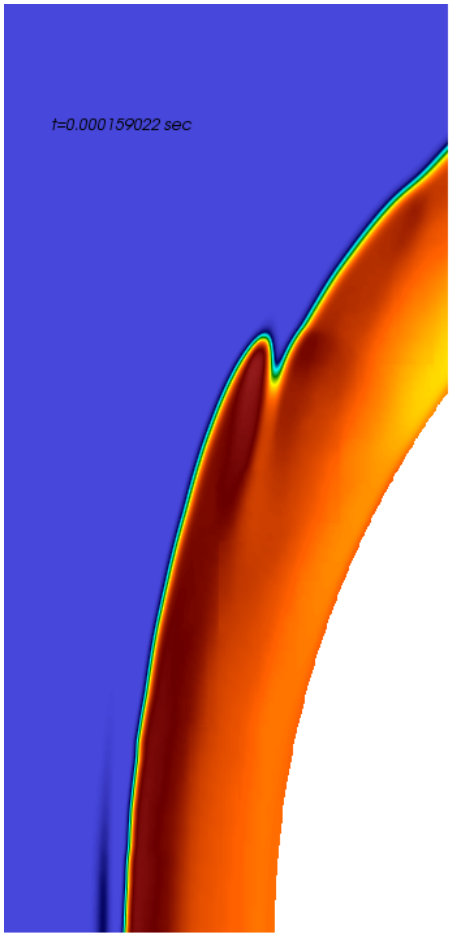

Pressure

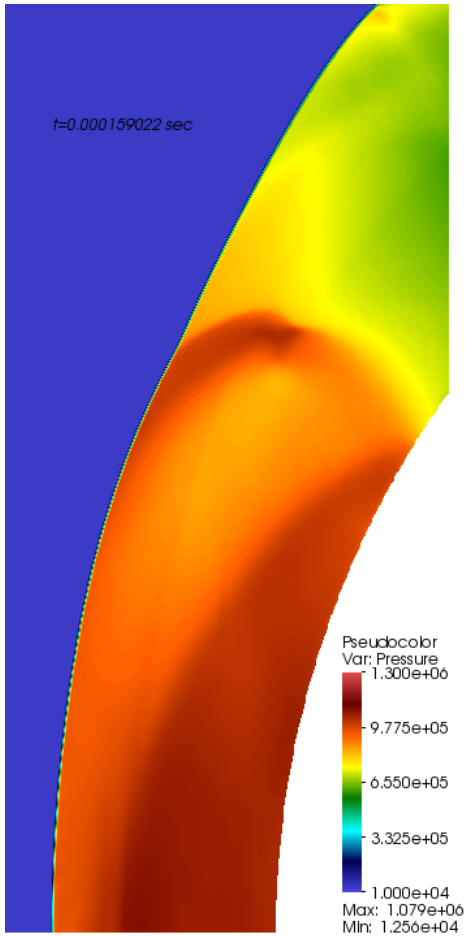

Oscillation mechanism

Schlieren of density

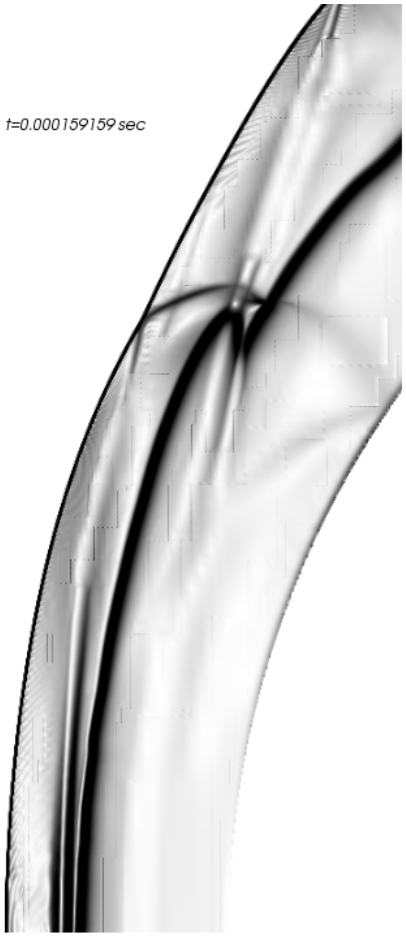

Temperature

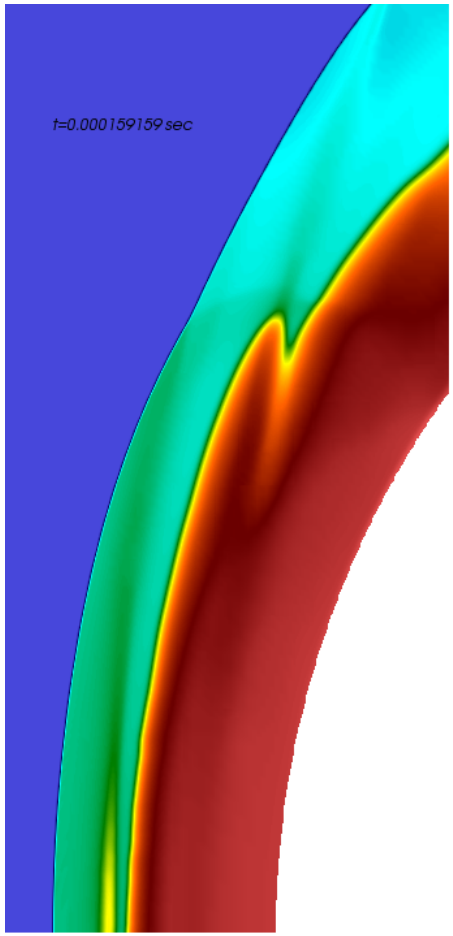

Mass fraction OH

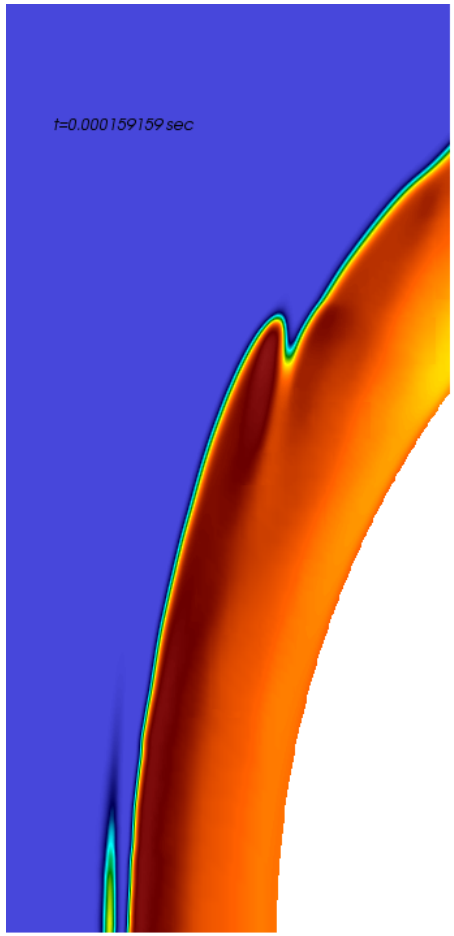

Pressure

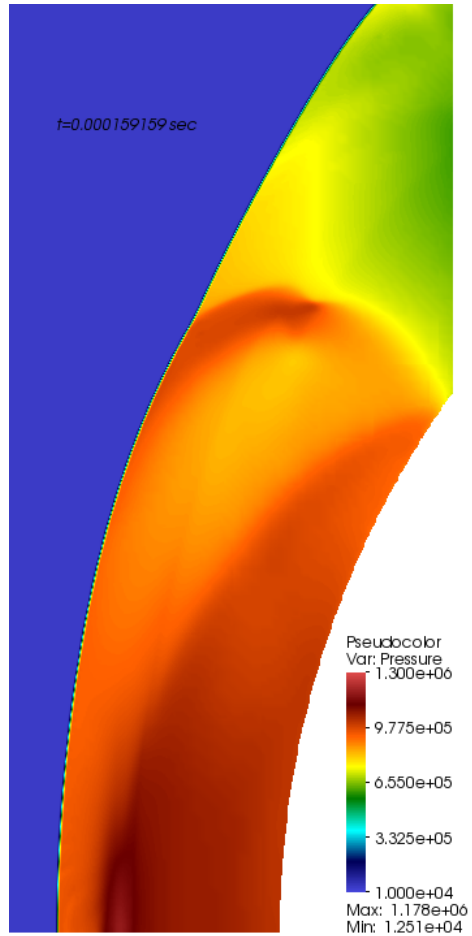

Oscillation mechanism

Schlieren of density

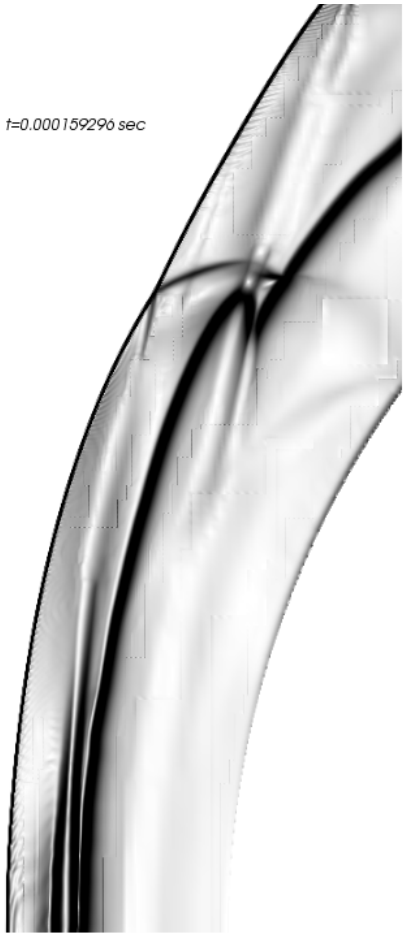

Temperature

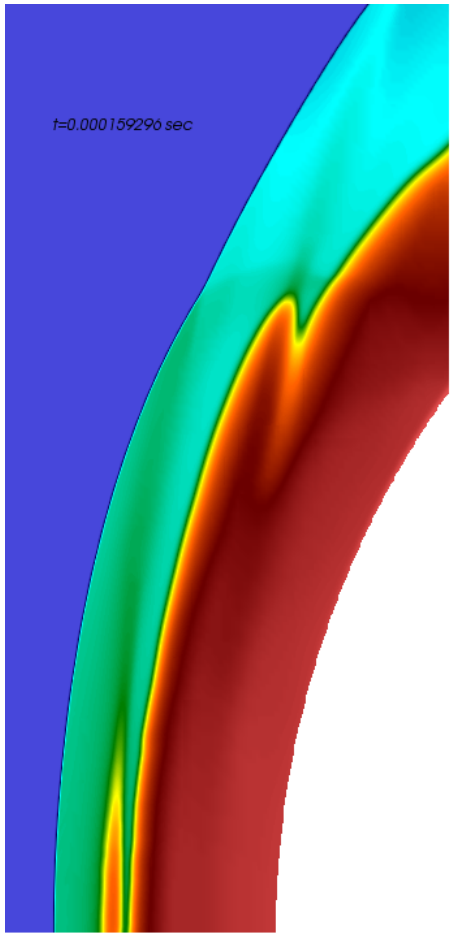

Mass fraction OH

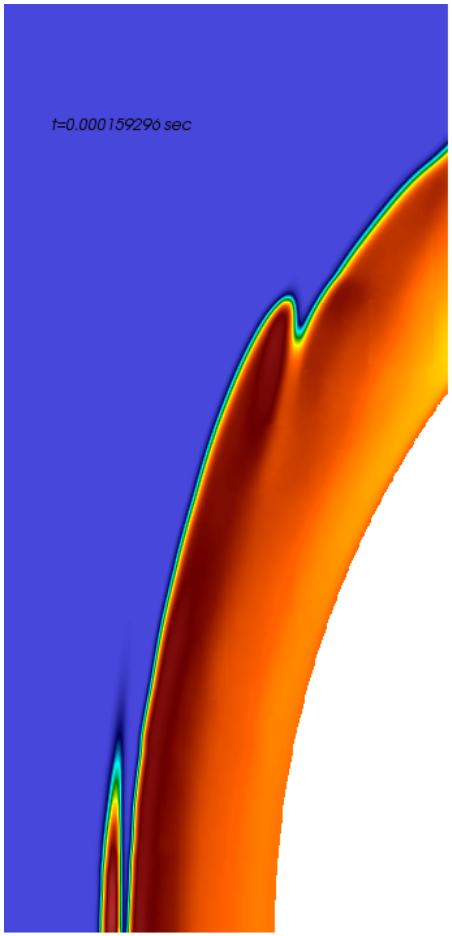

Pressure

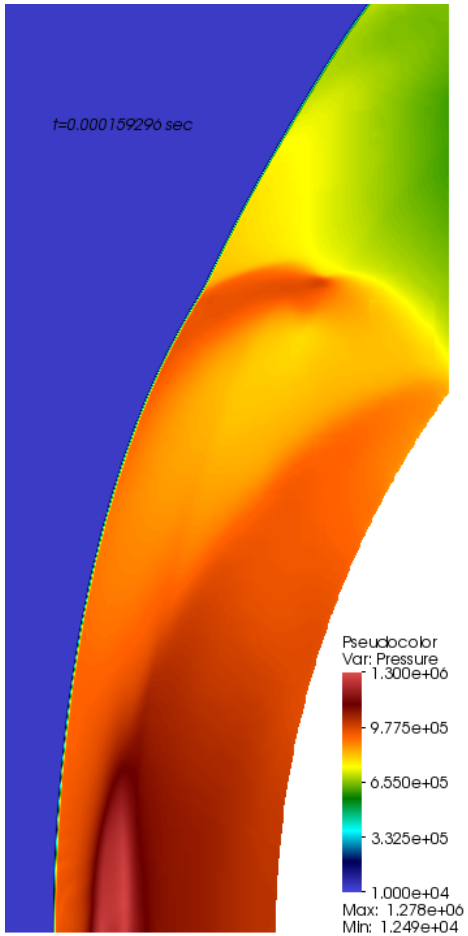

Oscillation mechanism

Schlieren of density

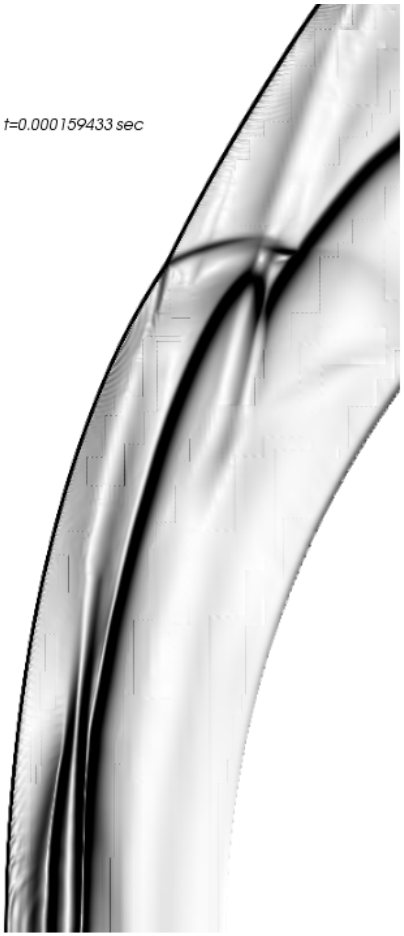

Temperature

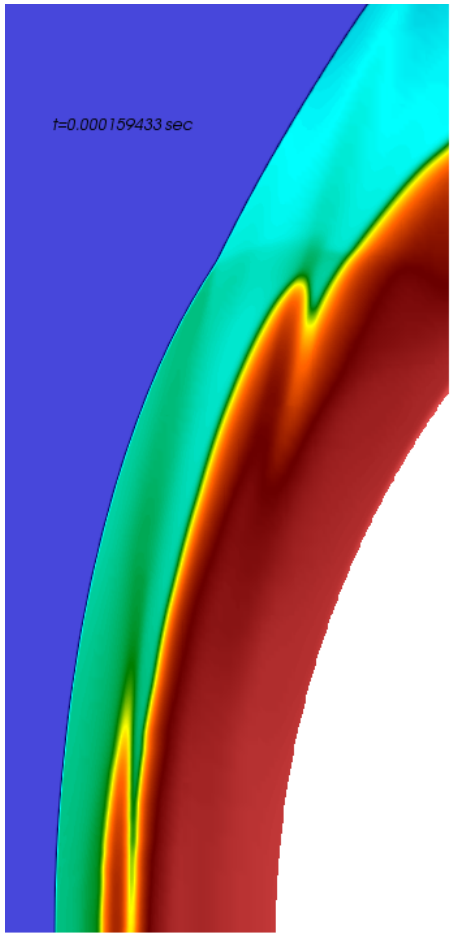

Mass fraction OH

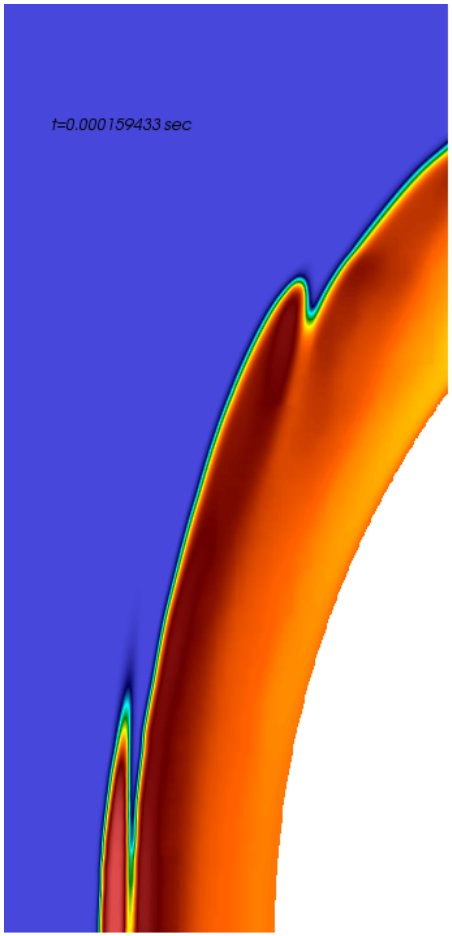

Pressure

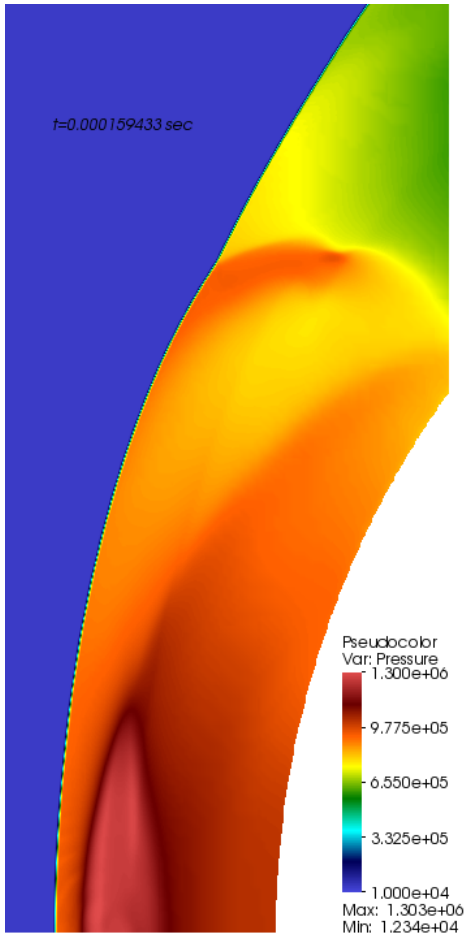

Oscillation mechanism

Schlieren of density

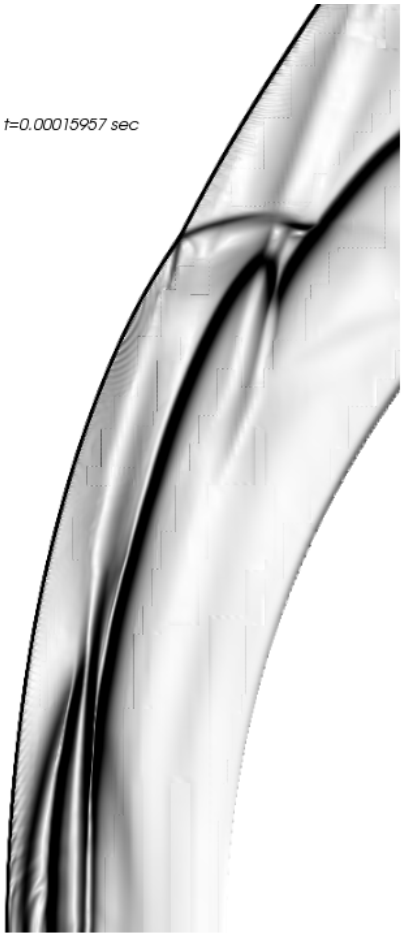

Temperature

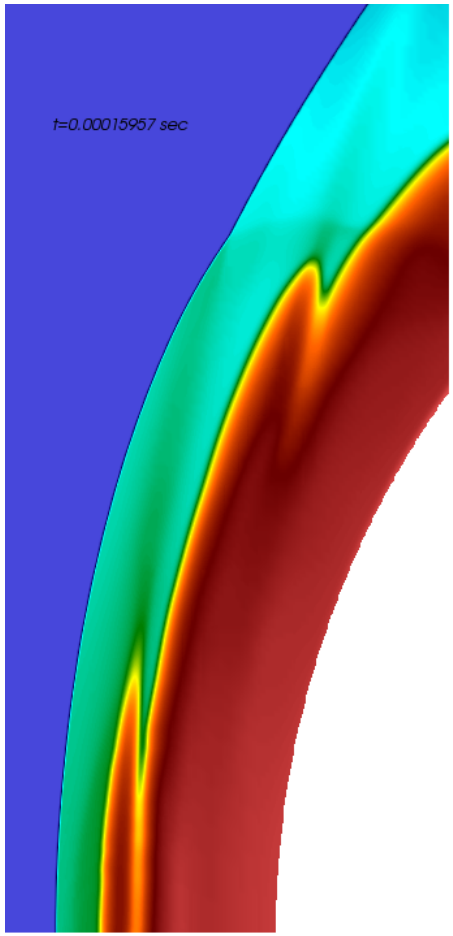

Mass fraction OH

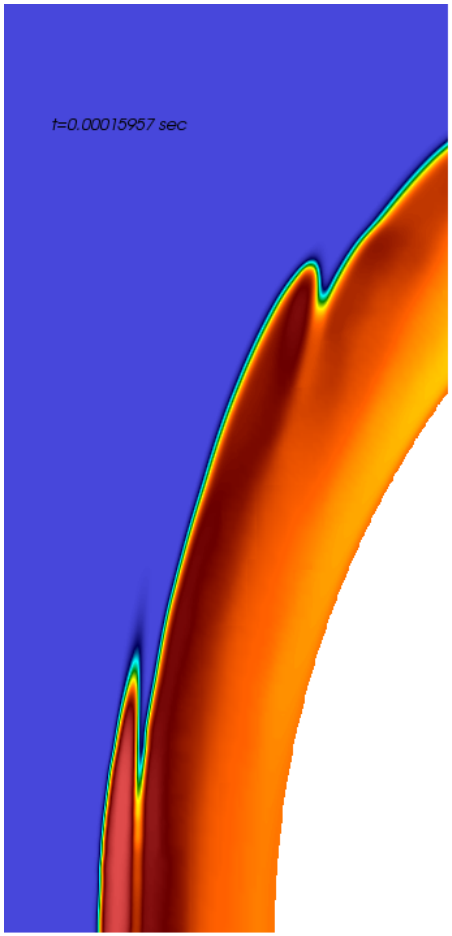

Pressure

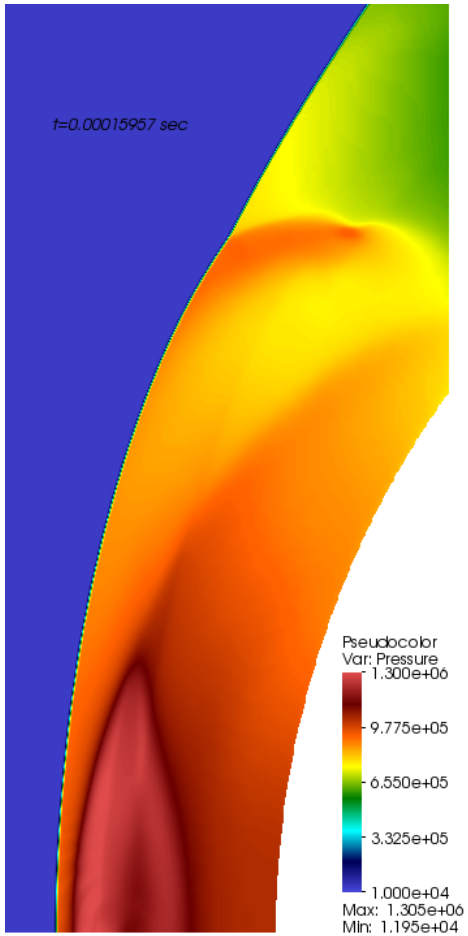

Oscillation mechanism

Schlieren of density

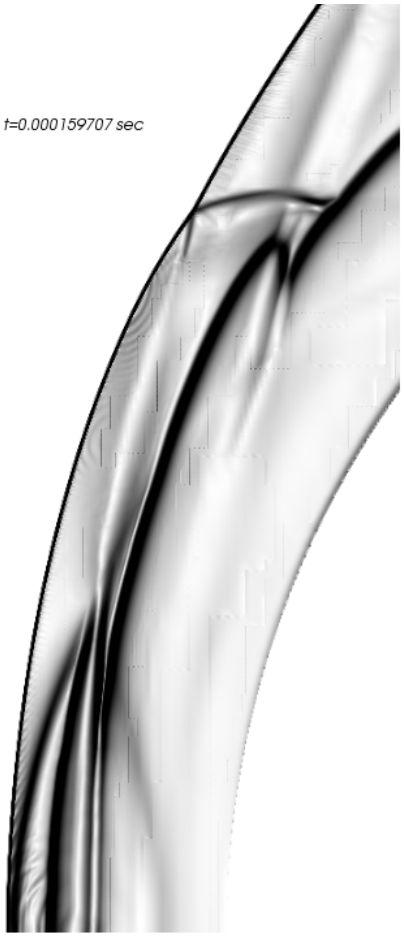

Temperature

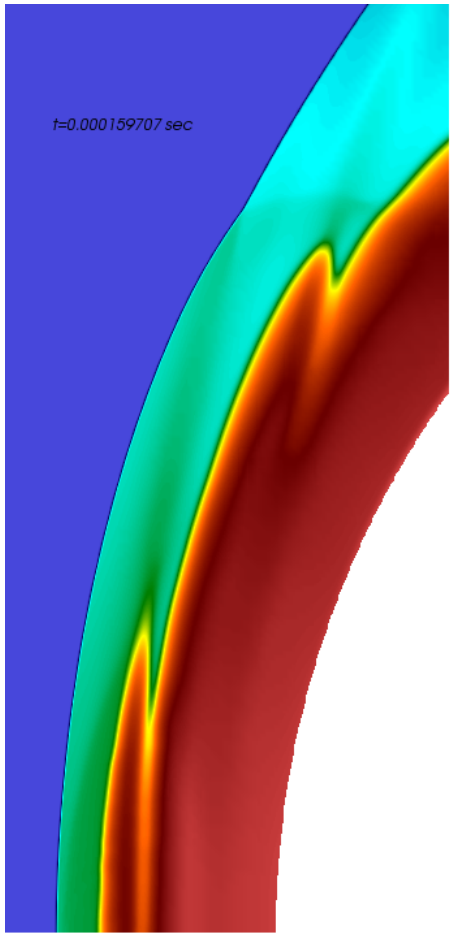

Mass fraction OH

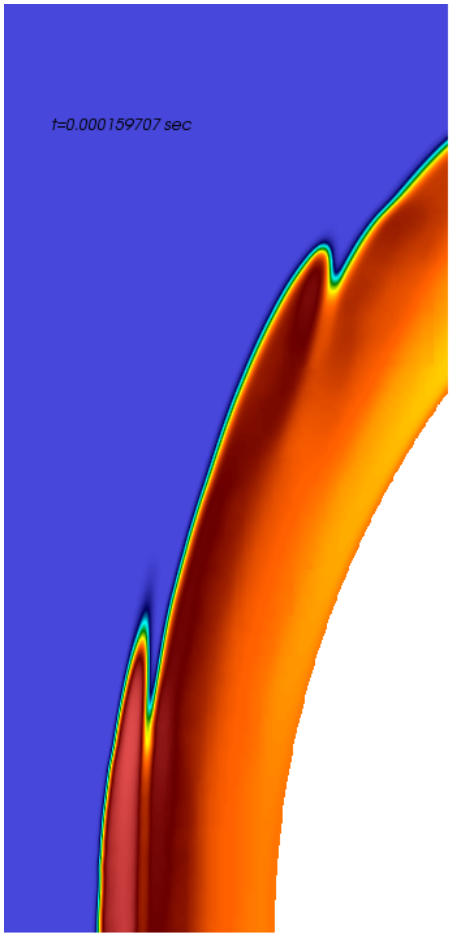

Pressure

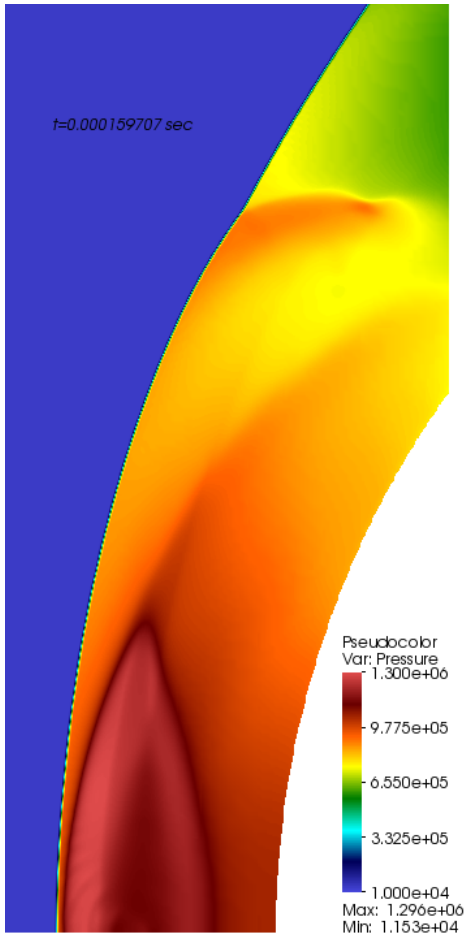

Oscillation mechanism

Schlieren of density

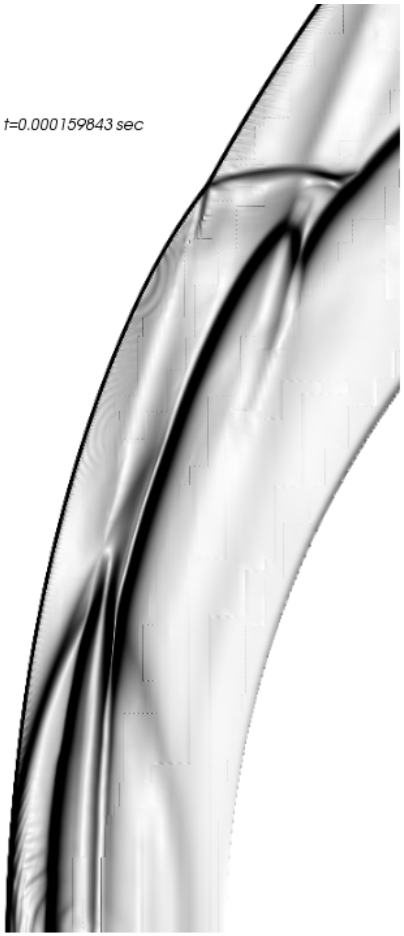

Temperature

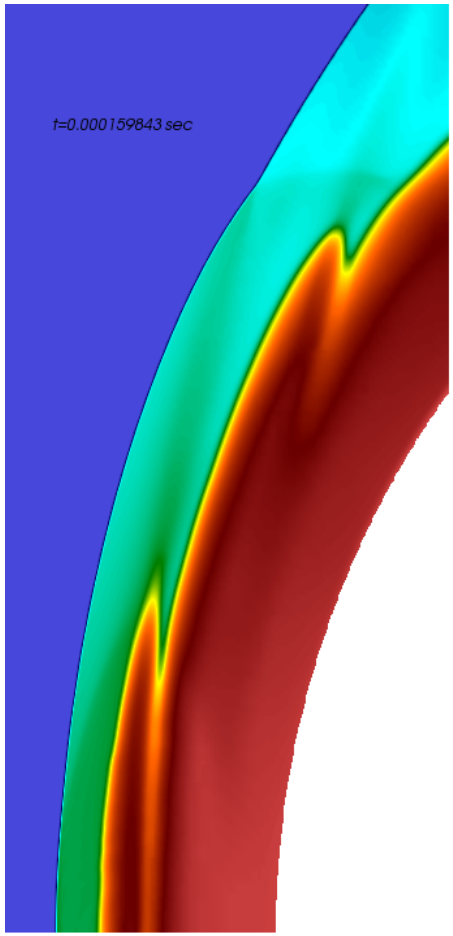

Mass fraction OH

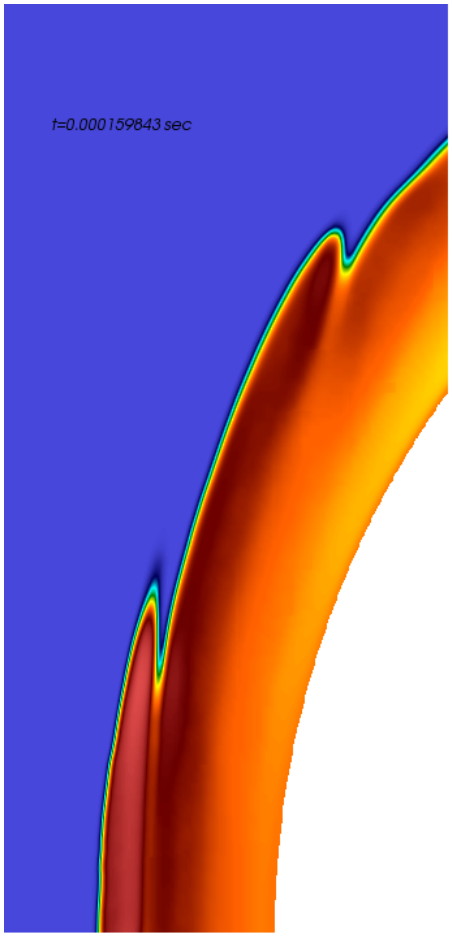

Pressure

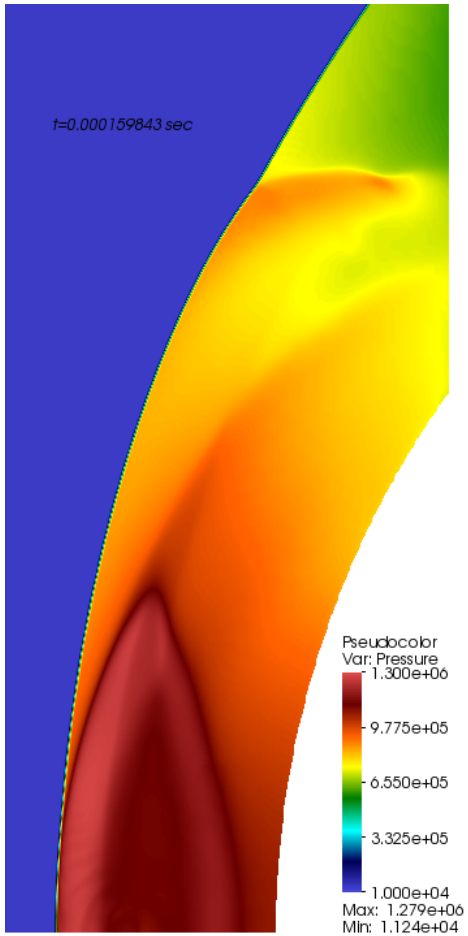

Oscillation mechanism

Schlieren of density

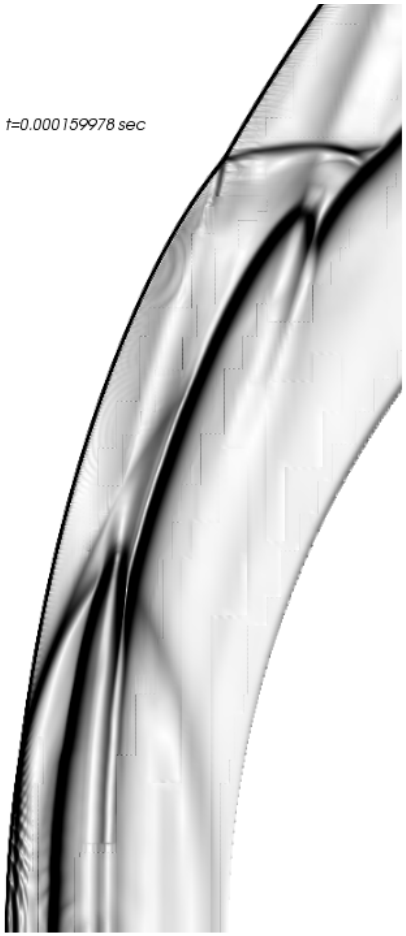

Temperature

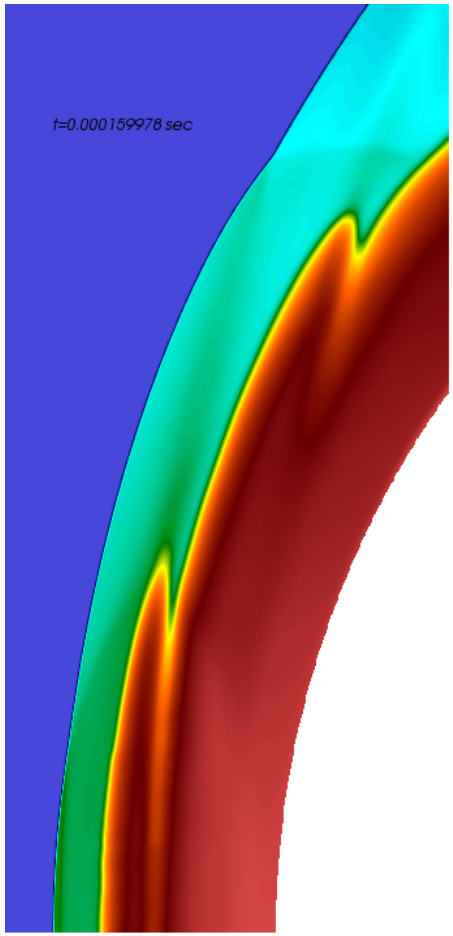

Mass fraction OH

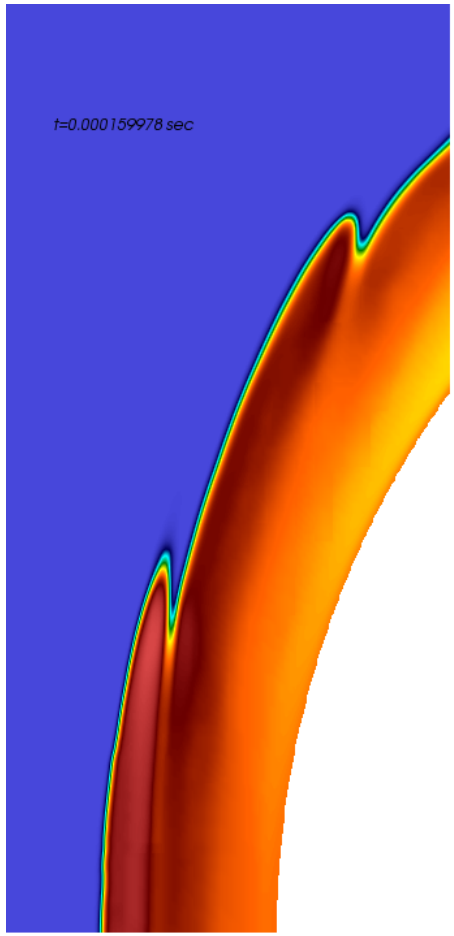

Pressure

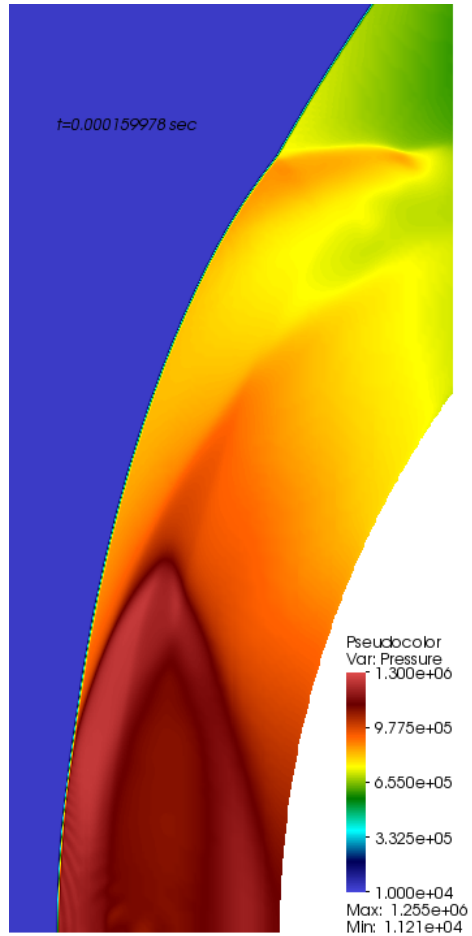

Oscillation mechanism

Schlieren of density

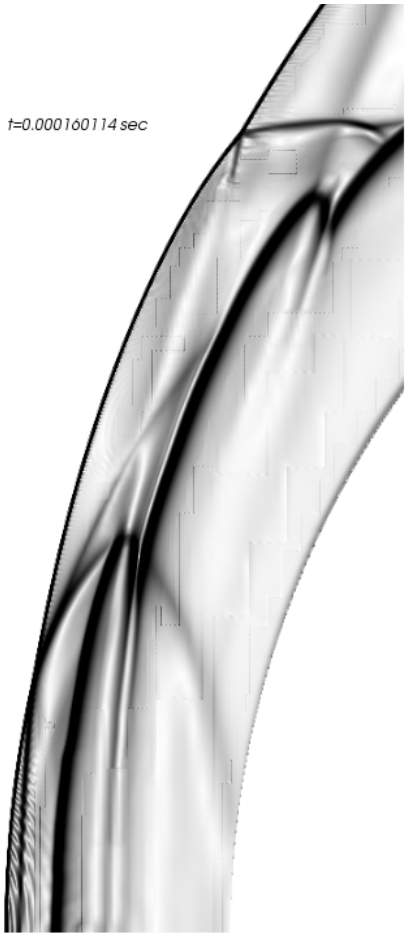

Temperature

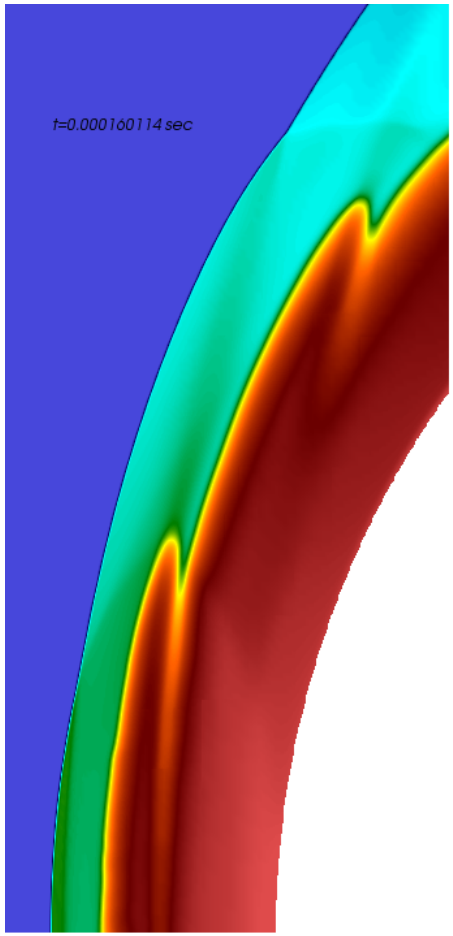

Mass fraction OH

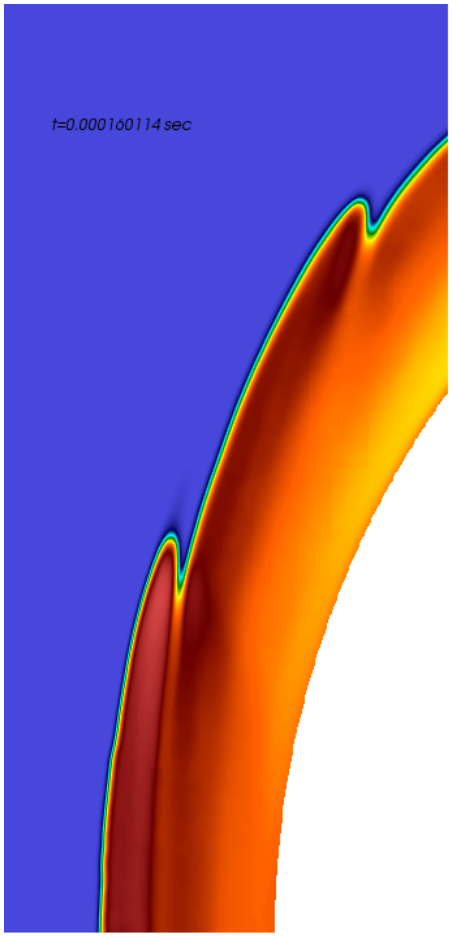

Pressure

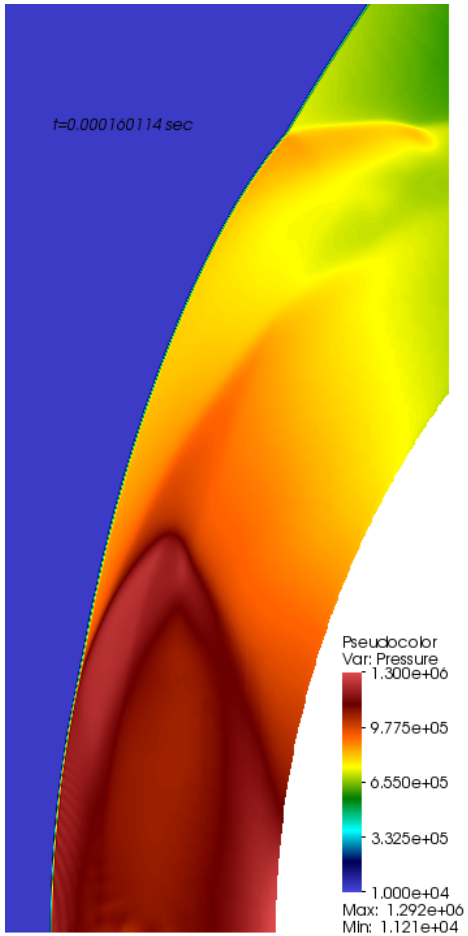

Oscillation mechanism

Schlieren of density

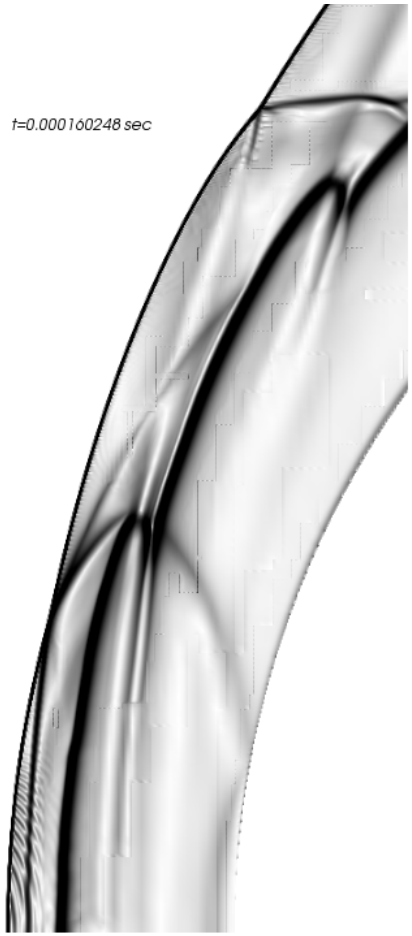

Temperature

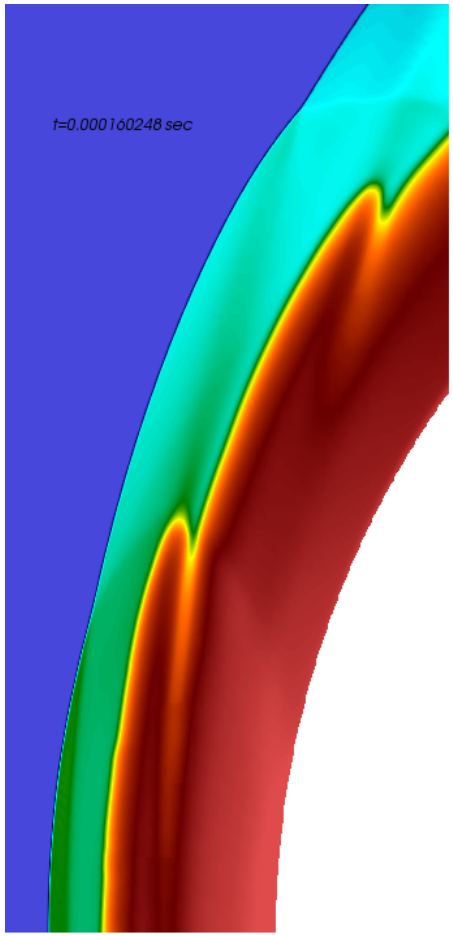

Mass fraction OH

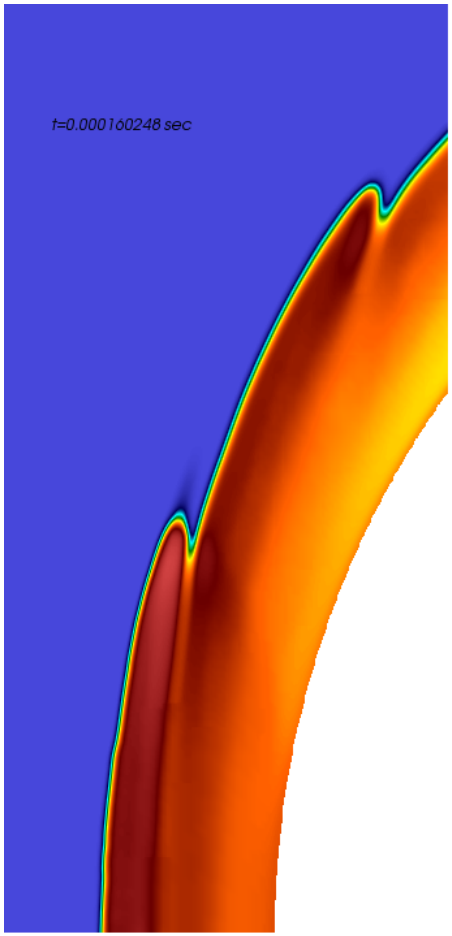

Pressure

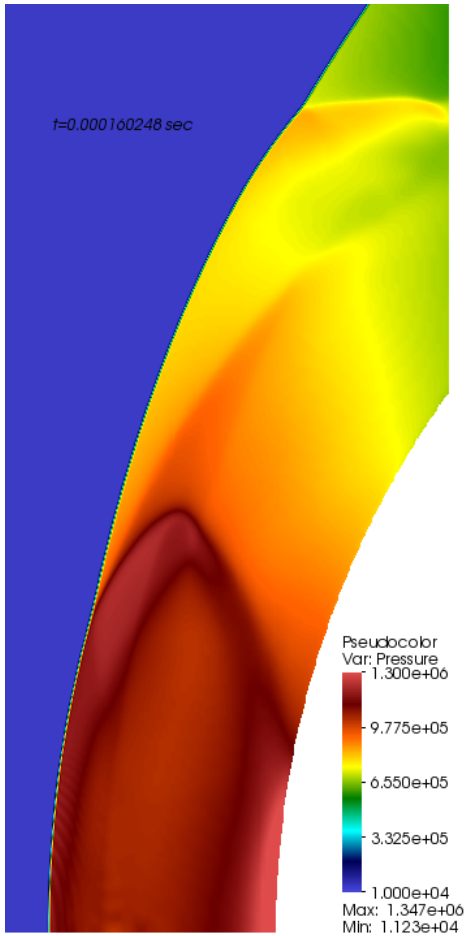

Oscillation mechanism

Schlieren of density

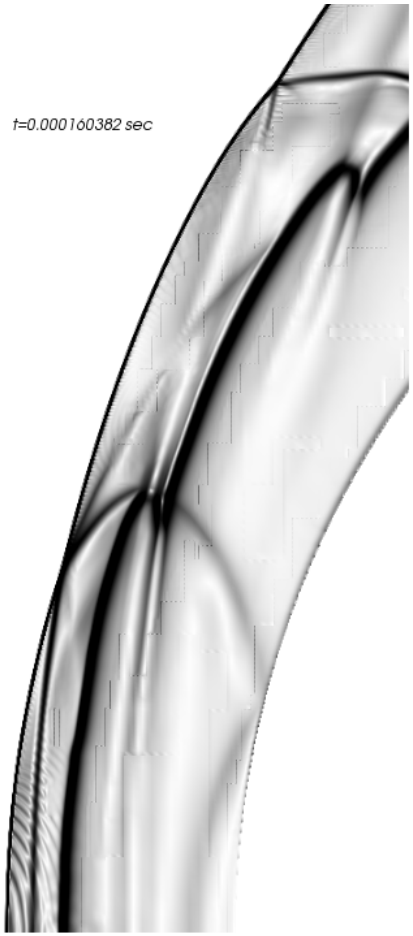

Temperature

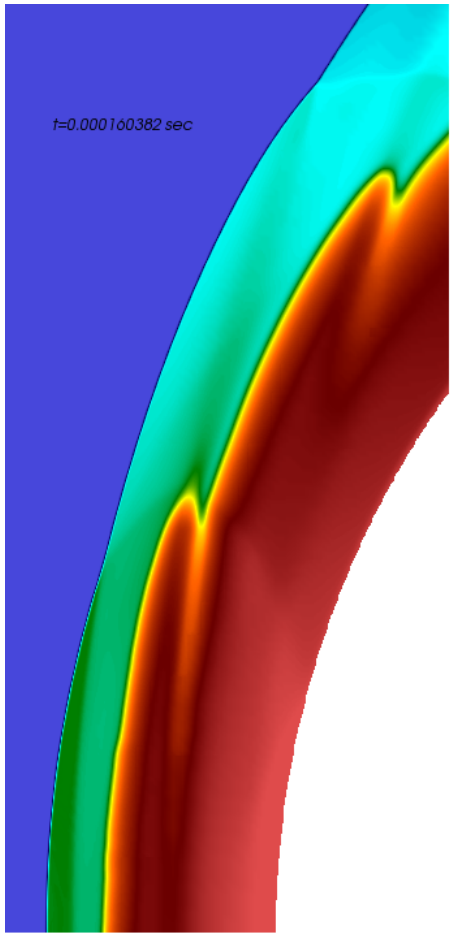

Mass fraction OH

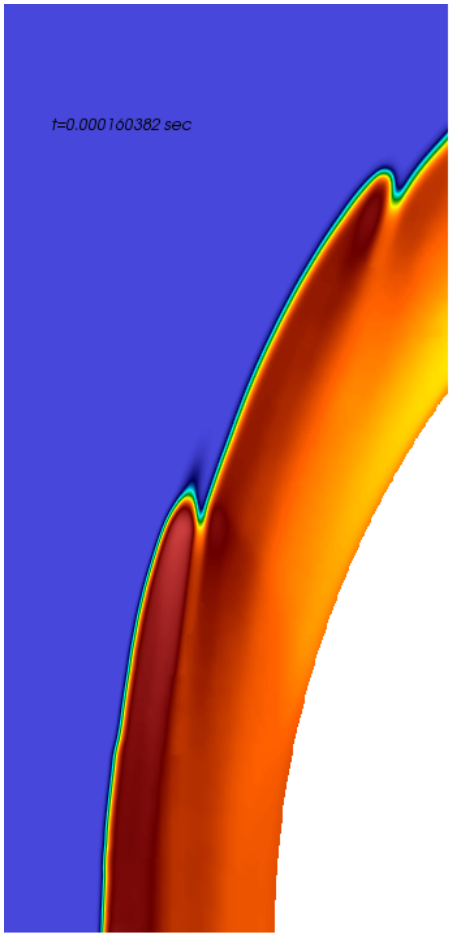

Pressure

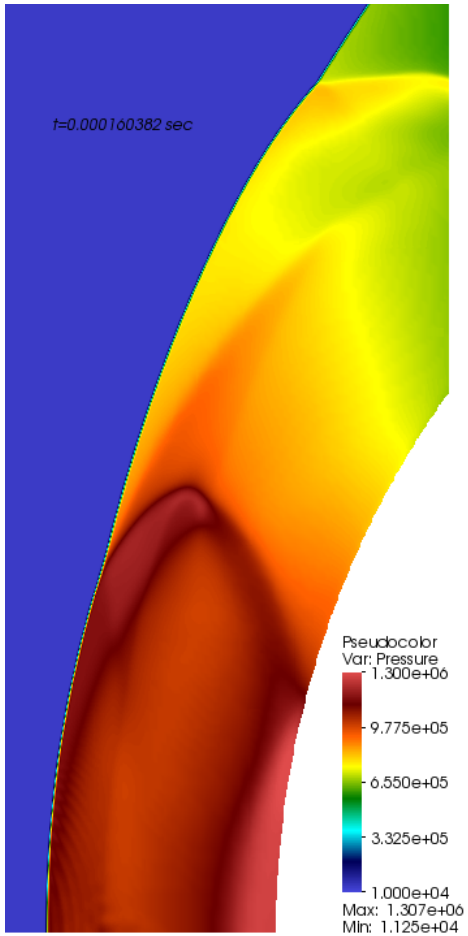

Oscillation mechanism

Schlieren of density

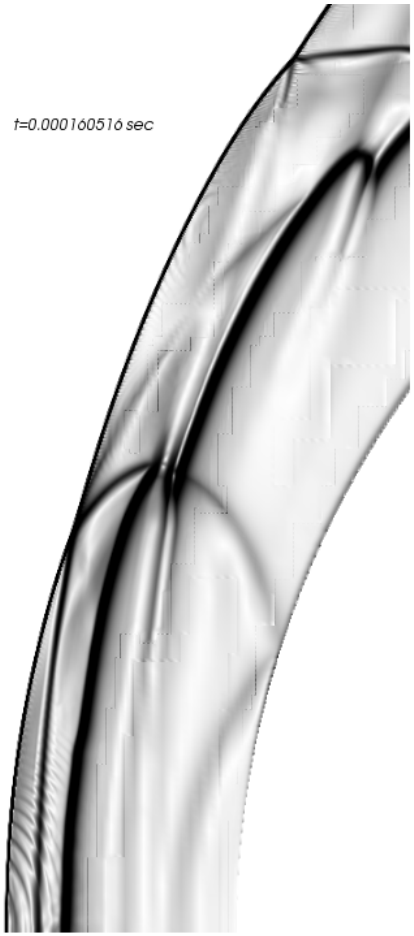

Temperature

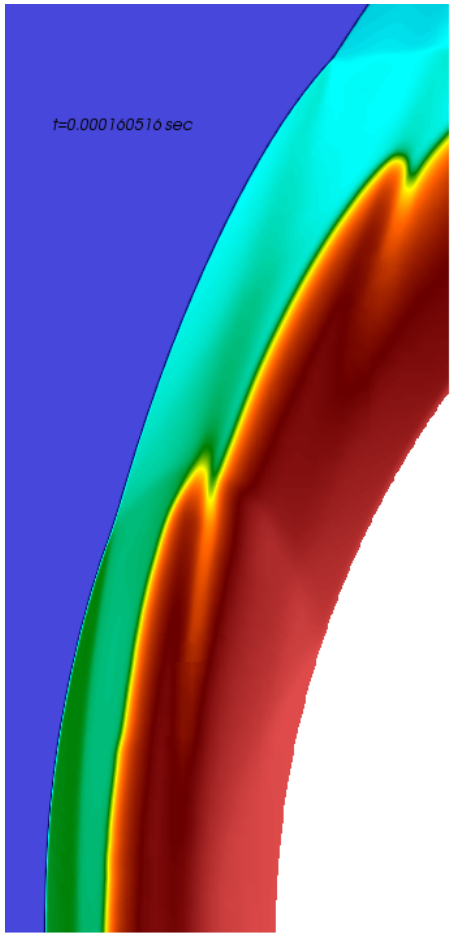

Mass fraction OH

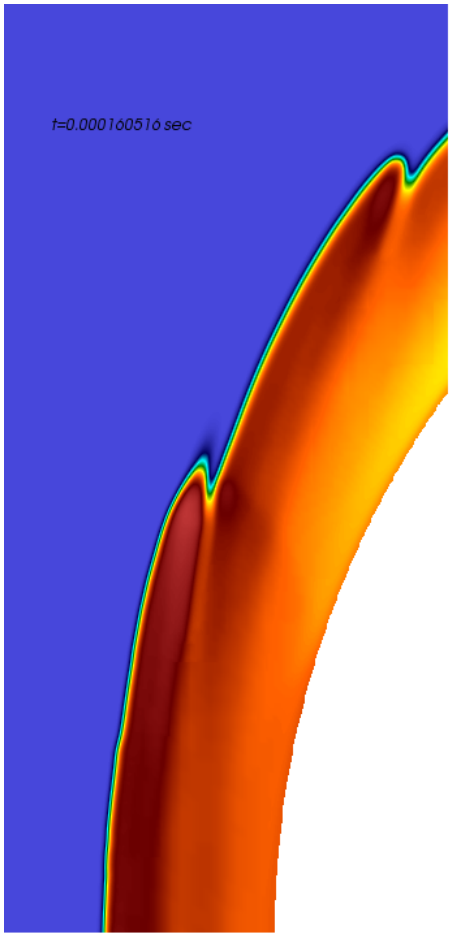

Pressure

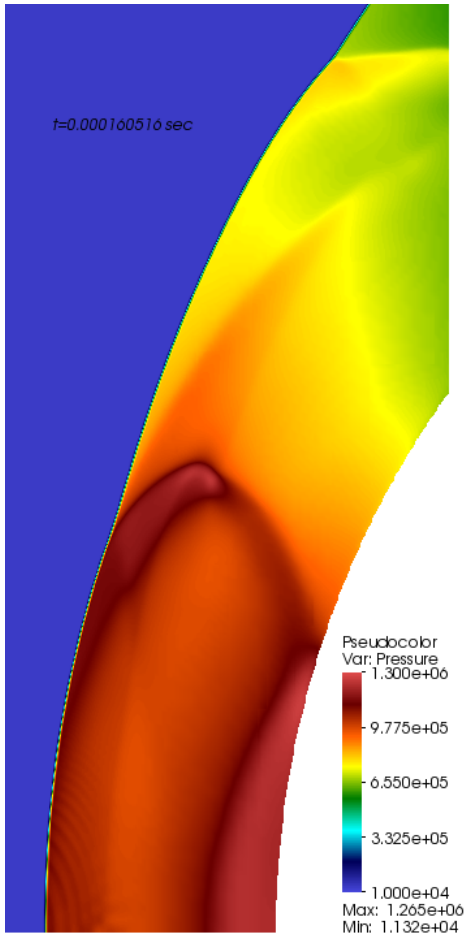

Oscillation mechanism

Schlieren of density

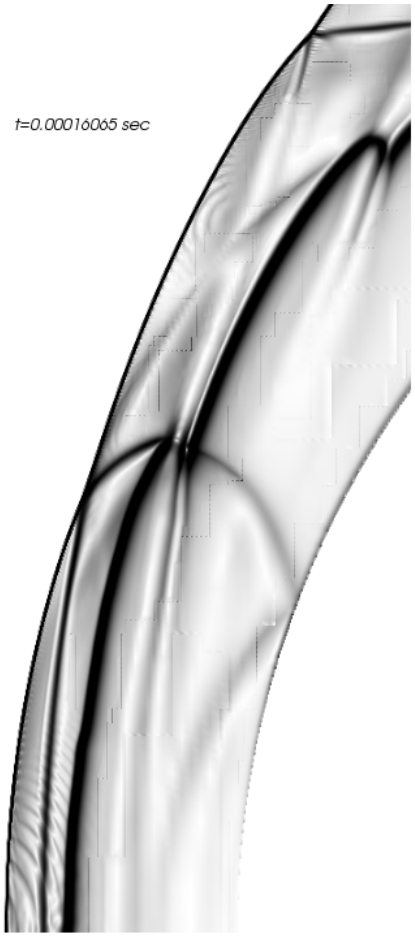

Temperature

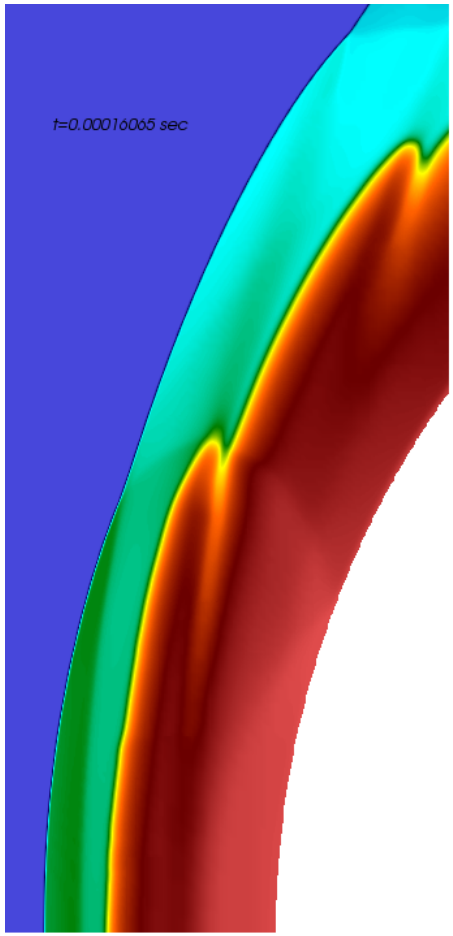

Mass fraction OH

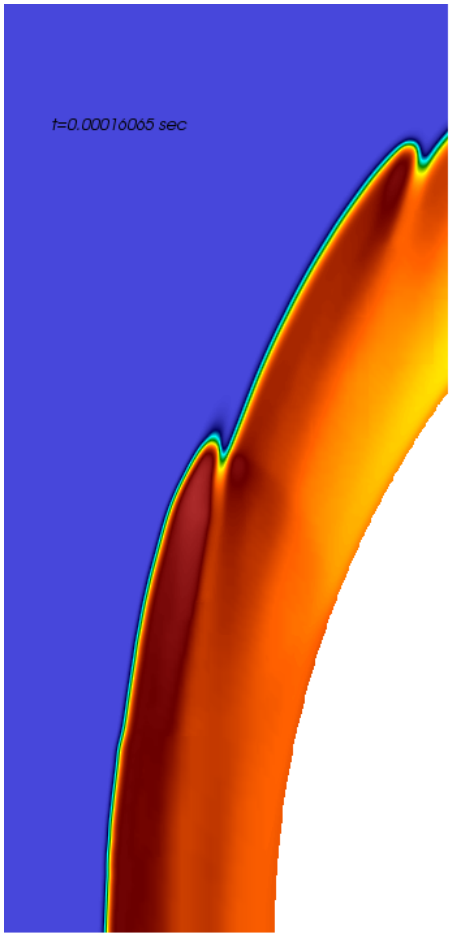

Pressure

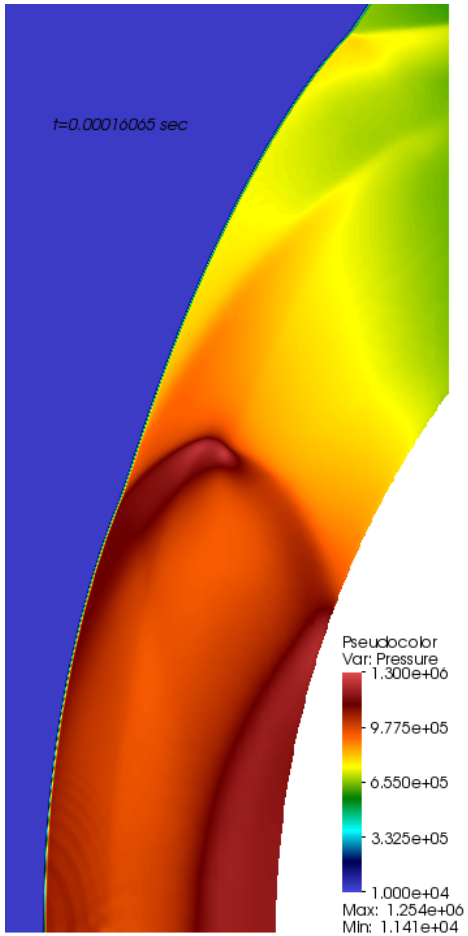

Oscillation mechanism

Schlieren of density

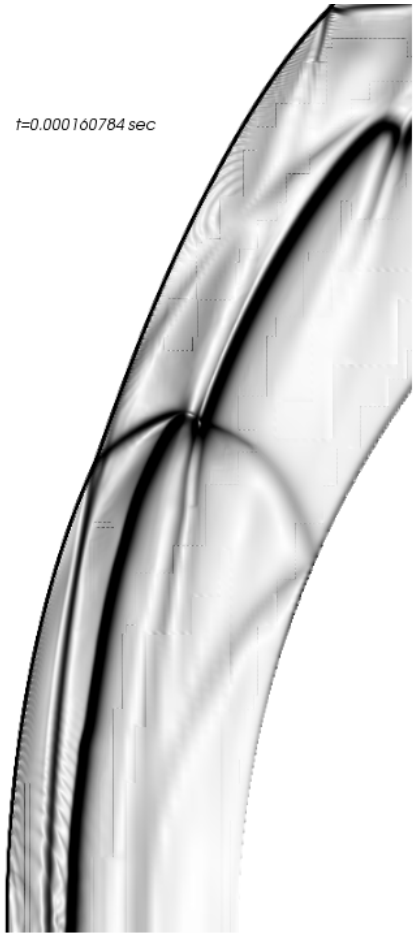

Temperature

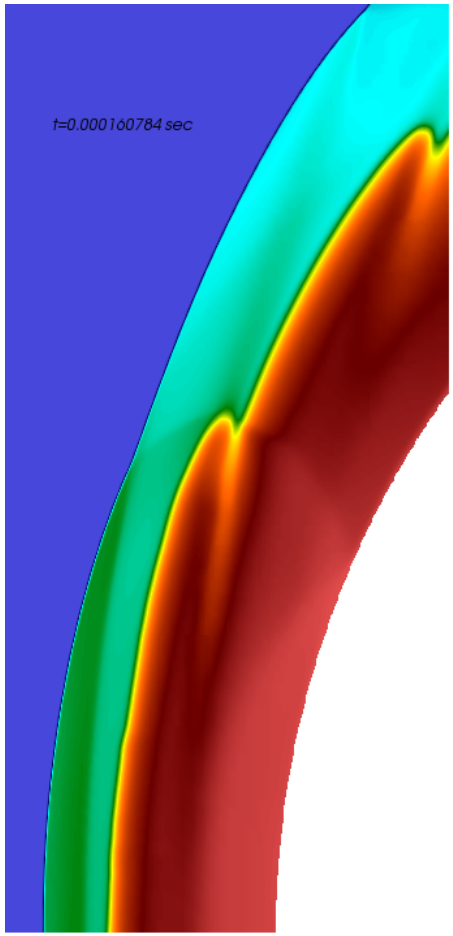

Mass fraction OH

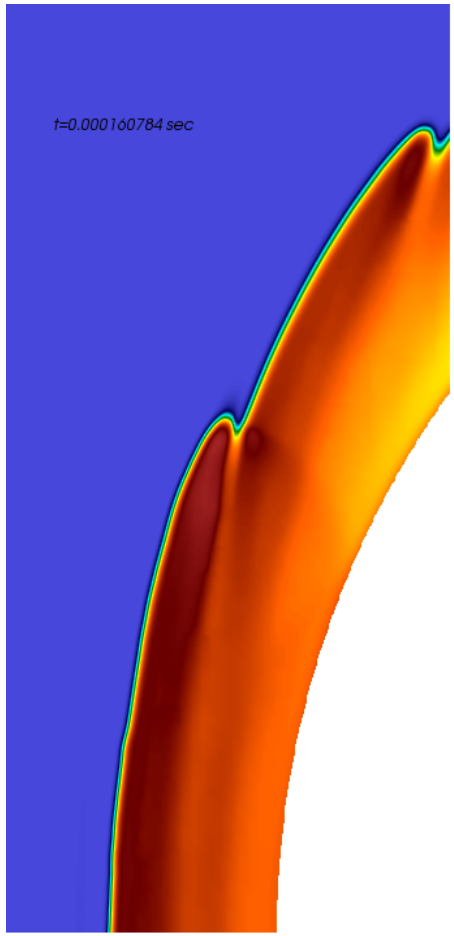

Pressure

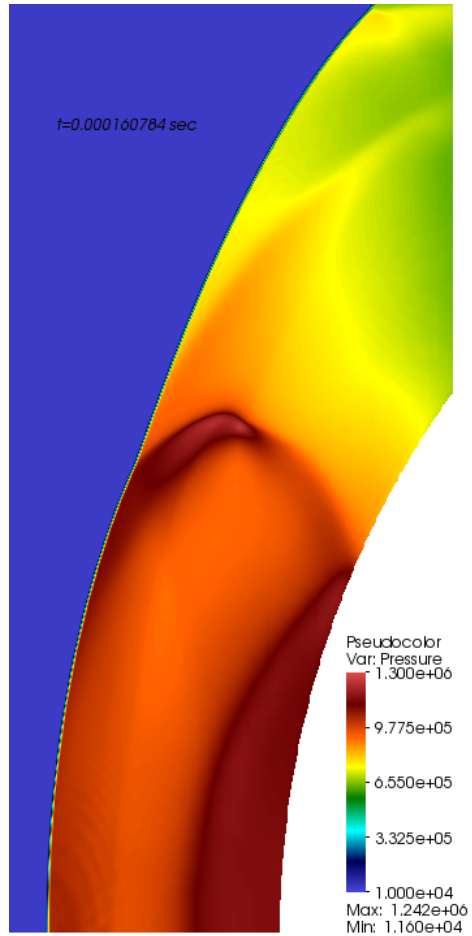

Oscillation mechanism

Schlieren of density

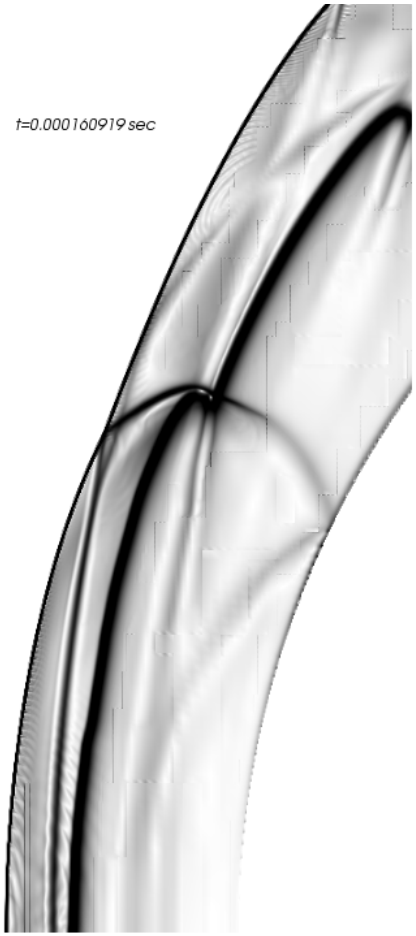

Temperature

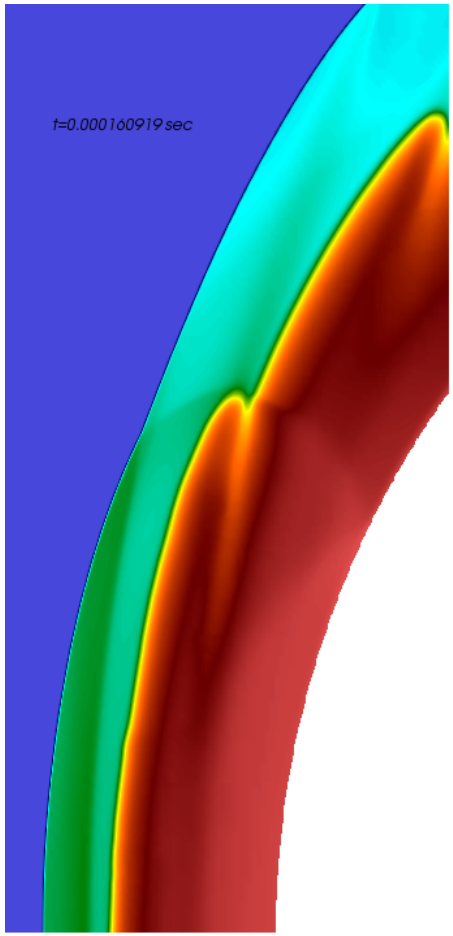

Mass fraction OH

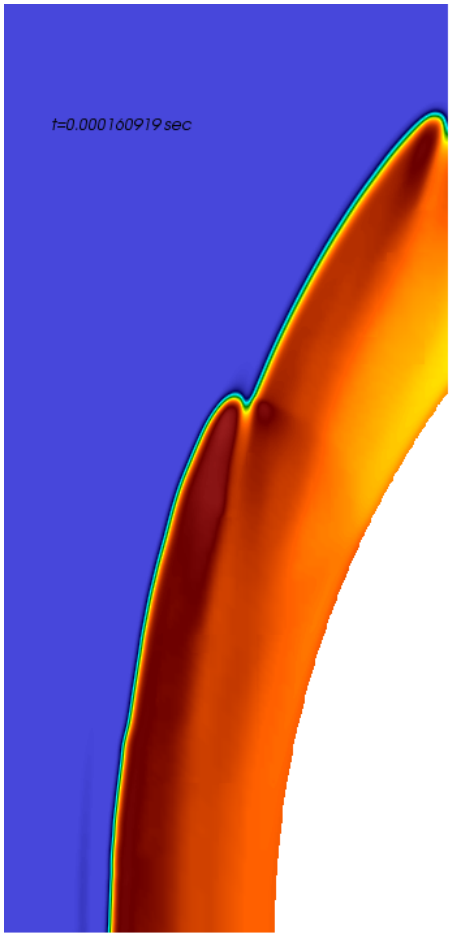

Pressure

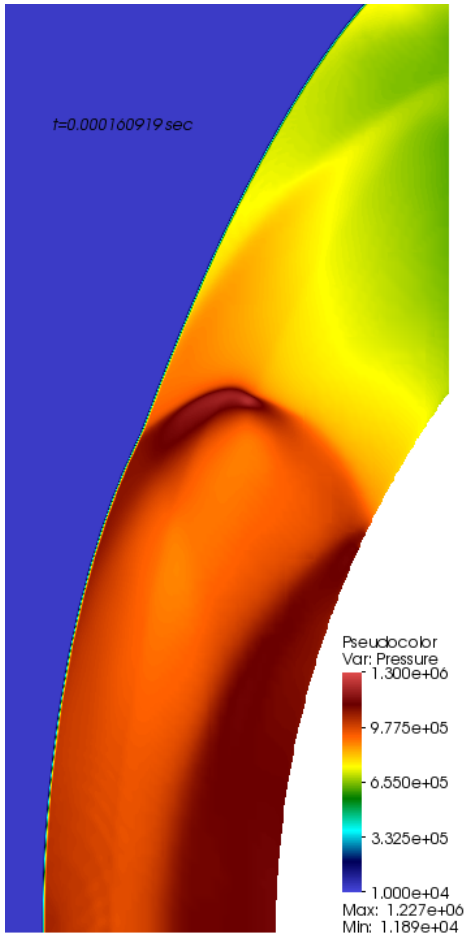

Oscillation mechanism

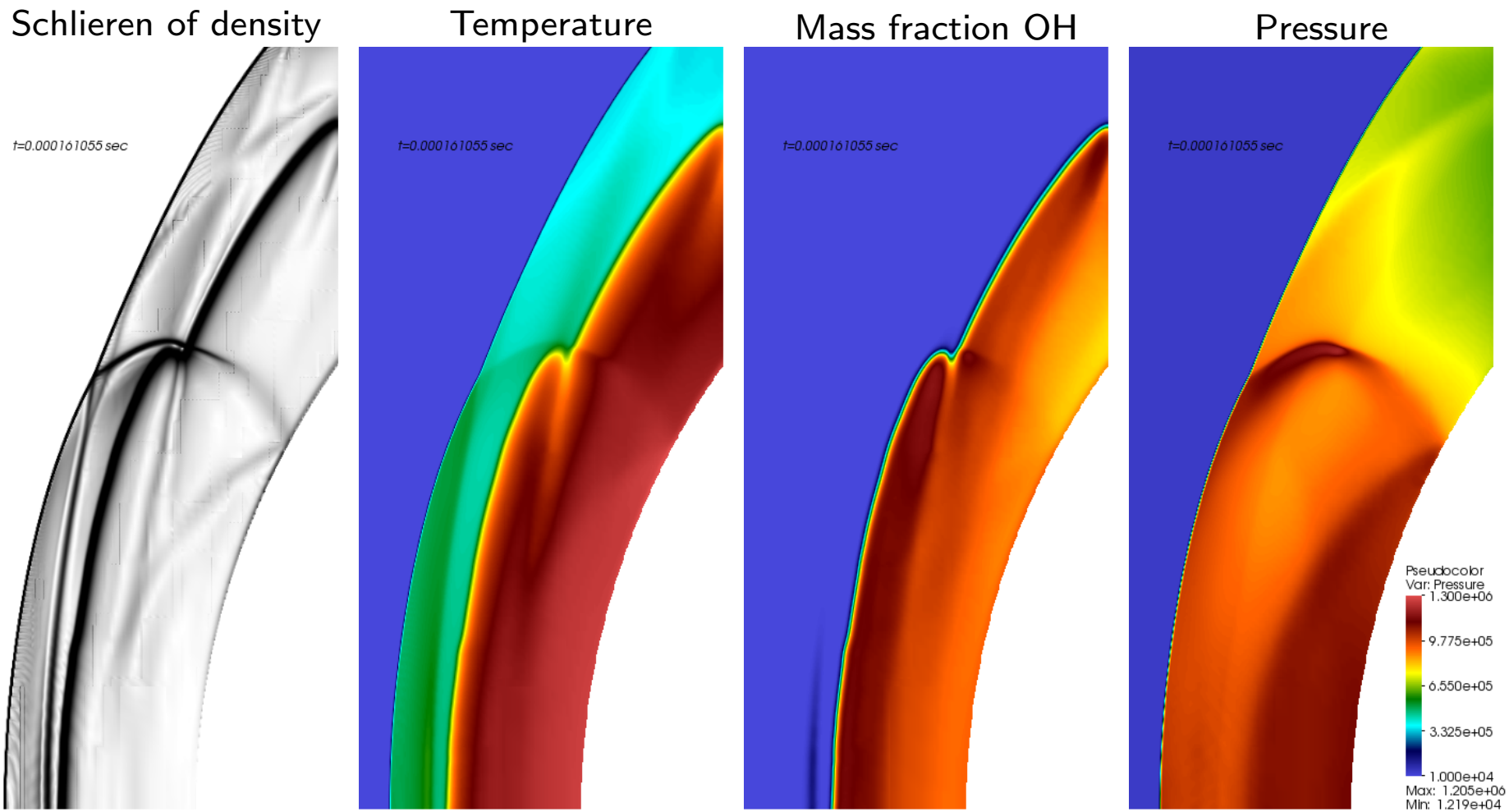

- Oscillation created by accelerated reaction due to slip line from previous triple point

Inviscid case – $M = 4.48$

- 4048 iterations with CFL=0.9 to $t = 170\,\mu\mathrm{s}$
- Oscillation frequency in last $20\,\mu\mathrm{s}$: $\sim 395\,\mathrm{kHz}$
- Experimental value: $\sim 425\,\mathrm{kHz}$

Schlieren plot of density

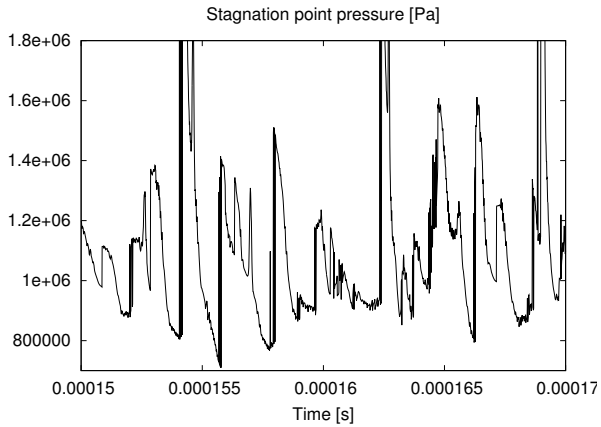

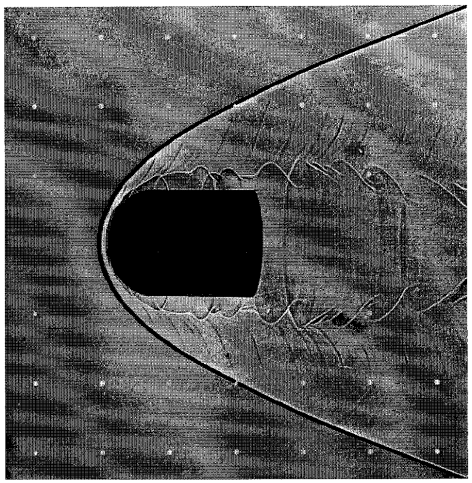

Deflagration to detonation transition in 2d

Hot sphere of 2500 K in stoichiometric H_2/O_2 in closed-end chamber of 2 cm diameter

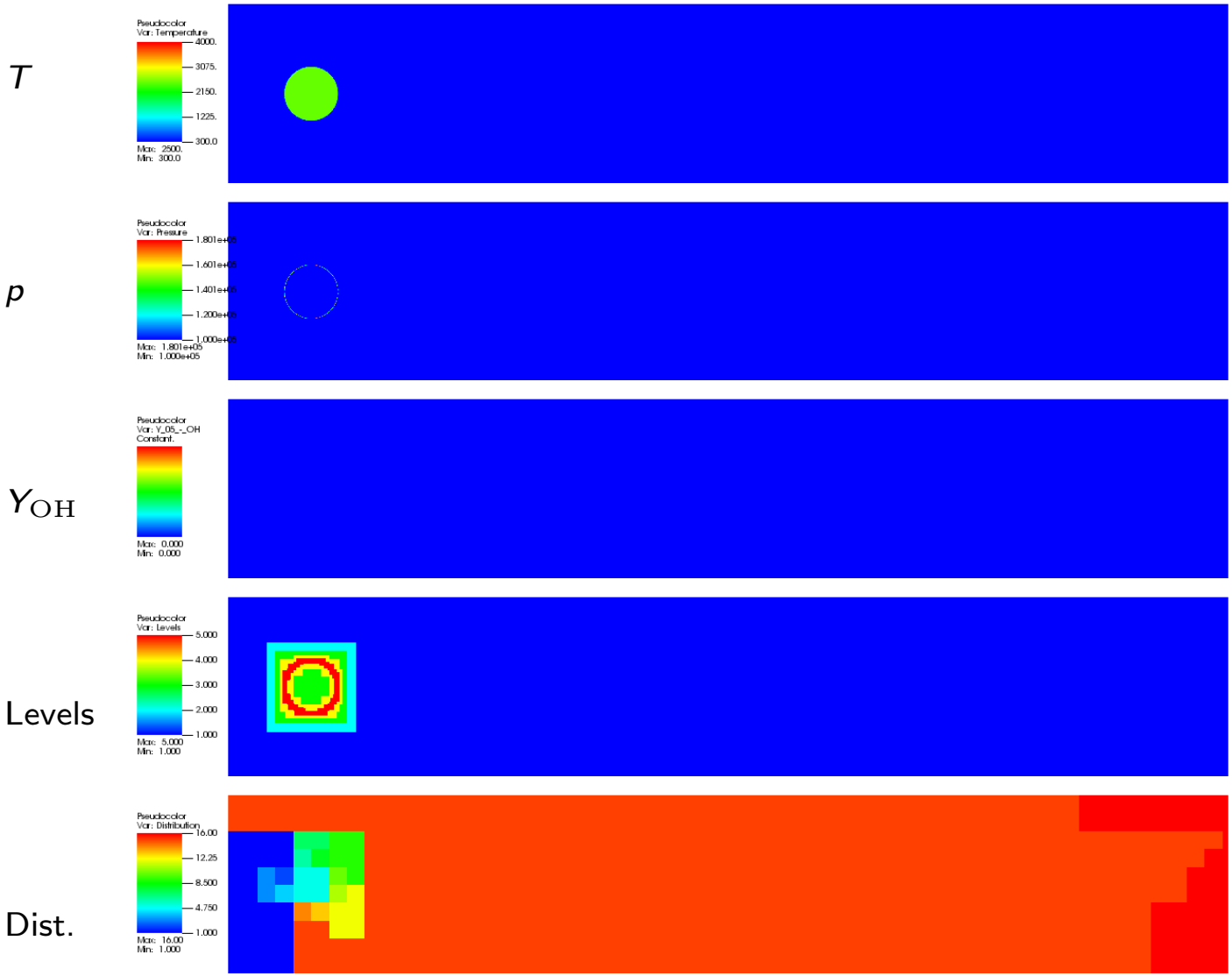

Deflagration to detonation transition in 2d

Hot sphere of 2500 K in stoichiometric H_2/O_2 in closed-end chamber of 2 cm diameter

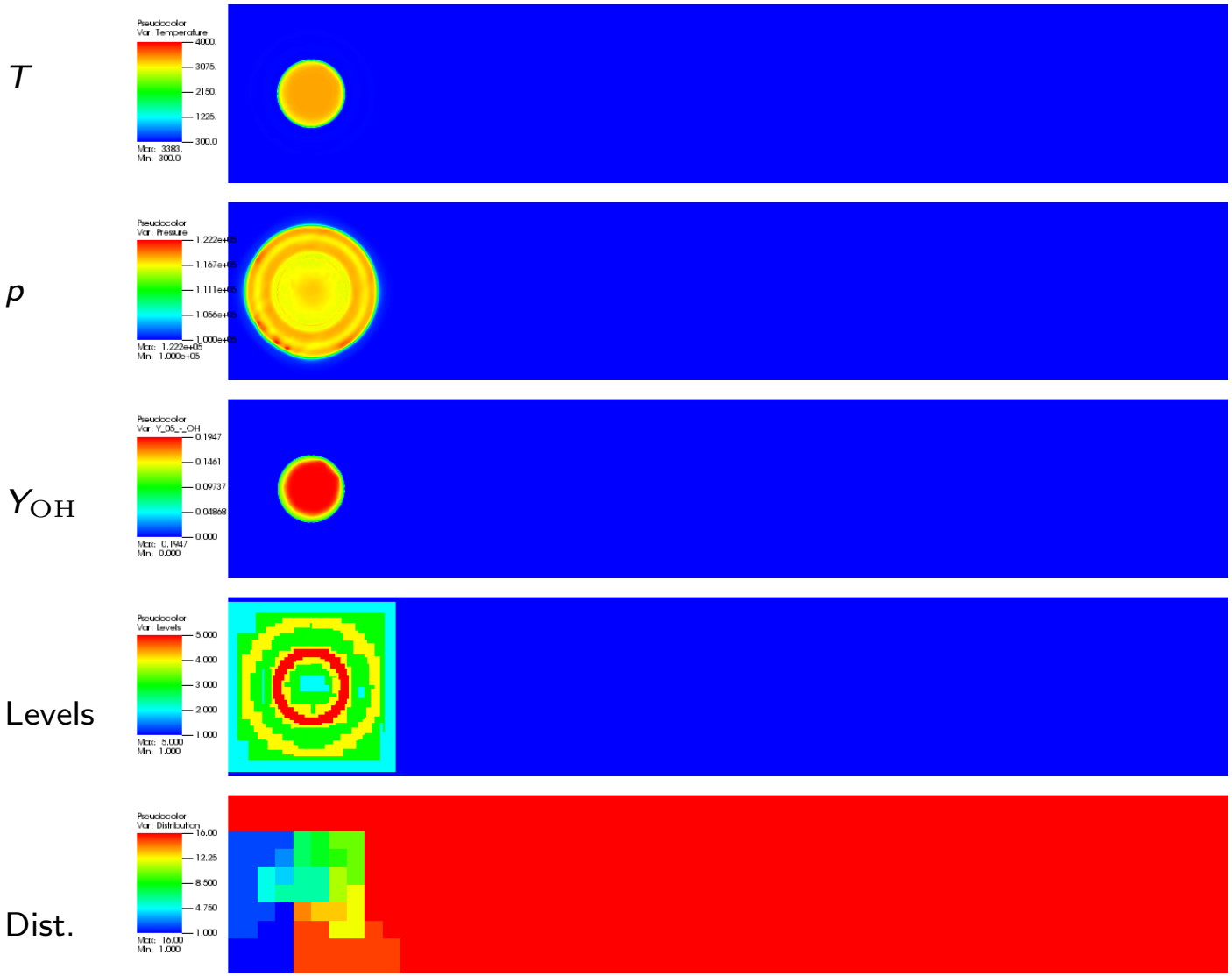

Deflagration to detonation transition in 2d

Hot sphere of 2500 K in stoichiometric H_2/O_2 in closed-end chamber of 2 cm diameter

T

p

Y_{OH}

Levels

Dist.

Deflagration to detonation transition in 2d

Hot sphere of 2500 K in stoichiometric H_2/O_2 in closed-end chamber of 2 cm diameter

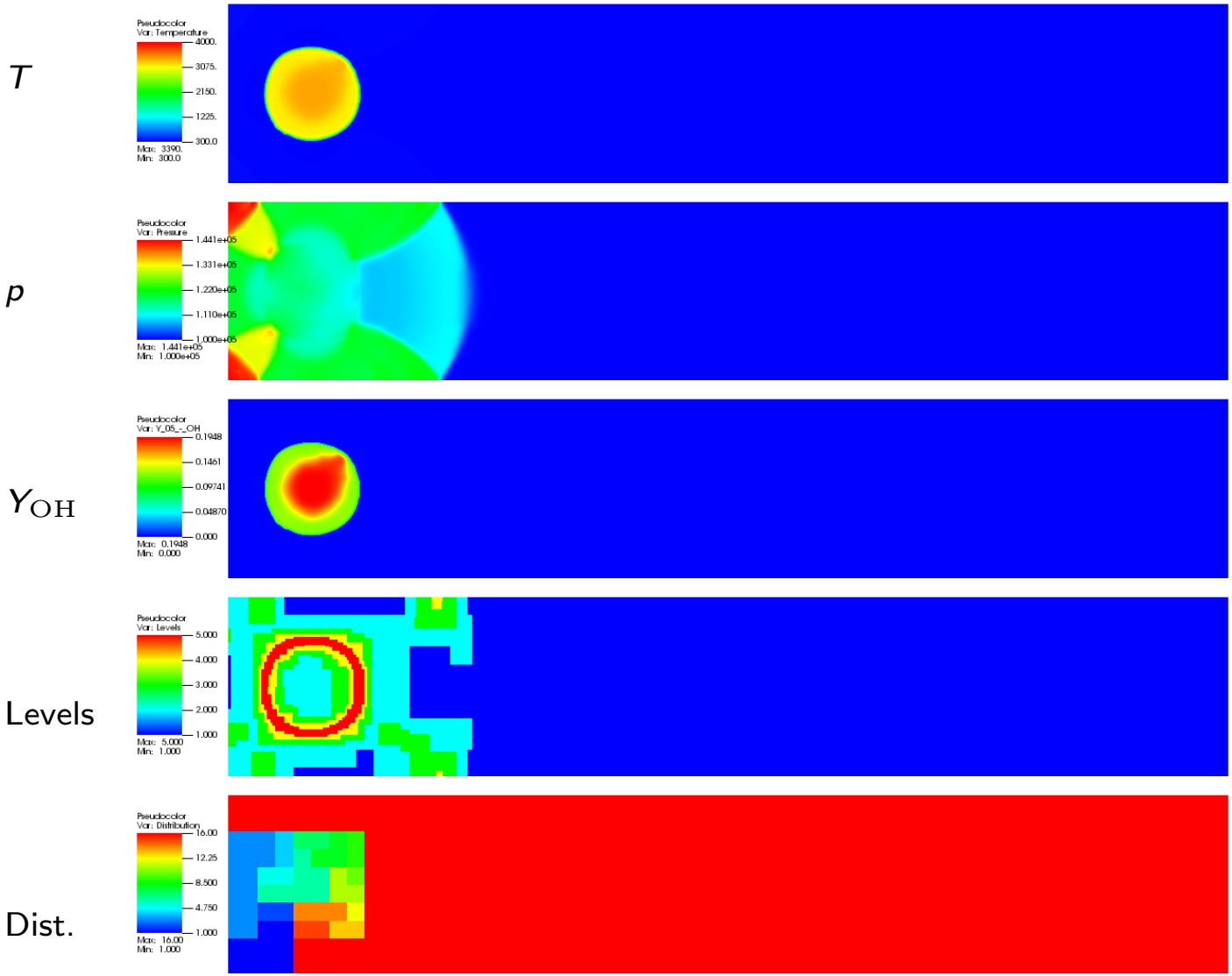

Deflagration to detonation transition in 2d

Hot sphere of 2500 K in stoichiometric H_2/O_2 in closed-end chamber of 2 cm diameter

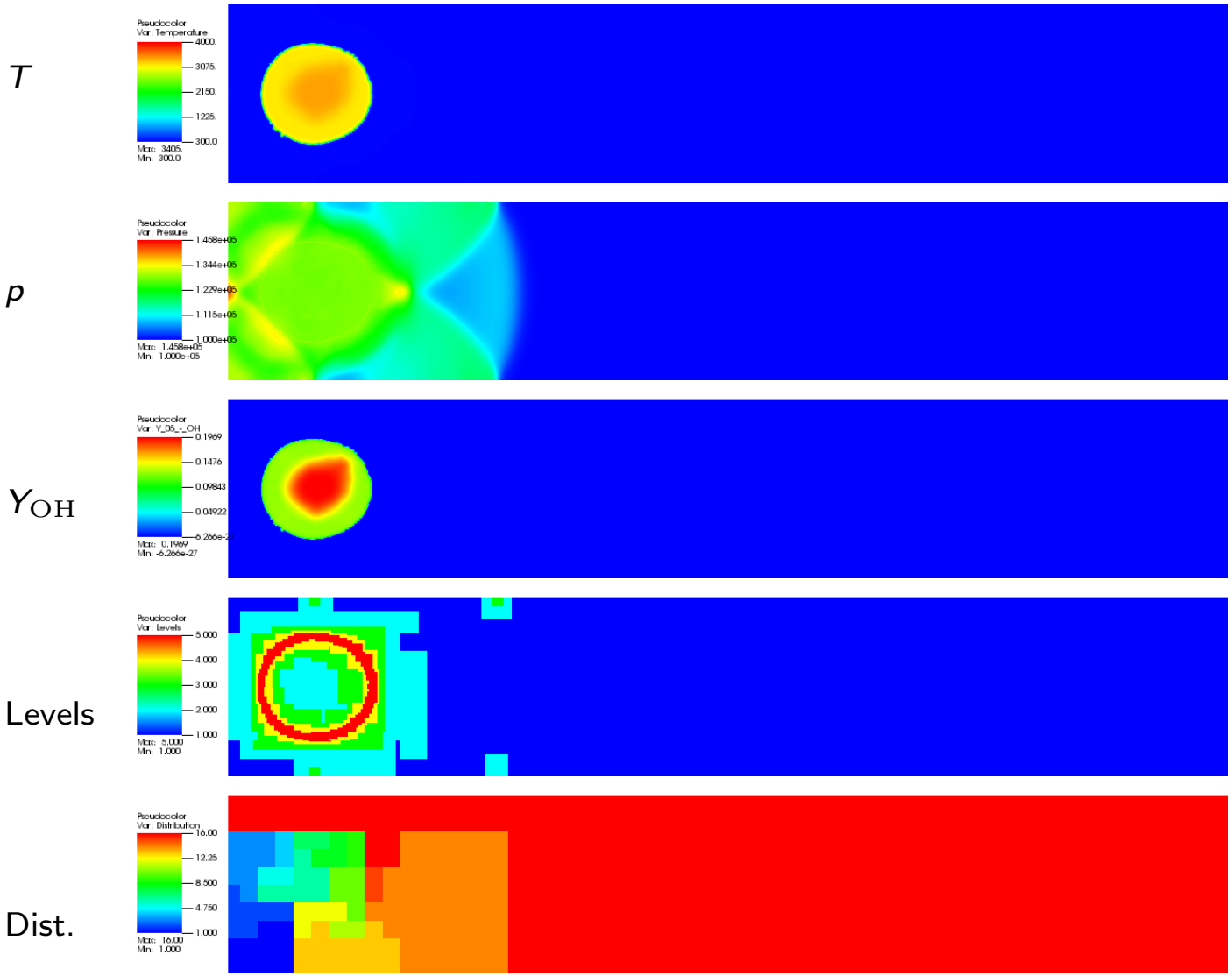

Deflagration to detonation transition in 2d

Hot sphere of 2500 K in stoichiometric H_2/O_2 in closed-end chamber of 2 cm diameter

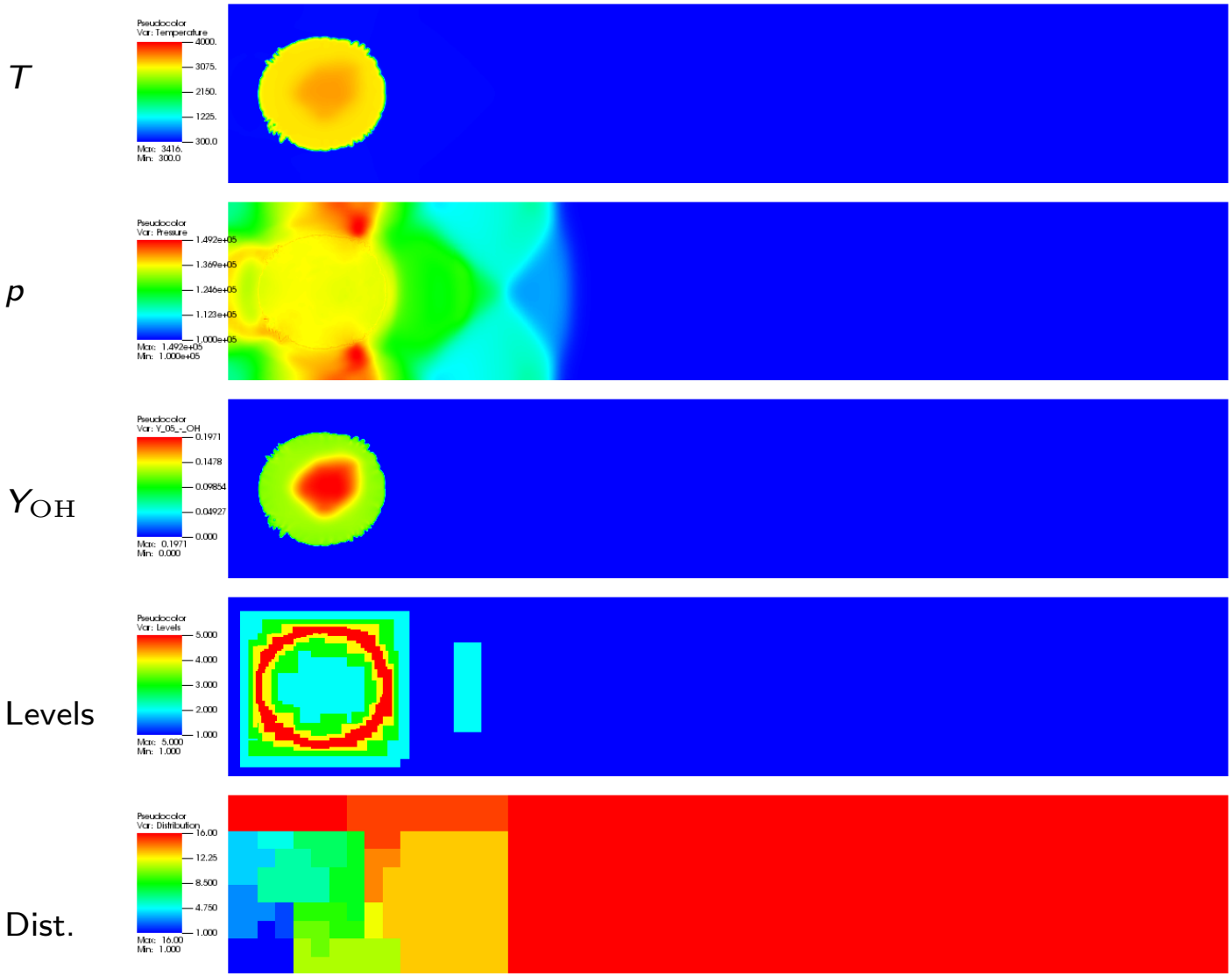

Deflagration to detonation transition in 2d

Hot sphere of 2500 K in stoichiometric H_2/O_2 in closed-end chamber of 2 cm diameter

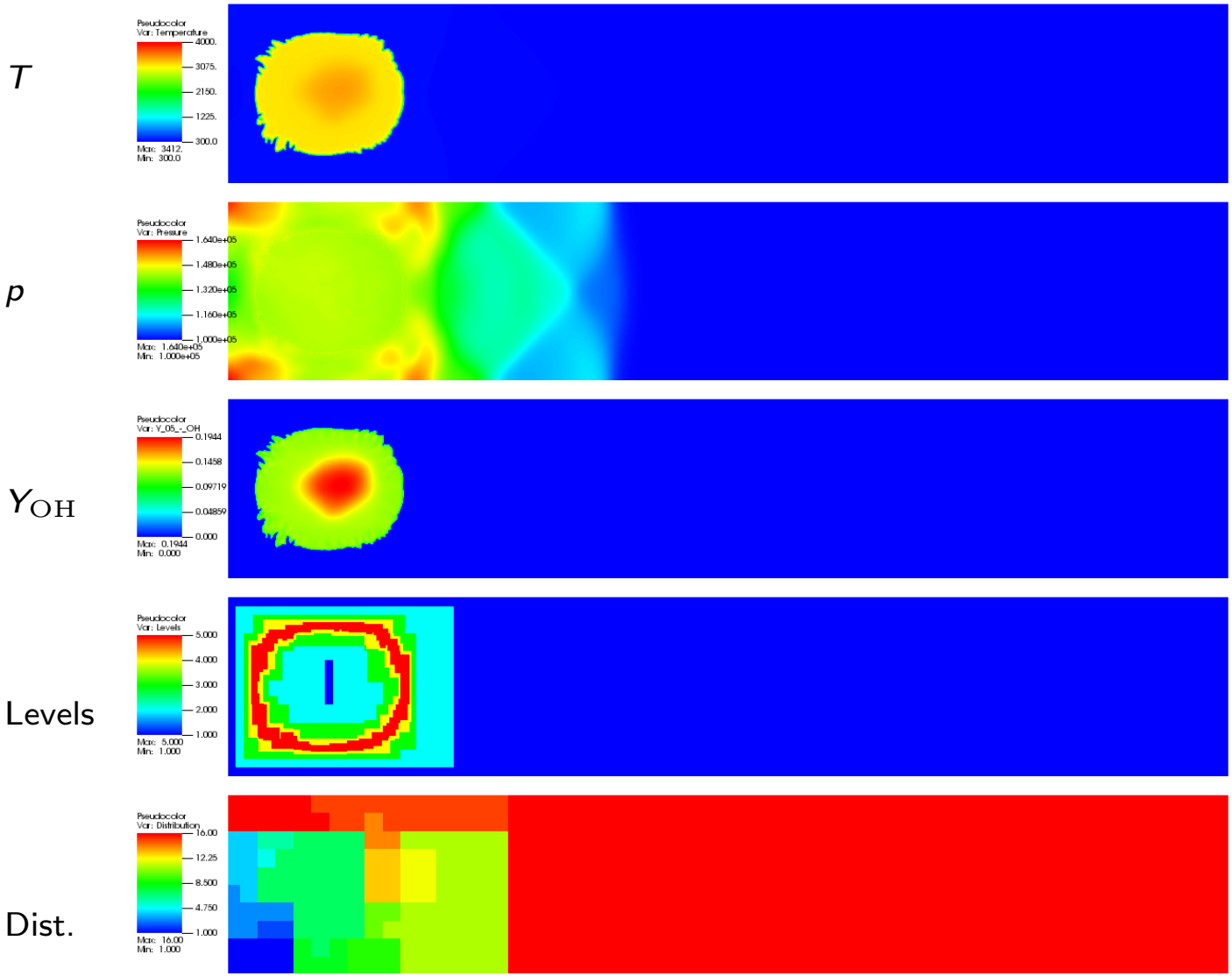

Deflagration to detonation transition in 2d

Hot sphere of 2500 K in stoichiometric H_2/O_2 in closed-end chamber of 2 cm diameter

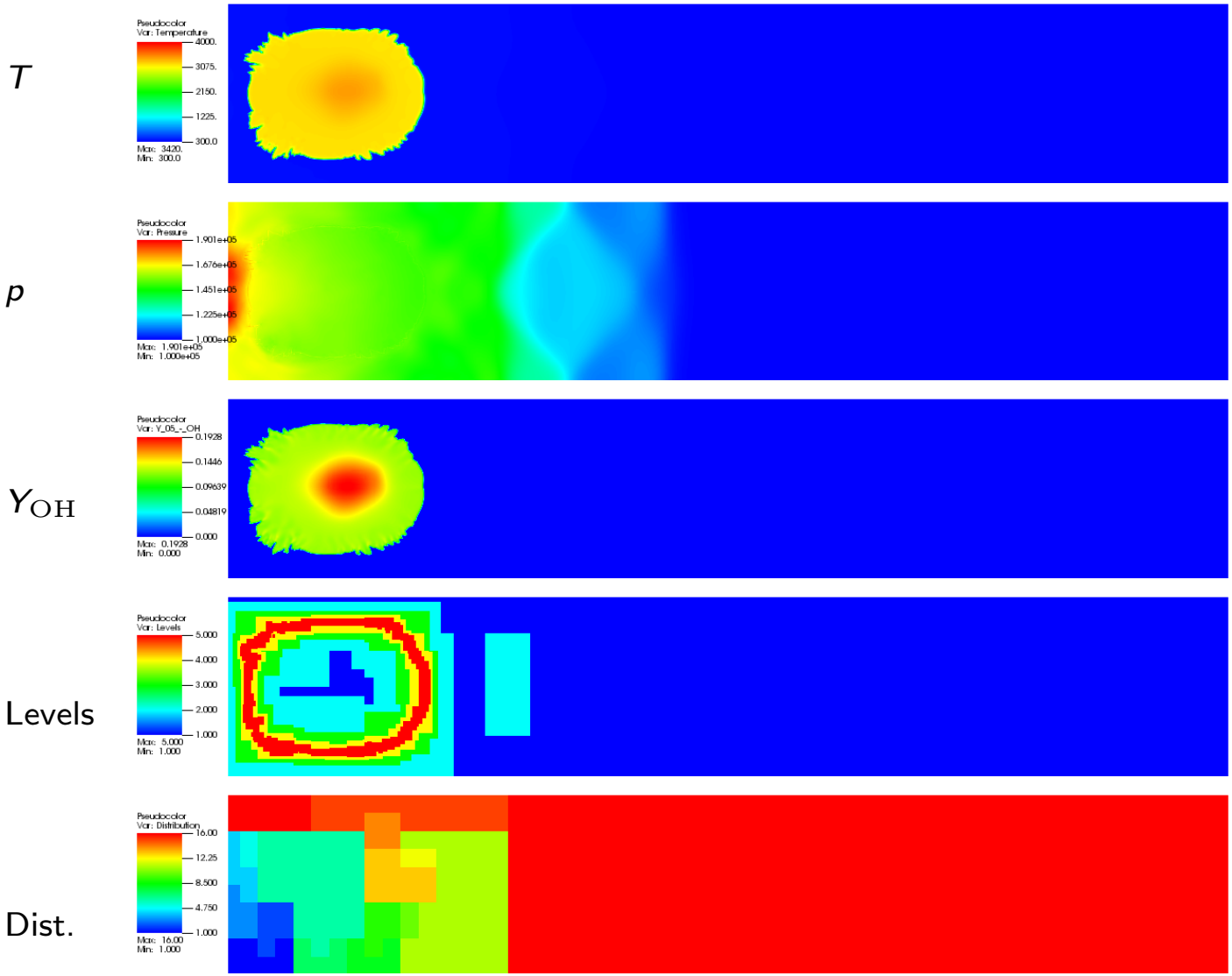

Deflagration to detonation transition in 2d

Hot sphere of 2500 K in stoichiometric H_2/O_2 in closed-end chamber of 2 cm diameter

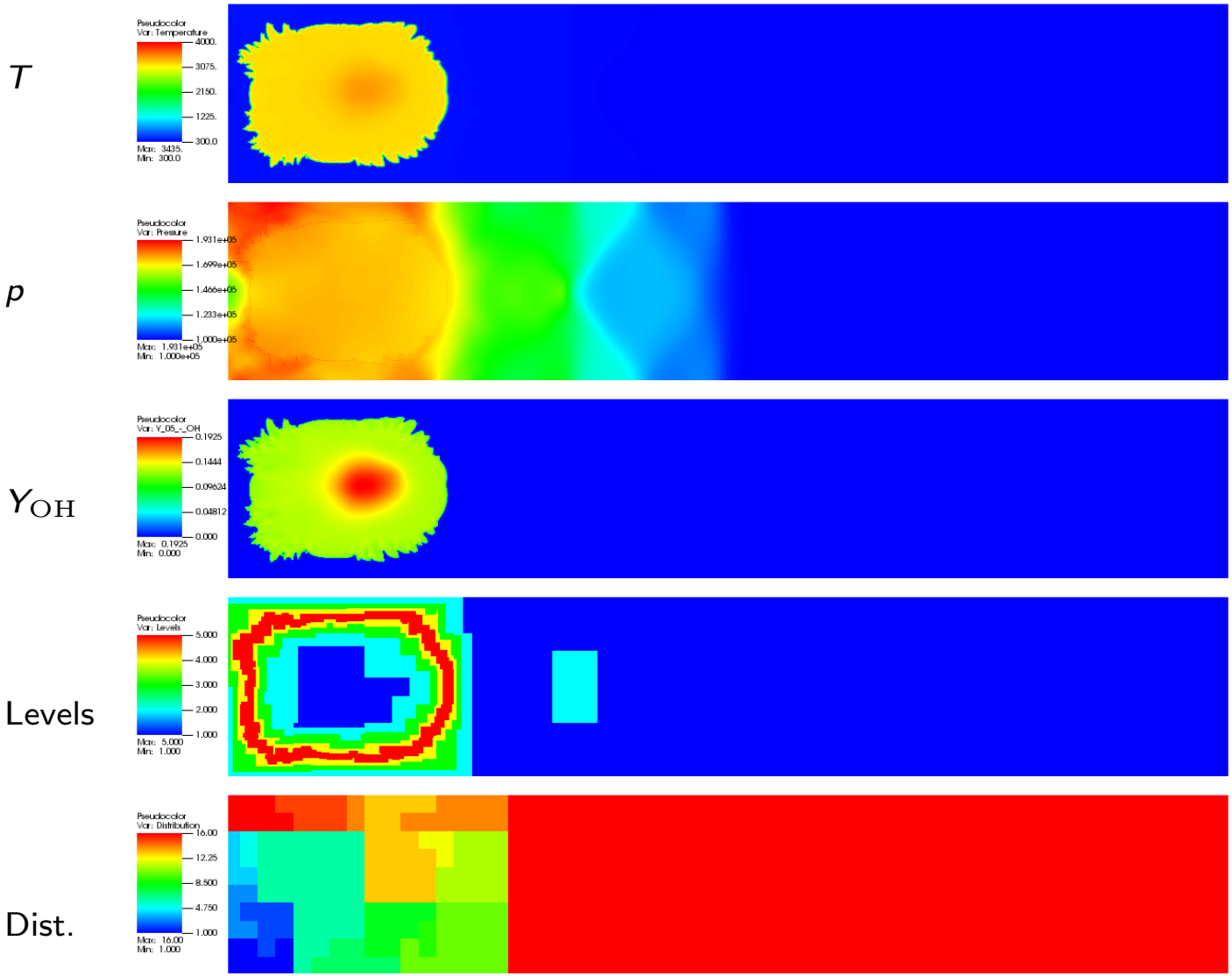

Deflagration to detonation transition in 2d

Hot sphere of 2500 K in stoichiometric H_2/O_2 in closed-end chamber of 2 cm diameter

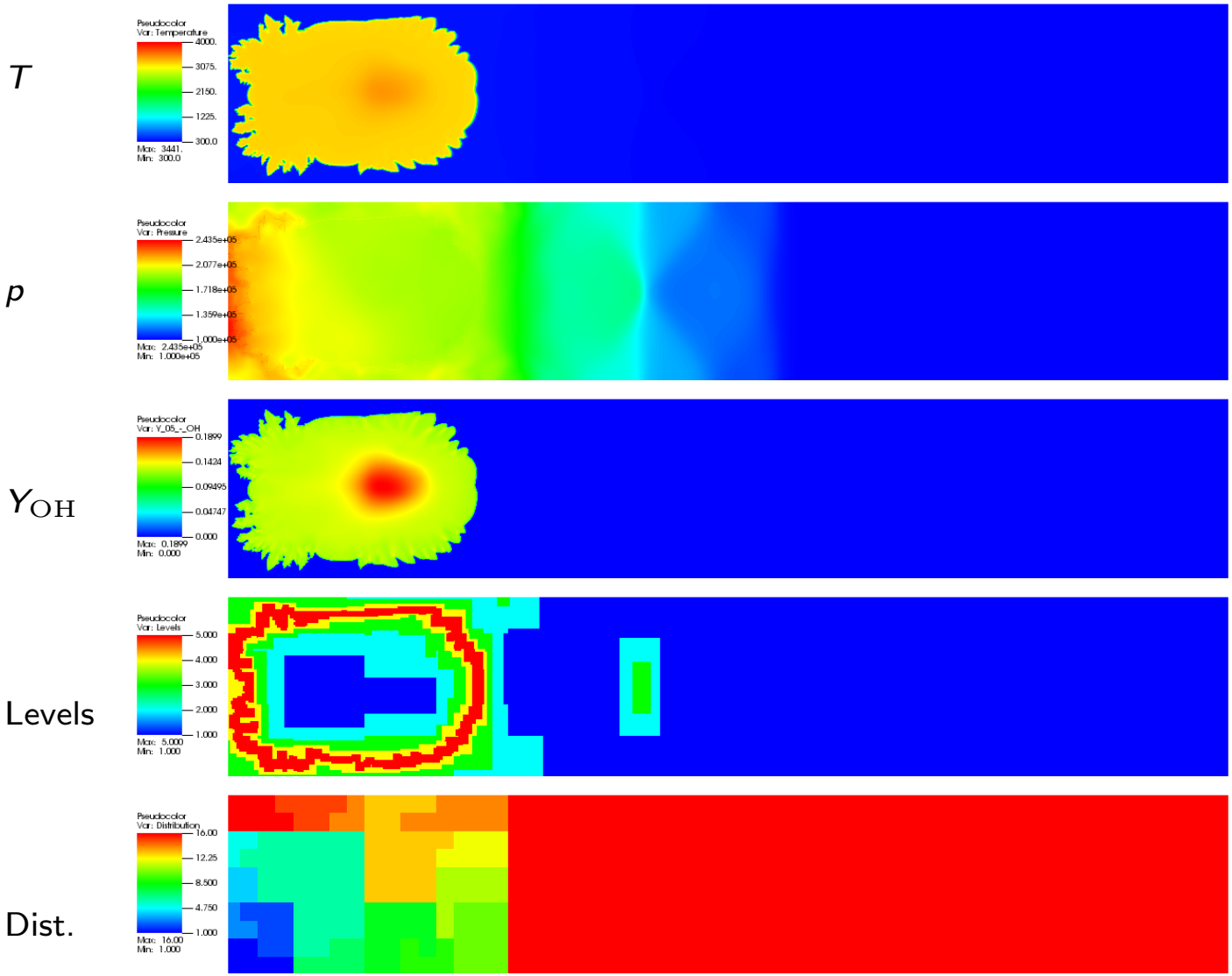

Deflagration to detonation transition in 2d

Hot sphere of 2500 K in stoichiometric H_2/O_2 in closed-end chamber of 2 cm diameter

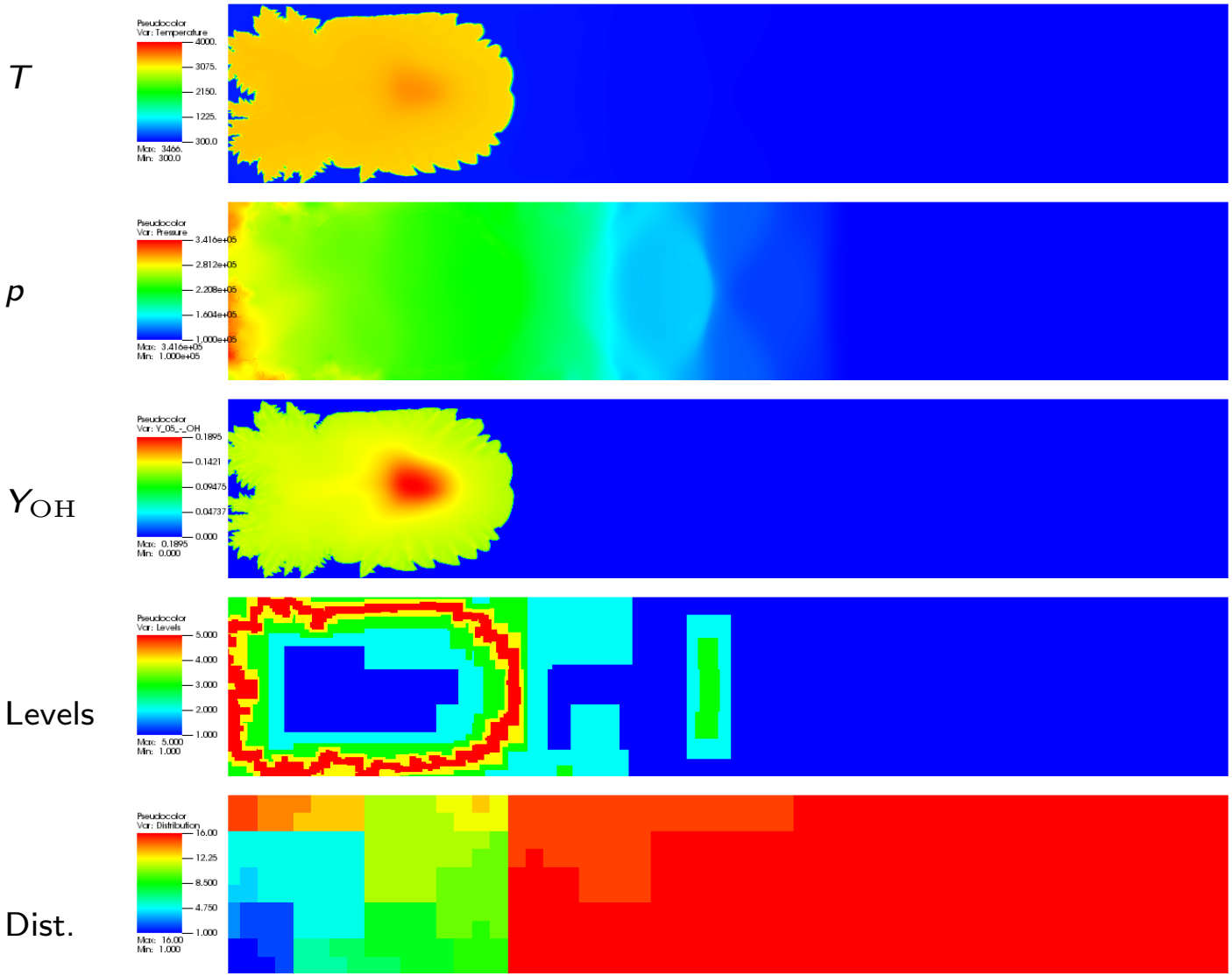

Deflagration to detonation transition in 2d

Hot sphere of 2500 K in stoichiometric H_2/O_2 in closed-end chamber of 2 cm diameter

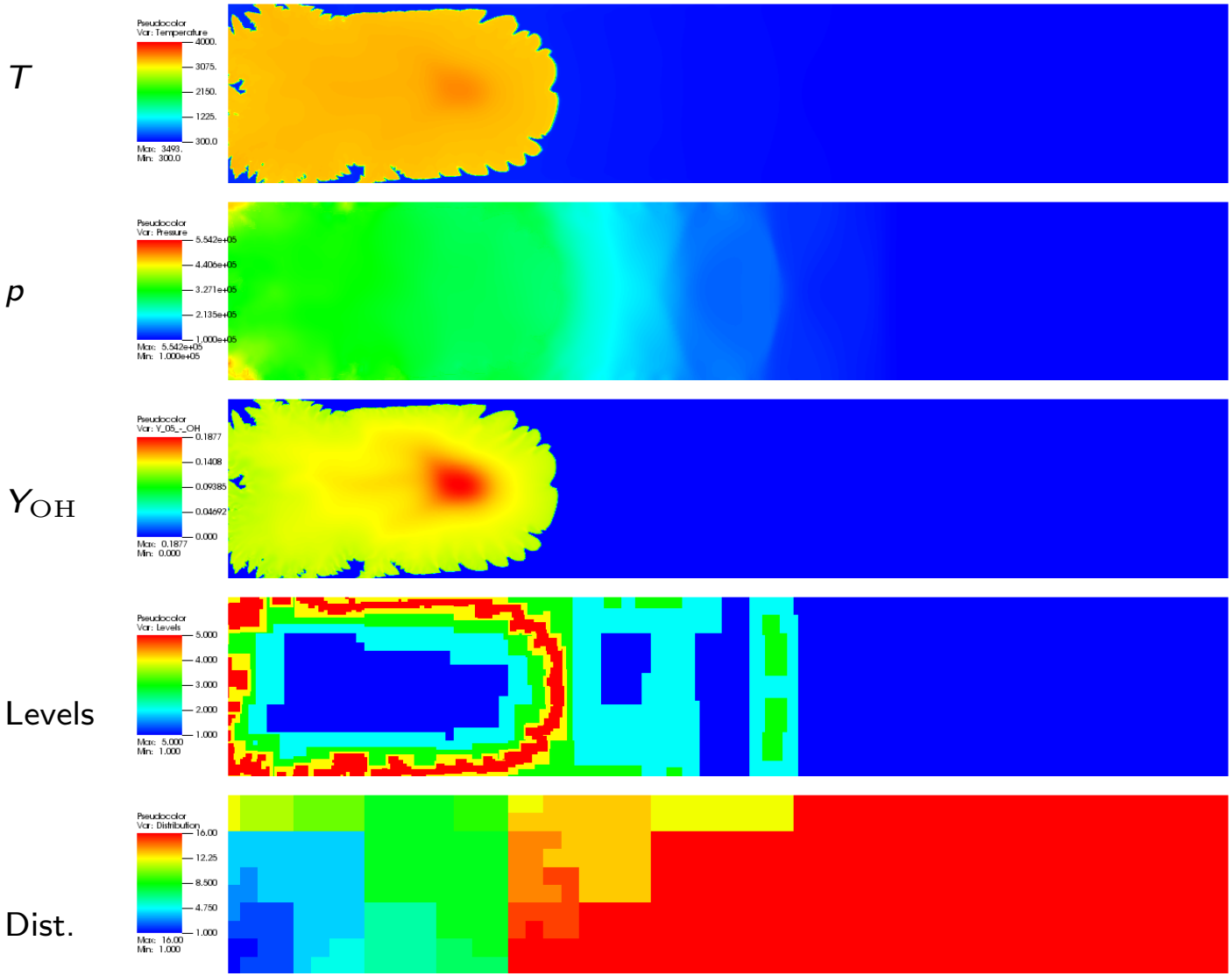

Deflagration to detonation transition in 2d

Hot sphere of 2500 K in stoichiometric H_2/O_2 in closed-end chamber of 2 cm diameter

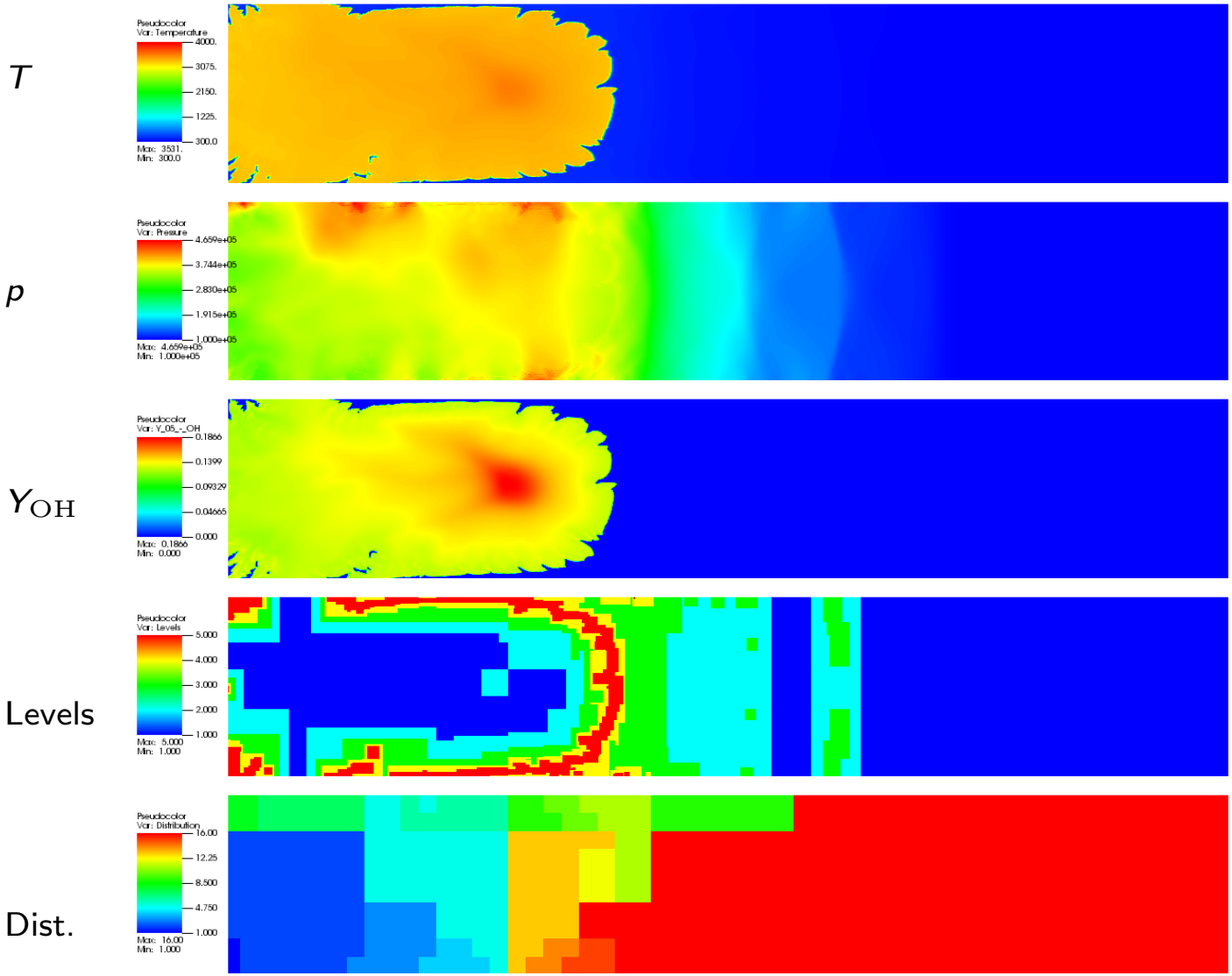

Deflagration to detonation transition in 2d

Hot sphere of 2500 K in stoichiometric H_2/O_2 in closed-end chamber of 2 cm diameter

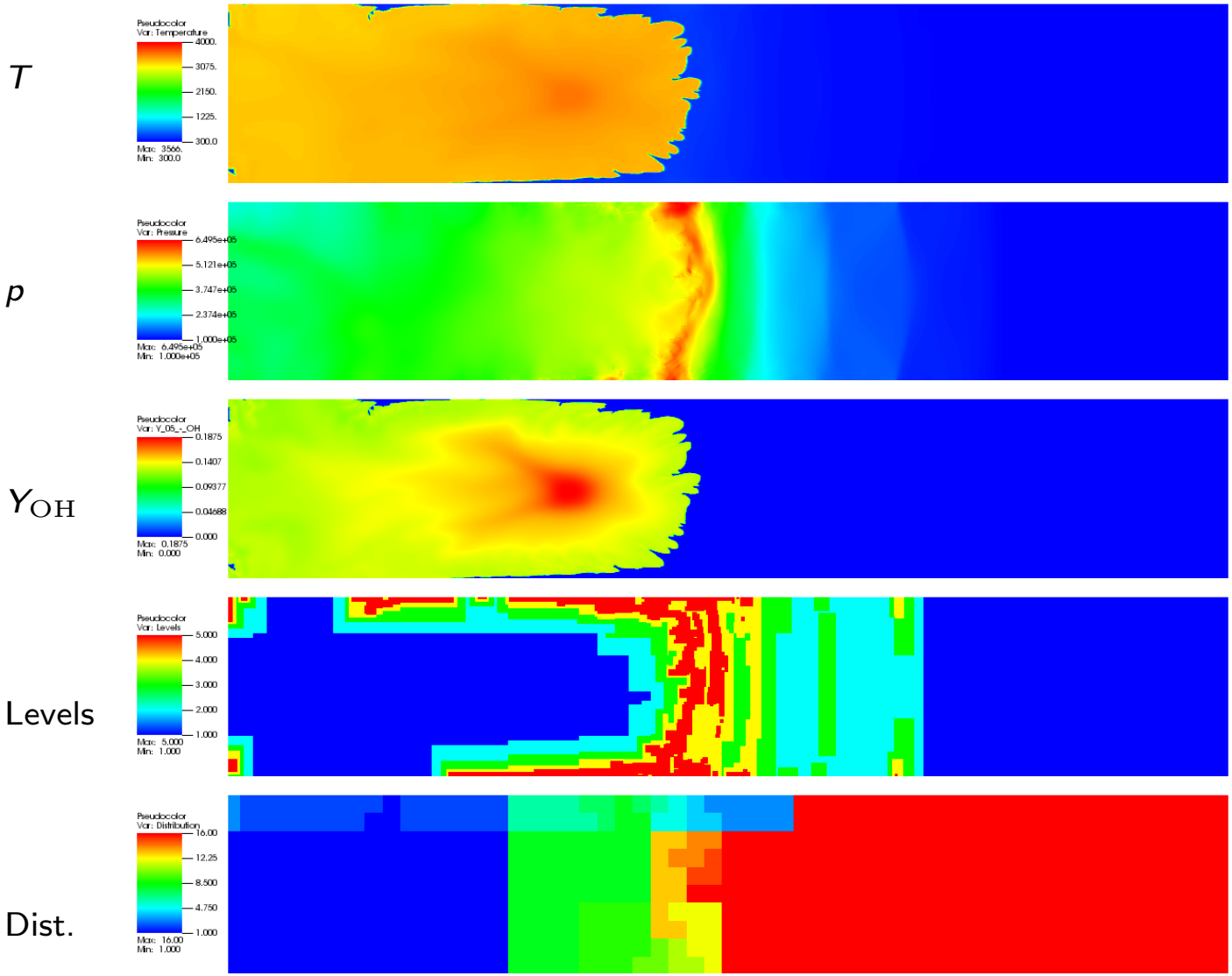

Deflagration to detonation transition in 2d

Hot sphere of 2500 K in stoichiometric H_2/O_2 in closed-end chamber of 2 cm diameter

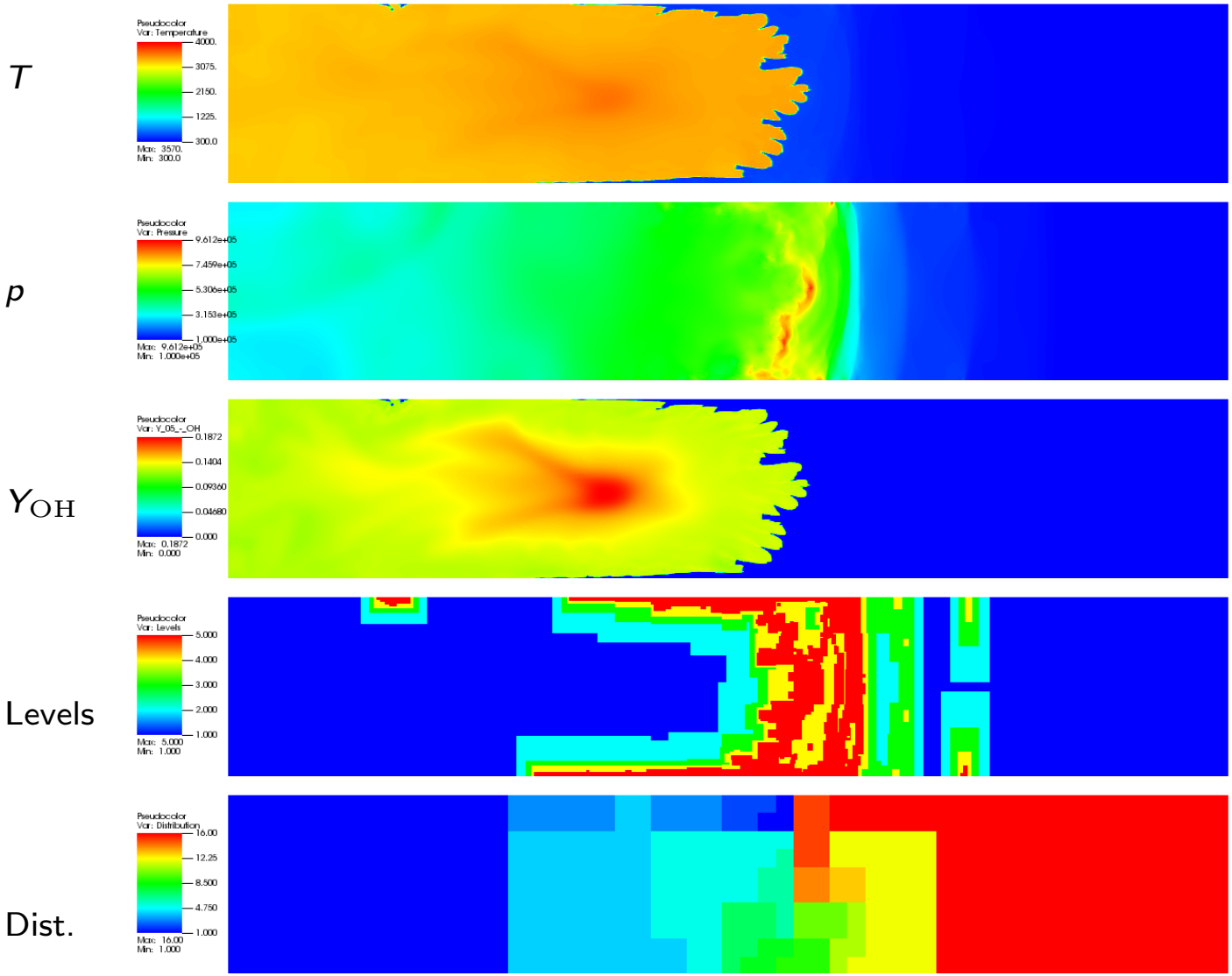

Deflagration to detonation transition in 2d

Hot sphere of 2500 K in stoichiometric H_2/O_2 in closed-end chamber of 2 cm diameter

T

p

Y_{OH}

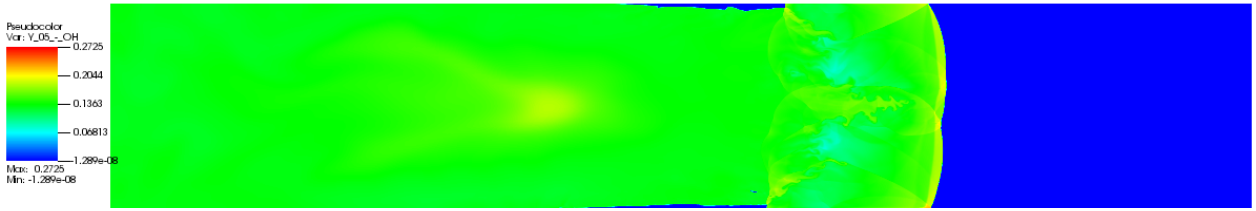

Levels

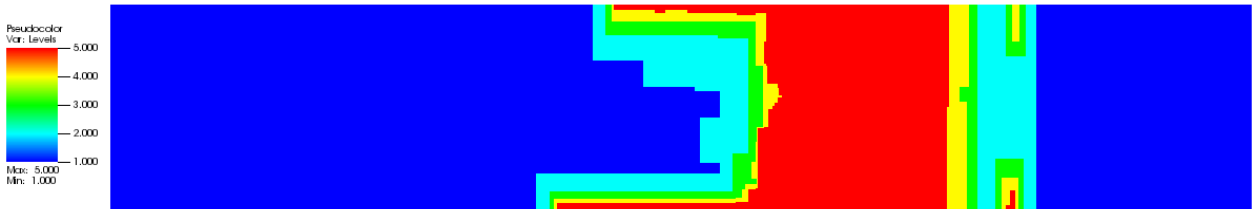

Dist.

Deflagration to detonation transition in 2d

Hot sphere of 2500 K in stoichiometric H_2/O_2 in closed-end chamber of 2 cm diameter

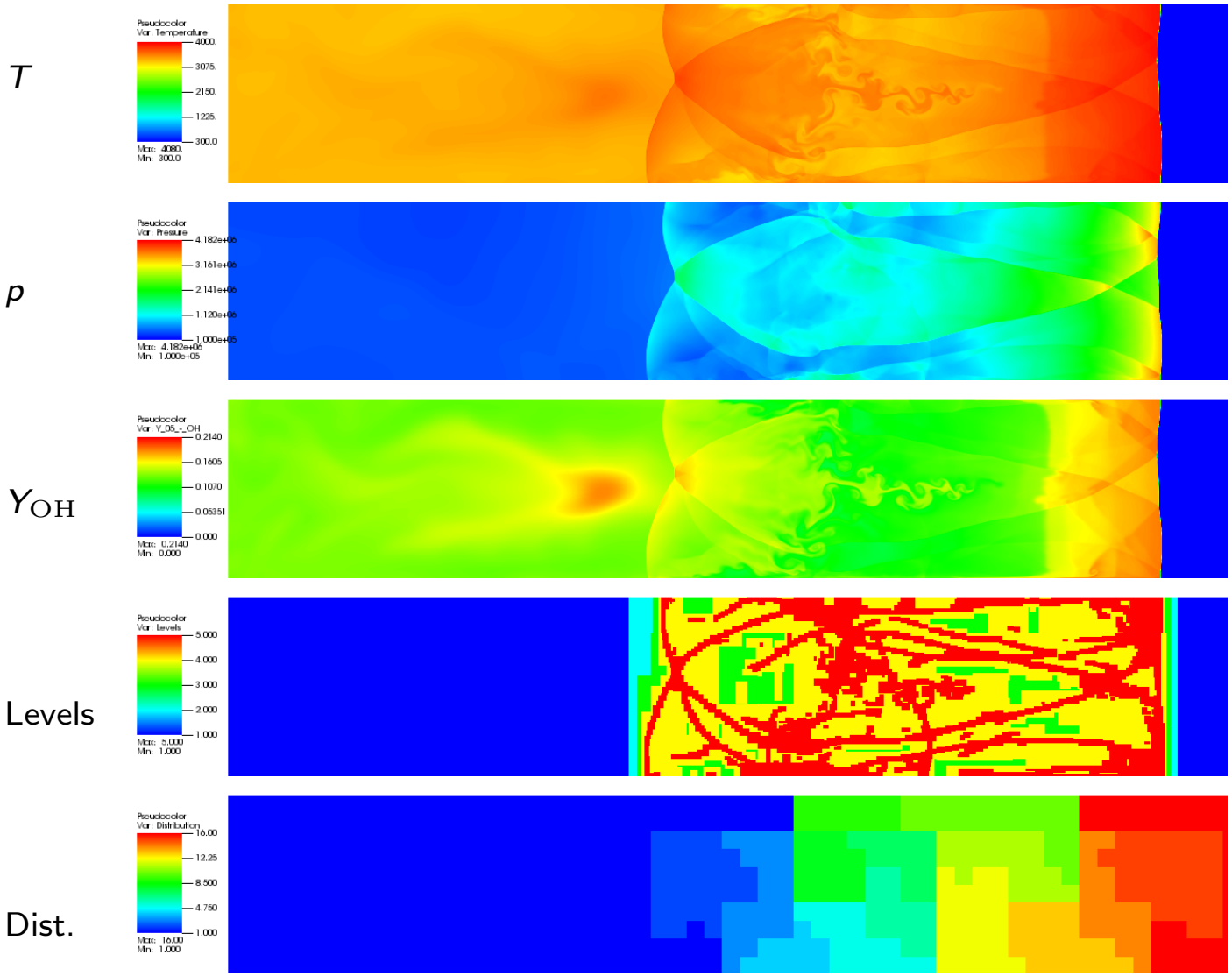

Deflagration to detonation transition in 2d

Hot sphere of 2500 K in stoichiometric H_2/O_2 in closed-end chamber of 2 cm diameter

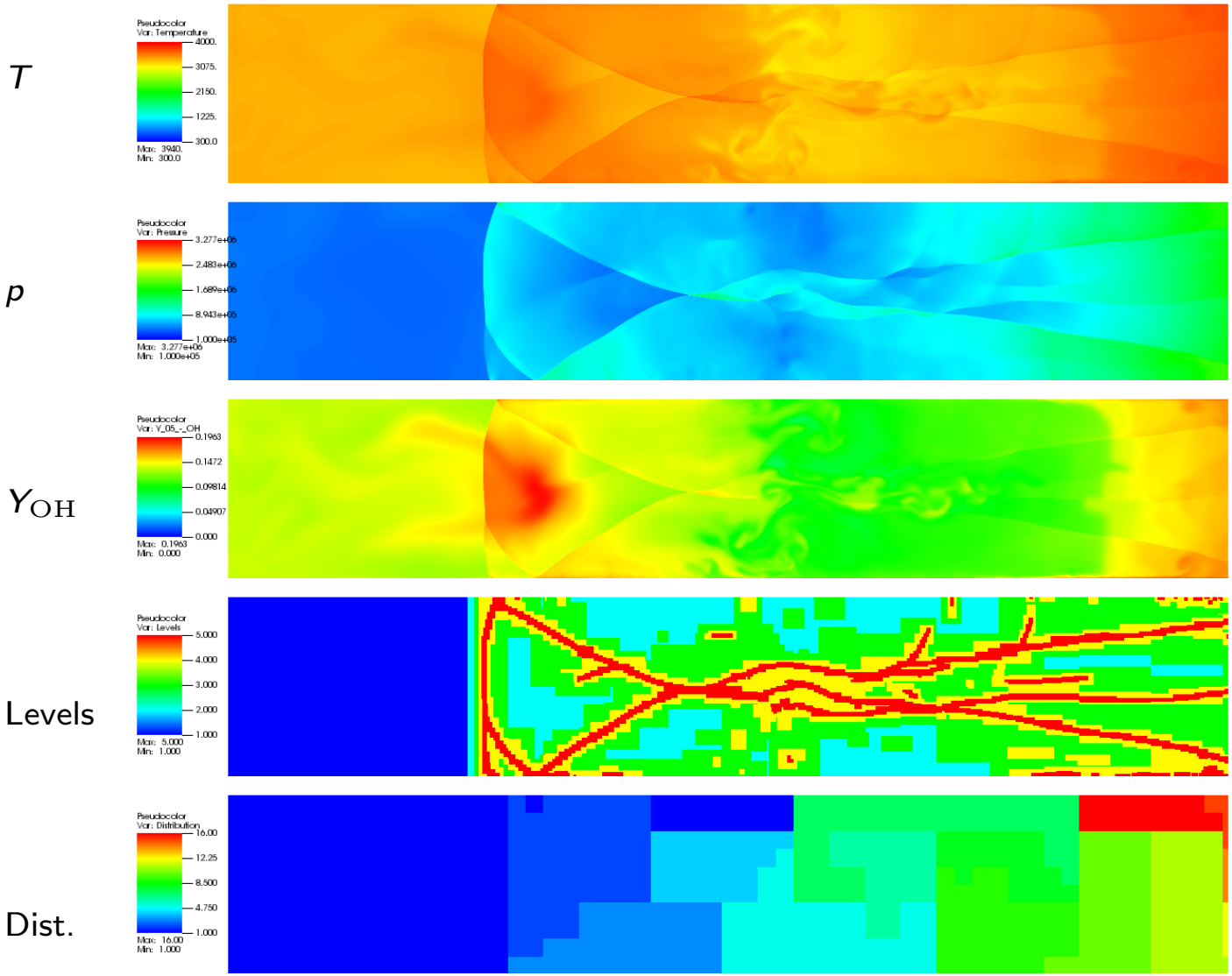

Deflagration to detonation transition in 2d

Hot sphere of 2500 K in stoichiometric H_2/O_2 in closed-end chamber of 2 cm diameter

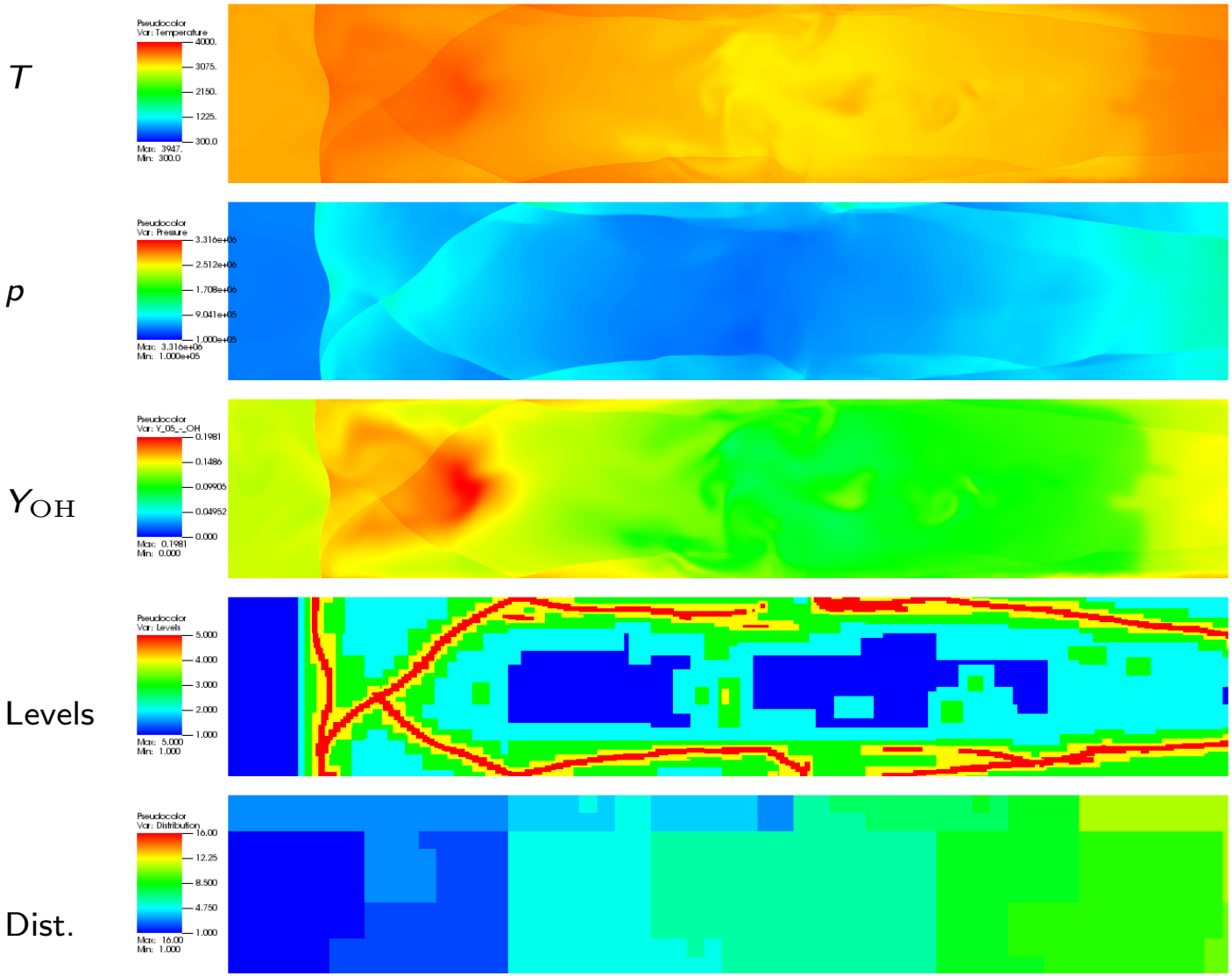

Deflagration to detonation transition in 2d

Hot sphere of 2500 K in stoichiometric H_2/O_2 in closed-end chamber of 2 cm diameter

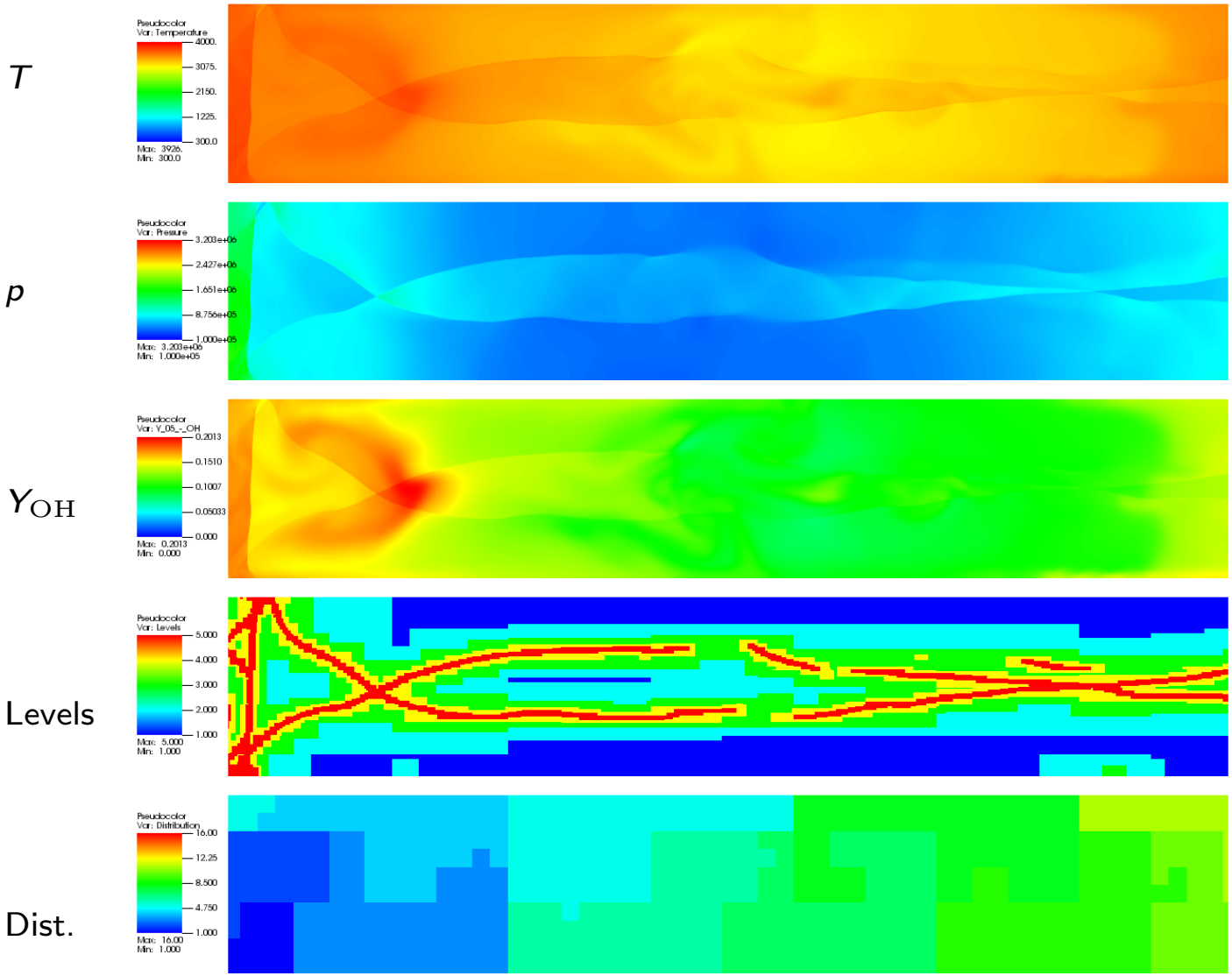

Simulation of regular structures

- CJ detonation for $H_2 : O_2 : Ar$ (2:1:7) at $T_0 = 298\,\mathrm{K}$ and $p_0 = 10\,\mathrm{kPa}$, cell width $1.6\,\mathrm{cm}$
- Perturb 1d solution with unreacted high-pressure pocket behind front
- Triple point trajectories by tracking max $|\omega|$ on auxiliary mesh shifted through grid with CJ velocity. $\omega = \dfrac{\partial v}{\partial x} - \dfrac{\partial u}{\partial y}$
- SAMR simulation with 4 additional levels (2,2,2,4), $67.6\,\mathrm{Pts}/l_{ig}$
- Configuration similar to Oran et al., J. Combustion and Flame 113, 1998.

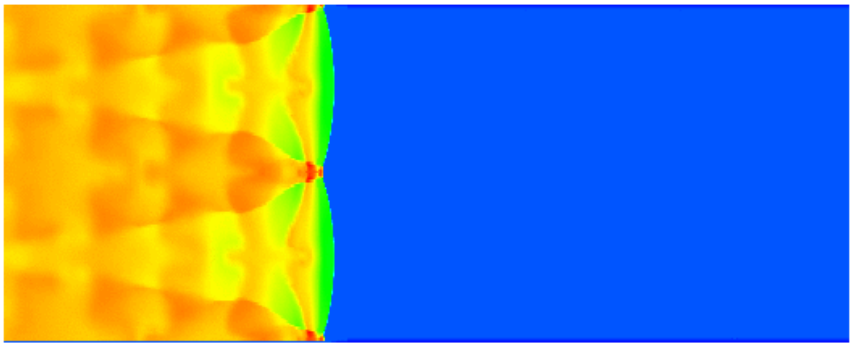

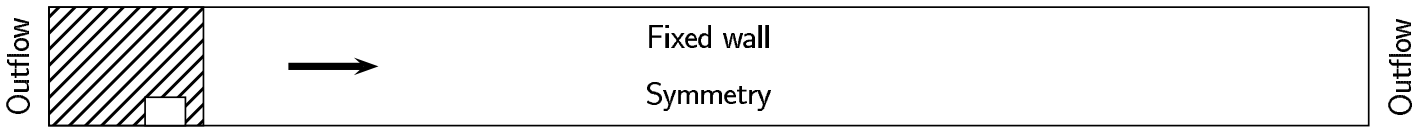

Simulation of regular structures

- CJ detonation for $H_2 : O_2 : Ar$ (2:1:7) at $T_0 = 298\,\mathrm{K}$ and $p_0 = 10\,\mathrm{kPa}$, cell width $1.6\,\mathrm{cm}$
- Perturb 1d solution with unreacted high-pressure pocket behind front
- Triple point trajectories by tracking max $|\omega|$ on auxiliary mesh shifted through grid with CJ velocity. $\omega = \frac{\partial v}{\partial x} - \frac{\partial u}{\partial y}$
- SAMR simulation with 4 additional levels (2,2,2,4), $67.6\,\mathrm{Pts}/l_{ig}$
- Configuration similar to Oran et al., J. Combustion and Flame 113, 1998.

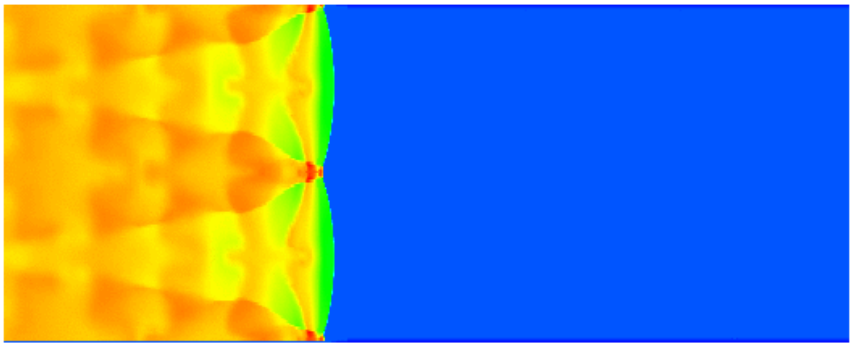

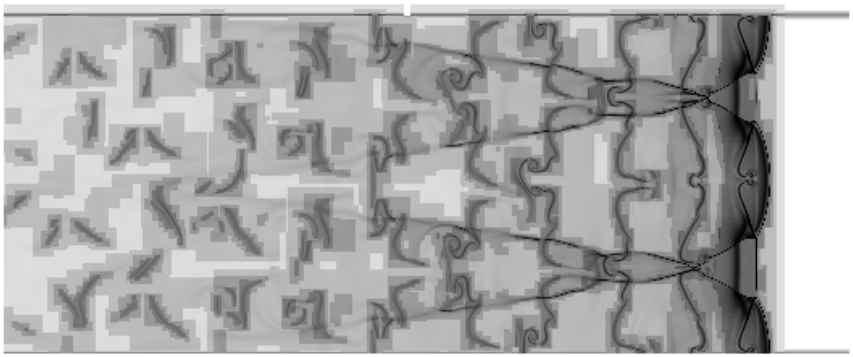

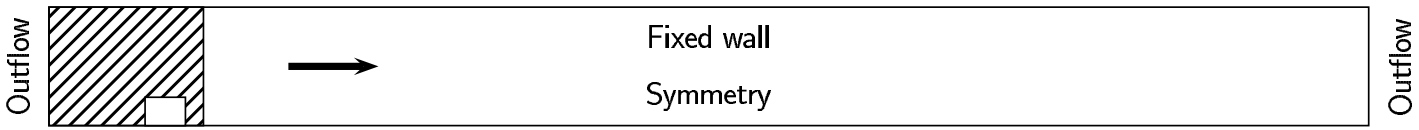

Simulation of regular structures

- CJ detonation for $H_2 : O_2 : Ar$ (2:1:7) at $T_0 = 298\,\mathrm{K}$ and $p_0 = 10\,\mathrm{kPa}$, cell width $1.6\,\mathrm{cm}$
- Perturb 1d solution with unreacted high-pressure pocket behind front
- Triple point trajectories by tracking max $|\omega|$ on auxiliary mesh shifted through grid with CJ velocity. $\omega = \dfrac{\partial v}{\partial x} - \dfrac{\partial u}{\partial y}$
- SAMR simulation with 4 additional levels (2,2,2,4), $67.6\,\mathrm{Pts}/l_{ig}$
- Configuration similar to Oran et al., J. Combustion and Flame 113, 1998.

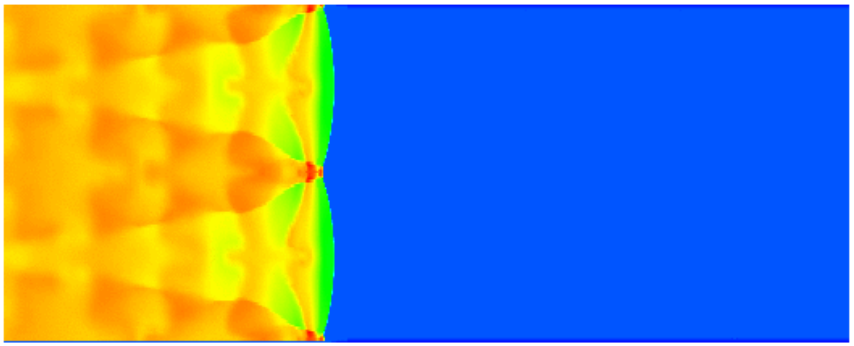

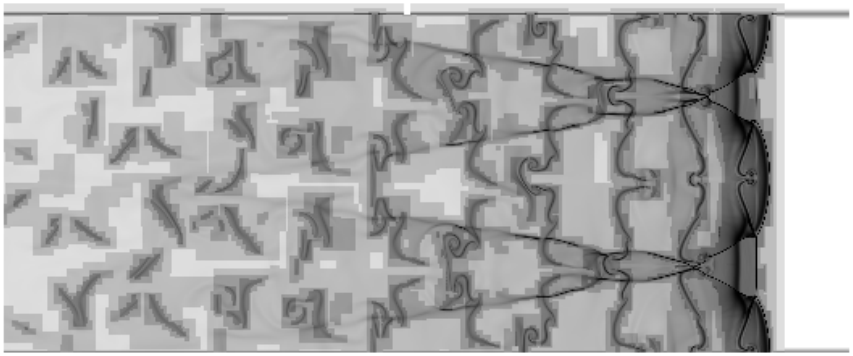

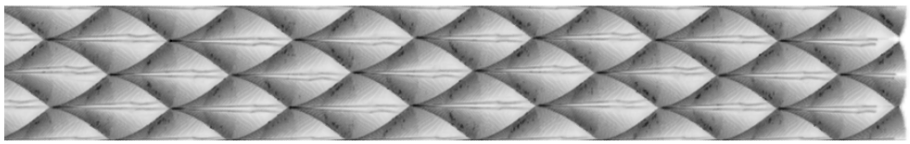

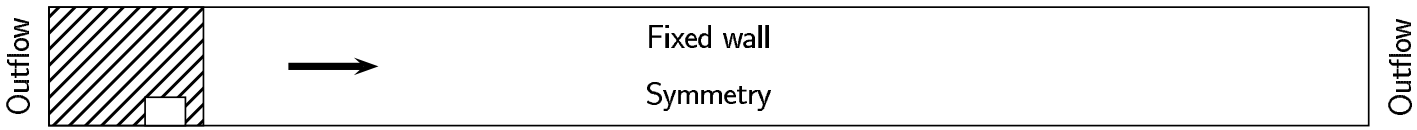

Triple point analysis

Double Mach reflection structure shortly before the next collision

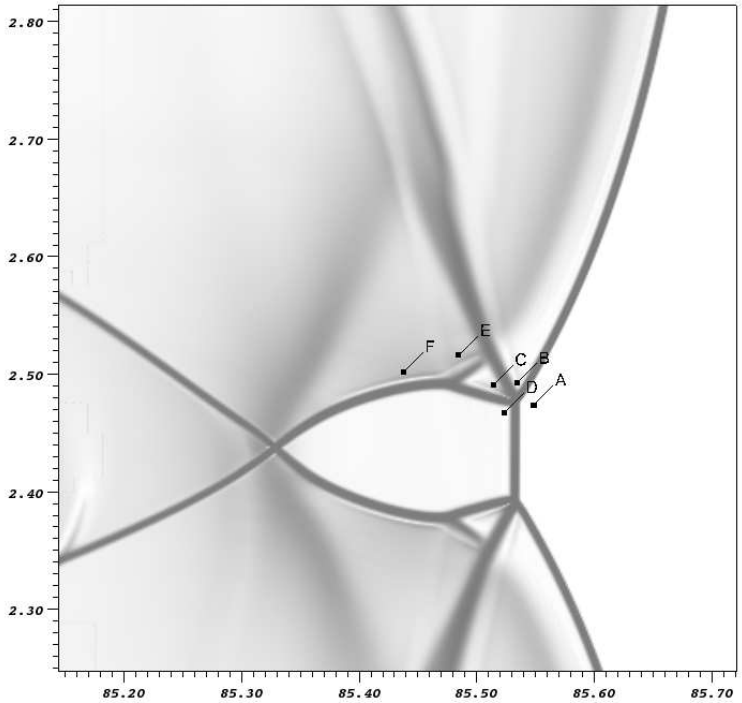

	p/p_0	ρ/ρ_0	T [K]	u[m/s]	M
A	1.00	1.00	298	1775	5.078
B	31.45	4.17	2248	447	0.477
C	31.69	5.32	1775	965	1.153
D	19.17	3.84	1487	1178	1.533
E	35.61	5.72	1856	901	1.053
F	40.61	6.09	1987	777	0.880

Triple point analysis

Double Mach reflection structure shortly before the next collision

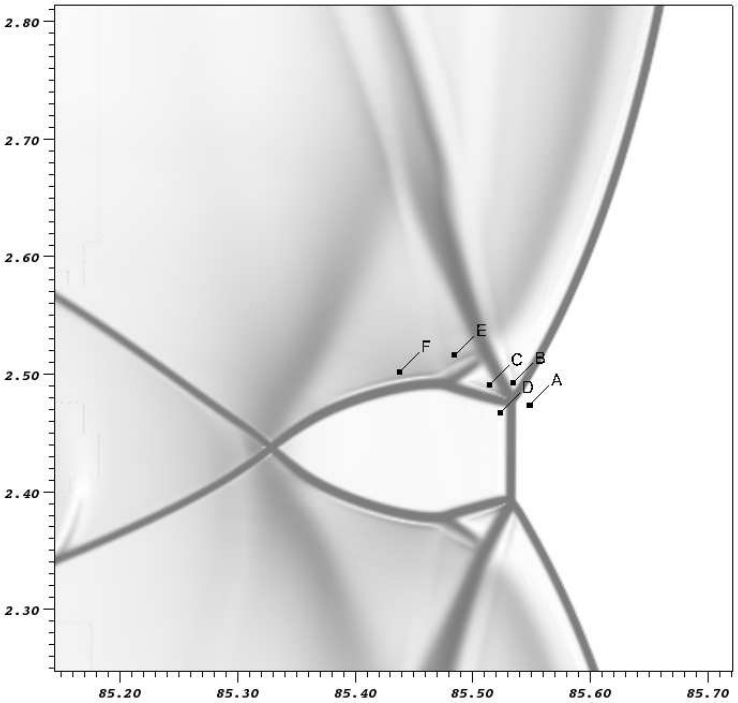

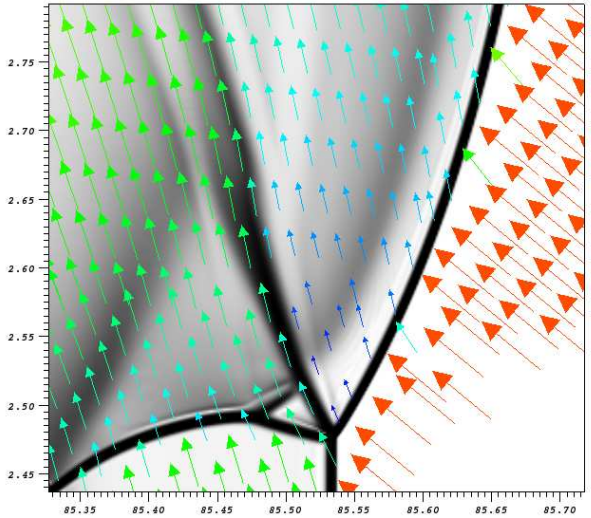

	p/p_0	ρ/ρ_0	T [K]	u[m/s]	M
A	1.00	1.00	298	1775	5.078
B	31.45	4.17	2248	447	0.477
C	31.69	5.32	1775	965	1.153
D	19.17	3.84	1487	1178	1.533
E	35.61	5.72	1856	901	1.053
F	40.61	6.09	1987	777	0.880

Triple point analysis

Double Mach reflection structure shortly before the next collision

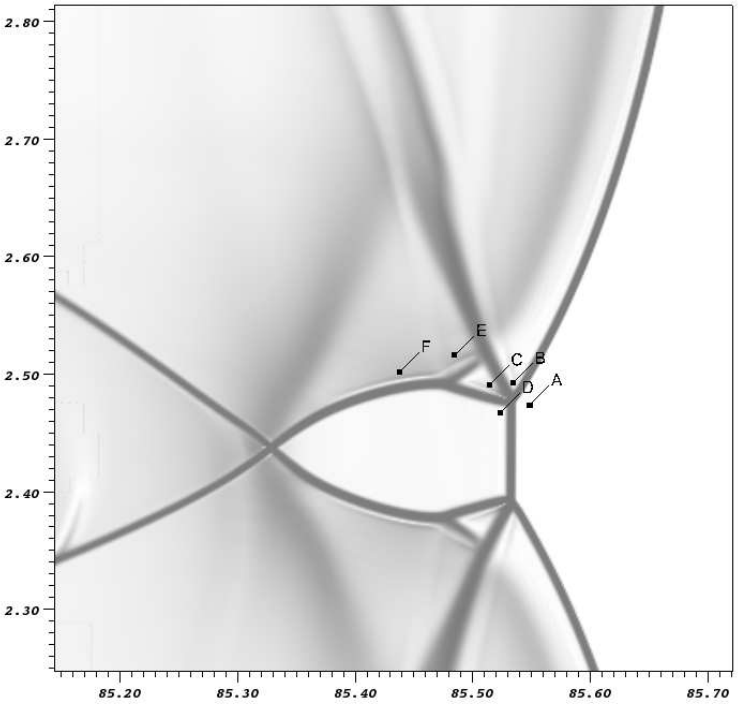

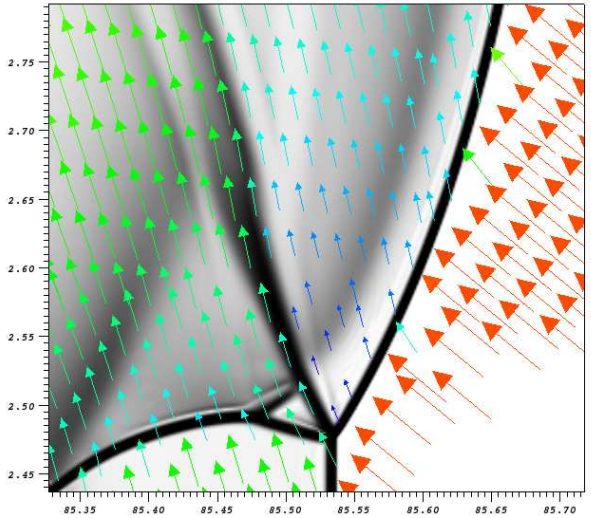

	p/p_0	ρ/ρ_0	T [K]	u[m/s]	M
A	1.00	1.00	298	1775	5.078
B	31.45	4.17	2248	447	0.477
C	31.69	5.32	1775	965	1.153
D	19.17	3.84	1487	1178	1.533
E	35.61	5.72	1856	901	1.053
F	40.61	6.09	1987	777	0.880

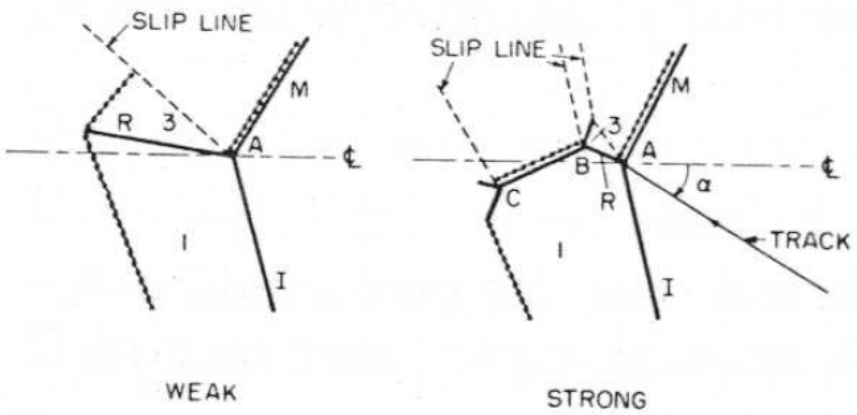

Detonation propagation through pipe bends

- 2D Simulation of CJ detonation for $H_2 : O_2 : Ar/2 : 1 : 7$ at $T_0 = 298\,\mathrm{K}$ and $p_0 = 10\,\mathrm{kPa}$. Tube width of 5 detonation cells
- AMR base grid 1200×992. 4 additional refinement levels (2,2,2,4). $67.6\,\mathrm{Pts}/l_{ig}$
- Adaptive computations use up to $7.1 \cdot 10^6$ cells ($4.8 \cdot 10^6$ on highest level) instead of $1.22 \cdot 10^9$ cells (uniform grid)
- $\sim 70,000\,\mathrm{h}$ CPU on 128 CPUs Pentium-4 2.2GHz

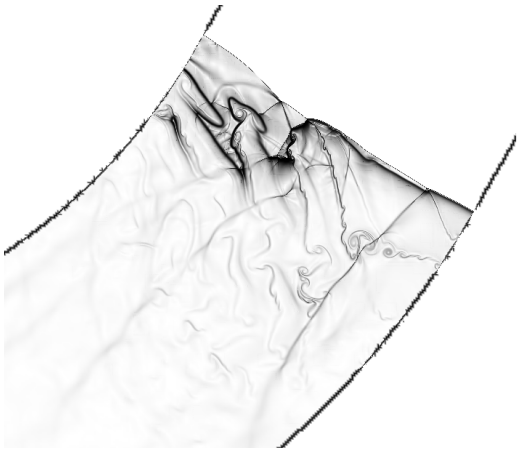

Detonation propagation through pipe bends

- 2D Simulation of CJ detonation for $\mathrm{H_2} : \mathrm{O_2} : \mathrm{Ar}/2 : 1 : 7$ at $T_0 = 298\,\mathrm{K}$ and $p_0 = 10\,\mathrm{kPa}$. Tube width of 5 detonation cells
- AMR base grid 1200×992. 4 additional refinement levels (2,2,2,4). $67.6\,\mathrm{Pts}/l_{ig}$
- Adaptive computations use up to $7.1 \cdot 10^6$ cells ($4.8 \cdot 10^6$ on highest level) instead of $1.22 \cdot 10^9$ cells (uniform grid)
- $\sim 70,000\,\mathrm{h}$ CPU on 128 CPUs Pentium-4 2.2GHz

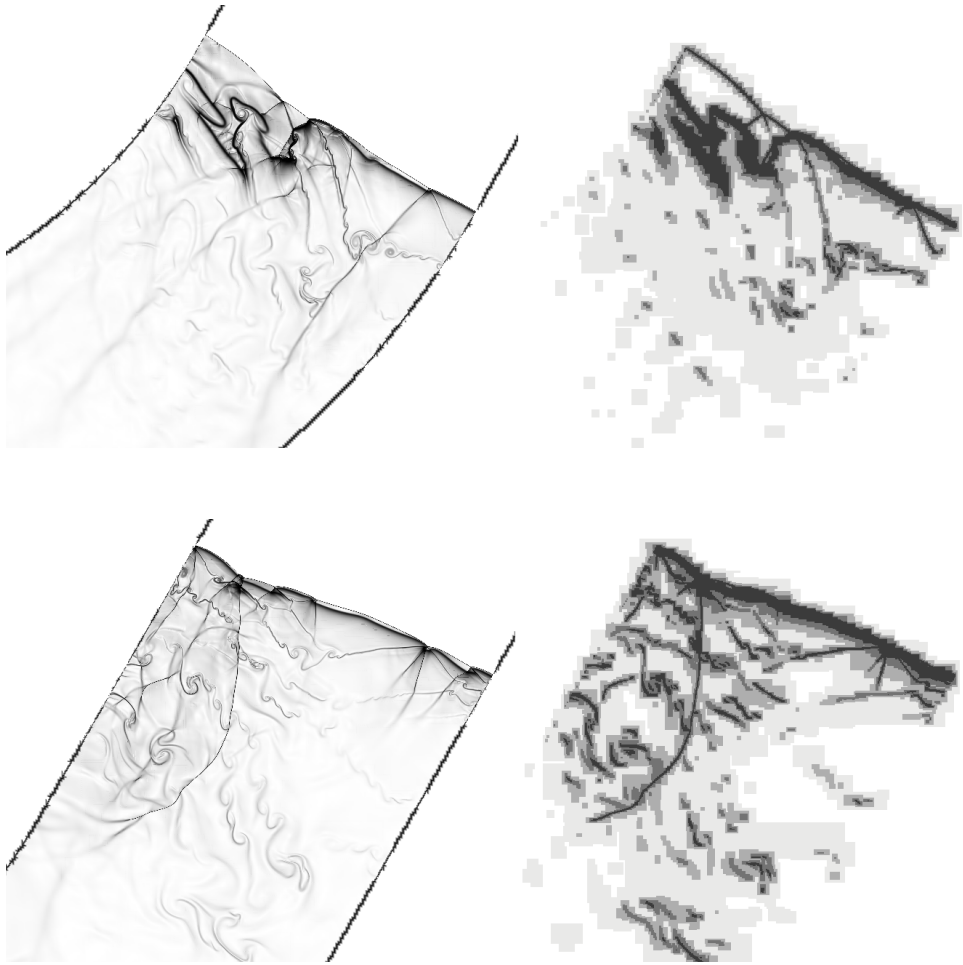

Detonation propagation through pipe bends

- 2D Simulation of CJ detonation for $H_2 : O_2 : Ar/2 : 1 : 7$ at $T_0 = 298\,\mathrm{K}$ and $p_0 = 10\,\mathrm{kPa}$. Tube width of 5 detonation cells
- AMR base grid 1200×992. 4 additional refinement levels (2,2,2,4). $67.6\,\mathrm{Pts}/l_{ig}$
- Adaptive computations use up to $7.1 \cdot 10^6$ cells ($4.8 \cdot 10^6$ on highest level) instead of $1.22 \cdot 10^9$ cells (uniform grid)
- $\sim 70,000\,\mathrm{h}$ CPU on 128 CPUs Pentium-4 2.2GHz

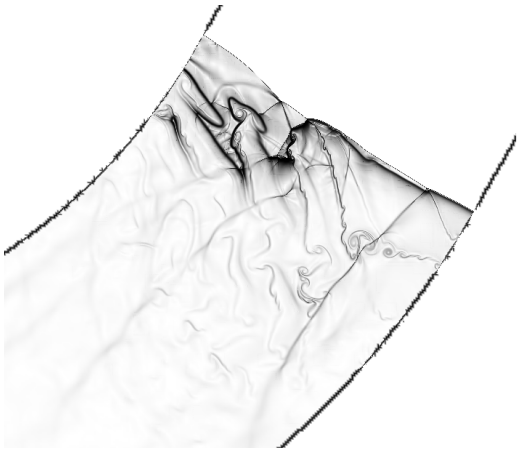

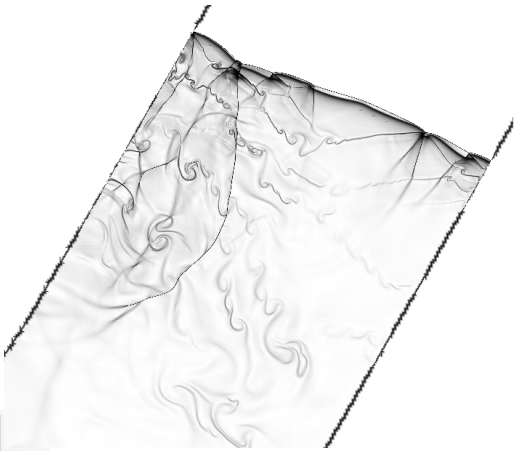

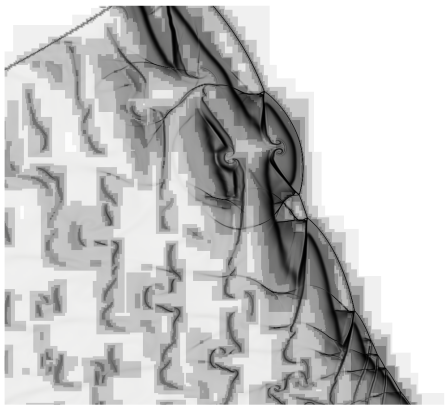
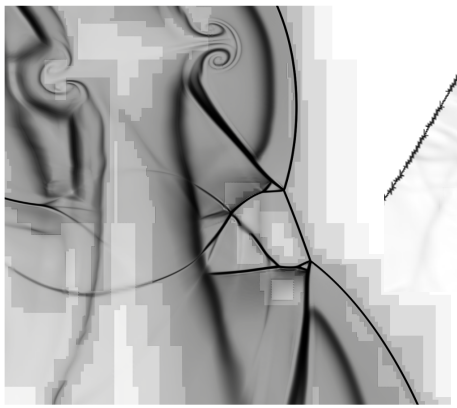

Triple point tracks

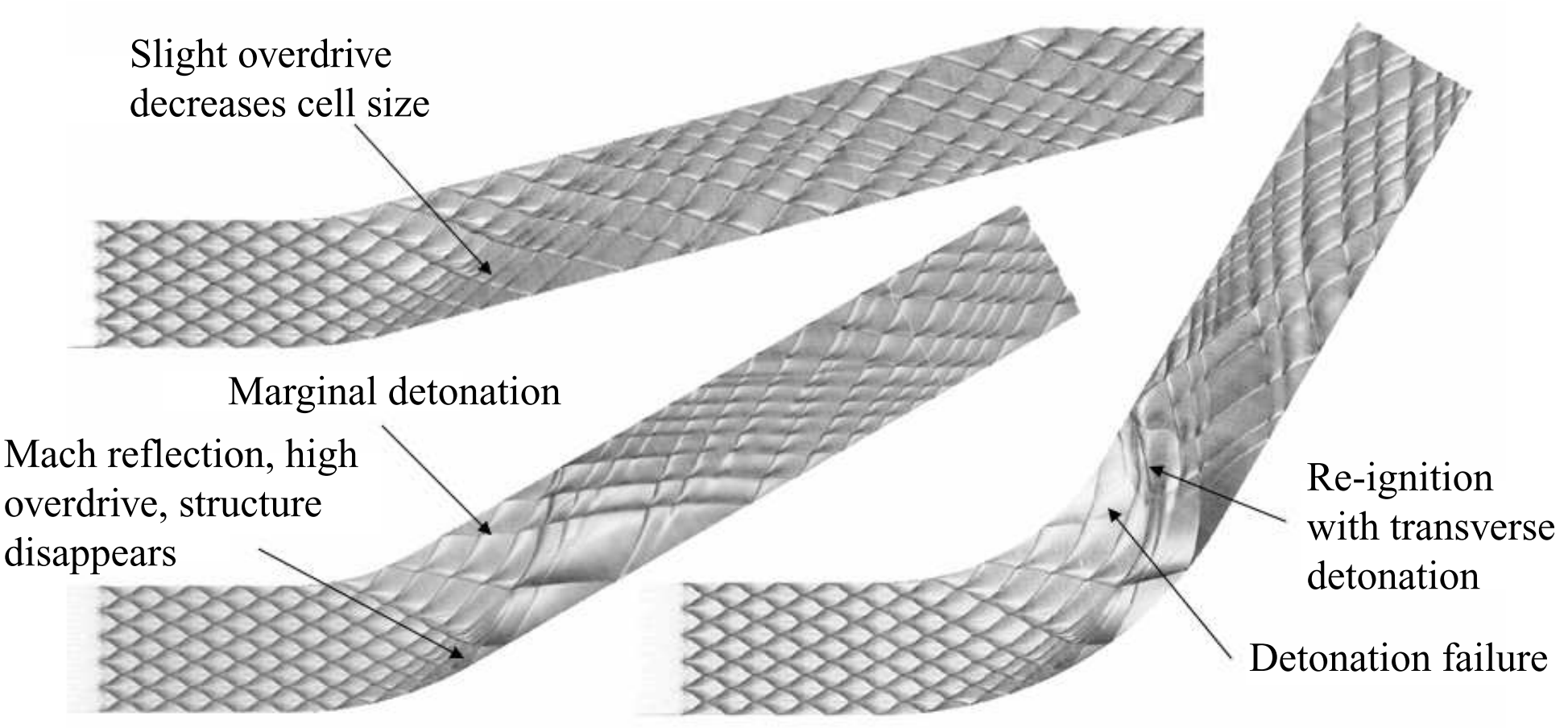

$\varphi = 15^o$ (left, top), $\varphi = 30^o$ (left, bottom), and $\varphi = 60^o$ (right)

The effect of resolution - $\varphi = 15^{\mathrm{o}}$

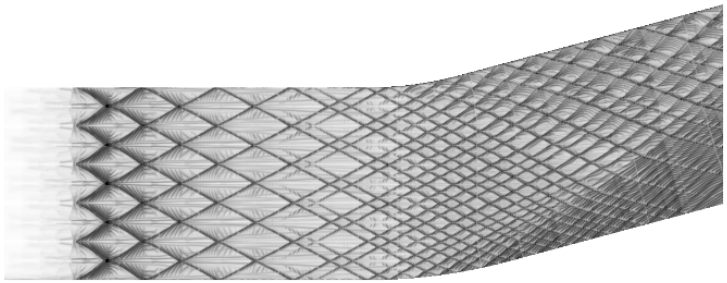

$14.05\,\mathrm{Pts}/l_{ig}$

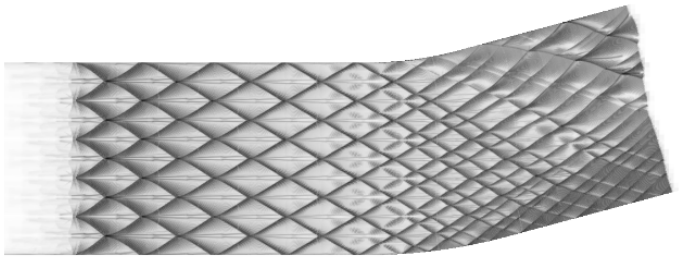

$28.1\,\mathrm{Pts}/l_{ig}$

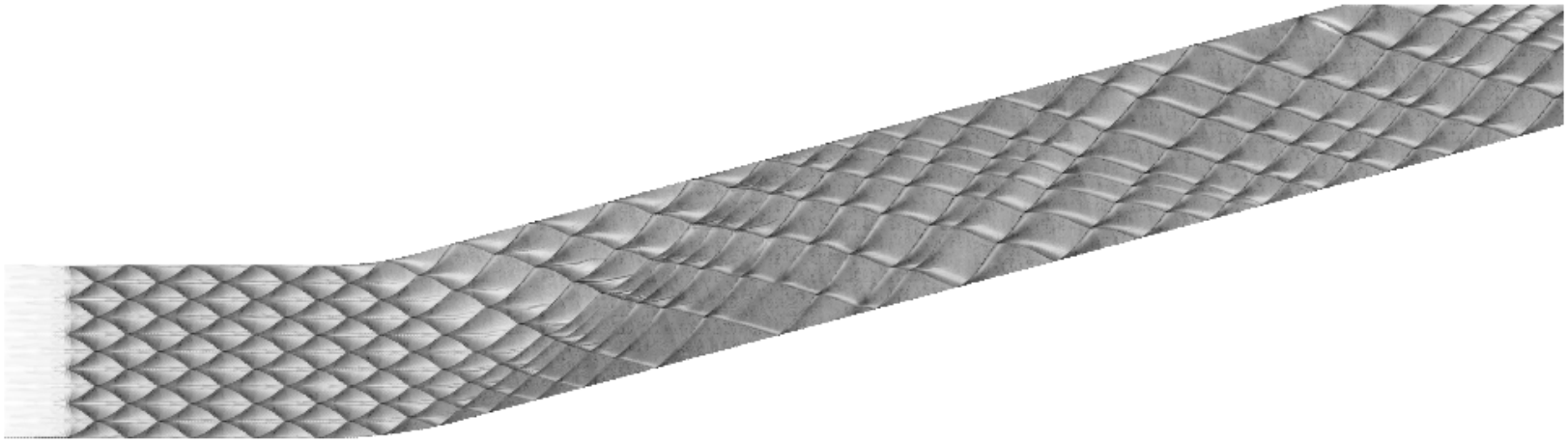

$56.2\,\mathrm{Pts}/l_{ig}$

The effect of resolution - $\varphi = 15^{\mathrm{o}}$

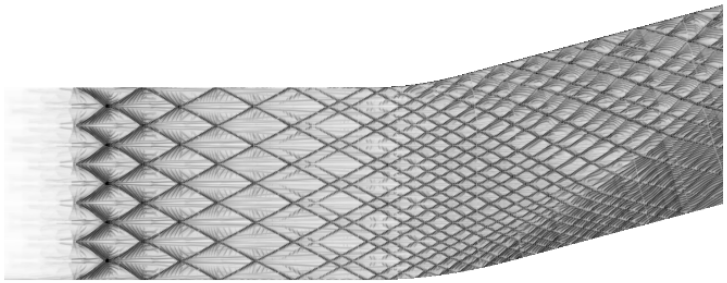

$14.05\,\mathrm{Pts}/l_{ig}$

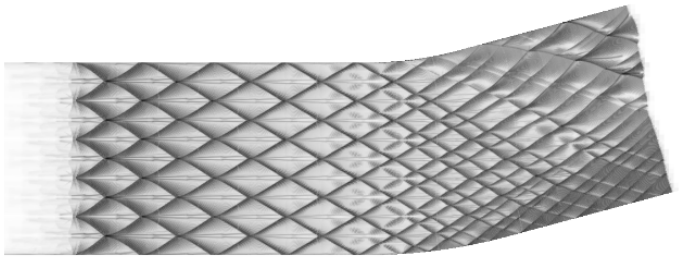

$28.1\,\mathrm{Pts}/l_{ig}$

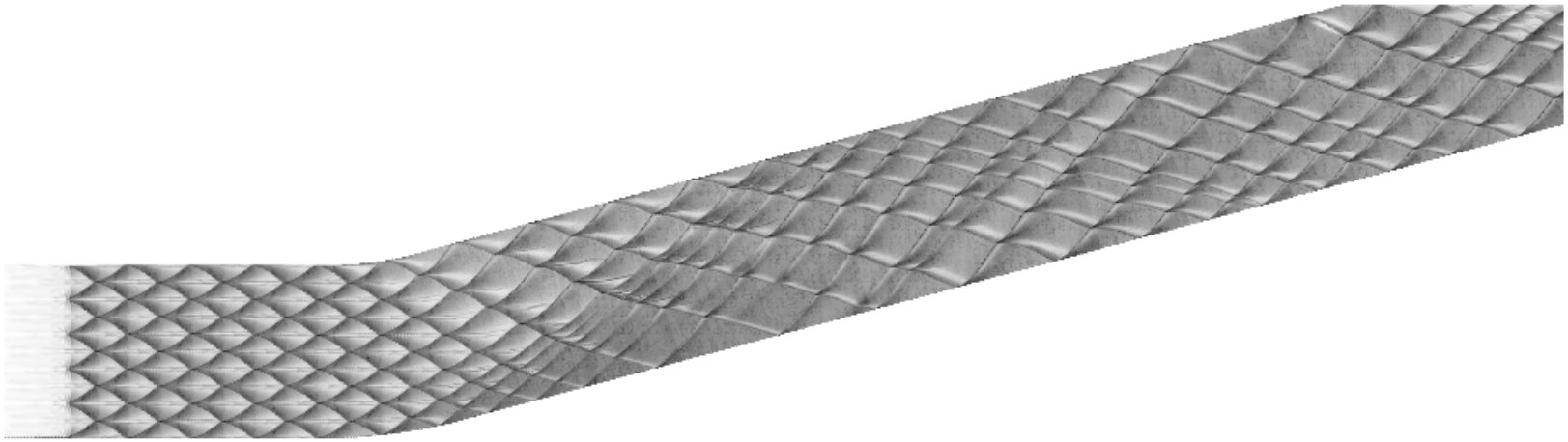

$56.2\,\mathrm{Pts}/l_{ig}$

- On coarse meshes, the high energy release in triple points cannot be captured
- Under sufficient resolution, the oscillation frequency is recovered after the bend

Triple point structures – $\varphi = 15^{\mathrm{o}}$

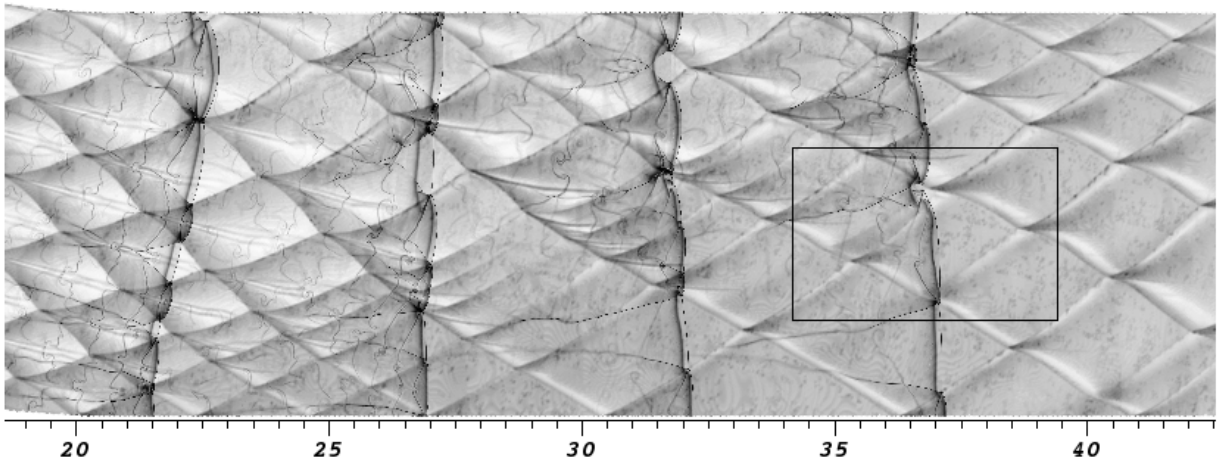

Triple point structures – $\varphi = 15^{\mathrm{o}}$

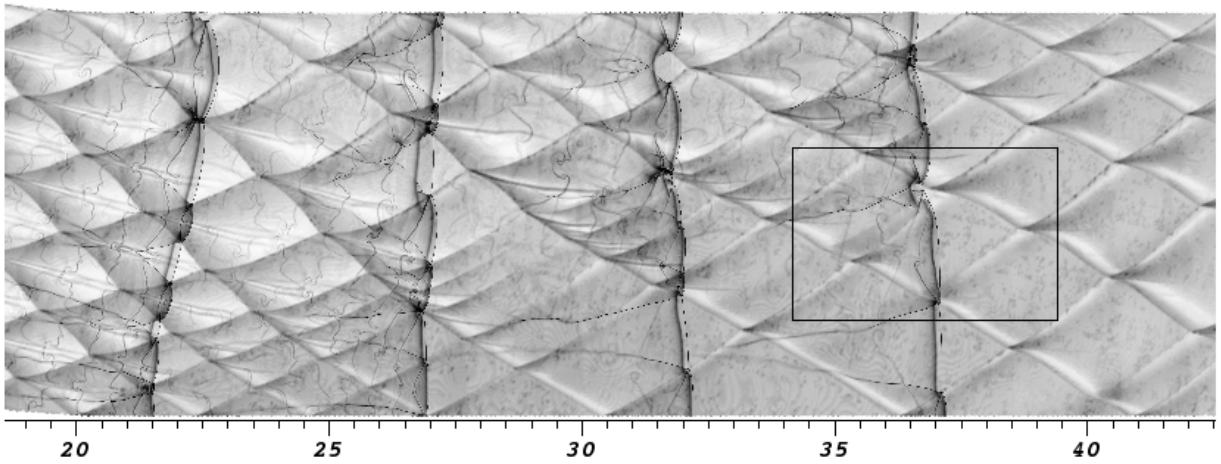

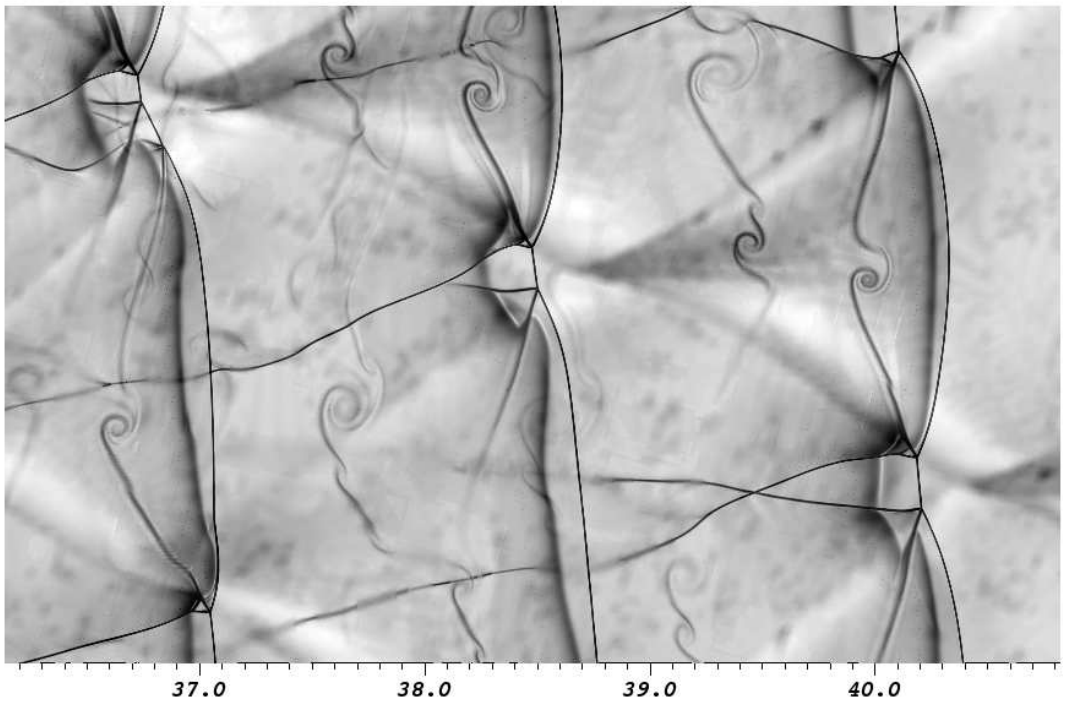

Triple point structures – $\varphi = 15^{\mathrm{o}}$

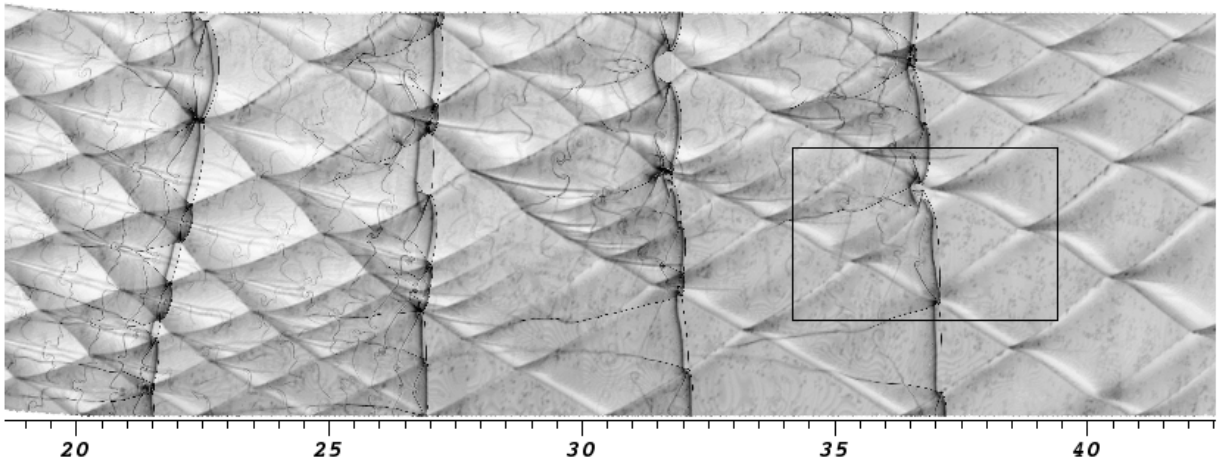

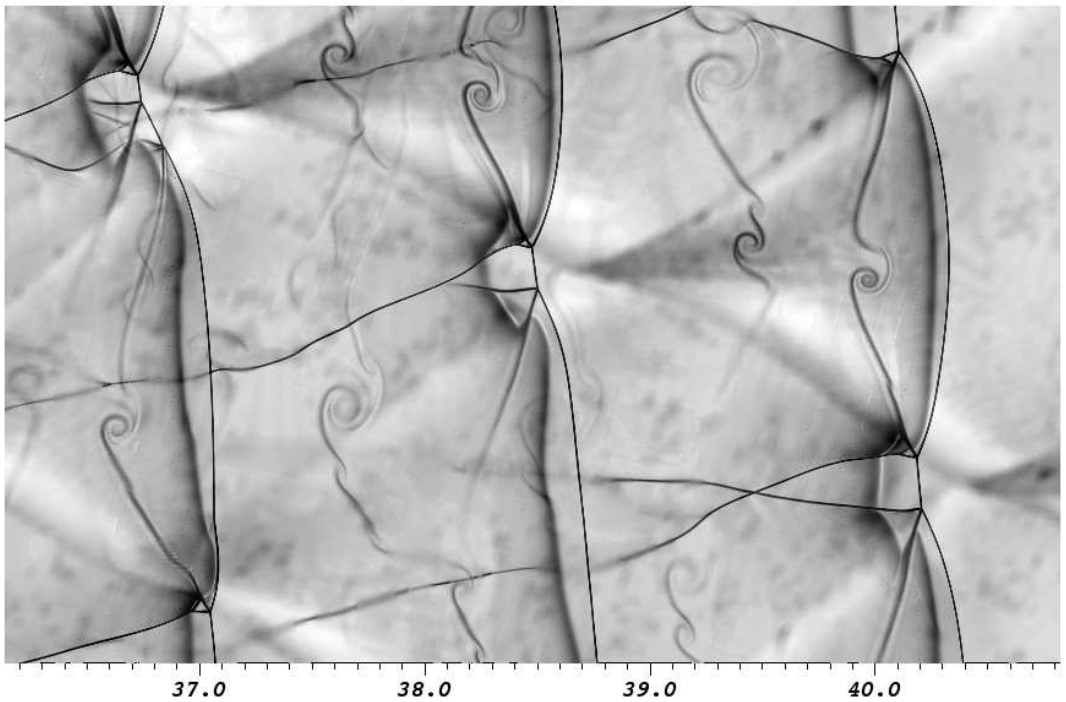

- Triple point re-initiation after bend with change from transitional to Double Mach reflection

Triple point structures – $\varphi = 30^{\mathrm{o}}$

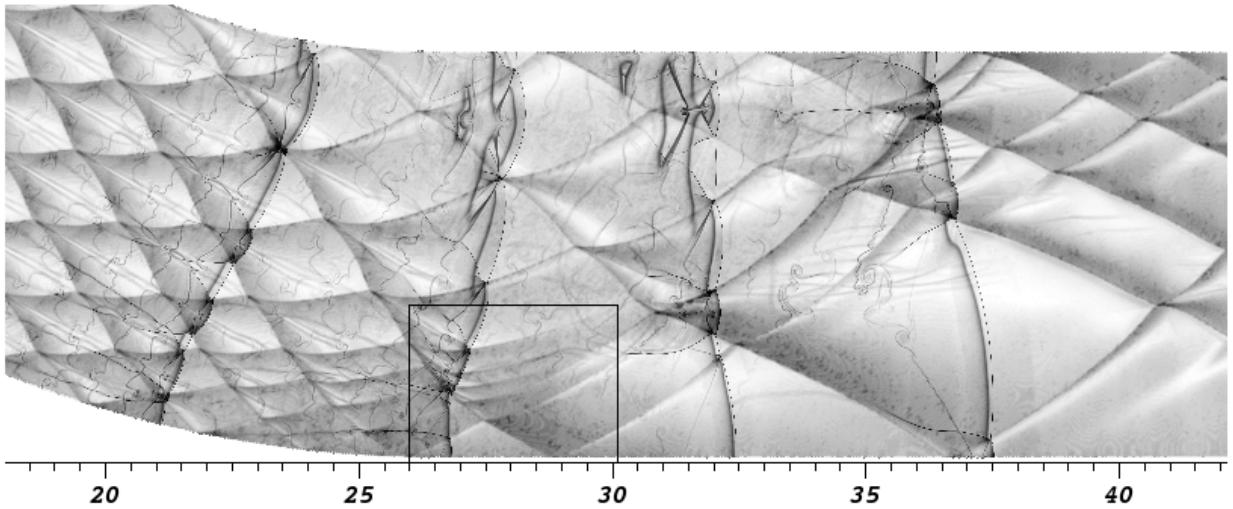

Triple point structures – $\varphi = 30^{\circ}$

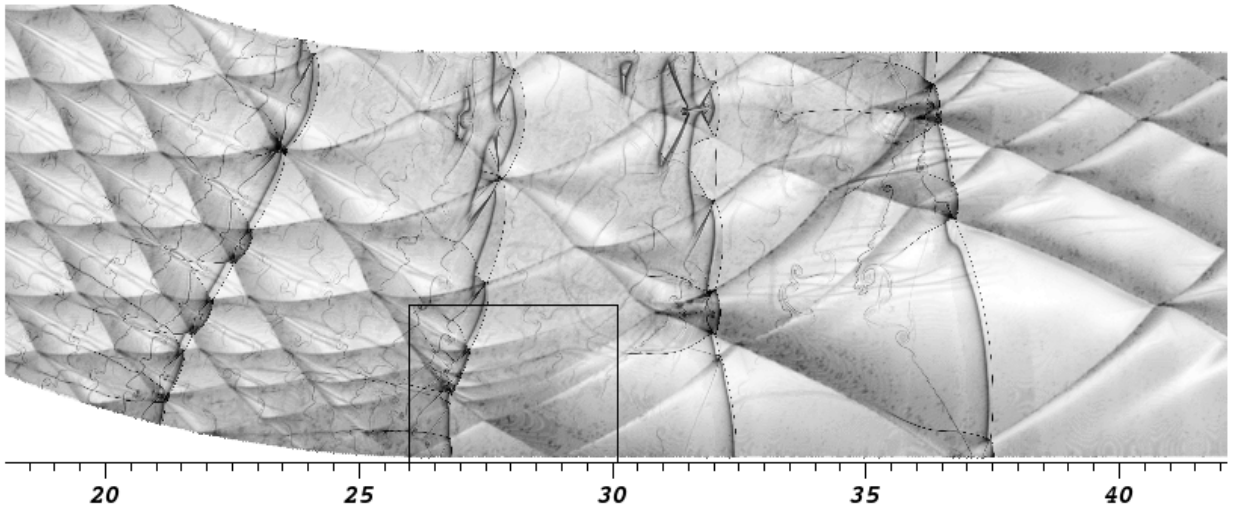

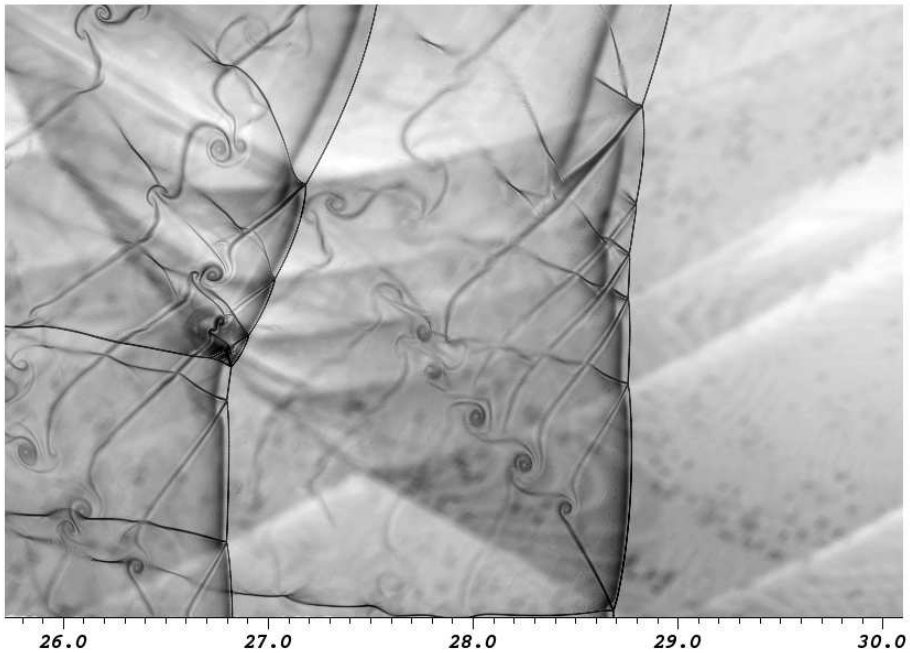

Triple point structures – $\varphi = 30^{\circ}$

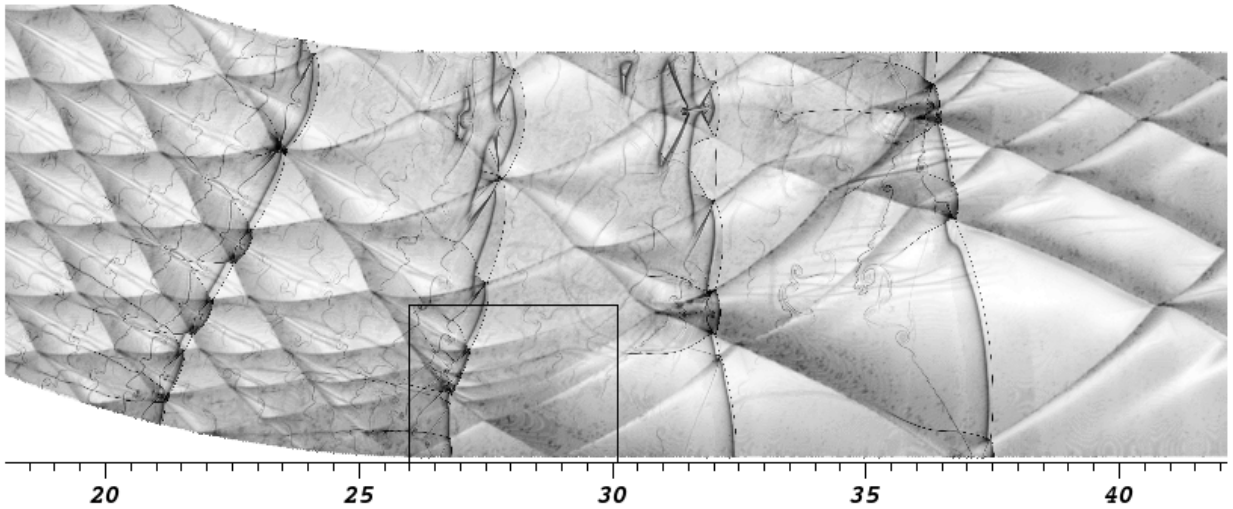

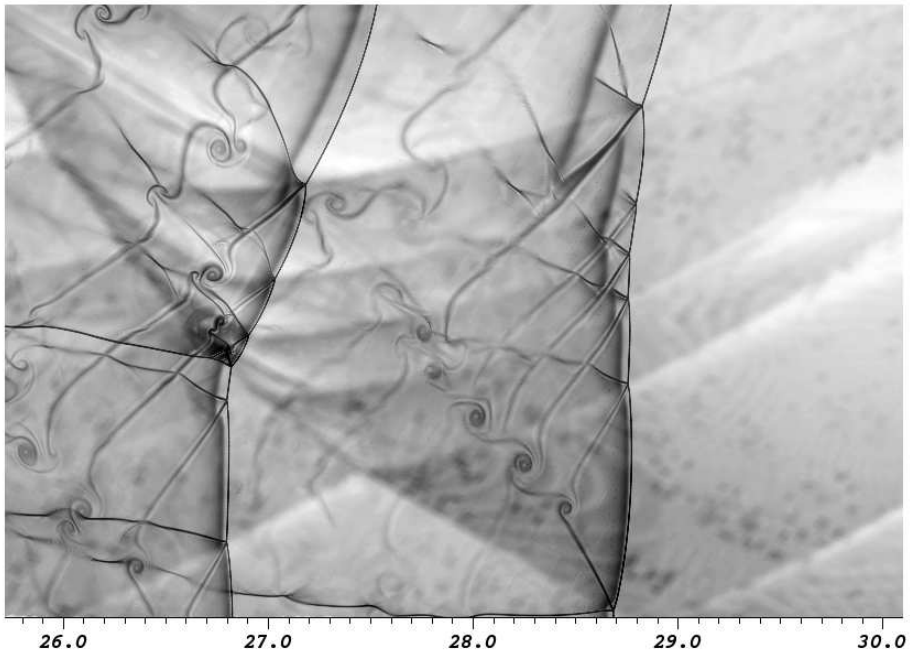

- Triple point quenching and failure as single Mach reflection

Detonation cell structure in 3D

- $44.8\,\mathrm{Pts}/l_{ig}$ for $\mathrm{H_2} : \mathrm{O_2} : \mathrm{Ar}$ CJ detonation
- SAMR base grid 400x24x24 for one quadrant, 2 additional refinement levels (2, 4)
- Simulation uses $\sim 18\,\mathrm{M}$ cells instead of $\sim 118\,\mathrm{M}$ (unigrid)
- $\sim 51,000\,\mathrm{h}$ CPU on 128 CPU Compaq Alpha. $\mathcal{H}$: 37.6 %, $\mathcal{S}$: 25.1 %

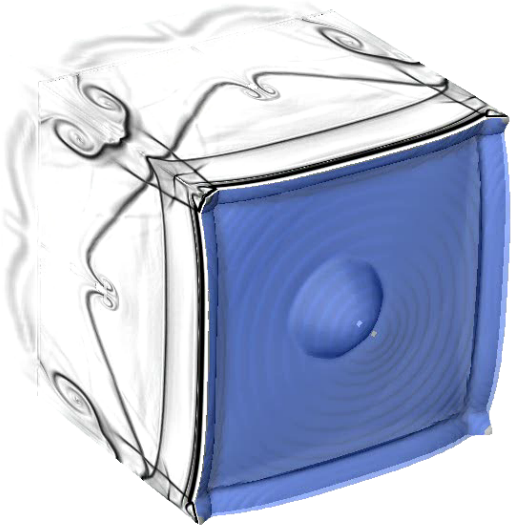

Schlieren plots of Y_{OH}

Detonation cell structure in 3D

- 44.8 Pts/l_{ig} for $\mathrm{H_2} : \mathrm{O_2} : \mathrm{Ar}$ CJ detonation
- SAMR base grid 400x24x24 for one quadrant, 2 additional refinement levels (2, 4)
- Simulation uses $\sim 18\,\mathrm{M}$ cells instead of $\sim 118\,\mathrm{M}$ (unigrid)
- $\sim 51,000\,\mathrm{h}$ CPU on 128 CPU Compaq Alpha. $\mathcal{H}$: 37.6 %, $\mathcal{S}$: 25.1 %

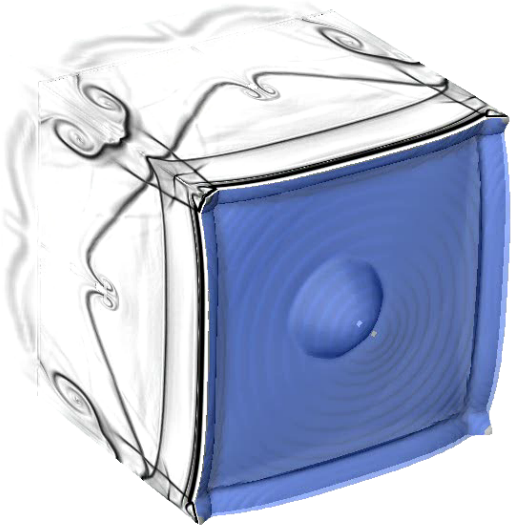

Schlieren plots of Y_{OH}

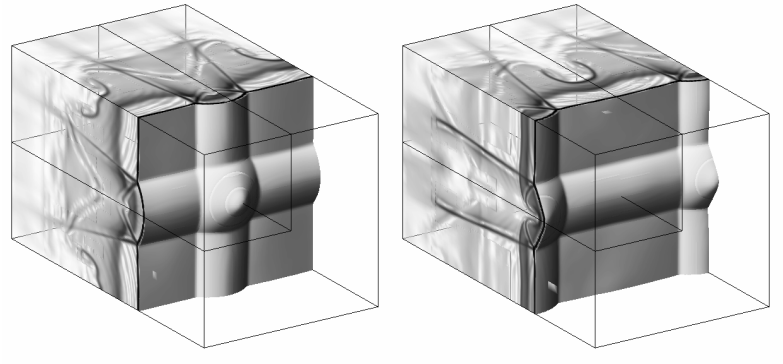

Schlieren plots of density, mirrored for visualization

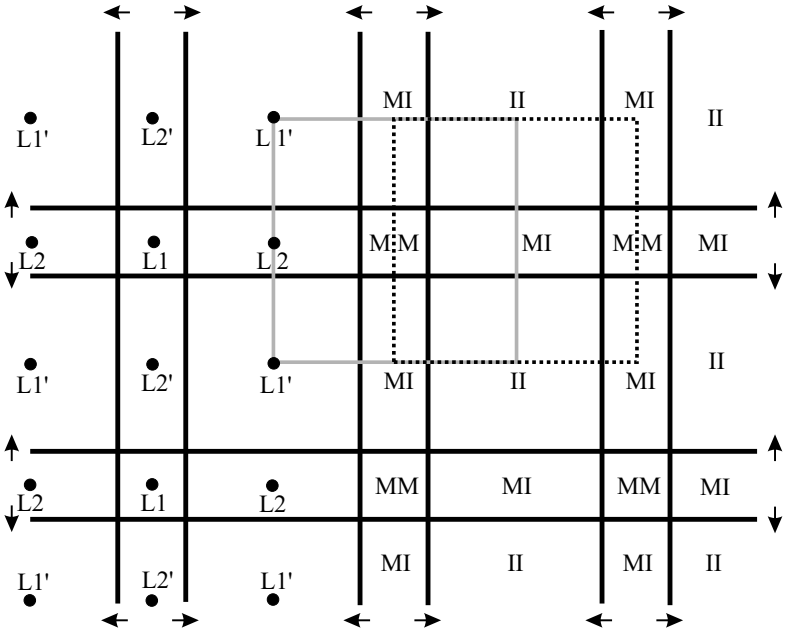

Schematic front view of the periodic triple point line structure right plot at the same time.

Temporal Development of Detonation Velocity

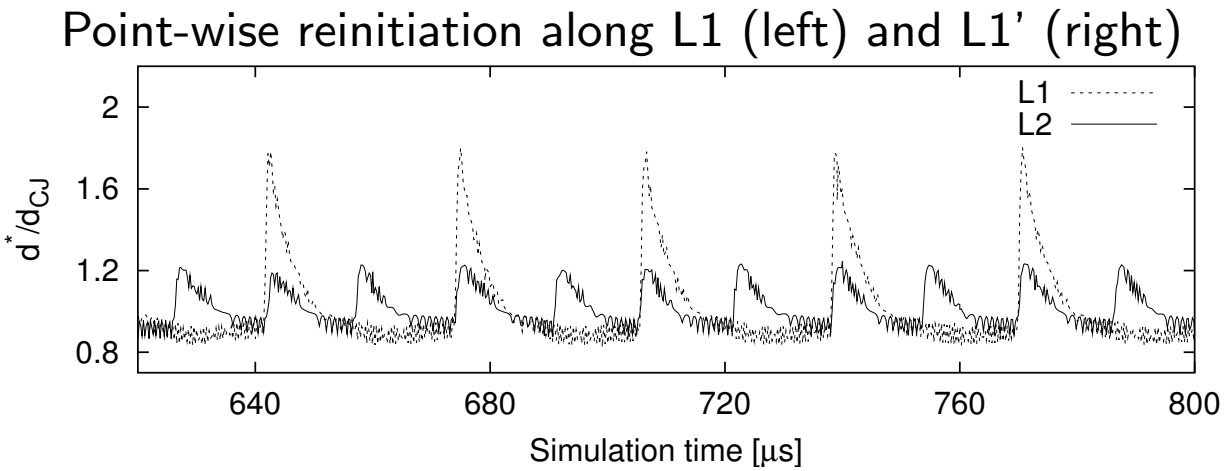

Temporal Development of Detonation Velocity

Point-wise reinitiation along L1 (left) and L1' (right)

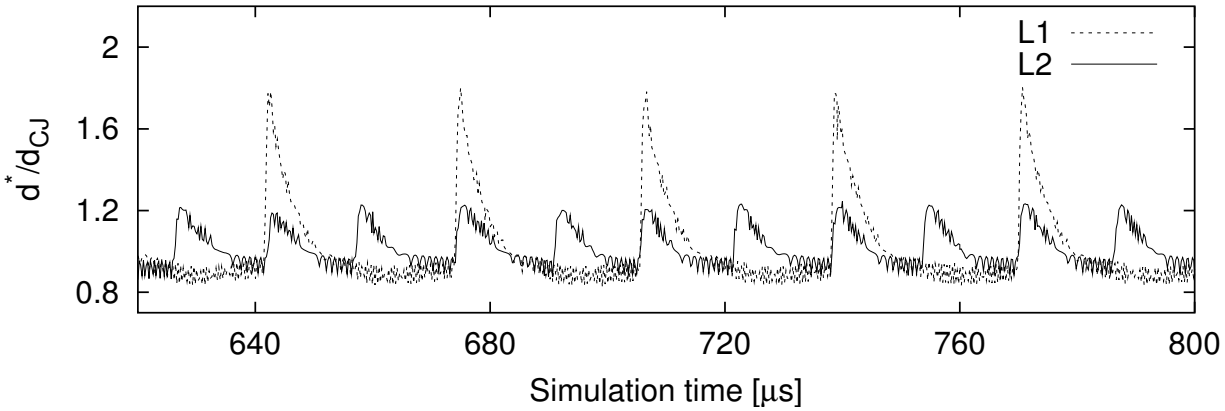

Comparison with 2D Simulation

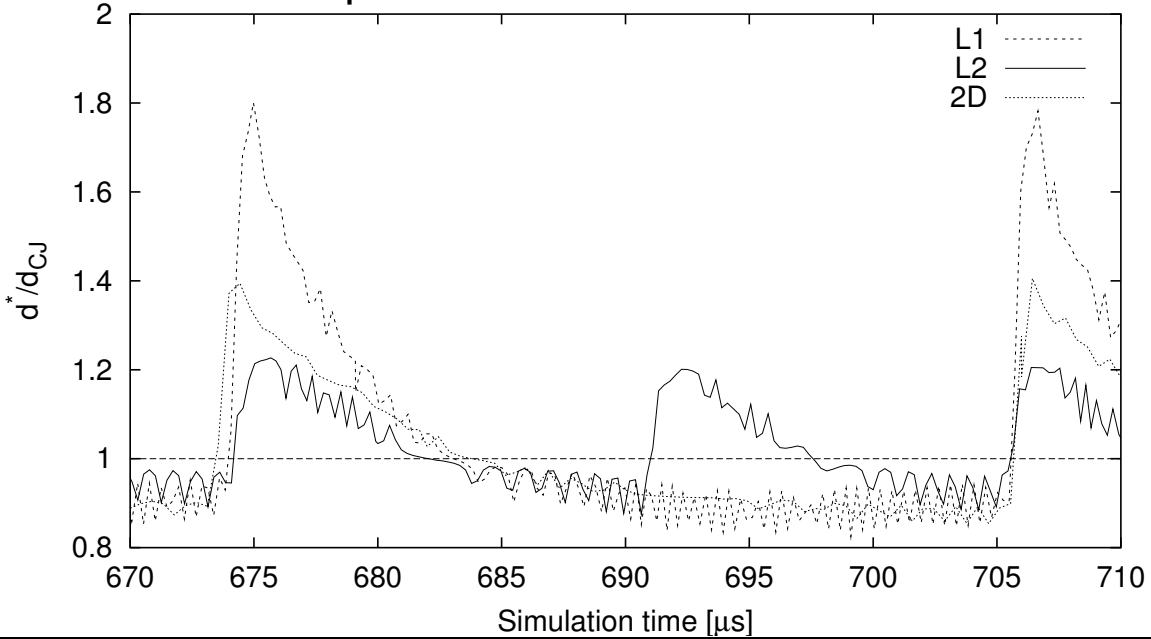

Triple point analysis

Tracks of triple point lines

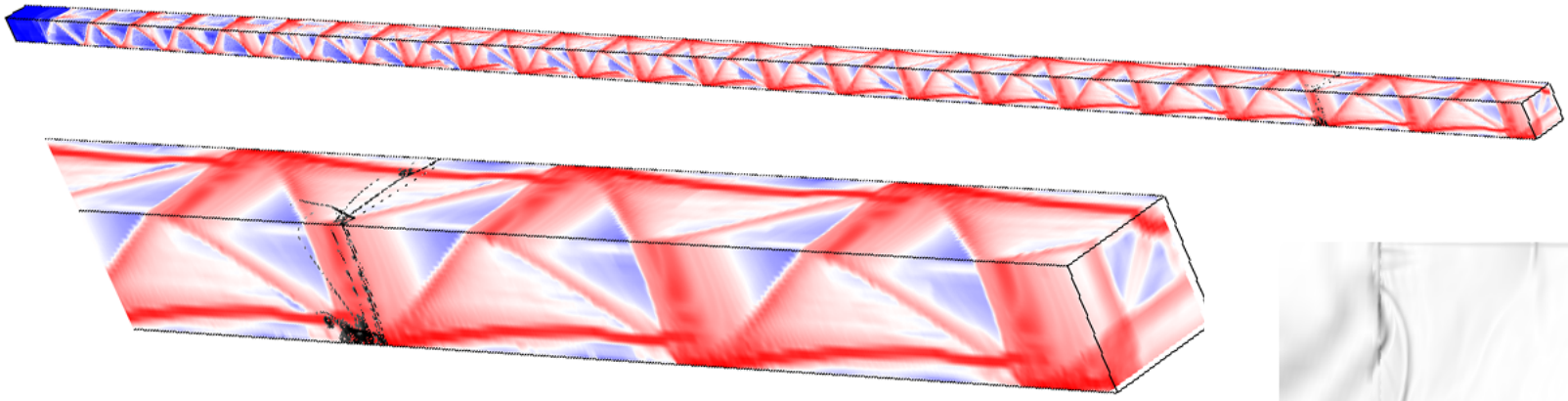

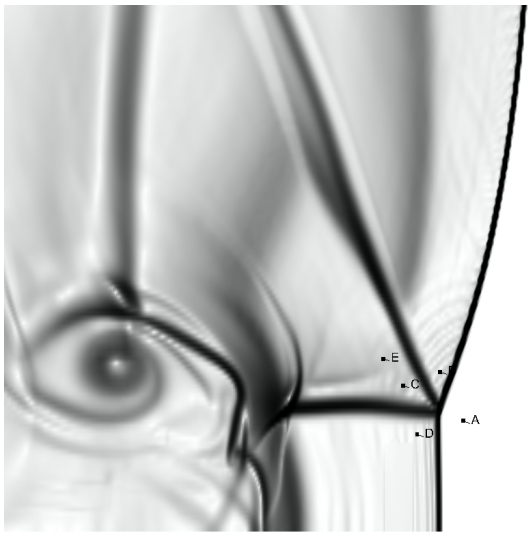

Weakest TMR structure in Incident-Incident region immediately before collision

Schlieren plots perpendicular to y- and z-plane (right) and on triple point line tracks (below)

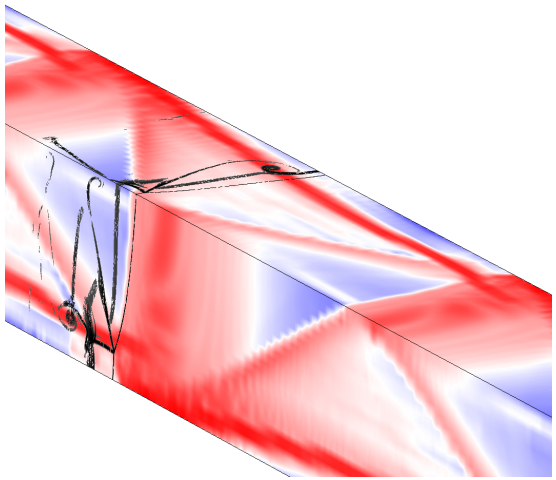

Triple point analysis

Tracks of triple point lines

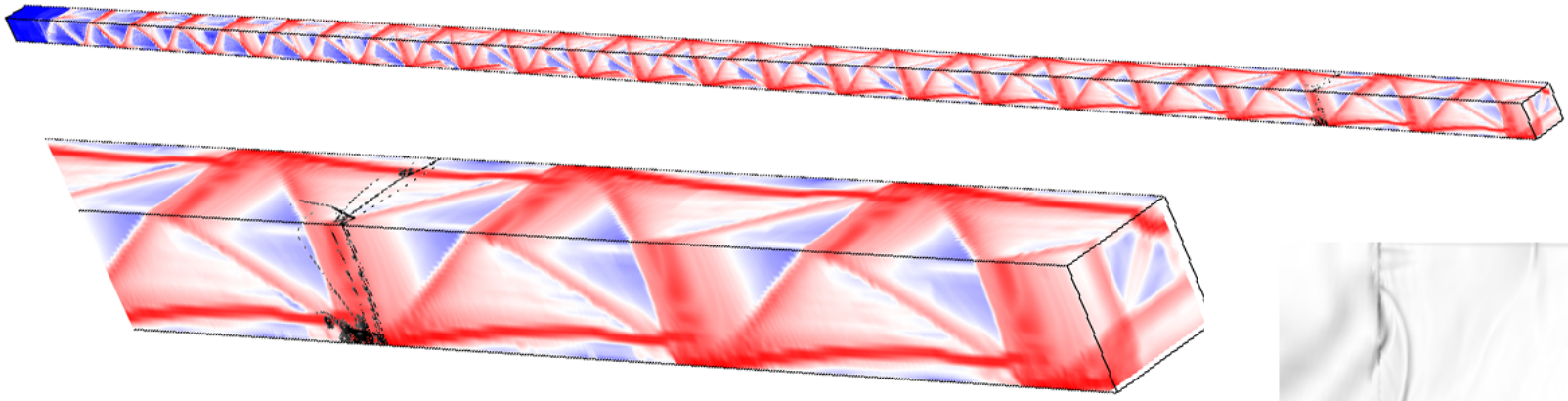

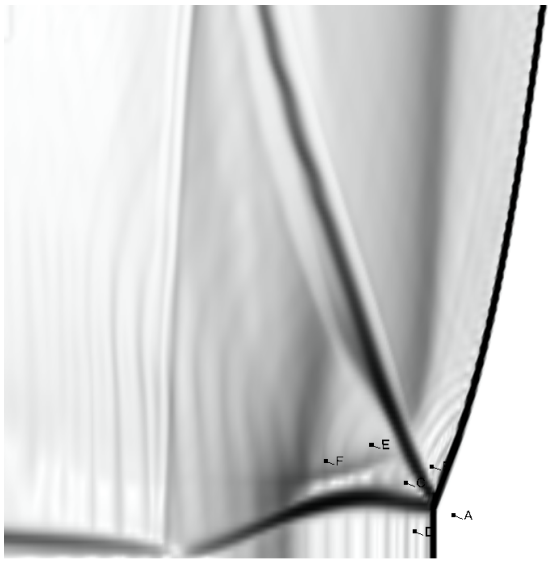

TMR structure in Mach-Incident region immediately before collision

Schlieren plots perpendicular to y- and z-plane (right) and on triple point line tracks (below)

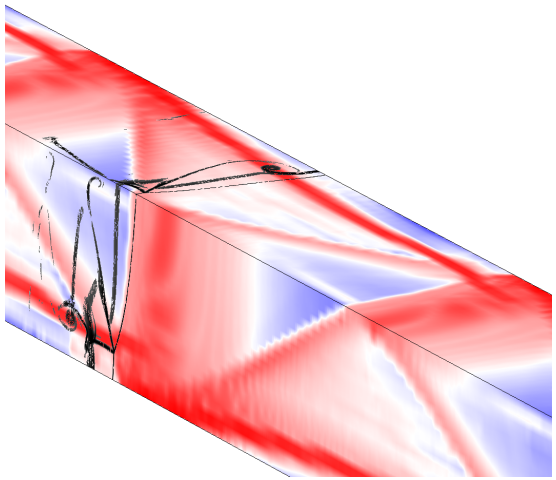

Triple point analysis

Tracks of triple point lines

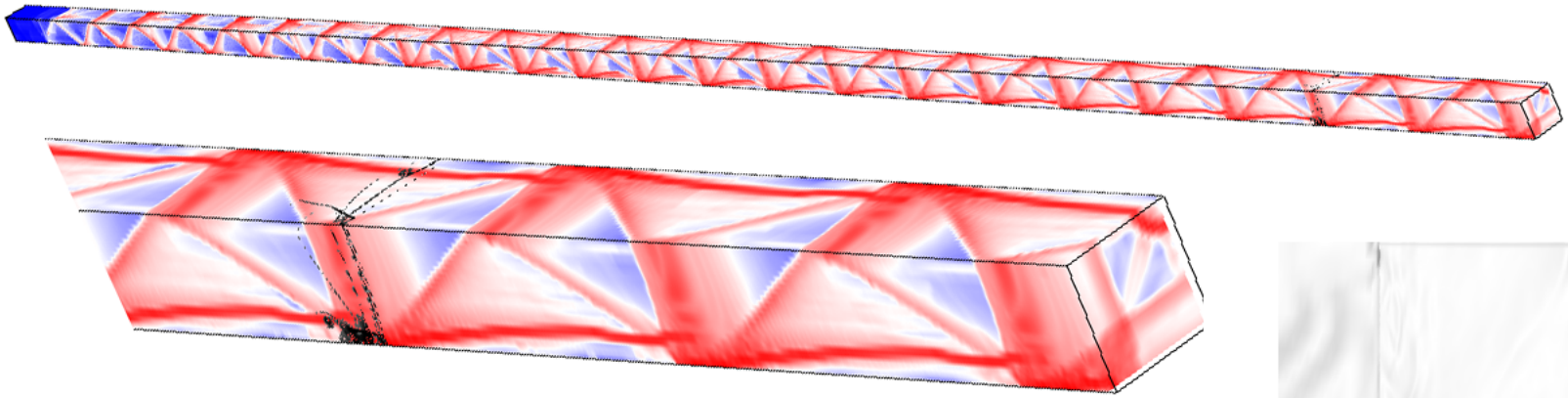

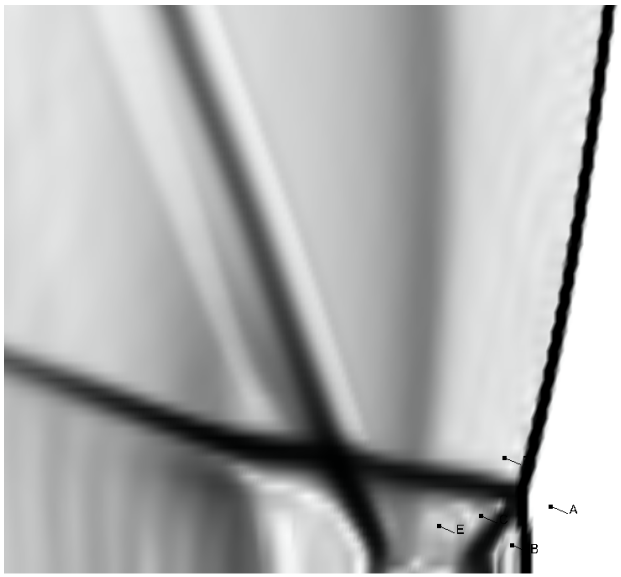

DMR structure in Mach-Incident region after re-initation

Schlieren plots perpendicular to y- and z-plane (right) and on triple point line tracks (below)

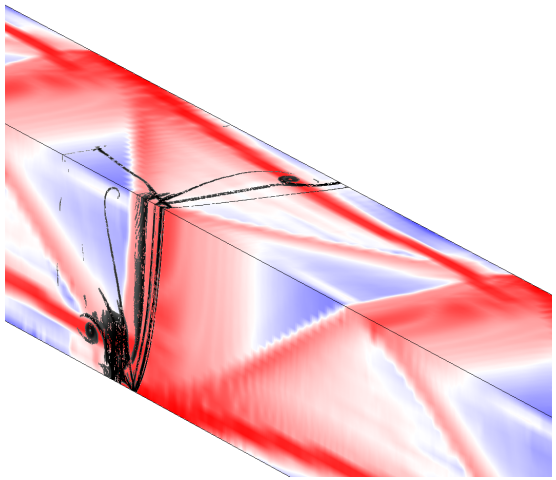

Triple point analysis

Tracks of triple point lines

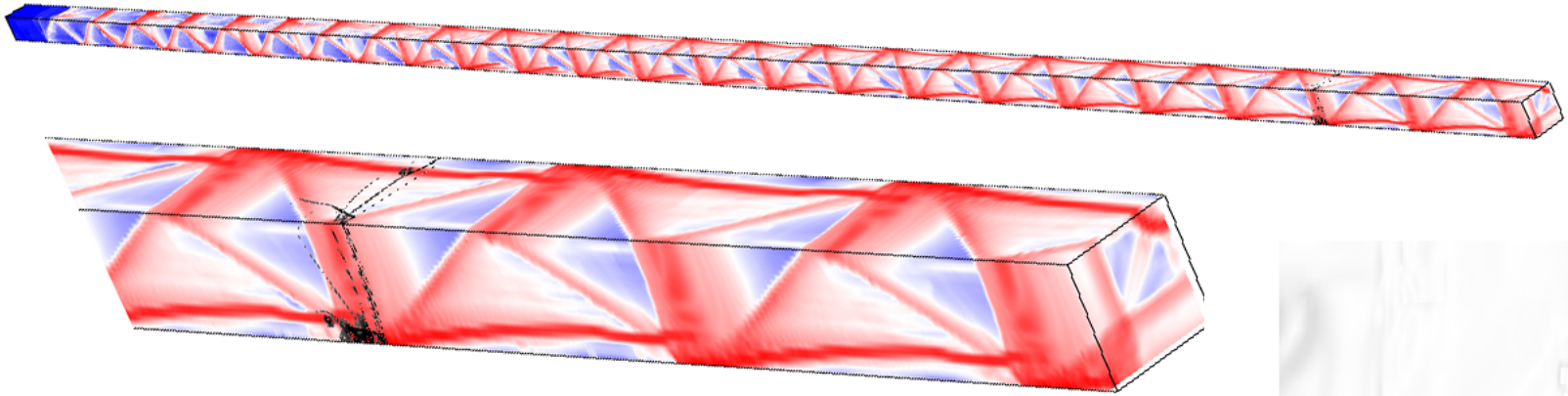

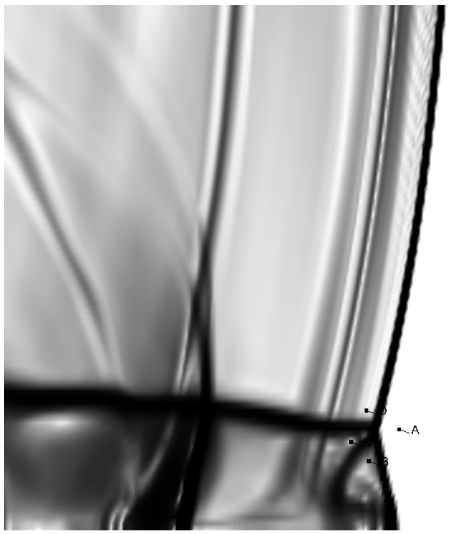

Strongest DMR structure in Mach-Mach region after re-initation

Schlieren plots perpendicular to y- and z-plane (right) and on triple point line tracks (below)

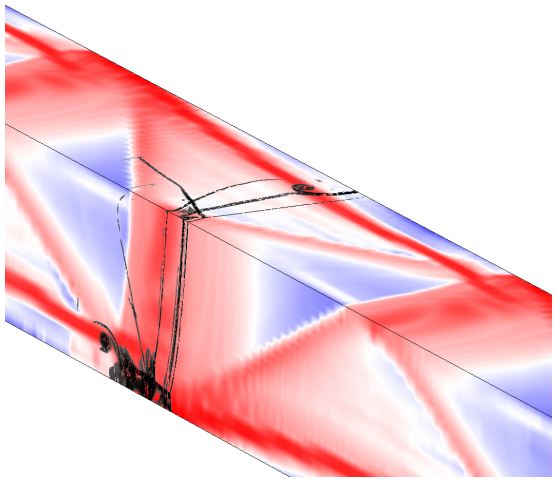

Detonation ignition by a hot jet in 3d

- 3d Euler simulation on AMR base mesh of $64 \times 32 \times 16$ cells
- Domain size $3.2\,\mathrm{cm} \times 1.6\,\mathrm{cm} \times 0.8\,\mathrm{cm}$
- Inflow of $\mathrm{H_2} : \mathrm{O_2} : \mathrm{Ar}$ mixture (molar ratios 2:1:7) at $10\,\mathrm{kPa}$ and $T = 298\,\mathrm{K}$ at CJ velocity $V_{\mathrm{CJ}} = 1627\,\mathrm{m/s}$
- Hot jet inflow with fully reacted CJ conditions, i.e., $T = 3296\,\mathrm{K}$, $p = 172.7\,\mathrm{kPa}$ and $\rho = 0.0893\,\mathrm{kg/m^3}$
- Mechanism by [Westbrook, 1982]: 34 forward reactions, 9 species
- Computations on 1024 cores Intel E5-2692 2.20 GHz (Tianhe-2)
- X. Cai, J. Liang, RD, Y. Che, Z. Lin, *Int. J. Hydrogen Energy* 41(4): 3222–3239, 2016

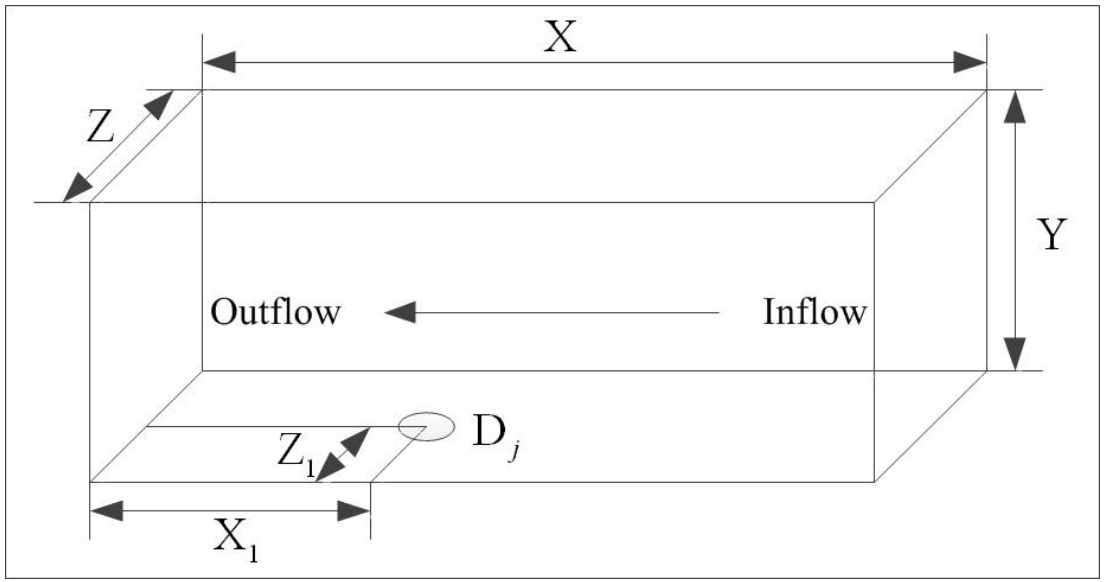

Detonation ignition process - Front view

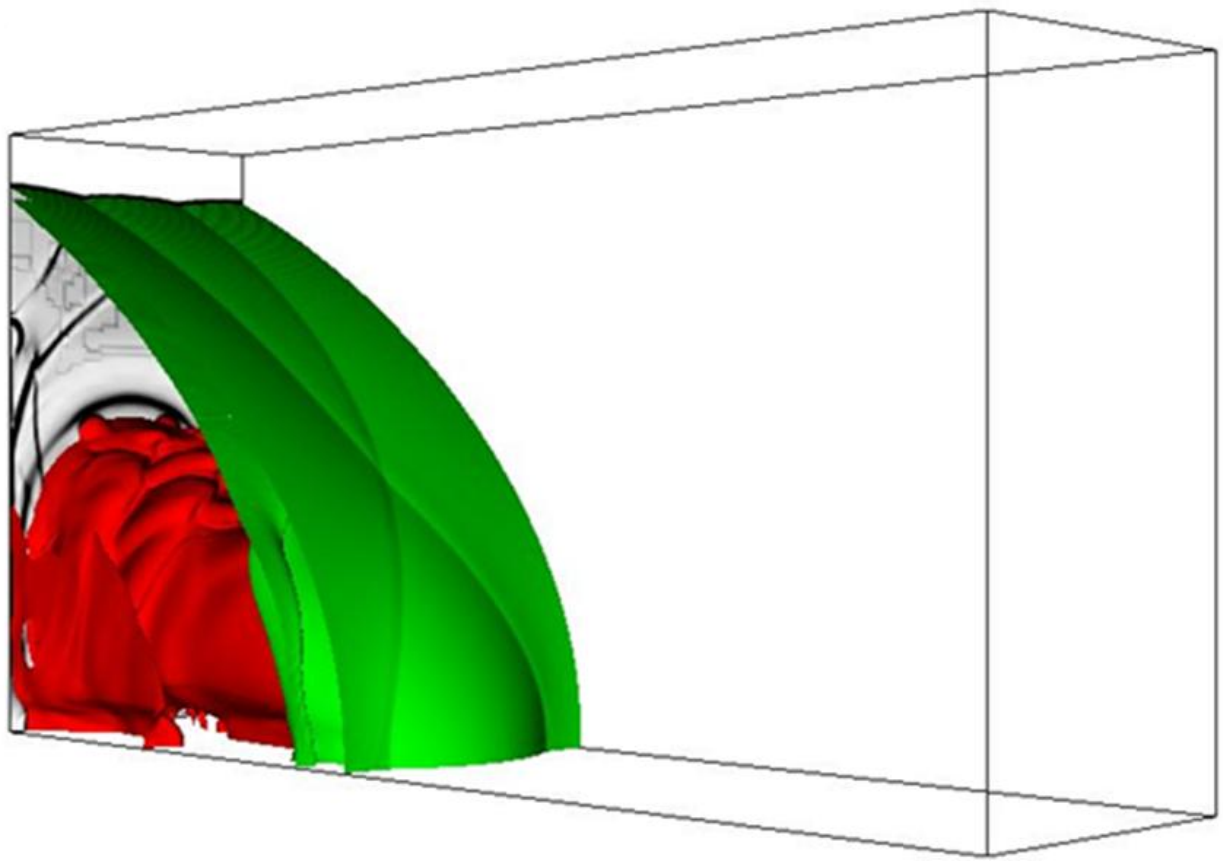

Isosurfaces of ρ at $t = 18.85\,\mu\mathrm{s}$

Detonation ignition process - Front view

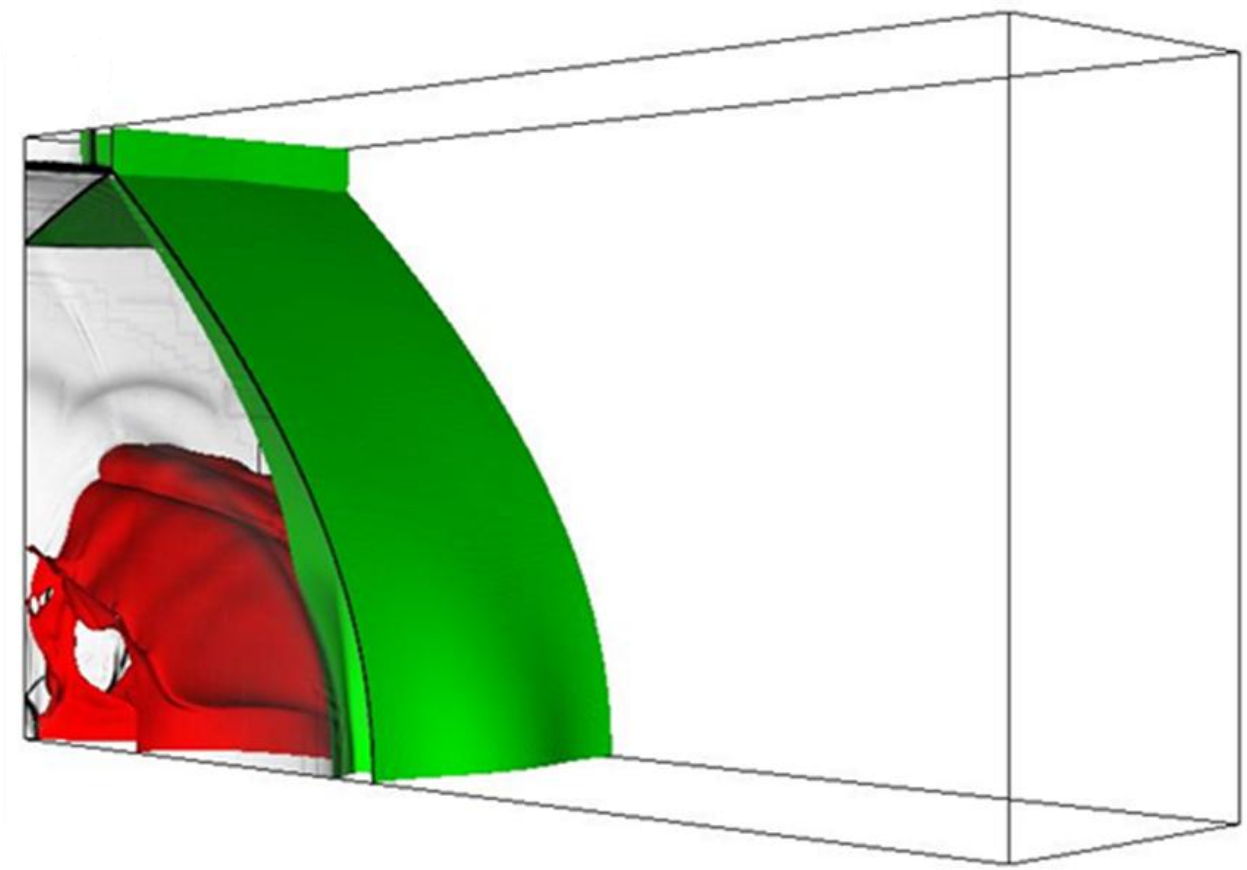

Isosurfaces of ρ at $t = 224.34\,\mu\mathrm{s}$

Detonation ignition process - Front view

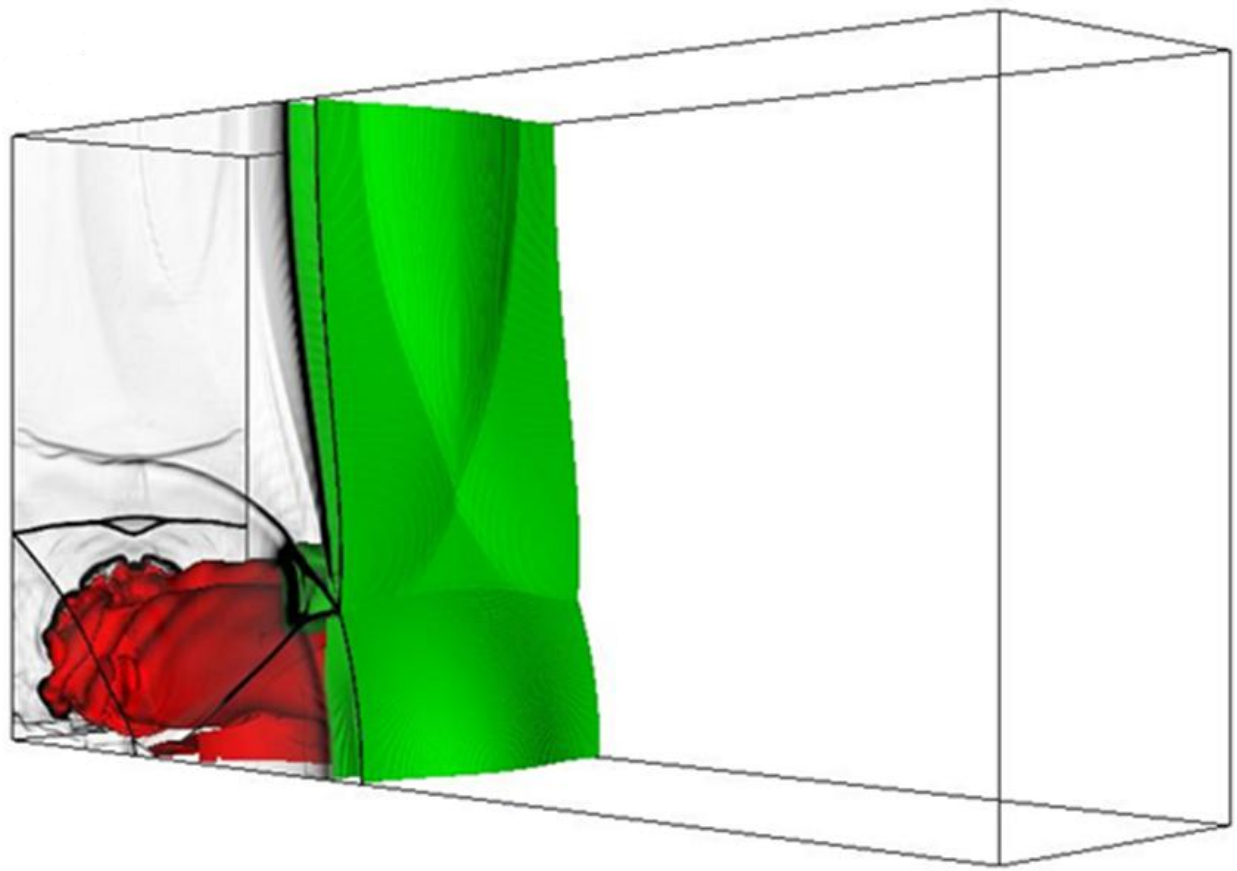

Isosurfaces of ρ at $t = 323.07\,\mu\mathrm{s}$

Detonation ignition process - Front view

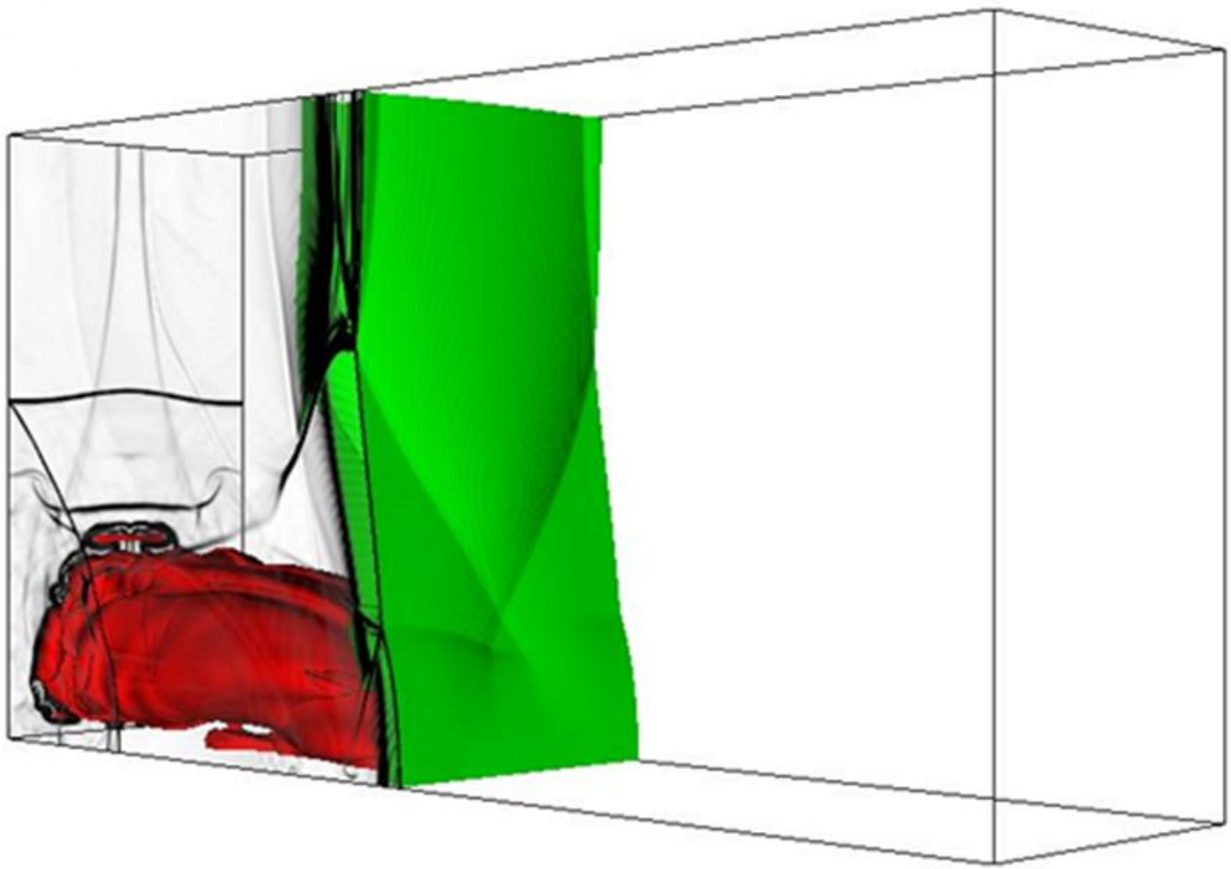

Isosurfaces of ρ at $t = 334.10\,\mu\mathrm{s}$

Detonation propagation

Detonation propagation

Detonation propagation

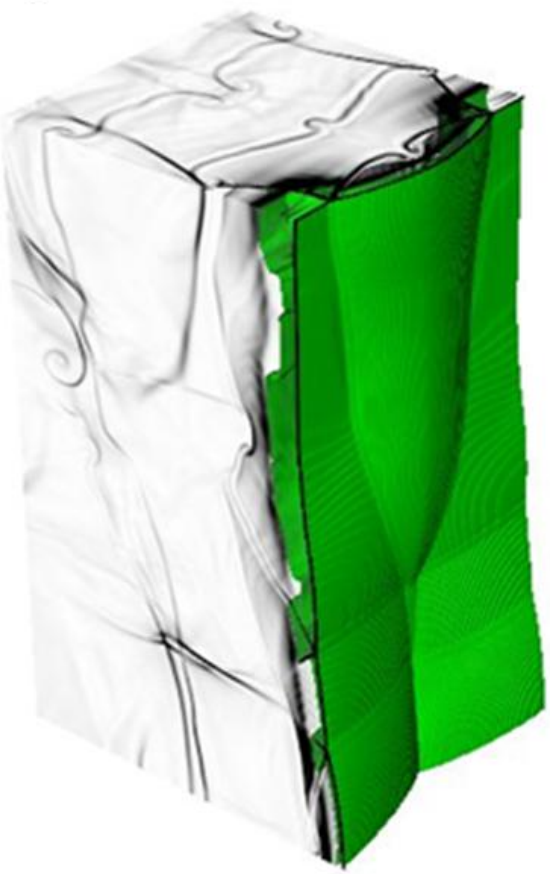

- Continuous jet injection overdrives the detonation to $f \approx 1.07$

Detonation propagation

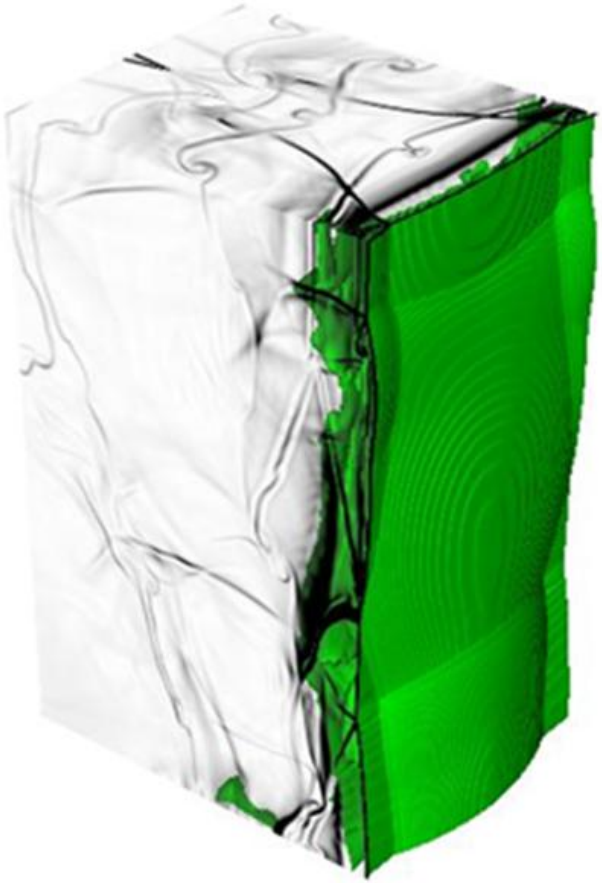

- Continuous jet injection overdrives the detonation to $f \approx 1.07$

Detonation propagation

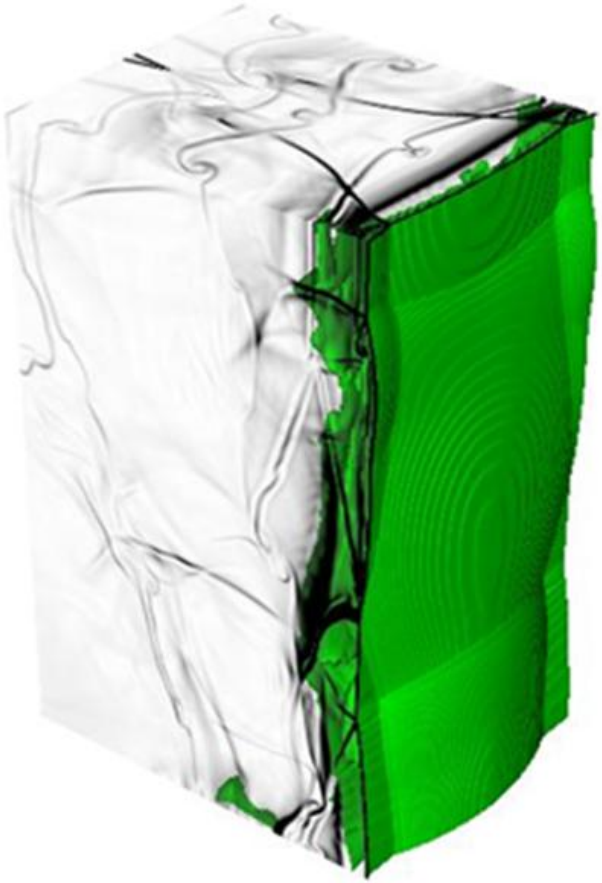

- Continuous jet injection overdrives the detonation to $f \approx 1.07$
- Number of triple point lines is increased compared to CJ case
- Rectangular domain straightens triple point lines

Detonation propagation

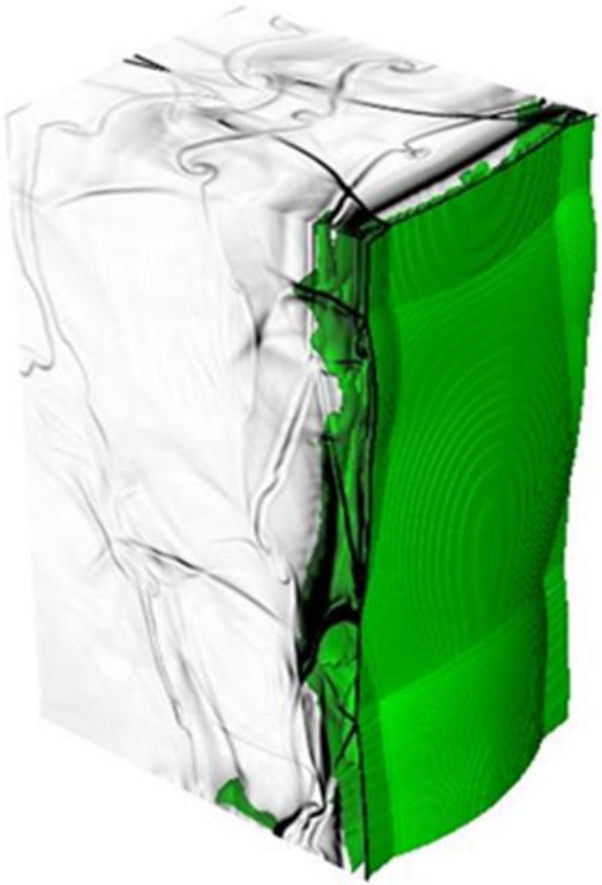

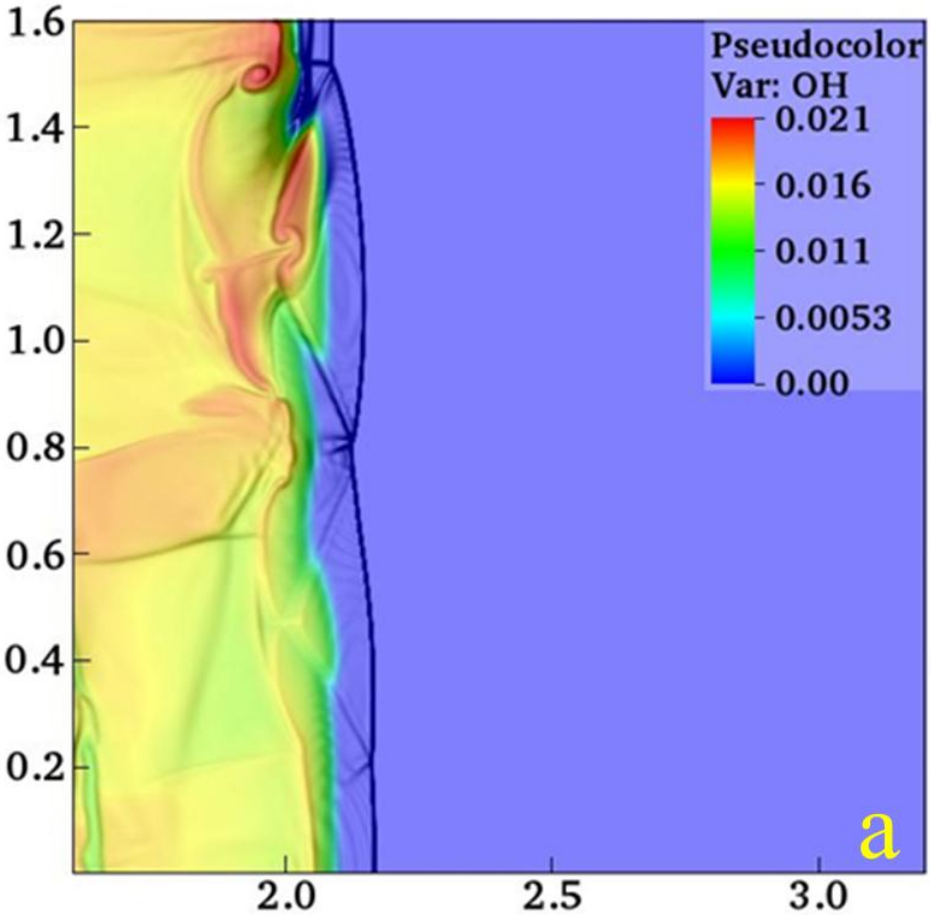

- Continuous jet injection overdrives the detonation to $f \approx 1.07$
- Number of triple point lines is increased compared to CJ case
- Rectangular domain straightens triple point lines

Detonation propagation

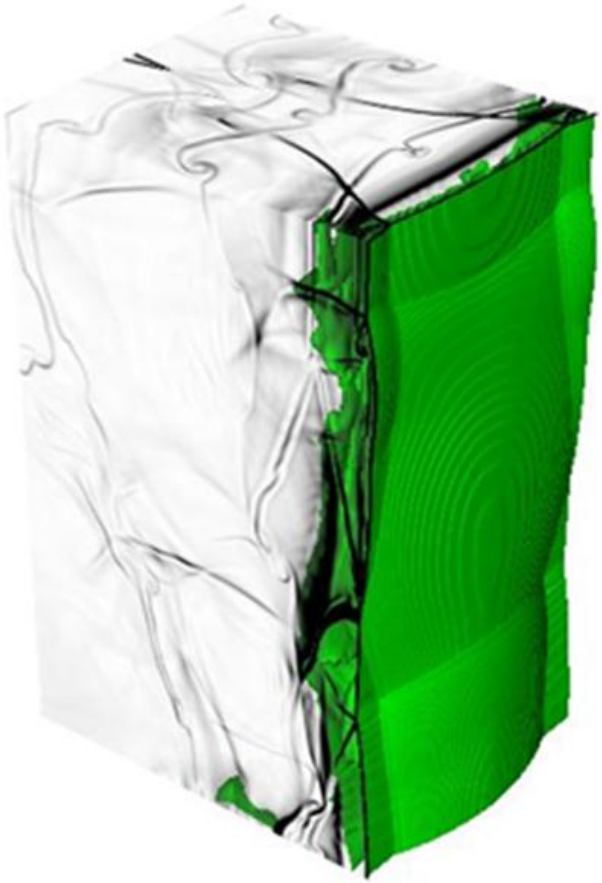

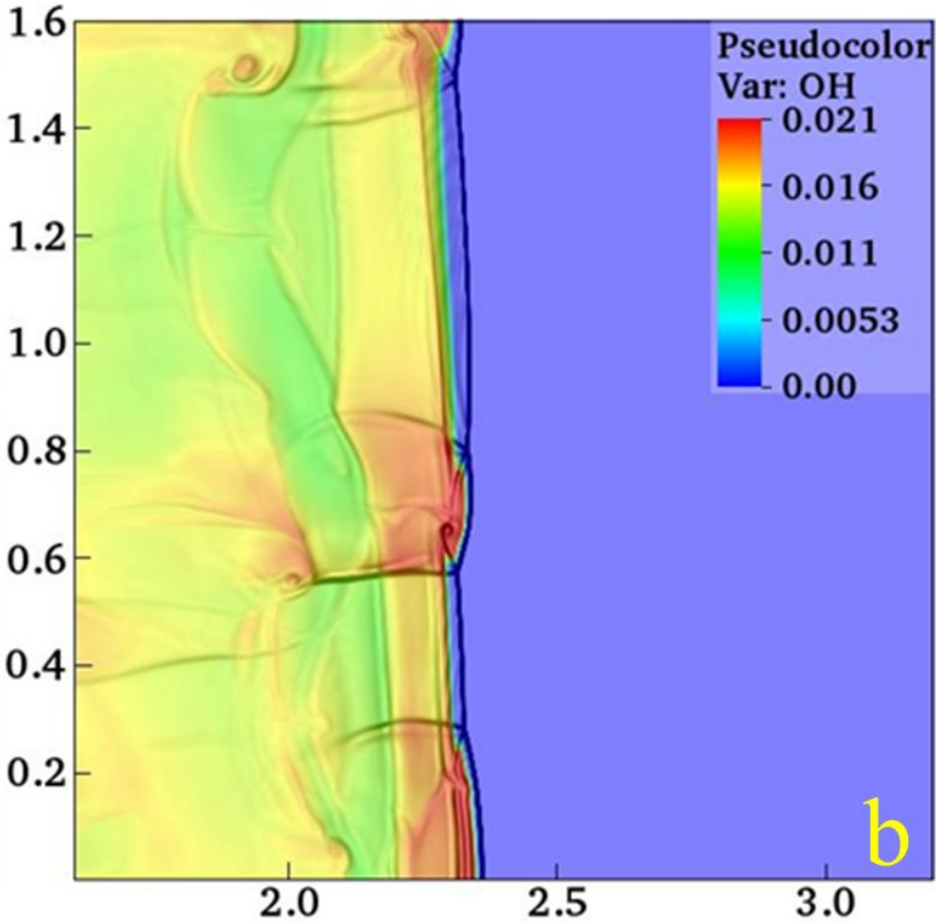

- Continuous jet injection overdrives the detonation to $f \approx 1.07$
- Number of triple point lines is increased compared to CJ case
- Rectangular domain straightens triple point lines

Detonation propagation

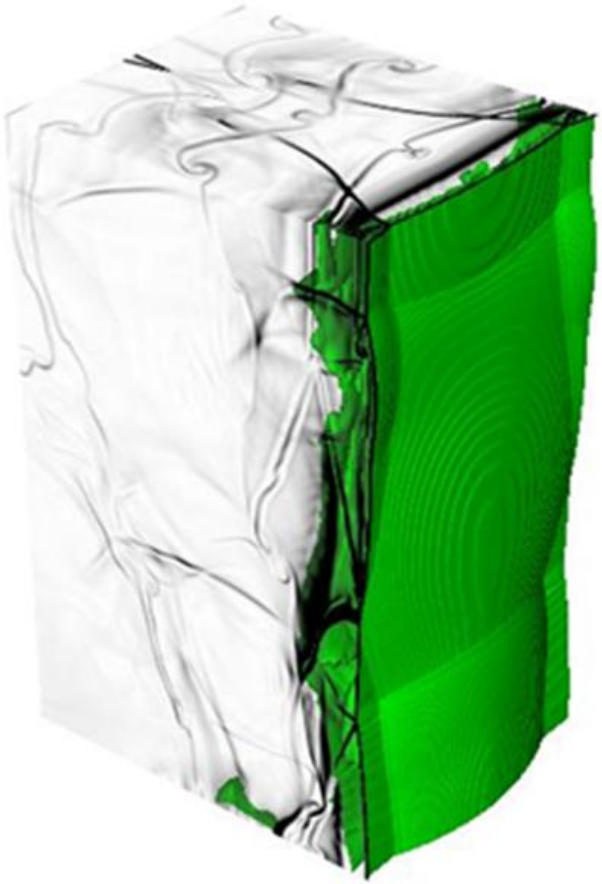

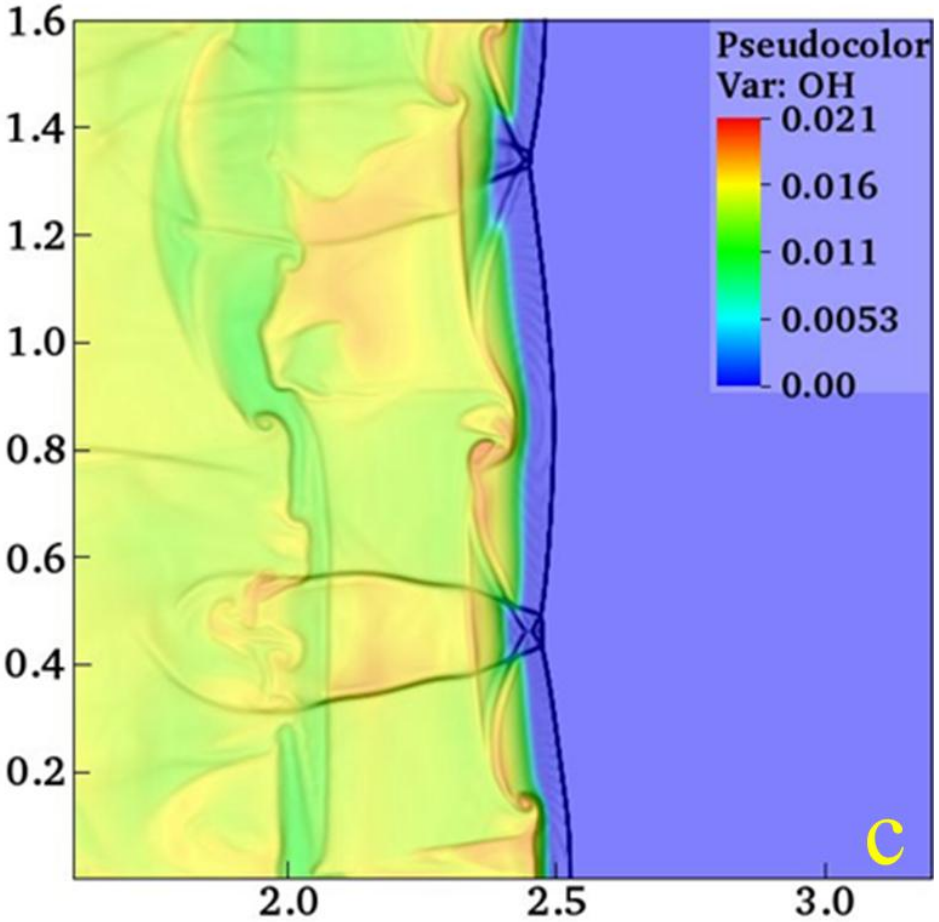

- Continuous jet injection overdrives the detonation to $f \approx 1.07$
- Number of triple point lines is increased compared to CJ case
- Rectangular domain straightens triple point lines
- Primarily TMR triple point line structures visible as in previous case

Detonation propagation

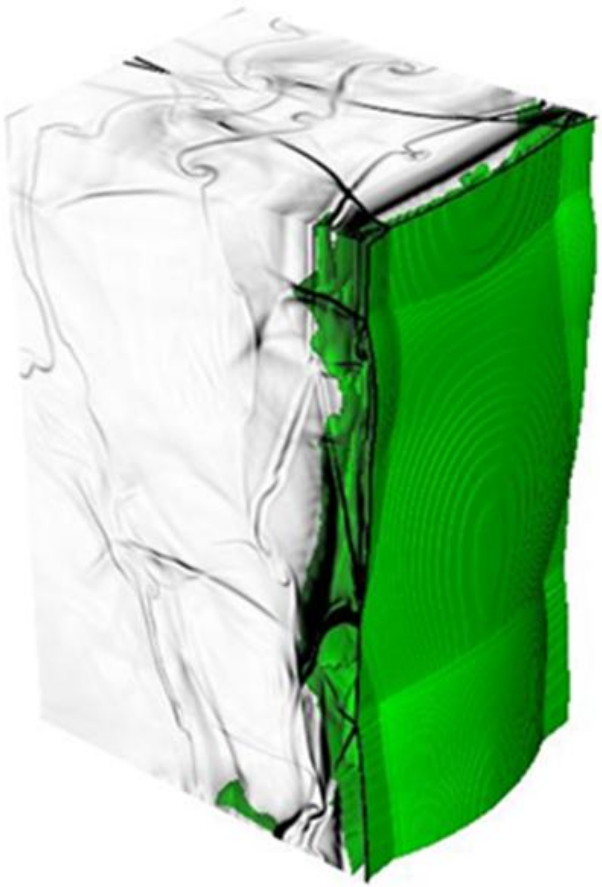

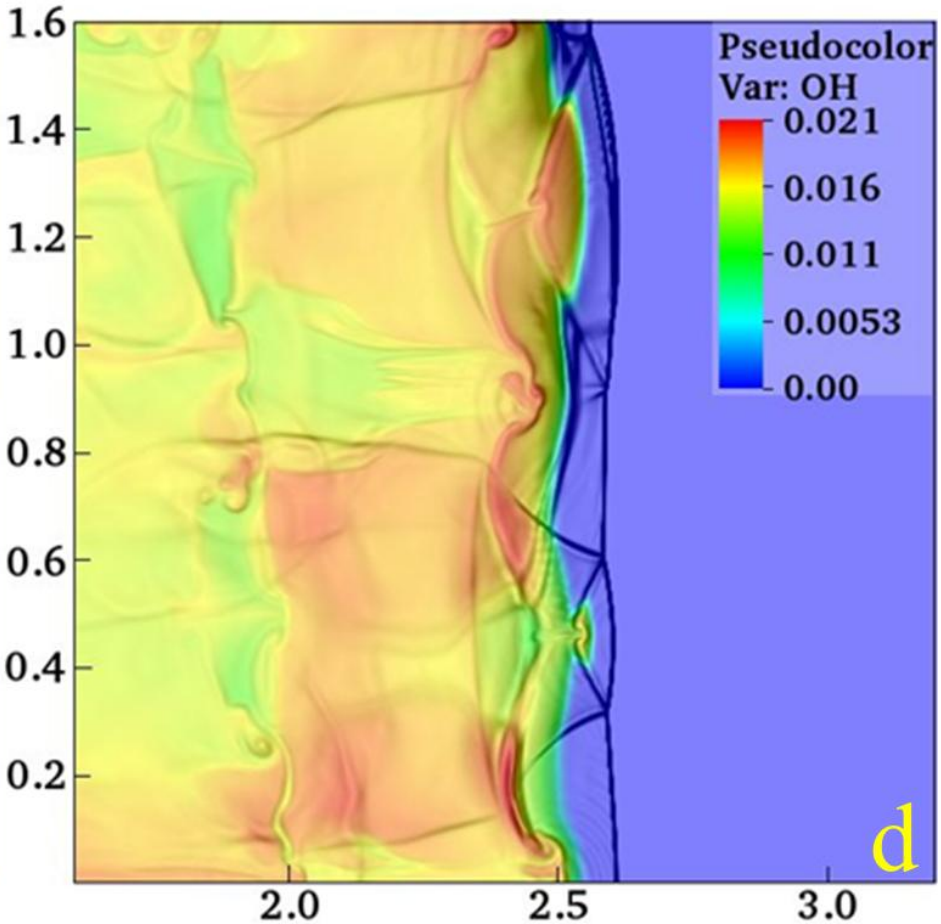

- Continuous jet injection overdrives the detonation to $f \approx 1.07$
- Number of triple point lines is increased compared to CJ case
- Rectangular domain straightens triple point lines
- Primarily TMR triple point line structures visible as in previous case

Dynamic mesh refinement

- Mesh adaptation with 4 additional levels refined by factors 2, 2, 2, 2 $\longrightarrow$ $\sim 30.85\,\mathrm{Pts}/l_{ig}$
- Adaptation indicators similar as before

$$t = 234.10\,\mu\mathrm{s}$$

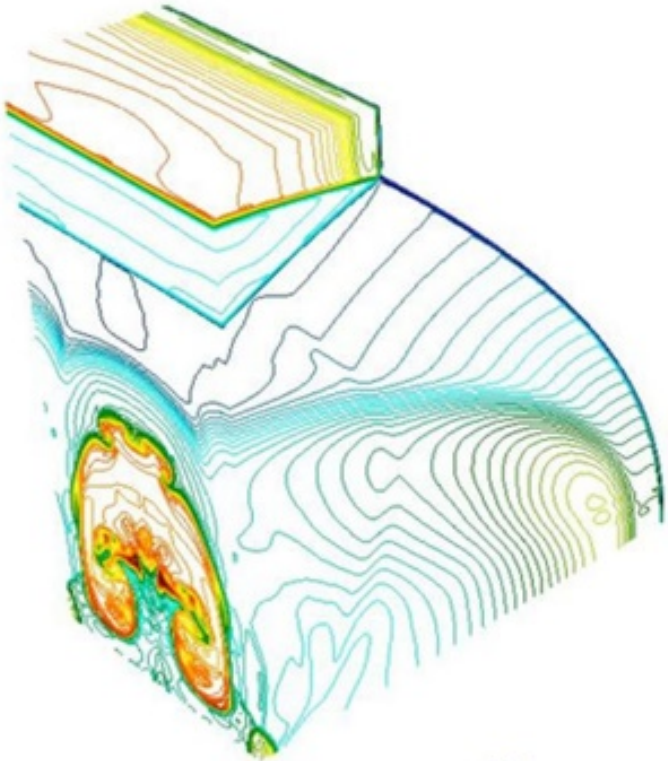

Contours of temperature

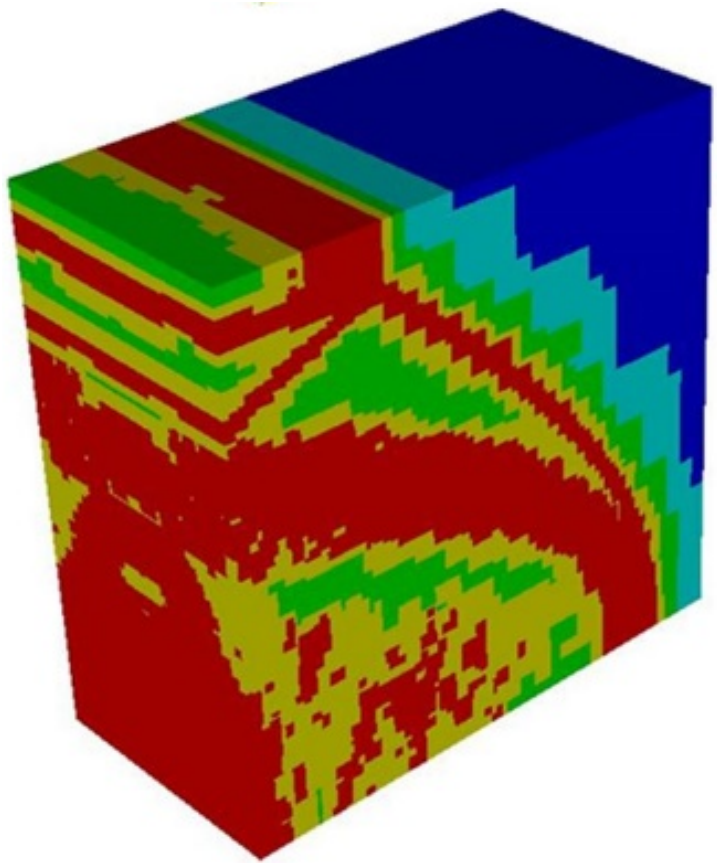

Refinement levels

Dynamic mesh refinement

- Mesh adaptation with 4 additional levels refined by factors 2, 2, 2, 2 $\longrightarrow$ $\sim 30.85\,\mathrm{Pts}/l_{ig}$
- Adaptation indicators similar as before

$$t = 253.32\,\mu\mathrm{s}$$

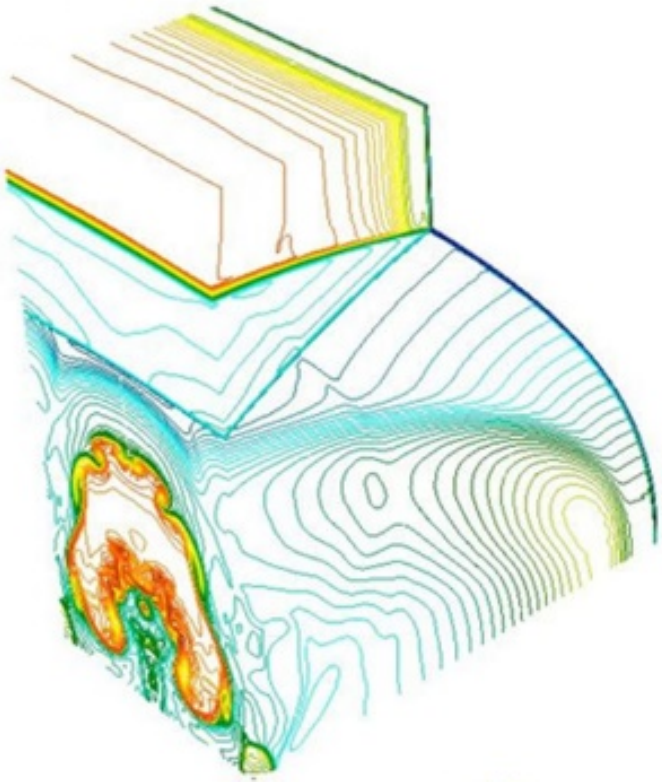

Contours of temperature

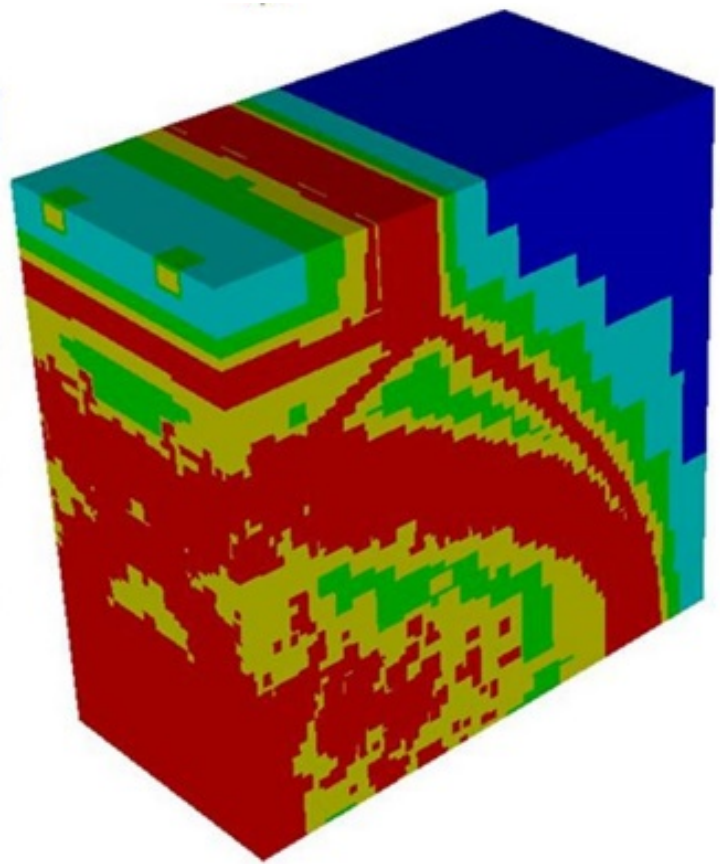

Refinement levels

Dynamic mesh refinement

- Mesh adaptation with 4 additional levels refined by factors 2, 2, 2, 2 $\longrightarrow$ $\sim 30.85\,\mathrm{Pts}/l_{ig}$
- Adaptation indicators similar as before

$$t = 272.78\,\mu\mathrm{s}$$

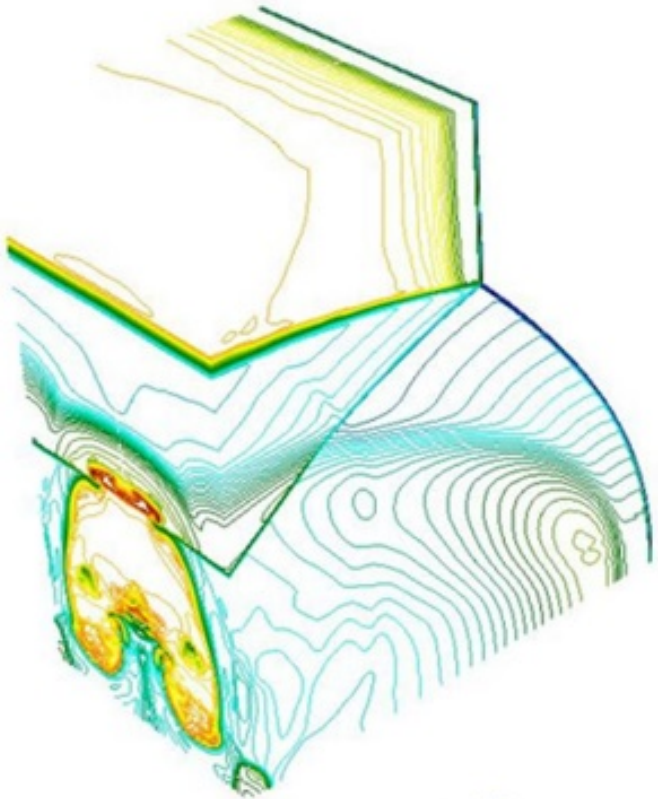

Contours of temperature

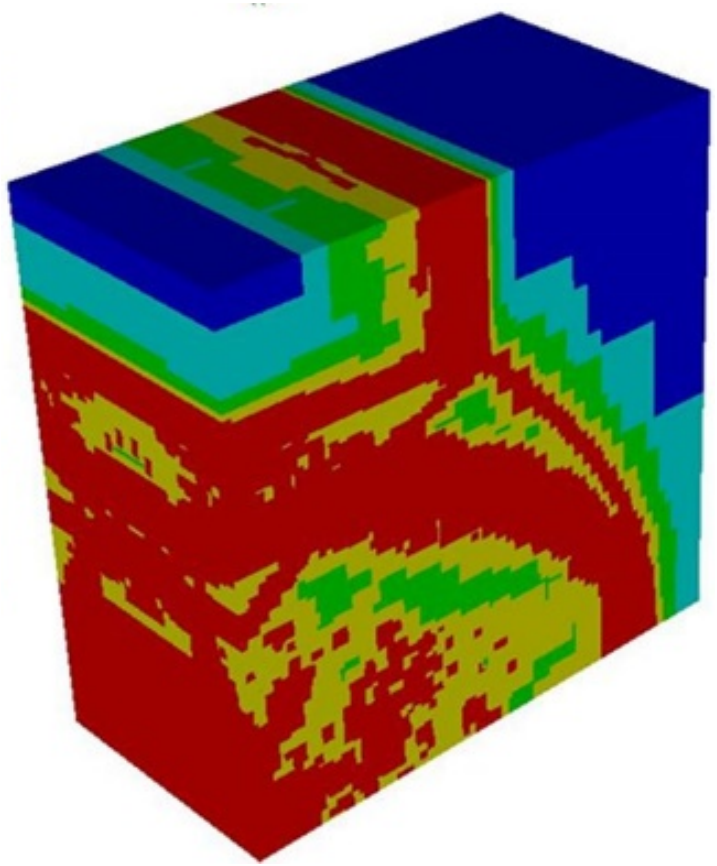

Refinement levels

Dynamic mesh refinement

- Mesh adaptation with 4 additional levels refined by factors 2, 2, 2, 2 $\longrightarrow$ $\sim 30.85\,\mathrm{Pts}/l_{ig}$
- Adaptation indicators similar as before

$$t = 292.46\,\mu\mathrm{s}$$

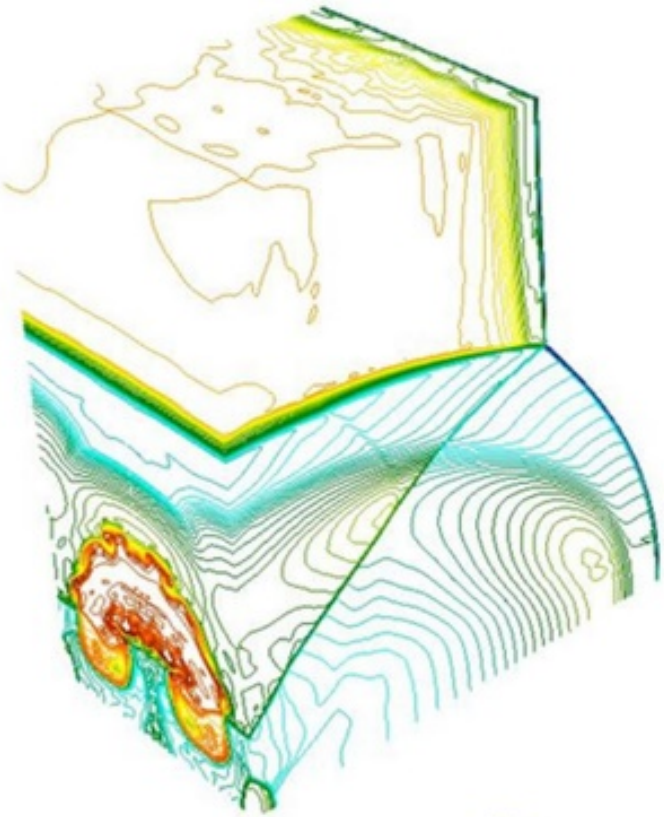

Contours of temperature

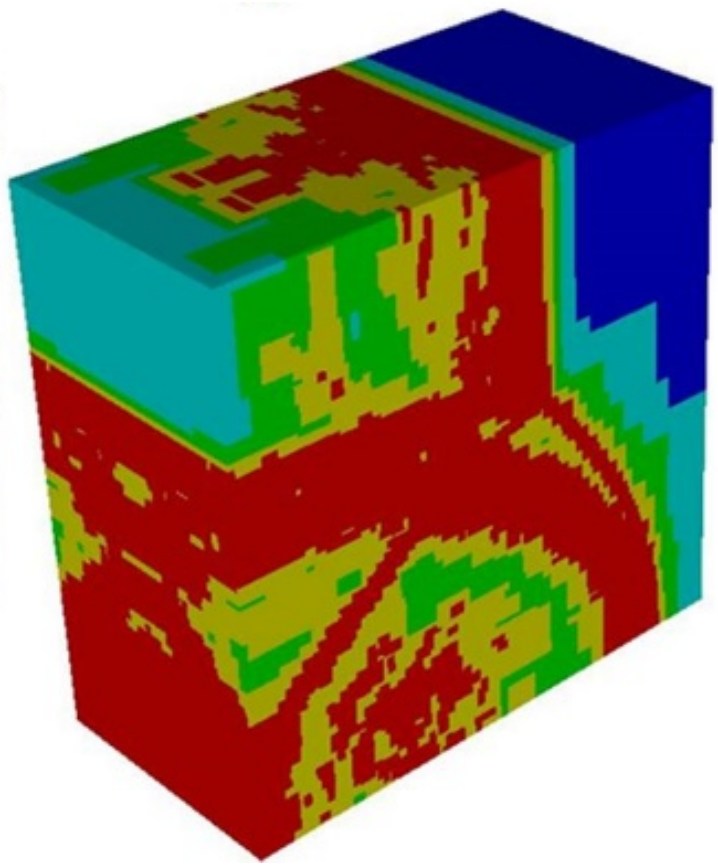

Refinement levels

Shock-boundary layer interaction

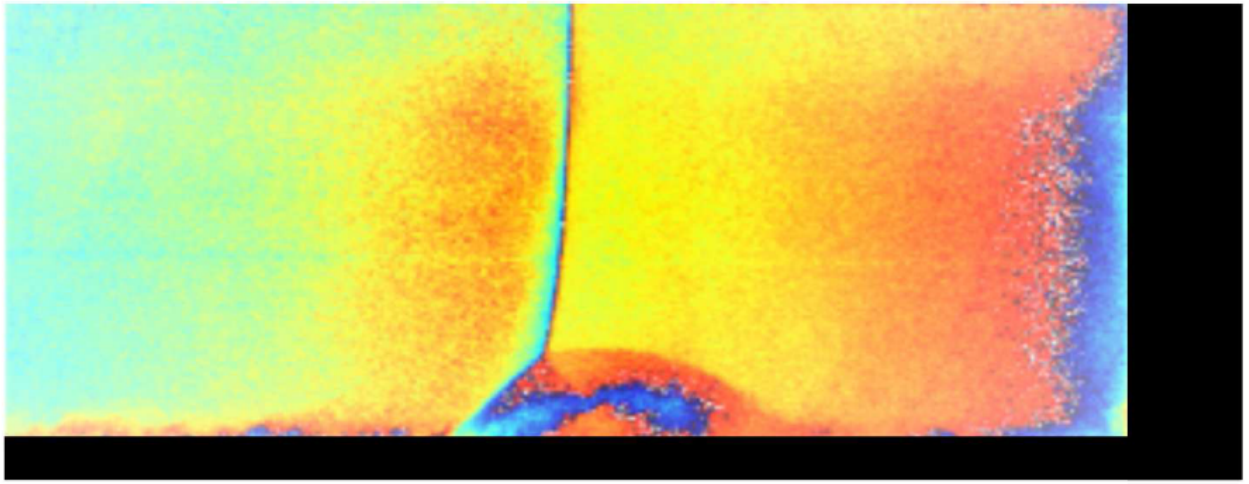

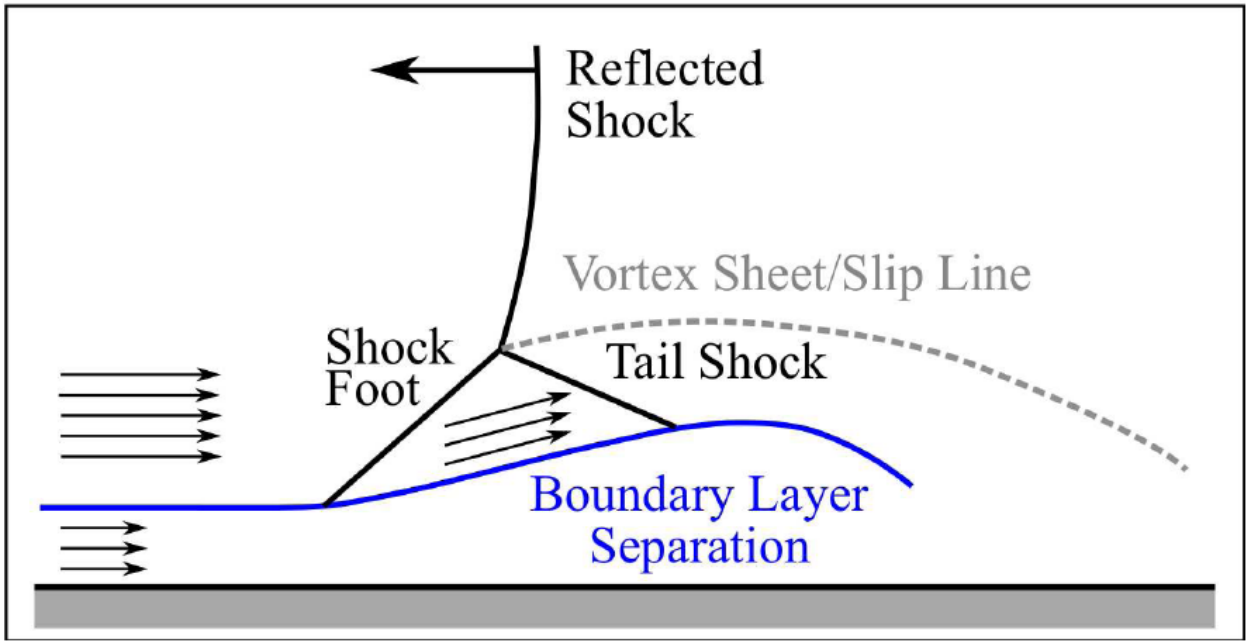

Non-reactive case

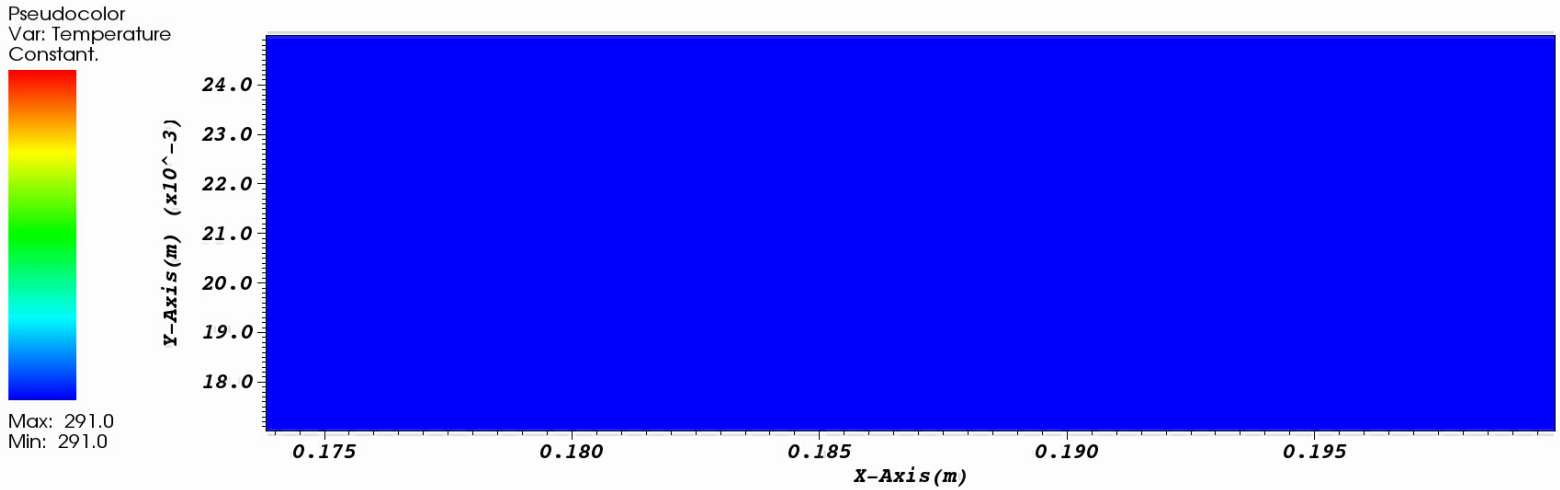

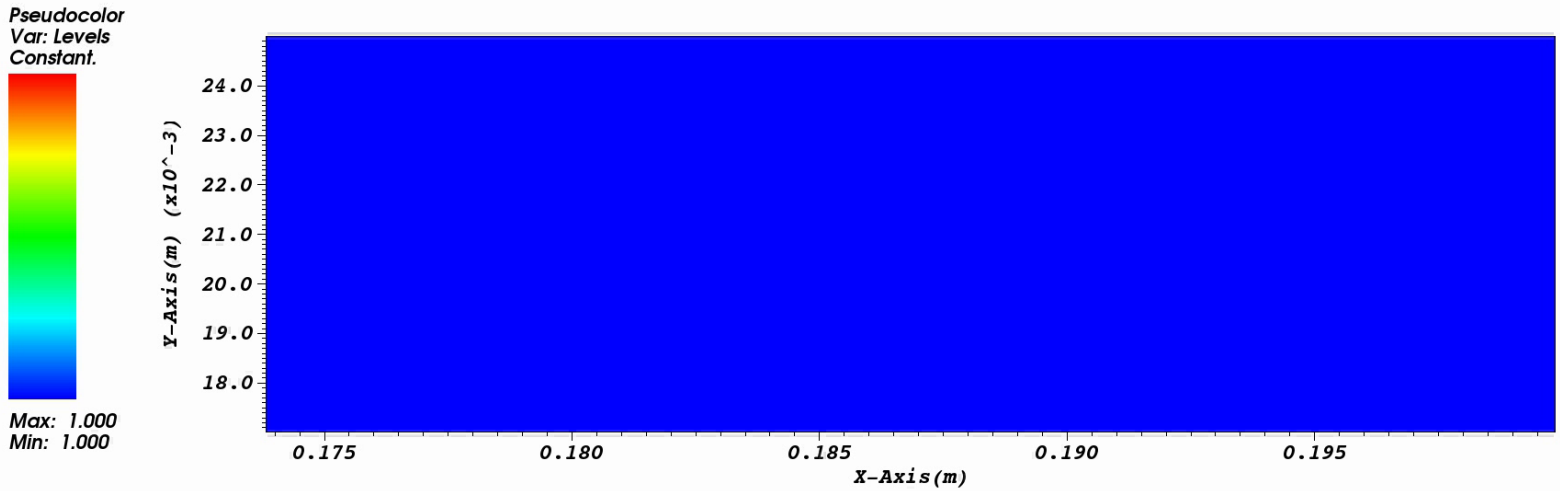

M. Ihme, Y. Sun, RD, *51st AIAA Aerospace Sciences Meeting*, AIAA-2013-0538 ,2013

Reactive case: $H_2 : O_2 : Ar - 15 : 17.85 : 67.15$

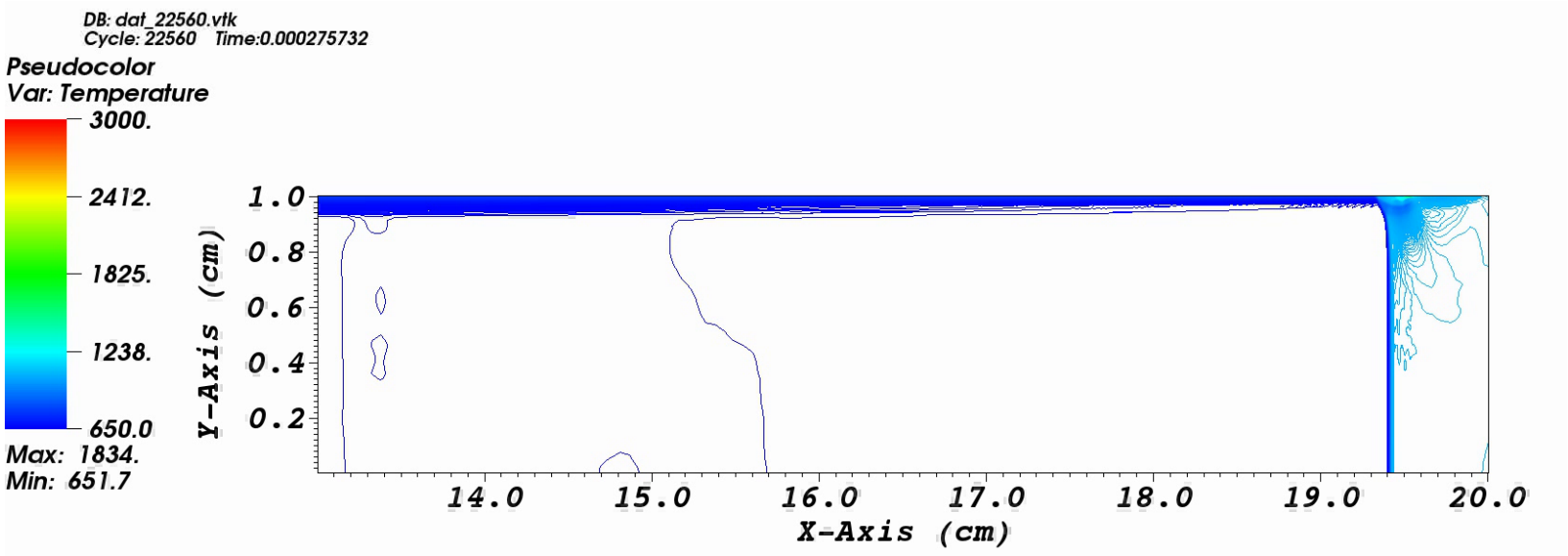

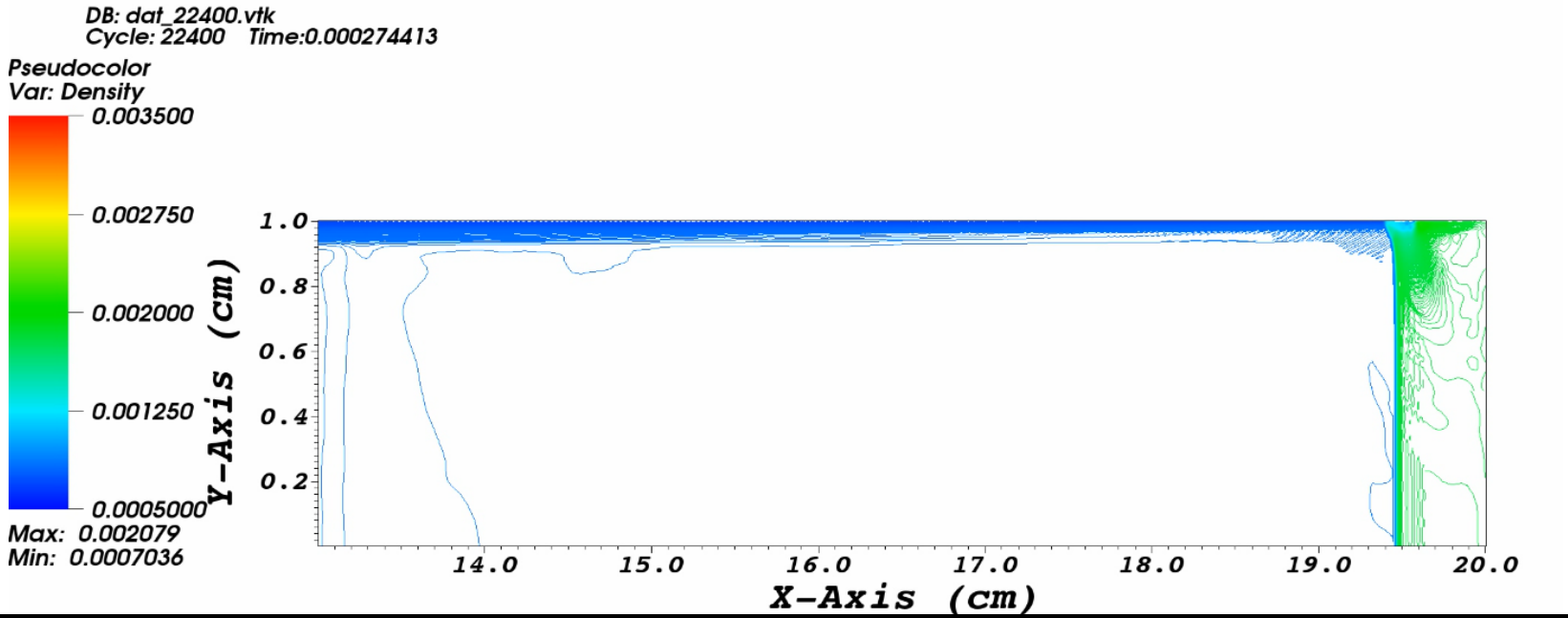

Detonation establishment in a scramjet combustor

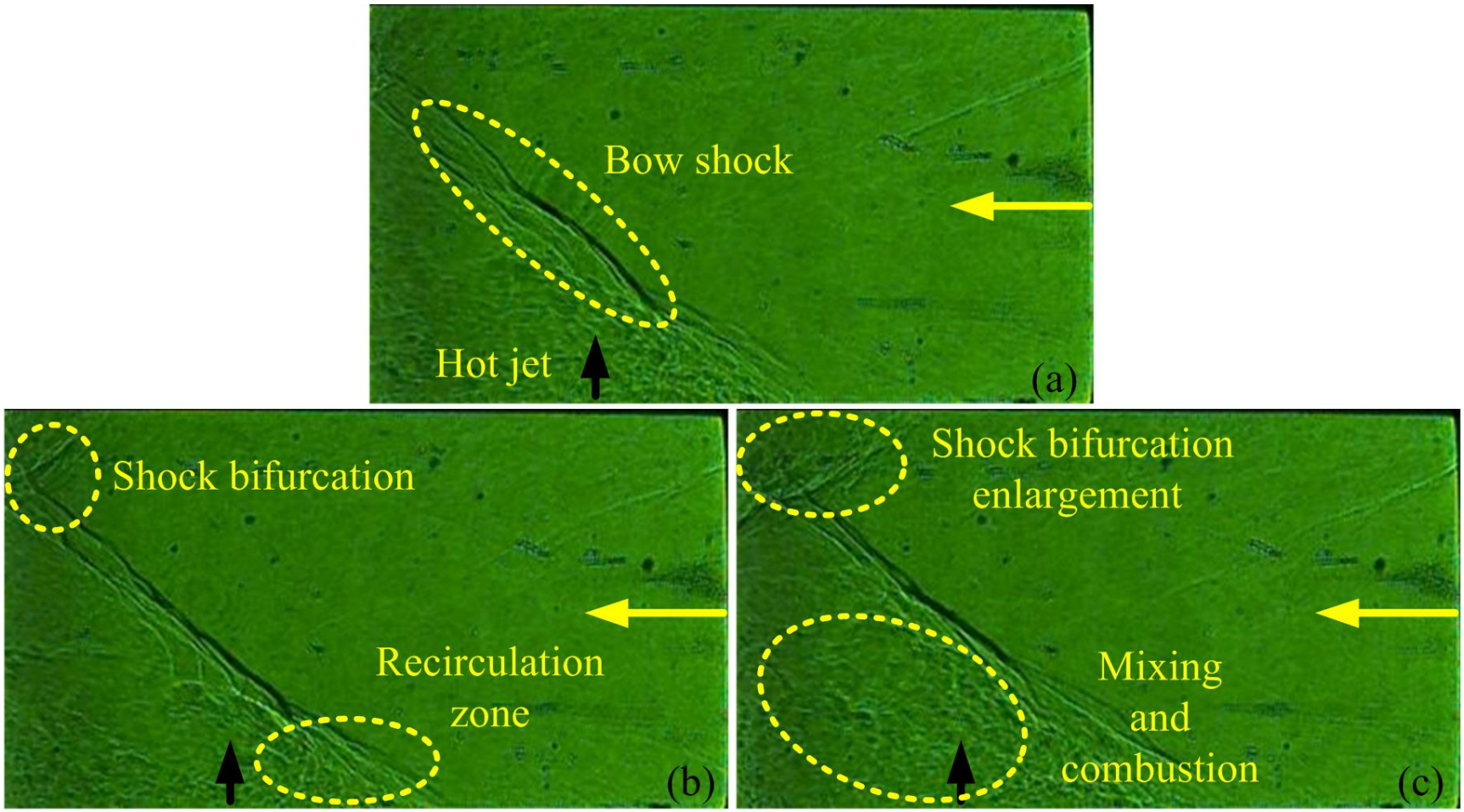

C. Cai, RD, J. Liang, M. Sun, Y. Mahmoudi, *Combust. Flame* 190: 201–215, 2018

Setup 1 – Experiment $\phi = 0.28$

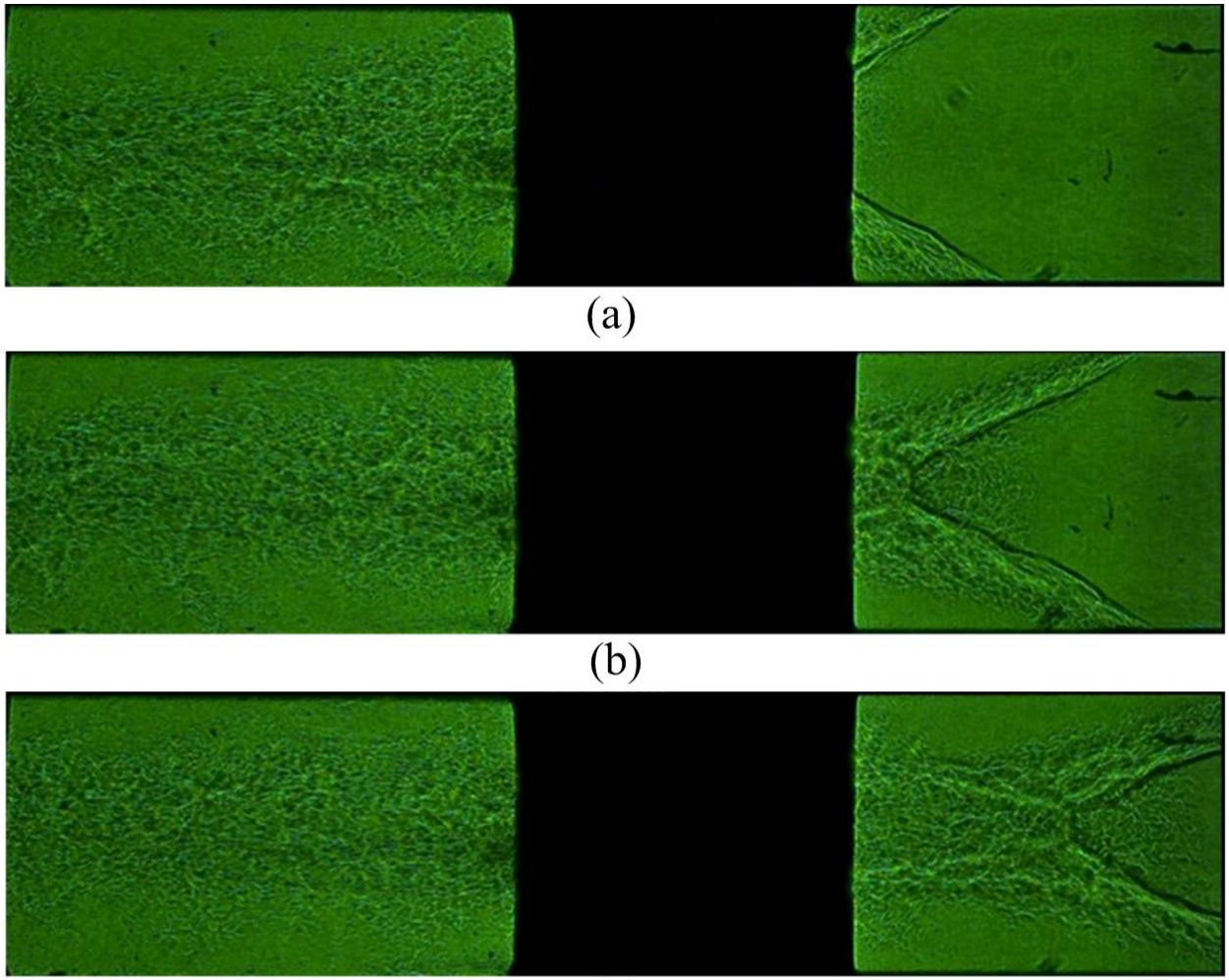

$H_2 : O_2 : N_2 - 0.56 : 1.0 : 2.9$, $p_0 = 36.1\,\mathrm{kPa}$, $T_0 = 581\,\mathrm{K}$, inflow $V_I = 1532\,\mathrm{m/s}$, $V_{CJ} = 1431\,\mathrm{m/s}$

Setup 1 – Numerical simulation $\phi = 0.28$

ρ

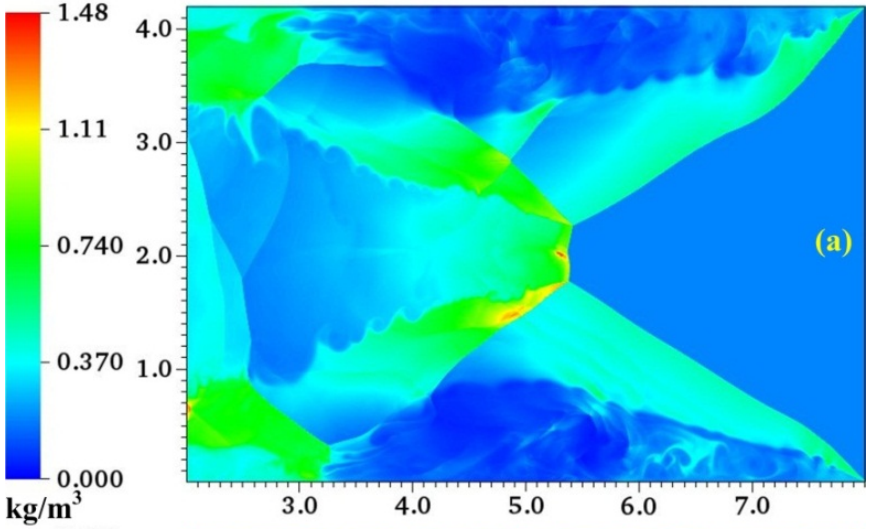

Y_{OH}

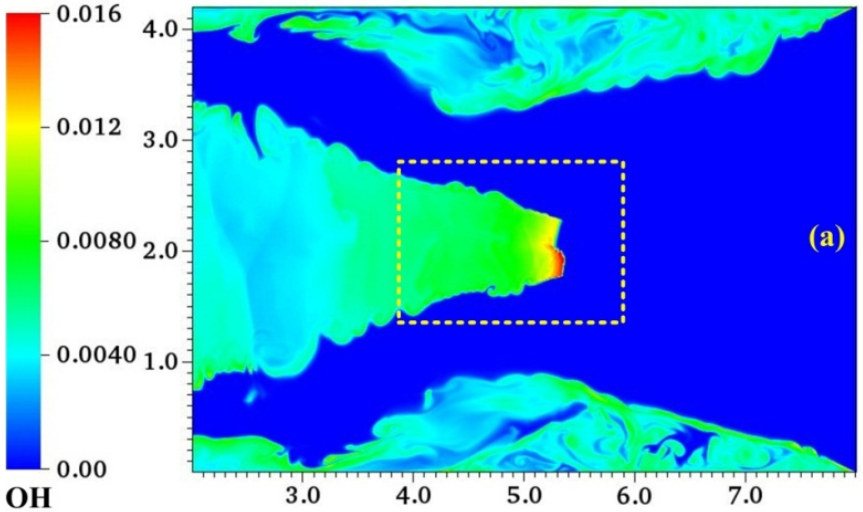

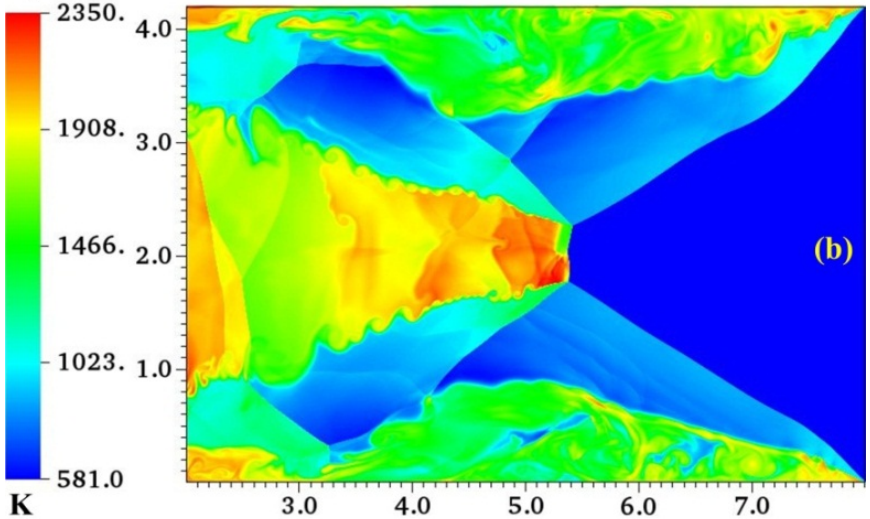

T

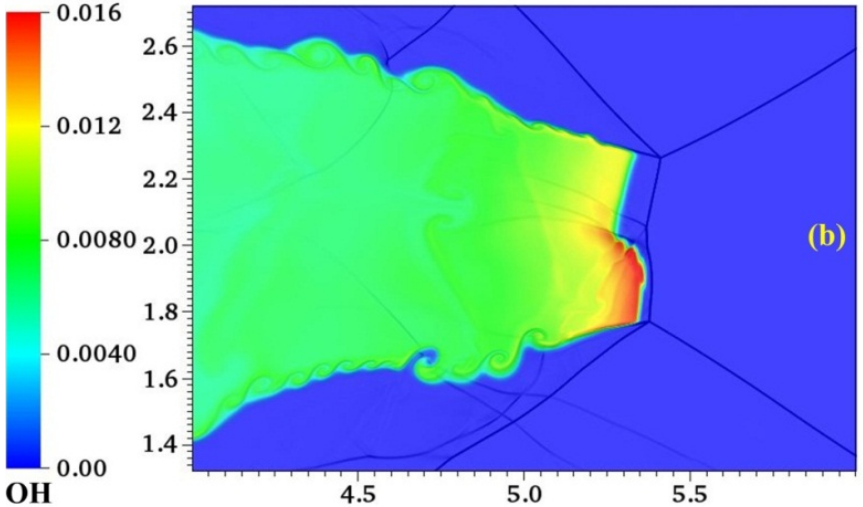

Y_{OH}

Setup 1 – Numerical simulation $\phi = 0.28$

ρ

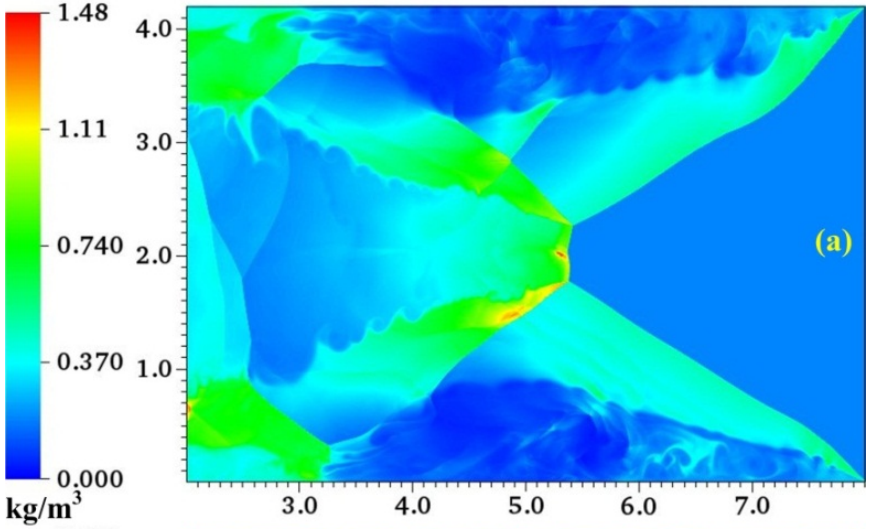

Y_{OH}

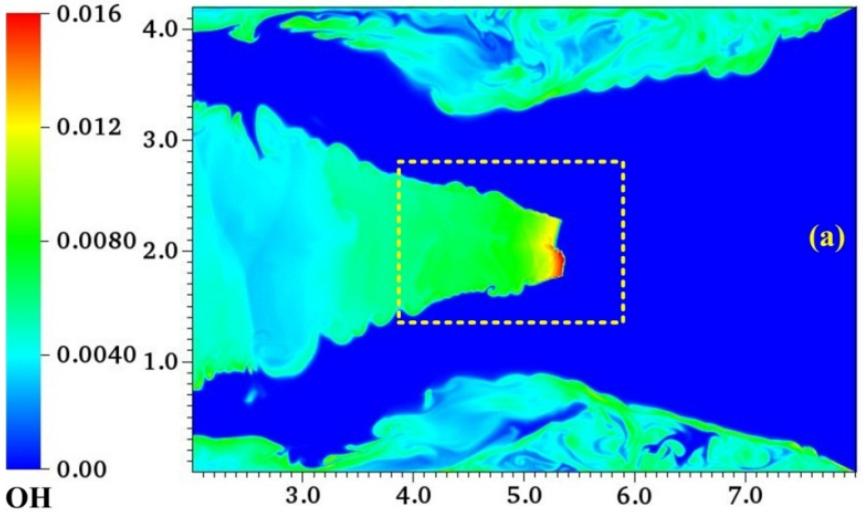

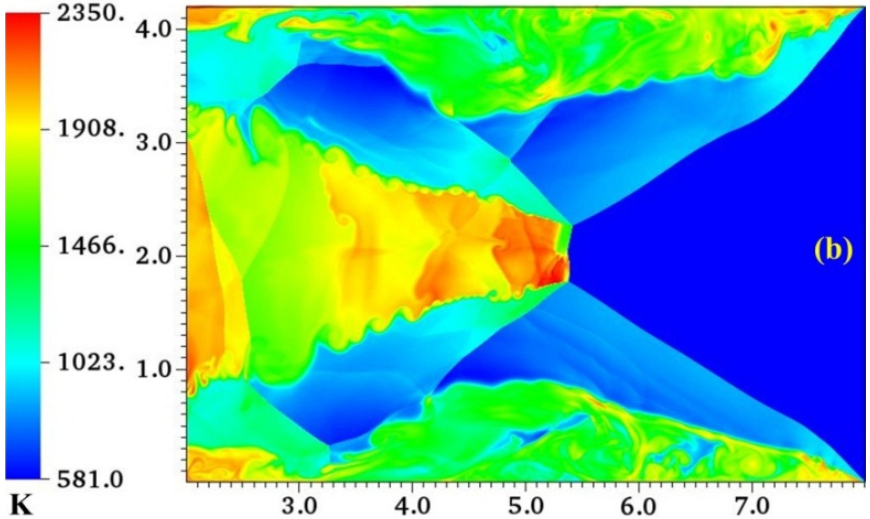

T

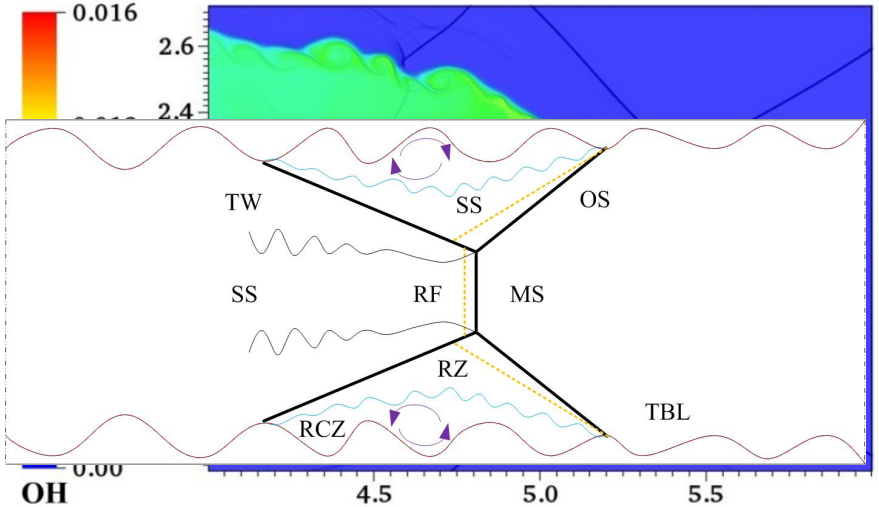

Y_{OH}

Setup 2 – Experiment $\phi = 0.29$

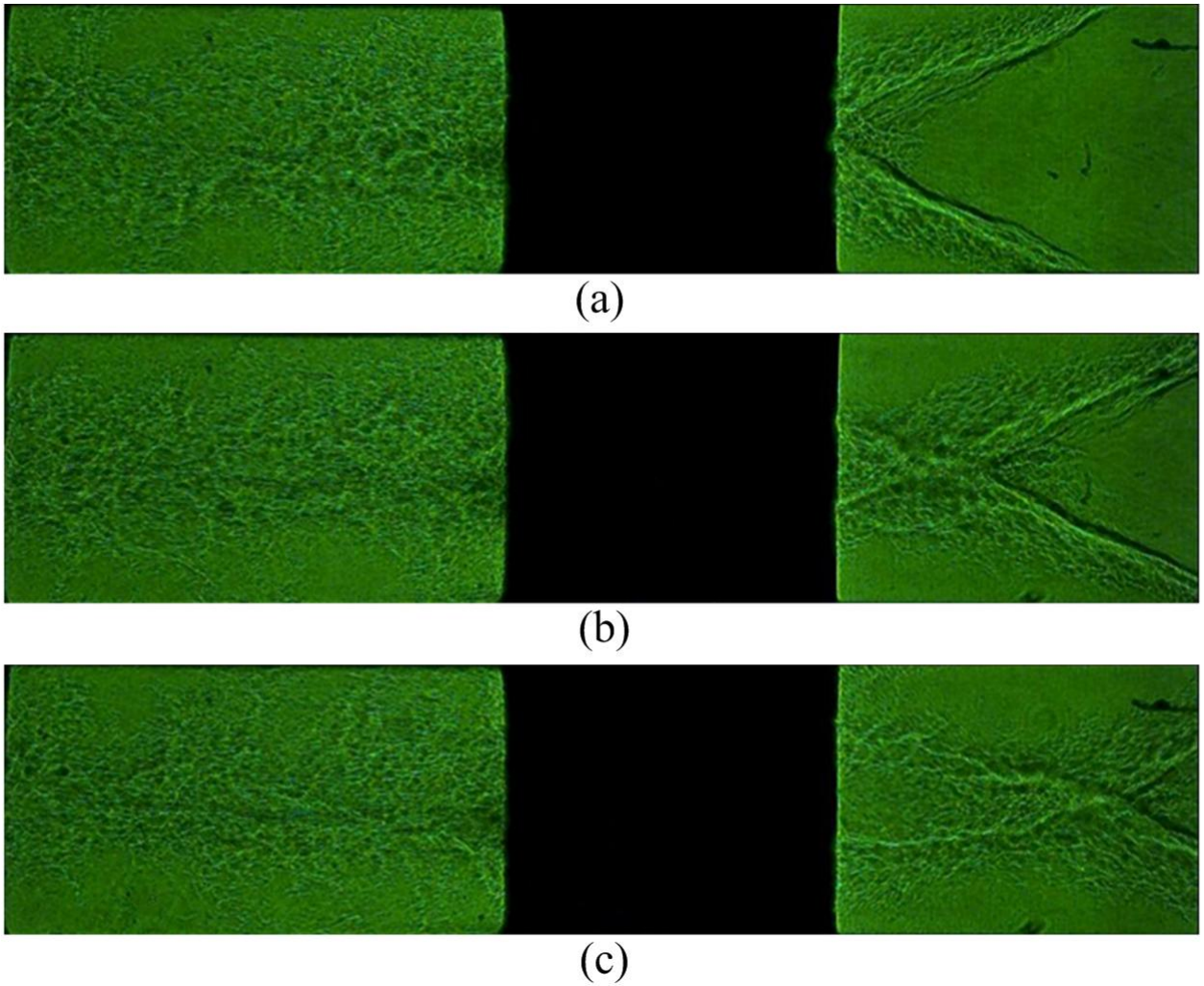

$H_2 : O_2 : N_2 - 0.58 : 1.0 : 2.9$, $p_0 = 36.1\,\mathrm{kPa}$, $T_0 = 581\,\mathrm{K}$, inflow $V_I = 1532\,\mathrm{m/s}$

Numerical simulation $\phi = 0.29$

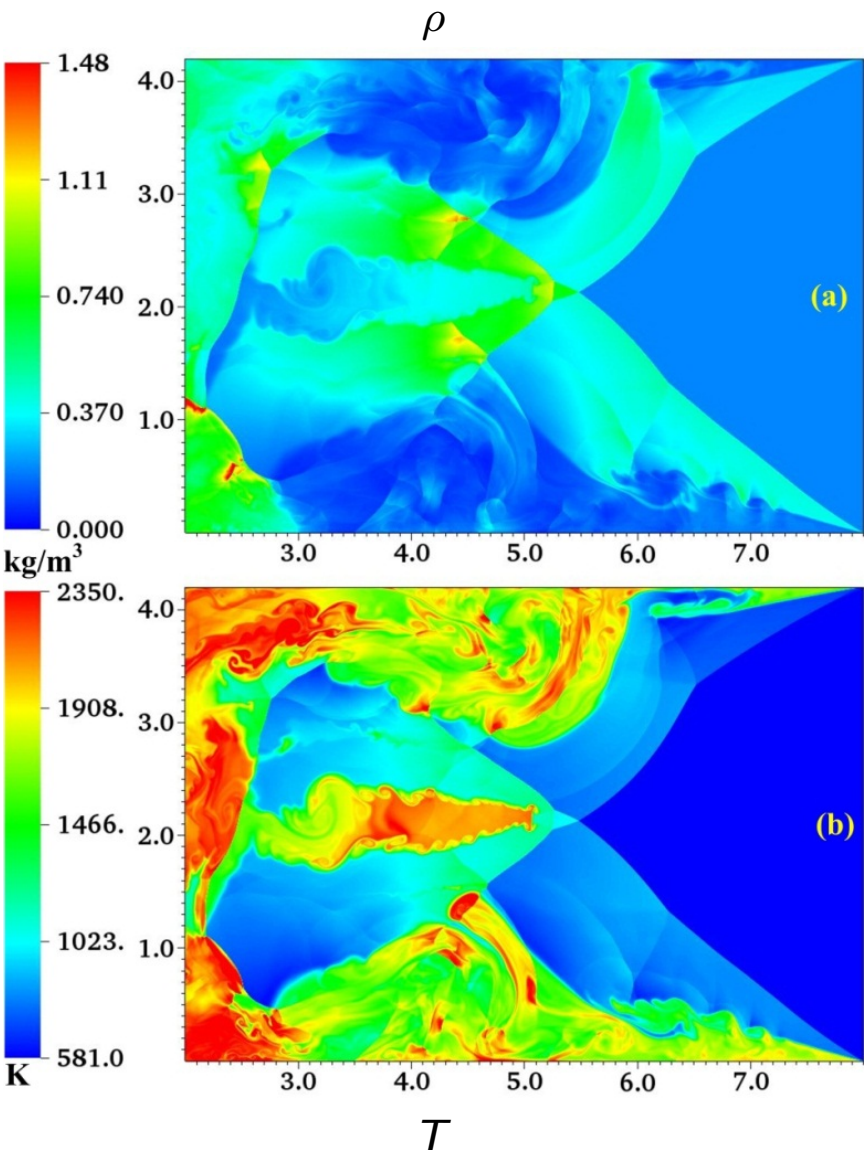

- SAMR simulation with 4 additional levels (2,2,2,2), 137.8 Pts/l_{ig}

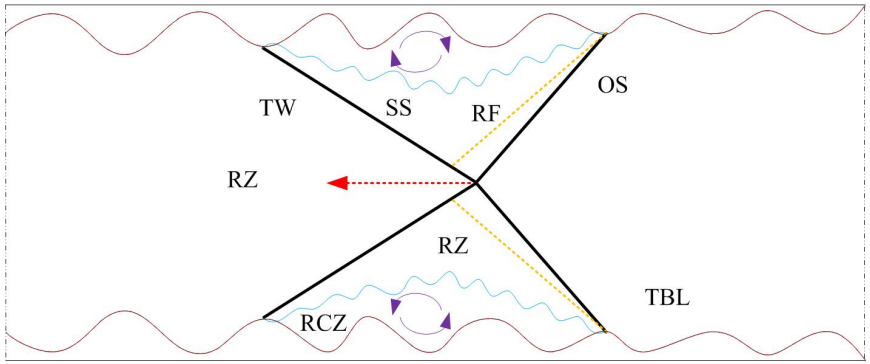

Conclusions – Detonations

- For small mechanisms, detailed detonation structure simulations and accurate DNS are nowadays possible for realistic 2d geometries
- Accurate studies for idealized 3d configurations feasible
- Resolution down to the scale of secondary triple points can be provided on parallel capacity computing systems

Conclusions – Detonations

- For small mechanisms, detailed detonation structure simulations and accurate DNS are nowadays possible for realistic 2d geometries
- Accurate studies for idealized 3d configurations feasible
- Resolution down to the scale of secondary triple points can be provided on parallel capacity computing systems
- Enabling components:
  - Splitting methods combined with high-resolution FV schemes for hyrodynamic transport
  - SAMR provides a sufficient spatial and temporal resolution. Savings from SAMR for pipe bend simulations: up to >680x

Conclusions – Detonations

- For small mechanisms, detailed detonation structure simulations and accurate DNS are nowadays possible for realistic 2d geometries
- Accurate studies for idealized 3d configurations feasible
- Resolution down to the scale of secondary triple points can be provided on parallel capacity computing systems
- Enabling components:
  - Splitting methods combined with high-resolution FV schemes for hyrodynamic transport
  - SAMR provides a sufficient spatial and temporal resolution. Savings from SAMR for pipe bend simulations: up to >680x
- Future work will concentrate on non-Cartesian and higher order schemes with low numerical dissipation geared to DNS.

References I

[Axdahl et al., 2011] Axdahl, E., Kumar, A., and Wilhite, A. (2011). Study of unsteady, sphere-driven, shock-induced combustion for application to hypervelocity airbreathing propulsio. In *Proc. 47th AIAA/ASME/SAE/SAEE Joint Propulsion Conference & Exhibit*.

[Barton et al., 2013] Barton, P. T., Deiterding, R., Meiron, D. I., and Pullin, D. I. (2013). Eulerian continuum model and adaptive finite-difference method for high-velocity impact and penetration problems. *J. Comput. Phys.*, 240:76–99.

[Bell et al., 1994] Bell, J., Berger, M., Saltzman, J., and Welcome, M. (1994). Three-dimensional adaptive mesh refinement for hyperbolic conservation laws. *SIAM J. Sci. Comp.*, 15(1):127–138.

[Berger, 1986] Berger, M. (1986). Data structures for adaptive grid generation. *SIAM J. Sci. Stat. Comput.*, 7(3):904–916.

[Berger and Colella, 1988] Berger, M. and Colella, P. (1988). Local adaptive mesh refinement for shock hydrodynamics. *J. Comput. Phys.*, 82:64–84.

[Berger and Rigoutsos, 1991] Berger, M. and Rigoutsos, I. (1991). An algorithm for point clustering and grid generation. *IEEE Transactions on Systems, Man, and Cybernetics*, 21(5):1278–1286.

[Cai et al., 2018] Cai, X., Deiterding, R., Liang, J., Sun, M., and Mahmoudi, Y. (2018). Experimental and numerical investigations on propagating modes of detonations: detonation wave/boundary layer interaction. *Combust. Flame*, 190:201–215.

References II

[Cai et al., 2016] Cai, X., Liang, J., Deiterding, R., Che, Y., and Lin, Z. (2016). Adaptive mesh refinement based simulations of three-dimensional detonation combustion in supersonic combustible mixtures with a detailed reaction model. *Int. J. Hydrogen Energy*, 41:3222–3239.

[Cerminara et al., 2018] Cerminara, A., Deiterding, R., and Sandham, N. (2018). Dns of hypersonic flow over porous surfaces with a hybrid method. In *AIAA Aerospace Sciences Meeting, AIAA Science and Technology Forum and Exposition*.

[Cirak et al., 2007] Cirak, F., Deiterding, R., and Mauch, S. P. (2007). Large-scale fluid-structure interaction simulation of viscoplastic and fracturing thin shells subjected to shocks and detonations. *Computers & Structures*, 85(11-14):1049–1065.

[Deiterding, 2003] Deiterding, R. (2003). *Parallel adaptive simulation of multi-dimensional detonation structures*. PhD thesis, Brandenburgische Technische Universität Cottbus.

[Deiterding, 2005] Deiterding, R. (2005). Construction and application of an AMR algorithm for distributed memory computers. In Plewa, T., Linde, T., and Weirs, V. G., editors, *Adaptive Mesh Refinement - Theory and Applications*, volume 41 of *Lecture Notes in Computational Science and Engineering*, pages 361–372. Springer.

[Deiterding, 2009] Deiterding, R. (2009). A parallel adaptive method for simulating shock-induced combustion with detailed chemical kinetics in complex domains. *Computers & Structures*, 87:769–783.

[Deiterding, 2011a] Deiterding, R. (2011a). Block-structured adaptive mesh refinement - theory, implementation and application. *European Series in Applied and Industrial Mathematics: Proceedings*, 34:97–150.

References III

[Deiterding, 2011b] Deiterding, R. (2011b). High-resolution numerical simulation and analysis of Mach reflection structures in detonation waves in low-pressure $\mathrm{h_2} : \mathrm{o_2} : \mathrm{ar}$ mixtures: a summary of results obtained with adaptive mesh refinement framework AMROC. *J. Combustion*, 2011:738969.

[Deiterding and Bader, 2005] Deiterding, R. and Bader, G. (2005). High-resolution simulation of detonations with detailed chemistry. In Warnecke, G., editor, *Analysis and Numerics for Conservation Laws*, pages 69–91. Springer.

[Deiterding et al., 2009a] Deiterding, R., Cirak, F., and Mauch, S. P. (2009a). Efficient fluid-structure interaction simulation of viscoplastic and fracturing thin-shells subjected to underwater shock loading. In Hartmann, S., Meister, A., Schäfer, M., and Turek, S., editors, *Int. Workshop on Fluid-Structure Interaction. Theory, Numerics and Applications, Herrsching am Ammersee 2008*, pages 65–80. kassel university press GmbH.

[Deiterding et al., 2007] Deiterding, R., Cirak, F., Mauch, S. P., and Meiron, D. I. (2007). A virtual test facility for simulating detonation- and shock-induced deformation and fracture of thin flexible shells. *Int. J. Multiscale Computational Engineering*, 5(1):47–63.

[Deiterding et al., 2009b] Deiterding, R., Domingues, M. O., Gomes, S. M., Roussel, O., and Schneider, K. (2009b). Adaptive multiresolution or adaptive mesh refinement? A case study for 2D Euler equations. *European Series in Applied and Industrial Mathematics: Proceedings*, 29:28–42.

References IV

[Deiterding et al., 2006] Deiterding, R., Radovitzky, R., Mauch, S. P., Noels, L., Cummings, J. C., and Meiron, D. I. (2006). A virtual test facility for the efficient simulation of solid materials under high energy shock-wave loading. *Engineering with Computers*, 22(3-4):325–347.

[Deiterding and Wood, 2016] Deiterding, R. and Wood, S. L. (2016). Predictive wind turbine simulation with an adaptive lattice Boltzmann method for moving boundaries. *J. Phys. Conf. Series*, 753:082005.

[Feldhusen et al., 2016] Feldhusen, K., Deiterding, R., and Wagner, C. (2016). A dynamically adaptive lattice Boltzmann method for thermal convection problems. *J. Applied Math. and Computer Science*, 26:735–747.

[Fragner and Deiterding, 2016] Fragner, M. M. and Deiterding, R. (2016). Investigating cross-wind stability of high speed trains with large-scale parallel cfd. *Int. J. Comput. Fluid Dynamics*, 30:402–407.

[Gomes et al., 2015] Gomes, A. K. F., Domingues, M. O., Schneider, K., Mendes, O., and Deiterding, R. (2015). An adaptive multiresolution method for ideal magnetohydrodynamics using divergence cleaning with parabolic-hyperbolic correction. *Applied Numerical Mathematics*, 95:199–213.

[Harten, 1983] Harten, A. (1983). High resolution schemes for hyperbolic conservation laws. *J. Comput. Phys.*, 49:357–393.

[Harten and Hyman, 1983] Harten, A. and Hyman, J. M. (1983). Self-adjusting grid methods for one-dimensional hyperbolic conservation laws. *J. Comput. Phys.*, 50:235–269.

References V

[Jachimowski, 1988] Jachimowski, C. J. (1988). An analytical study of the hydrogen-air reaction mechanism with application to scramjet combustion. Technical Report TP-2791, NASA.

[Lehr, 1972] Lehr, H. F. (1972). Experiments on shock-induced combustion. *Astronautica Acta*, 17:589–597.

[Lombardini and Deiterding, 2010] Lombardini, M. and Deiterding, R. (2010). Large-eddy simulation of Richtmyer-Meshkov instability in a converging geometry. *Physics of Fluids*, 22(9):091112.

[Mauch, 2003] Mauch, S. P. (2003). *Efficient Algorithms for Solving Static Hamilton-Jacobi Equations*. PhD thesis, California Institute of Technology.

[Pantano et al., 2007] Pantano, C., Deiterding, R., Hill, D. J., and Pullin, D. I. (2007). A low-numerical dissipation patch-based adaptive mesh refinement method for large-eddy simulation of compressible flows. *J. Comput. Phys.*, 221(1):63–87.

[Perotti et al., 2013] Perotti, L. E., Deiterding, R., Inaba, K., Shepherd, J. E., and Ortiz, M. (2013). Elastic response of water-filled fiber composite tubes under shock wave loading. *Int. J. Solids and Structures*, 50(3-4):473–486.

[Quirk, 1994] Quirk, J. J. (1994). A contribution to the great Riemann solver debate. *Int. J. Numer. Meth. Fluids*, 18:555–574.

[Sanders et al., 1998] Sanders, R., Morano, E., and Druguett, M.-C. (1998). Multidimensional dissipation for upwind schemes: Stability and applications to gas dynamics. *J. Comput. Phys.*, 145:511–537.

References VI

[Souza Lopes et al., 2018] Souza Lopes, M. M., Deiterding, R., Gomes, A. K. F., Mendes, O., and Domingues, M. O. (2018). An ideal compressible magnetohydrodynamic solver with parallel block-structured adaptive mesh refinement. *Computers & Fluids*. in press.

[Wan et al., 2017] Wan, Q., Jeon, H., Deiterding, R., and Eliasson, V. (2017). Numerical and experimental investigation of oblique shock wave reflection off a water wedge. *J. Fluid Mech.*, 826:732–758.

[Westbrook, 1982] Westbrook, C. K. (1982). Chemical kinetics of hydrocarbon oxidation in gaseous detonations. *Combust. Flame*, 46:191–210.

[Yungster and Radhakrishnan, 1996] Yungster, S. and Radhakrishnan, K. (1996). A fully implicit time accurate method for hypersonic combustion: application to shock-induced combustion instability. *Shock Waves*, 5:293–303.

[Ziegler et al., 2011] Ziegler, J. L., Deiterding, R., Shepherd, J. E., and Pullin, D. I. (2011). An adaptive high-order hybrid scheme for compressive, viscous flows with detailed chemistry. *J. Comput. Phys.*, 230(20):7598–7630.

Riemann solver for combustion: carbuncle fix

Entropy corrections

Riemann solver for combustion: carbuncle fix

Entropy corrections [Harten, 1983]

1. $|\tilde{s}_\iota| = \begin{cases} |s_\iota| & \text{if} |s_\iota| \geq 2\eta \\ \frac{|s_\iota^2|}{4\eta} + \eta & \text{otherwise} \end{cases}$

$\eta = \frac{1}{2} \max_\iota \left\{ |s_\iota(\mathbf{q}_R) - s_\iota(\mathbf{q}_L)| \right\}$

Riemann solver for combustion: carbuncle fix

Entropy corrections [Harten, 1983]
[Harten and Hyman, 1983]

1. $|\tilde{s}_\iota| = \begin{cases} |s_\iota| & \text{if} |s_\iota| \geq 2\eta \\ \frac{|s_\iota^2|}{4\eta} + \eta & \text{otherwise} \end{cases}$
   $\eta = \frac{1}{2} \max_\iota \left\{ |s_\iota(\mathbf{q}_R) - s_\iota(\mathbf{q}_L)| \right\}$
2. Replace $|s_\iota|$ by $|\tilde{s}_\iota|$ only if
   $s_\iota(\mathbf{q}_L) < 0 < s_\iota(\mathbf{q}_R)$

Riemann solver for combustion: carbuncle fix

Entropy corrections [Harten, 1983] [Harten and Hyman, 1983]

1. $|\tilde{s}_\iota| = \begin{cases} |s_\iota| & \text{if} |s_\iota| \geq 2\eta \\ \frac{|s_\iota^2|}{4\eta} + \eta & \text{otherwise} \end{cases}$
   $\eta = \frac{1}{2} \max_\iota \left\{ |s_\iota(\mathbf{q}_R) - s_\iota(\mathbf{q}_L)| \right\}$
2. Replace $|s_\iota|$ by $|\tilde{s}_\iota|$ only if $s_\iota(\mathbf{q}_L) < 0 < s_\iota(\mathbf{q}_R)$

2D modification of entropy correction [Sanders et al., 1998]:

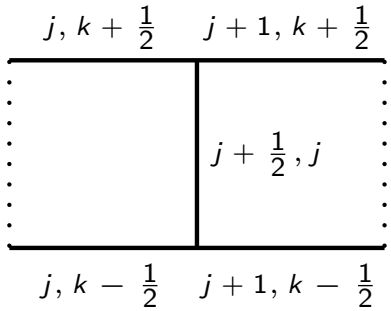

$$\tilde{\eta}_{j+1/2,k} = \max \left\{ \eta_{j+1/2,k}, \eta_{j,k-1/2}, \ \eta_{j,k+1/2}, \eta_{j+1,k-1/2}, \eta_{j+1,k+1/2} \right\}$$

Riemann solver for combustion: carbuncle fix

Entropy corrections [Harten, 1983] [Harten and Hyman, 1983]

1. $|\tilde{s}_\iota| = \begin{cases} |s_\iota| & \text{if} |s_\iota| \geq 2\eta \\ \frac{|s_\iota^2|}{4\eta} + \eta & \text{otherwise} \end{cases}$
   $\eta = \frac{1}{2} \max_\iota \left\{ |s_\iota(\mathbf{q}_R) - s_\iota(\mathbf{q}_L)| \right\}$
2. Replace $|s_\iota|$ by $|\tilde{s}_\iota|$ only if $s_\iota(\mathbf{q}_L) < 0 < s_\iota(\mathbf{q}_R)$

2D modification of entropy correction [Sanders et al., 1998]:

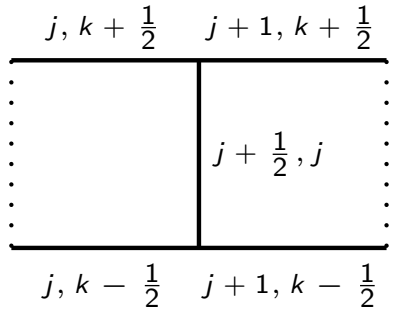

$$\tilde{\eta}_{j+1/2,k} = \max \left\{ \eta_{j+1/2,k}, \eta_{j,k-1/2}, \ \eta_{j,k+1/2}, \eta_{j+1,k-1/2}, \eta_{j+1,k+1/2} \right\}$$

Carbuncle phenomenon

- [Quirk, 1994]
- Test from [Deiterding, 2003]

Roe + EC 1.

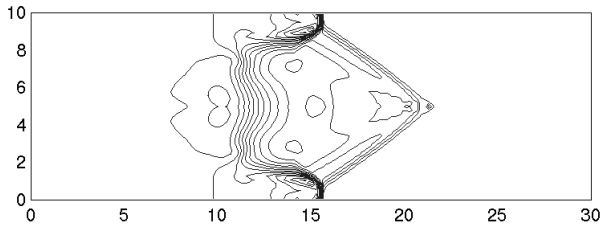

Exact Riemann solver

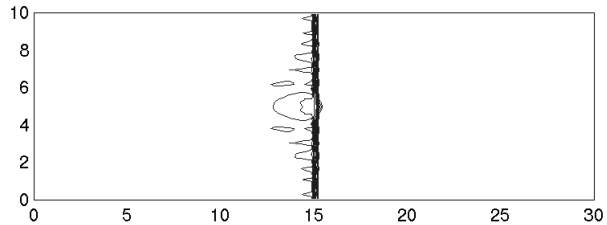

Roe + EC 2.

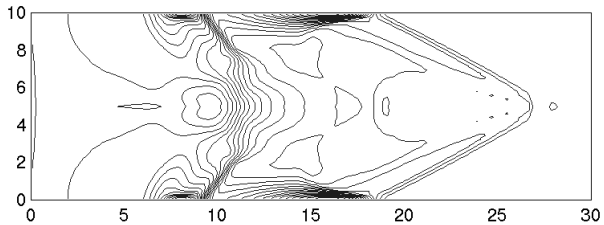

SW FVS, VL FVS, HLL, Roe + EC 2.+2D

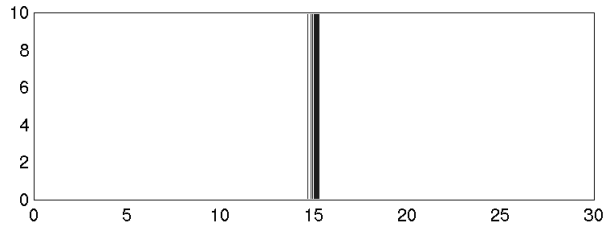

Clustering by signatures

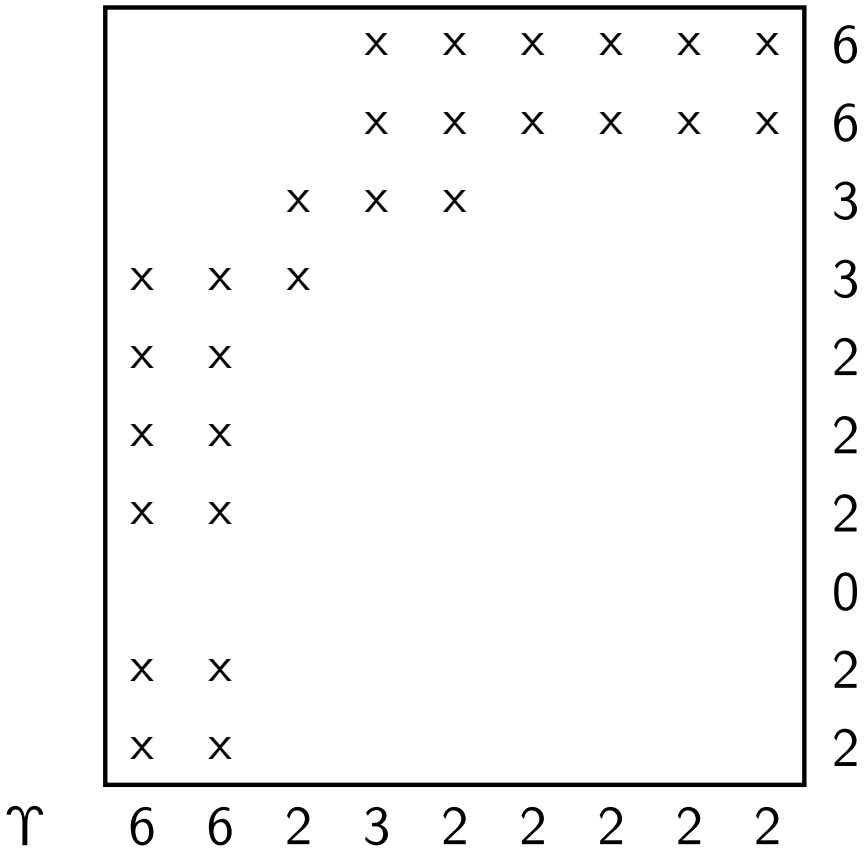

ϒ Flagged cells per row/column

Δ Second derivative of ϒ, $\Delta = \Upsilon_{\nu+1} - 2\,\Upsilon_{\nu} + \Upsilon_{\nu-1}$

Technique from image detection: [Bell et al., 1994], see also [Berger and Rigoutsos, 1991], [Berger, 1986]

Clustering by signatures

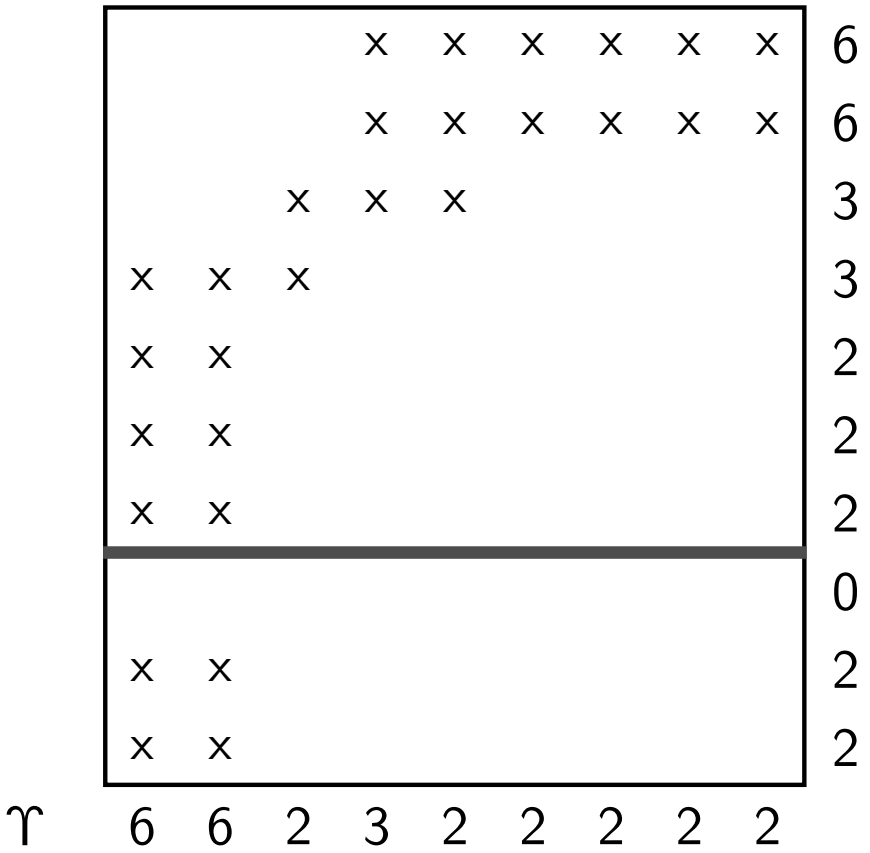

ϒ Flagged cells per row/column

Δ Second derivative of ϒ, $\Delta = \Upsilon_{\nu+1} - 2\,\Upsilon_{\nu} + \Upsilon_{\nu-1}$

Technique from image detection: [Bell et al., 1994], see also [Berger and Rigoutsos, 1991], [Berger, 1986]

Clustering by signatures

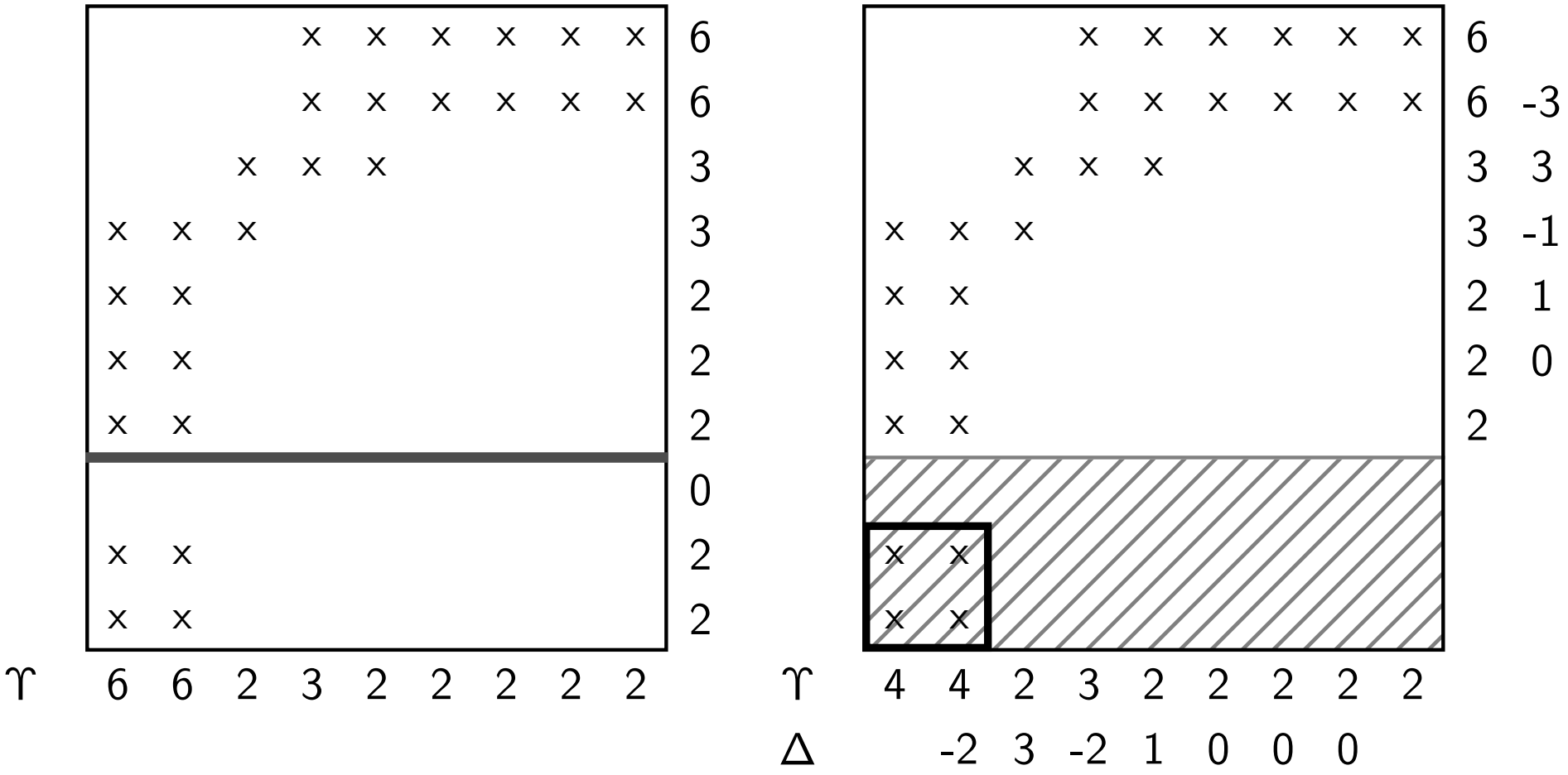

ϒ Flagged cells per row/column

Δ Second derivative of ϒ, $\Delta = \Upsilon_{\nu+1} - 2\,\Upsilon_{\nu} + \Upsilon_{\nu-1}$

Technique from image detection: [Bell et al., 1994], see also [Berger and Rigoutsos, 1991], [Berger, 1986]

Clustering by signatures

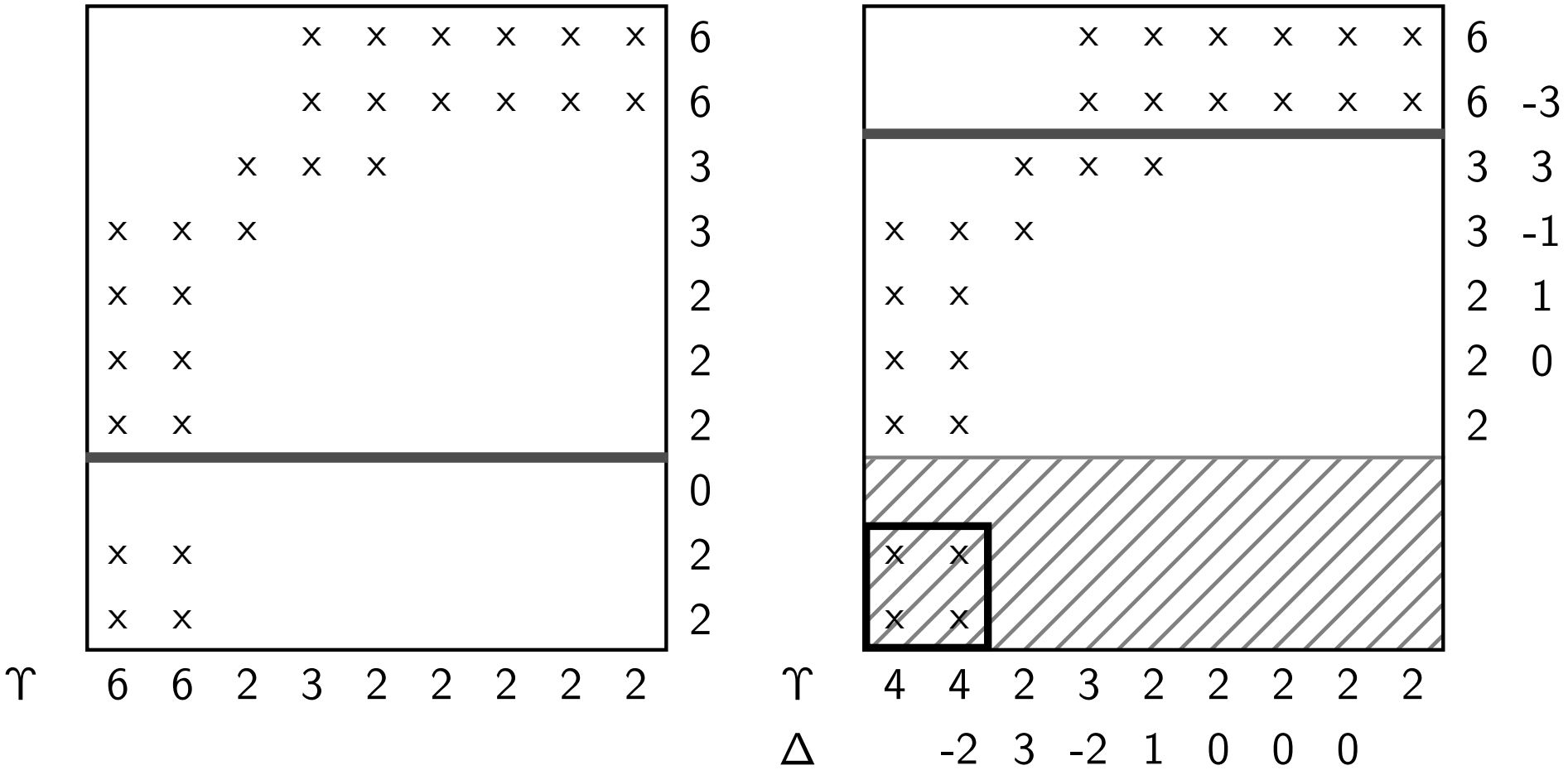

ϒ Flagged cells per row/column

Δ Second derivative of ϒ, $\Delta = \Upsilon_{\nu+1} - 2\,\Upsilon_{\nu} + \Upsilon_{\nu-1}$

Technique from image detection: [Bell et al., 1994], see also [Berger and Rigoutsos, 1991], [Berger, 1986]

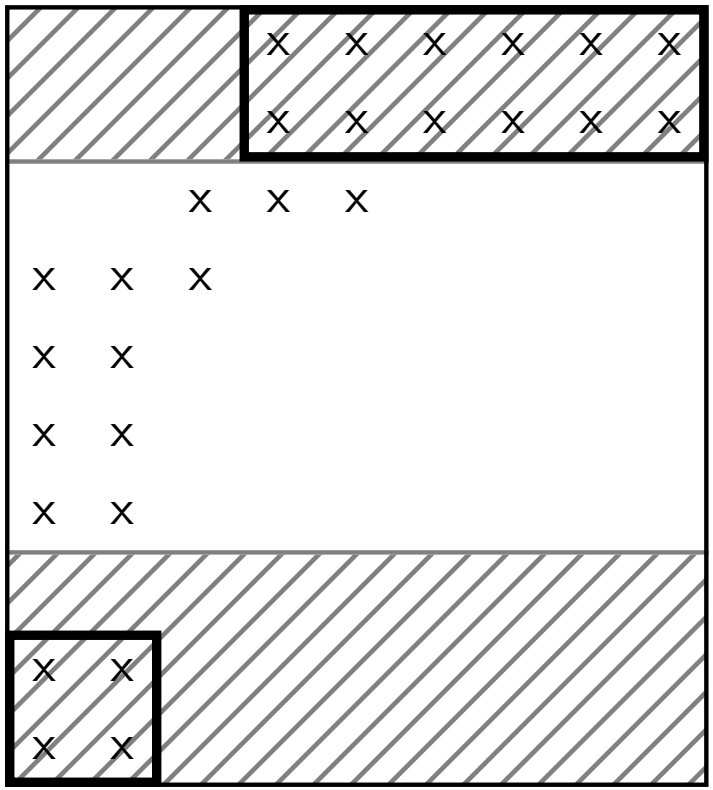

Recursive generation of $\breve{G}_{l,m}$

1. 0 in Υ
2. Largest difference in Δ
3. Stop if ratio between flagged and unflagged cell $> \eta_{tol}$

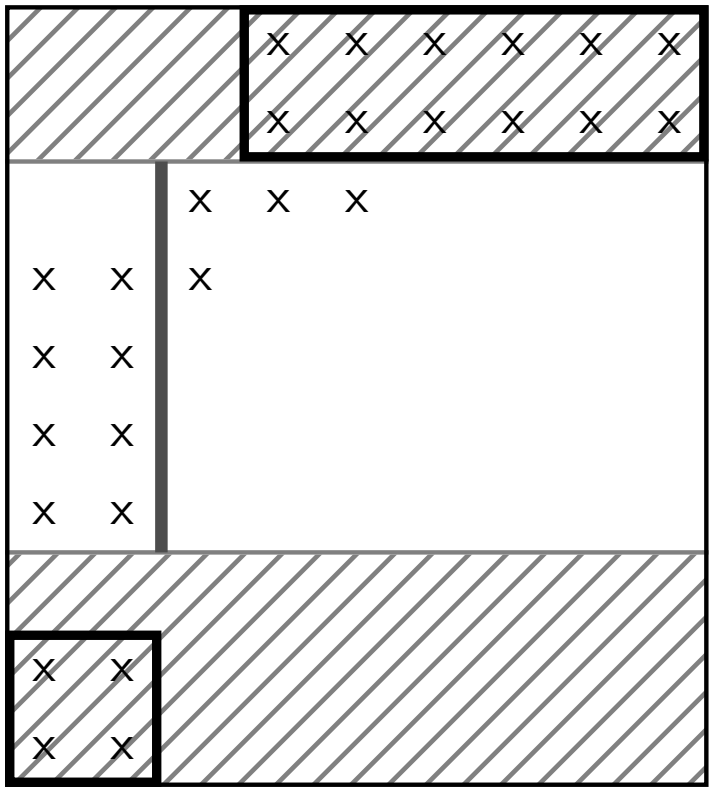

Recursive generation of $\breve{G}_{l,m}$

1. 0 in Υ
2. Largest difference in Δ
3. Stop if ratio between flagged and unflagged cell $> \eta_{tol}$

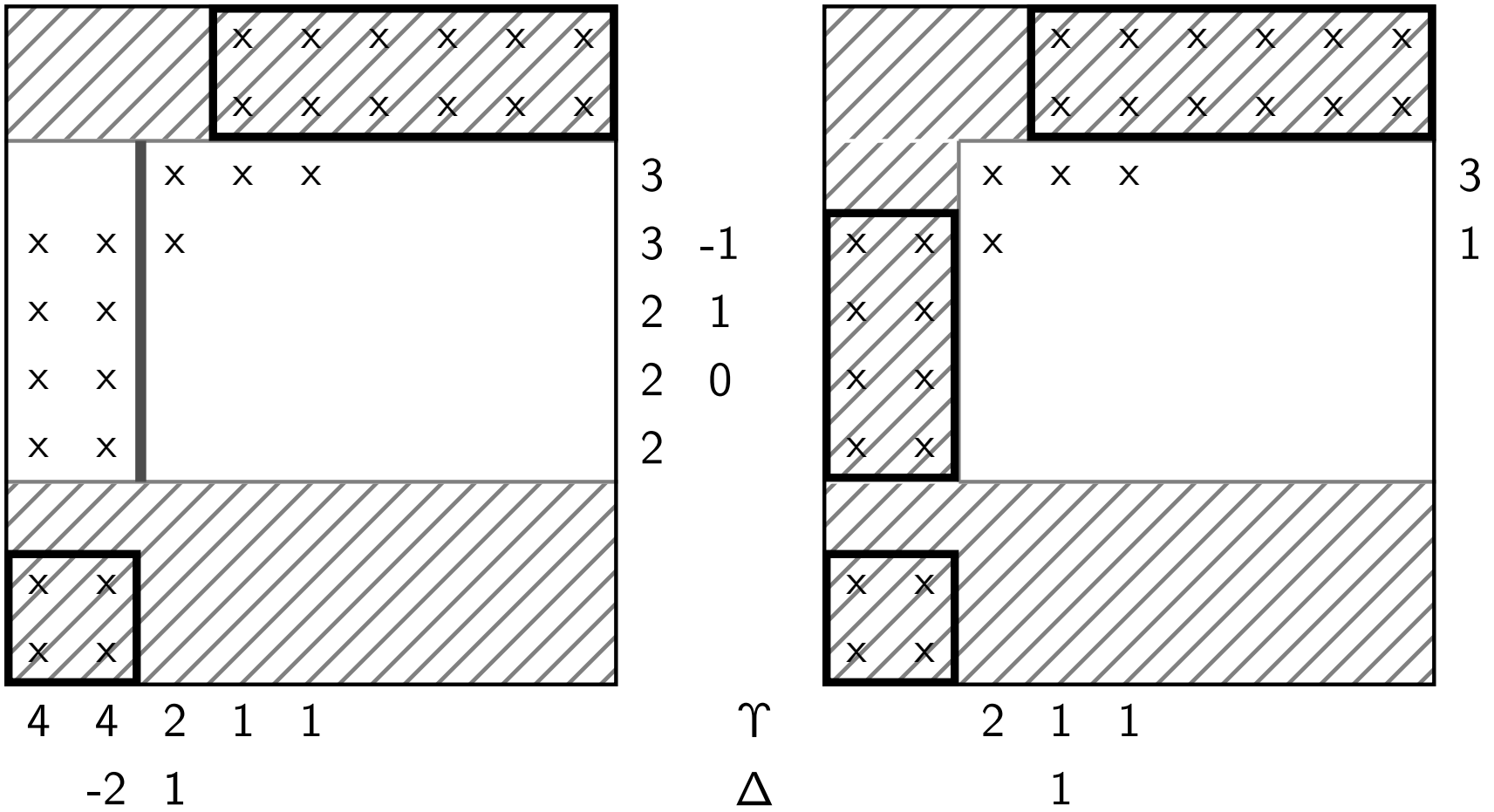

Recursive generation of $\breve{G}_{l,m}$

1. 0 in Υ
2. Largest difference in Δ
3. Stop if ratio between flagged and unflagged cell $> \eta_{tol}$

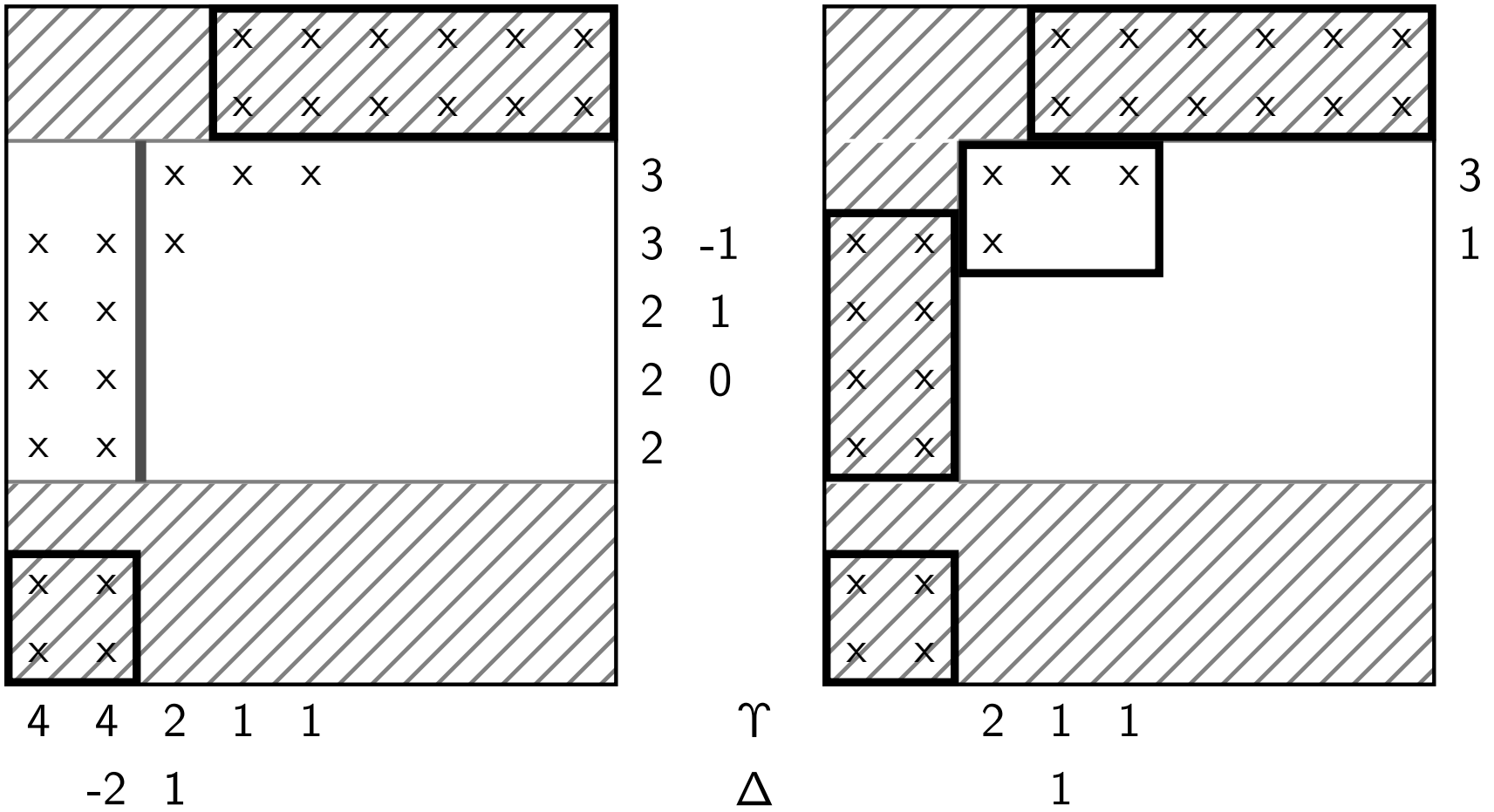

Recursive generation of $\breve{G}_{l,m}$

1. 0 in Υ
2. Largest difference in Δ
3. Stop if ratio between flagged and unflagged cell $> \eta_{tol}$